

**Study of Electric Multipole Transition
Probabilities & their importance
in reaction dynamics**

By

ANANYA KUNDU

(PHYS01201504021)

Bhabha Atomic Research Centre, Mumbai

*A thesis submitted to the
Board of Studies in Physical Sciences*

*In partial fulfilment of requirements
for the Degree of*

DOCTOR OF PHILOSOPHY

of

HOMI BHABHA NATIONAL INSTITUTE



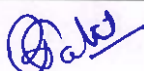
August, 2019

Homi Bhabha National Institute

Recommendations of the Viva Voce Committee

As members of the Viva Voce Committee, we certify that we have read the dissertation prepared by Ms. Ananya Kundu entitled "Study of electric multipole transition probabilities and their importance in reaction dynamics" and recommend that it may be accepted as fulfilling the thesis requirement for the award of Degree of Doctor of Philosophy.

Chairman – Dr. R. Palit



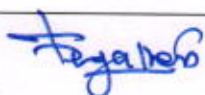
Date: 13/12/19

Guide / Convener – Dr. S. Santra



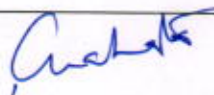
Date: 11/11/2019

Examiner – Dr. P. Sugathan



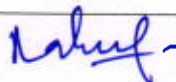
Date: 11/11/2019

Member 1- Dr. K. Mahata



Date: 11/11/2019

Member 2- Dr. R. Tripathi



Date: 11/11/2019

Technology Adviser- Dr. S. Mukhopadhyay



Date: 11/11/2019

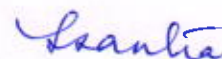
Final approval and acceptance of this thesis is contingent upon the candidate's submission of the final copies of the thesis to HBNI.

I/We hereby certify that I/we have read this thesis prepared under my/our direction and recommend that it may be accepted as fulfilling the thesis requirement.

Date: 13/12/2019

Place: BARC

Guide



STATEMENT BY THE AUTHOR

This dissertation has been submitted in partial fulfillment of requirements for an advanced degree at Homi Bhabha National Institute (HBNI) and is deposited in the library to be made available to borrowers under rules of the HBNI.

Brief quotations from this dissertation are allowable without special permission, provided that accurate acknowledgement of source is made. Requests for permission for extended quotation from or reproduction of this manuscript in whole or in part may be granted by the Competent Authority of HBNI when in his or her judgment the proposed use of the material is in the interests of scholarship. In all other instances, however, permission must be obtained from the author.

Ananya Kundu

(Ananya Kundu)

DECLARATION

I, hereby declare that the investigation presented in the thesis has been carried out by me. The work is original and the work has not been submitted earlier as a whole or in part for a degree/diploma at this or any other Institution/University.

Ananya Kundu
(Ananya Kundu)

List of publications arising from the thesis

I. Peer-reviewed Journals:

1. ‘Probing systematic model-dependence of complete fusion for reactions with weakly bound projectiles ${}^6,{}^7\text{Li}$ ’,
A. Kundu, S. Santra, A. Pal, D. Chattopadhyay, B. K. Nayak, A. Saxena and S. Kailas, *Phys. Rev. C* **94**, 014603 (2016).
2. ‘Elastic, inelastic and 1-nucleon transfer channels in ${}^7\text{Li}+{}^{120}\text{Sn}$ system’,
A. Kundu, S. Santra, A. Pal, D. Chattopadhyay, R. Tripathi, B. J. Roy, T. N. Nag, B. K. Nayak, A. Saxena and S. Kailas, *Phys. Rev. C* **95**, 034615 (2017).
3. ‘The low lying quadrupole and octupole collective excitations in ${}^{112,116,118,120,122,124}\text{Sn}$ isotopes’,
A. Kundu, S. Santra, A. Pal, D. Chattopadhyay, R. Tripathi, B. J. Roy, T. N. Nag, B. K. Nayak, A. Saxena and S. Kailas, *Phys. Rev. C* **99**, 034609 (2019).
4. ‘Reaffirmation of probe-dependence of the mass deformation length for low-lying excitations in ${}^{112,116,118,120,122,124}\text{Sn}$ isotopes’,
A. Kundu, S. Santra, A. Pal, D. Chattopadhyay, T. N. Nag, R. Gandhi, P. C. Rout, B. J. Roy, B. K. Nayak and S. Kailas, *Phys. Rev. C* **100**, 024614 (2019).
5. ‘Measurement of the 2_1^+ level lifetime in ${}^{120}\text{Sn}$ by Doppler Shift Attenuation Method: Evidence of enhanced collectivity’,
A. Kundu, S. Santra, A. Pal, D. Chattopadhyay, R. Raut, R. Palit, Md. S. R. Laskar, F. S. Babra, C. S. Palshetkar, B. K. Nayak and S. Kailas, *Phys. Rev. C* **100**, 034327 (2019).

II. Conference Proceedings:

1. ‘Systematic model-dependent behaviour of fusion involving weakly bound projectiles ${}^6,{}^7\text{Li}$ ’,
A. Kundu, S. Santra, A. Pal, D. Chattopadhyay, *Proceedings of the DAE-BRNS Symp. on Nucl. Phys.* **60**, 436 (2015).
2. ‘Simultaneous description of elastic, inelastic and 1-nucleon transfer channels in ${}^7\text{Li}+{}^{120}\text{Sn}$ system’,
A. Kundu, S. Santra, A. Pal, D. Chattopadhyay, R. Tripathi, B. J. Roy, T. N. Nag, B. K. Nayak, A. Saxena and S. Kailas, *Proceedings of the DAE-BRNS Symp. on Nucl. Phys.* **61**, 362 (2016).
3. ‘Unequal charge & matter deformation lengths for scattering to 3_1^- states in even-even nuclei’,
A. Kundu, S. Santra, A. Pal, D. Chattopadhyay, R. Tripathi, B. J. Roy, T. N. Nag, B. K. Nayak, A. Saxena and S. Kailas, *Proceedings of the International Conference in Nuclear Physics with Energetic Heavy Ion Beams, Chandigarh, INDIA: Abstract book*, **P-74**, 156 (2017).
4. ‘Neutron and proton transition matrix elements for low-lying collective excitations in Sn isotopes’,
A. Kundu, S. Santra, A. Pal, D. Chattopadhyay, R. Tripathi, B. J. Roy, T. N. Nag, B. K. Nayak, A. Saxena and S. Kailas, *Proceedings of the DAE-BRNS Symp. on Nucl. Phys.* **62**, 382 (2017).
5. ‘Probe dependence of the nuclear deformation length of ${}^{120}\text{Sn}$ ’,
A. Kundu, S. Santra, A. Pal, D. Chattopadhyay, T. N. Nag, R. Gandhi, P. C. Rout, B. J. Roy, B. K. Nayak and S. Kailas, *Proceedings of the DAE-BRNS Symp. on Nucl. Phys.* **63**, 432 (2018).

6. 'Low lying quadrupole & octupole collective excitations in $^{112,116,118,120,122,124}\text{Sn}$ isotopes',

A. Kundu, S. Santra, A. Pal, D. Chattopadhyay, R. Tripathi, B. J. Roy, T. N. Nag, B. K. Nayak, A. Saxena and S. Kailas, *Proceedings of NN2018 - 13th International Conference on Nucleus- Nucleus Collisions, Saitama, JAPAN, unpublished.*

Ananya Kundu

(Ananya Kundu)

Dedicated to

My Parents

Acknowledgements

Several people have been involved, directly or indirectly, in the accomplishment of this enormous task that I committed myself to, five years ago. I take this opportunity to extend my heartfelt acknowledgement and appreciation to them.

Foremost, I express my deep gratitude to my mentor and thesis supervisor, Dr. Satyaranjan Santra, Professor, HBNI, Mumbai. During my association with him, I have learnt extensively on how to raise new possibilities, regard an old question from a new perspective, and approach a problem by systematic thinking. The skilful guidance and steady encouragement rendered by him throughout the period of my work are greatly appreciated, starting from suggesting the research problem, patiently teaching me the intricacies involved in the elaborate nuclear physics experiments and analyses, right up to creating a stimulating environment and work-culture where my independent ideas could thrive, accompanied by his ever-willing help, have all fuelled me towards developing a meticulous aptitude for research, and in shaping my knowledge and skills. I am profoundly beholden to him.

My special words of thanks go to Dr. S. Kailas, for being deeply involved in the progress of this work over the years, with his endless encouragement and motivation, providing several necessary suggestions and being diligently involved in discussions. I feel privileged to be associated with a person of his stature.

I am highly grateful to my seniors, Dr. A. Pal and Dr. D. Chattopadhyay, for being actively involved in the experiments and participating in several sessions of thought-provoking discussions over the course of this work. Our interactions have immensely helped me in building my knowledge of the subject.

I take this opportunity to sincerely thank all the distinguished faculty members of my doctoral committee, Prof. R. Palit (TIFR), Dr. S. Santra, Dr. K. Mahata, Dr. R. Tripathi and Dr. S. Mukhopadhyay, for their suggestions and constructive feedback, steering me ahead towards fulfilling this task. I am thankful to Prof. B.

K. Nayak, Dean-Academic, Physical & Mathematical Sciences, HBNI, for valuable suggestions during various stages of my research work.

I am greatly indebted to Dr. R. Raut of UGC-DAE CSR, Kolkata, for helping, and taking a keen interest, in a crucial part of my work. This shaped the thesis in its current form.

A special mention of thanks to Dr. V. V. Parkar, Dr. P. C. Rout and Dr. K Ramachandran for several discussions, backed by constant encouragement, from time to time.

I extend my thanks to my collaborators at BARC, T. N. Nag and R. Gandhi, for their active support, as well as to the staff of the Pelletron-LINAC accelerator facility, Mumbai, for smooth working of the accelerator, during the experiments.

These last few years have had their share of inevitable stressful phases, and the onus of helping me sail through rested on the shoulders of my childhood friends back home, Mariyam Fatima and Neetu Sharma, who became a part of this journey and encouraged me to keep a positive outlook throughout. Leaving my home and moving to a new city has been an exhilarating experience, and I thank all the new friends I made here for their moral support. I shall forever cherish the memories.

Last but not the least, I come to the most basic source of my life energy : my family. I concede my heartiest gratitude to my Maa and Baba, Mrs. Supriti Kundu and Mr. Gautam Kundu, for their constant motivation, encouragement and countless blessings, enabling me to the successful completion of this thesis. They have been patiently waiting to see this day. I thank my family members for their support, with the hope that I have made them proud.

Ananya Kundu
(Ananya Kundu)

Contents

SYNOPSIS	xii
List of Figures	xxiii
List of Tables	xxvi
1 Introduction	1
1.1 Transition Probabilities	4
1.1.1 The single-particle model	8
1.1.2 The collective model	10
1.1.3 Vibrational & Rotational excitations	11
1.2 Heavy-ion inelastic scattering	17
1.3 The Sn isotopic chain	21
1.4 General motivation of the thesis	26
2 Experimental methods	28
2.1 Generation and acceleration of the projectile	29
2.2 Semiconductor radiation detectors	32
2.2.1 SSB detector for charged particles	33
2.2.2 HPGe clover detector for γ -radiation	35
2.3 Experimental setup & associated electronics	37
2.3.1 Heavy-ion scattering measurements	39

2.3.2	Level-lifetime measurements	42
3	Theoretical Framework : Coupled Channels Method	45
3.1	Generalized CC Model	47
3.2	Coupling Interactions	51
3.2.1	Inelastic excitations	51
3.2.2	Transfer processes	55
3.3	CCFULL Model	60
3.3.1	Isocentrifugal approximation	62
3.4	FRESCO Model	63
3.4.1	Effective Interaction	63
3.4.2	Coupled Reaction Channels (CRC) Formalism	69
3.4.3	Continuum Discretized Coupled Channels (CDCC) Formalism	70
4	Low-lying collective excitations in ^{112,116,118,120,122,124}Sn isotopes	74
4.1	Probe-dependence in heavy-ion scattering	75
4.2	⁷ Li-induced excitations	77
4.2.1	CRC Calculations	79
4.2.1.1	Effect of projectile excitation	83
4.2.1.2	Target structural parameters	85
4.2.1.3	Sensitivity of interaction potential	87
4.2.2	CDCC-CRC Calculations	89
4.3	¹² C-induced excitations	95
4.3.1	CRC Calculations	98
4.3.1.1	Effect of projectile excitation	100
4.3.1.2	Target structural parameters	101
4.3.1.3	Sensitivity of interaction potential	102
4.4	Neutron & proton transition matrix elements	103

4.5	Intrinsic deformation lengths	107
4.5.1	Quantifying the effect of probe-target interaction	114
4.6	Summary & Conclusions	115
5	Measurement of the 2_1^+ level lifetime in ^{120}Sn	116
5.1	The Doppler Shift Attenuation Method	117
5.2	γ -decay from excited levels in ^{120}Sn	120
5.2.1	Distribution of inelastically scattered ^{120}Sn nuclei	121
5.3	Lineshape Modelling	124
5.3.1	Evolution of the $0_{\text{g.s.}}^+ \rightarrow 2_1^+$ scattering cross section along the target depth	125
5.3.2	Stopping simulations of recoiling nuclei	126
5.3.3	Generating Doppler-broadened lineshapes	130
5.4	Enhanced $B(E2; 0_{\text{g.s.}}^+ \rightarrow 2_1^+)$	133
5.4.1	The $4_1^+ \rightarrow 2_1^+$ feeding transition	135
5.5	Non-zero moment of inertia for the 2_1^+ state	137
5.6	Summary & Conclusions	140
6	Importance of inelastic couplings in reaction dynamics	141
6.1	Elastic, inelastic and 1-nucleon transfer channels in $^7\text{Li}+^{120}\text{Sn}$ system	142
6.1.1	Calculations for existing data at 44 MeV	152
6.2	Systematic model-dependence of complete fusion cross section	153
6.2.1	Fusion Functions	155
6.2.2	The case of a tightly-bound projectile	162
6.3	Summary & Conclusions	164
7	Future outlook	165
	Bibliography	167

SYNOPSIS

The nucleus is a mesoscopic system that exhibits features from both quantum and macroscopic domains, consisting of $\sim 1 - 300$ strongly interacting nucleons, namely protons and neutrons. Recent attempts try to model the interactions between the nucleons based on their respective fundamental internal quark compositions [1] and involve different degrees of many-body terms. Given these considerations, one would expect the structure and interactions of the nucleus to be chaotic and complicated. However, empirical data on level schemes of stable even-even nuclei reveal a different observation: the low-lying excited states are often found to exhibit a pattern that repeats in different regions of the nuclear chart. A survey of the spin-parity of first excited states in even-even nuclei shows that they are predominantly 2^+ [2]. Also, the first negative parity state in a vast majority of even-even nuclei is 3^- . The study of nuclear structural properties is an exploration of the symmetries and degrees of freedom that define such a system, and different approaches have been established for the same. For nuclei near closed shells, the shell model is capable of a good description, provided that the underlying single-particle energies and interactions are known. Nuclei farther from closed shells exhibit characteristic features that can be described by the phenomenon of collectivity, which arises from a coherent motion of the nucleons, a phenomenon that can be observed in numerous even-even nuclei across the nuclear chart. A theoretical framework for the description of collectivity was introduced by Bohr and Mottelson [3], treating the nucleus as a shaped object of either spherical or cylindrical symmetry, which can be subject to excitations of vibrational and rotational character, respectively. The deformed nuclear shapes and sizes depend on dynamic deformations of both neutron and proton distributions within the nuclei. A measurement of their individual contributions provides an important tool for understanding the relative importance of valence and core contributions to the low-lying collective modes. The competition between valence and core con-

tributions is of particular interest in single-closed-shell nuclei, where the low-lying excitations can be expected to be composed exclusively of the valence neutrons or protons, if the closed core were truly inert. In such scenarios, the question of their relative participation in low-lying collective excitations is of considerable interest. This can be best evidenced by exclusively determining neutron and proton transition matrix elements involved in an excitation. The ratio of the neutron and proton transition matrix elements, M_n/M_p , has often been used to identify any inhomogeneity between their respective transition strengths, in comparison with the homogeneous value of $M_n/M_p \sim N/Z$. While proton transition matrix element can be obtained from electron scattering or Coulomb excitation measurements, the determination of neutron transition matrix element requires nuclear interactions, which are more complex and subject to nuclear models. The validity and applicability of theoretical models which describe the different phenomena of collectivity rely largely on experimental signatures of accessible quantities that are characteristic of the collective excitations in nuclei. Such observables can be relative quantities like decay branching ratios or γ -ray multipole mixing ratios. However, absolute quantities, such as transition probabilities, allow for more substantial interpretations of experimental data. The experimental identification of characteristic features of collectivity has often been subject to investigating the same nucleus under different experimental probes and techniques to combine the results for conclusive information. The experiments can be classified into two major categories, (i) those that measure the shape of the nuclear potential and (ii) those that measure the shape of the charge distribution in the nucleus. One of the most suitable experimental techniques is inelastic scattering in heavy-ion collisions, governed by the combined influence of both Coulomb and nuclear forces. Using this method in combination with contemporary accelerators and improved charged-particle and γ detector arrays opens new possibilities in this field of study. It is the purpose of this thesis work to demonstrate

the ability of this approach to systematically address crucial aspects of nuclear collectivity on an absolute scale along an isotopic chain of stable semi-magic even-even nuclei within single experiments.

Excitations in heavy-ion collisions are often induced by energetic ions not too far above the barrier; contributions from Coulomb and nuclear processes become comparable, leading to a distribution of scattered (excited) nuclei over a large angular range. The shape of the angular distribution is characterized by a Coulomb-nuclear interference (CNI) pattern, governed by the multipolarity, λ , of the transition and allows a simultaneous determination of charge and mass (or potential) deformation lengths, δ_λ^{ch} and δ_λ^m . These quantities are sensitive to deviations in charge (proton) and mass (neutron + proton) distributions from equilibrium shape during an excitation. However, such measurements are often found to be discrepant and probe-dependent [4]. In the course of this work, several experiments, using different probes, focusing on the signatures of vibrational collectivity have been performed on the stable even-mass semi-magic Sn nuclei. Complicated avenues of excitation are included by means of the coupled-channels (CC) calculations.

The tin isotopes ($Z = 50$) constitute the longest chain of semi-magic nuclei with 15 even-even isotopes between the ^{100}Sn ($N = 50$) and ^{132}Sn ($N = 82$) double-shell closures. Seven of these isotopes, $^{112,114,116,118,120,122,124}\text{Sn}$, are stable. These features have made the tin isotopes a prototypical benchmark of extensive microscopic theory and experiment. This is reflected in the large number of studies investigating the low-lying 2_1^+ and 3_1^- excited states of the even-mass tin isotopes in the past few decades, by means of Coulomb excitation, nuclear resonance fluorescence, level lifetime measurements, and inelastic scattering of electron, proton, α -particle and heavy ions. The transition characteristics are, however, usually inferred only through the $B(E\lambda)$ values, which, in principle, are related to the charge contributions to the excitation, and do not include the contributions due to the matter distribution, that

are contingent on the nuclear interactions. The existing experimental as well as theoretical estimates of the $B(E2)$ [5–10] and $B(E3)$ [11–15] values for the Sn isotopes have a wide range and there are inconsistencies in the existing data leading to different conclusions on the collectivity of the excitation modes. In the light of such discrepancies, unambiguous quantitative assessments of collective properties for the 2_1^+ and 3_1^- states in the stable Sn isotopes, is necessitated. Extensive measurements and understanding of the basic collective phenomena in low-lying transitions along an isotopic chain of stable neutron-excess nuclei, with better understood structures, could act as a reference for improved experimental and theoretical studies with unstable isotopes that are expected to be of similar complexity.

The main motivation of the present thesis work is to measure the charge and mass transition probabilities of the dominant low-lying $\lambda = 2, 3$ transitions in the $^{112,116,118,120,122,124}\text{Sn}$ nuclei, compare them with existing estimates and understand the underlying contributions from the neutron and proton densities. To verify the existence of probe dependence, measurements are carried out with a projectile with no spin and isospin (^{12}C) as well as another projectile with non-zero spin and isospin (^7Li). There also exists an experimental analogy between the excitation spectra of nuclei obtained by pure electromagnetic decay from the excited states, and by direct interactions such as the inelastic scattering of nuclear particles. However, the number of configurations which take part in the excitation and the interaction operator are different in the two cases. Thus one would expect some quantitative differences. In this context, the $B(E2)$ value for the most-abundant ^{120}Sn isotope has been determined by a measurement of the γ -decay lifetime of the 2_1^+ state, using updated methodologies. The result has been compared with the values deduced from heavy-ion scattering measurements. The importance of realistic estimation of structural parameters and deformation characteristics of the dominant low-lying states

in nuclei is realised through investigation of their effects on reaction dynamics in nuclear collisions, by demonstrating a simultaneous description of the elastic scattering channel along with the inelastic scattering and one-nucleon transfer channels in the ${}^7\text{Li} + {}^{120}\text{Sn}$ reaction system, at two bombarding energies. Further, as an extension of this work, it has been shown that inelastic couplings can couple to the relative motion between colliding nuclei and significantly affect predictions of fusion cross sections, particularly in systems involving weakly bound projectiles, where different model calculations lead to different conclusions about suppression/enhancement of complete fusion.

Based on the above-mentioned motivations, measurements were carried out at the 14UD BARC -TIFR Pelletron-LINAC facility at Mumbai. Self-supporting enriched Sn foils were used as targets. In order to detect all the desired projectile-like fragments generated by heavy-ion collisions, arrays of maximum ten telescopes consisting of silicon surface barrier charged-particle detectors ($\Delta E - E$) have been used. In addition, measurements of the γ -ray spectra from the decay of the dominant excited states in ${}^{120}\text{Sn}$ have been carried out using an array of HPGe clover detectors, to determine the mean lifetime of the states involved. The outcomes of the above measurements and subsequent analyses are as follows:

I. Low-lying quadrupole and octupole collective excitations in ${}^{112,116,118,120,122,124}\text{Sn}$

Systematic measurements of the differential cross sections for the $\lambda = 2, 3$ inelastic scattering of the ${}^{112,116,118,120,122,124}\text{Sn}$ nuclei have been carried out with two heavy-ion probes – ${}^7\text{Li}$ [16] and ${}^{12}\text{C}$ [17], at bombarding energies $E_{\text{c.m.}}/V_{\text{B}} \sim 1.3$, and the data have been compared with explicit CC calculations. For the ${}^7\text{Li}$ -induced excitations, the effect of projectile breakup for the weakly bound ${}^7\text{Li}$ nucleus is incorporated

among other couplings. Reliable angular momentum transfer assignments can be made based on the shapes of the differential cross sections, and the magnitudes (strengths) are related to nuclear structure. Structural deformation parameters of Sn nuclei are found to be probe-dependent, significantly for the $\lambda = 3$ transition. The δ_2^{ch} and δ_3^{ch} values are nearly similar when measured with either probe. Considerable disagreement is found between δ_2^m and δ_3^m values measured with the ${}^7\text{Li}$ and the ${}^{12}\text{C}$ probe. Under the phenomenological approximation that neutron and proton transition densities scale as N/Z in collective excitations, the two sets of measurements lead to discrepant M_n/M_p ratios for all the Sn isotopes. Similar results are obtained on using a phenomenological optical potential, as well as a fundamental microscopic double-folded potential. This implies that nature of probe-target interactions have inconsequential effects on the extracted mass (potential) deformation lengths from inelastic scattering analysis. The root cause of probe-dependence lies elsewhere. It is observed that such measurements are highly dependent on the choice of interaction radius parameter that depends on the size of the probe. The experimentally observed mass deformation lengths are intricately convoluted over the finite size of the projectile radius and the optical potential governing the interaction between the colliding nuclei. The intrinsic M_n/M_p ratio for each Sn isotope can be deduced by removing the effects of probe size in the extraction of nuclear potential shapes [18]. The results indicate that neutron collectivity is the dominant contribution to the 2_1^+ and 3_1^- excited states in the Sn isotopes, as may be expected in proton-magic nuclei.

II. Measurement of lifetime of 2_1^+ state in ${}^{120}\text{Sn}$: Enhanced $B(E2)$

The mean lifetime of the 2_1^+ state in ${}^{120}\text{Sn}$ ($E_x = 1171$ keV) has been determined using updated techniques by means of the Doppler Shift Attenuation Method, and the corresponding $B(E2)$ value is deduced [19]. Levels in ${}^{120}\text{Sn}$ have been popu-

lated by inelastic collisions with ^{32}S projectile, at $E_{\text{lab}} < V_{\text{B}}$. The corresponding decay by γ -emission in flight leads to a Doppler-broadened lineshape, whose structure is sensitive to the level lifetime. Over the years, independent measurements of Coulomb excitation cross sections and 2_1^+ lifetimes of the stable Sn isotopes have reported discrepant transition probabilities and collective properties. The framework of analysis in this work relies on simulations for the slowing-down process and the consequent velocity profiles of scattered ^{120}Sn recoils traversing a thick stopping medium, using experimentally-benchmarked stopping powers. The extracted result gives an improved estimate of the 2_1^+ level lifetime in ^{120}Sn . This leads to an enhanced $B(E2)$ value that suggests significant collectivity for this excitation. This value is in excellent agreement with the results obtained earlier from scattering of heavy ions ^7Li and ^{12}C at above-barrier energies. An attempt has also been made to also extract the lifetime of the 4_1^+ state, which feeds the 2_1^+ level. The corresponding $B(E2; 4_1^+ \rightarrow 2_1^+)$ is in compliance with an existing estimate from Coulomb excitation measurement.

III. Elastic, inelastic and one-nucleon transfer channels in $^7\text{Li} + ^{120}\text{Sn}$ system

The comparison of experimental and theoretical values of structural parameters of excited states provides a test for the validity of nuclear models. The calculation of elastic scattering and fusion cross section, as well as all intermediate reaction channels, is largely dependent on coupling effects of the relevant bound/unbound peripheral channels. The dominant effect arises due to coupling of the low-lying excitations in the colliding nuclei to the relative motion coordinate for the reaction system. In conjunction with the previous measurements of differential cross sections for elastic and inelastic scattering in the $^7\text{Li} + ^{120}\text{Sn}$ system at beam energy of 28 MeV, new set of measurements have been undertaken at 30 MeV energy. In addition, several states corresponding to the dominant 1-nucleon transfer channels

have been measured at both 28 and 30 MeV [20]. CC calculations are performed to simultaneously describe the major direct reaction channels and incorporate the effect of projectile breakup couplings. The stripping reactions transfer a single nucleon to one of the empty states in the target nucleus and are thus useful for the study of single particle excitations. Realistic structural information such as one-nucleon spectroscopic factors are deduced by coupling around 30 reaction channels to the entrance channel. New structural parameters have been assigned for transfer to a few of the states in the residual nuclei, whose spectroscopic factors were not known. Cross sections obtained using a single set of potential and coupling parameters are able to simultaneously explain the measured data for all the channels at both bombarding energies, as well as the existing data for elastic and inelastic cross sections at 44 MeV.

IV. Systematic model dependence of complete fusion – influence of inelastic couplings

The coupling effects of dominant inelastic scattering channels is seen to sensitively influence the computation of fusion cross sections in heavy-ion collisions. Existing complete fusion cross sections for several reactions involving weakly bound projectiles ${}^6,7\text{Li}$ are compared with different sets of CC calculations [21]. The contribution due to target inelastic couplings, which constitute the dominant reaction modes in a system, towards overall fusion suppression/enhancement over that due to an uncoupled barrier, has been specifically calculated. This allows one to isolate the contribution due to breakup and/or transfer effects which are essentially significant for systems with ${}^6,7\text{Li}$ projectiles. The different CC models lead to contrasting results, owing to the differences in their respective theoretical framework. A conclusion on enhancement or suppression and their relative fractions of experimental fusion with respect to theoretical calculations becomes model dependent. The exer-

cise was repeated for a system with tightly bound ^{16}O projectile to focus essentially on inelastic couplings, and similar differences could be seen. To accomplish the task of having a realistic and model-independent prediction of fusion enhancement or suppression, one should measure and simultaneously describe the major reaction modes in a system, such as inelastic excitations and particle transfers, with realistic coupling parameters, that would possibly explain both extremes: elastic scattering and fusion. This is prohibitive for some common CC models.

To conclude, the present thesis work is primarily dedicated to the investigation of collectivity and associated properties for the low-lying 2_1^+ and 3_1^- states in the stable Sn isotopes using ^7Li and ^{12}C probes, and give an estimate of the intrinsic mass deformation lengths and M_n/M_p ratios for the transitions. Further, to support the validity of the structural information deduced from heavy ion scattering, an independent measurement for the lifetime of the 2_1^+ state in ^{120}Sn has been carried out to compare with the $B(E2)$ value from ^7Li and ^{12}C scattering. The independent roles of neutron and proton distributions of the Sn nuclei in collective excitations have been investigated, which is expected to advance the understanding of the nature of excitations in proton shell closed nuclei. The detailed study of elastic, inelastic and transfer channels provides realistic coupling parameters for understanding the reaction mechanisms in a projectile-target system, and their subsequent impact on fusion cross sections.

The thesis has been organized as follows: In Chapter 1, an introduction to heavy-ion inelastic collisions and the current status in the field has been presented along with the general motivation for the thesis work. Chapter 2 describes the general experimental techniques used for the detection of charged particles emitted during nucleus-nucleus collisions as well as for γ -rays emitted during nuclear de-excitations. A description of the coupled channels formalism used in the analysis has been pre-

sented in Chapter 3. Chapter 4 highlights the determination of deformation lengths and related properties of $^{112,116,118,120,122,124}\text{Sn}$ by inelastic collisions with ^7Li and ^{12}C . In Chapter 5, a measurement of the lifetime of the 2_1^+ state in ^{120}Sn has been discussed. The importance of unambiguous determination of deformation characteristics of nuclei is emphasized in Chapter 6 where (i) a simultaneous description of elastic, inelastic and transfer channels is attempted to assign new spectroscopic factors for several states populated by 1-nucleon transfers, and (ii) a theoretical study of the model dependence of the effect of dominant inelastic couplings on fusion cross sections is presented for several projectile-target systems. The future scope of the work is highlighted in Chapter 7.

References

- [1] E. Epelbaum, H.-W. Hammer, and Ulf-G. Meißner. *Rev. Mod. Phys.*, 81:1773–1825, 2009.
- [2] G. Scharff-Goldhaber. *Phys. Rev.*, 90:587–602, 1953.
- [3] A. Bohr and B. R. Mottelson. *Nuclear Structure*, volume 2. Benjamin, New York, 1975.
- [4] A. M. Bernstein, V. R. Brown, and V. A. Madsen. *Comments Nucl. Part. Phys.*, 11(5):203–215, 1983.
- [5] J. M. Allmond, A. E. Stuchbery, A. Galindo-Uribarri, et al. *Phys. Rev. C*, 92:041303(R), 2015.
- [6] A. Jungclaus, J. Walker, J. Leske, et al. *Phys. Lett. B*, 695:110 – 114, 2011.
- [7] D. C. Radford, C. Baktash, J. R. Beene, et al. *Nucl. Phys. A*, 746:83c – 89c, 2004.

- [8] P. Doornenbal, P. Reiter, H. Grawe, et al. *Phys. Rev. C*, 78:031303, 2008.
- [9] C. Vaman, C. Andreoiu, D. Bazin, et al. *Phys. Rev. Lett.*, 99:162501, 2007.
- [10] A. Ansari. *Phys. Lett. B*, 623:37 – 42, 2005.
- [11] N. G. Jonsson, A. Backlin, J. Kantele, et al. *Nucl. Phys. A*, 371:333, 1981.
- [12] D. G. Alkhazov, Y. P. Gangrskii, I. K. Lemberg, and Y. I. Udralov. *Bull. Acad. Sci. USSR (Phys. Ser.)*, 28:149, 1965.
- [13] G. Bruge , J. C. Faivre, H. Faraggi, and A. Bussiere. *Nucl. Phys. A*, 146:597 – 658, 1970.
- [14] O. Beer, A. El Behay, P. Lopato, et al. *Nucl. Phys. A*, 147:326 – 368, 1970.
- [15] V. Gillet, B. Giraud, and M. Rho. *Phys. Rev.*, 178:1695 – 1697, 1969.
- [16] A. Kundu, S. Santra, A. Pal, et al. *Phys. Rev. C*, 99:034609, 2019.
- [17] A. Kundu, S. Santra, A. Pal, et al. *Phys. Rev. C*, 100:024614, 2019.
- [18] D. L. Hendrie. *Phys. Rev. Lett.*, 31:478–481, 1973.
- [19] A. Kundu, S. Santra, A. Pal, et al. *Phys. Rev. C*, 100:034327, 2019.
- [20] A. Kundu, S. Santra, A. Pal, et al. *Phys. Rev. C*, 95:034615, 2017.
- [21] A. Kundu, S. Santra, A. Pal, et al. *Phys. Rev. C*, 94:014603, 2016.

List of Figures

1.1	Schematic of single particle transitions in a nucleus	8
1.2	Existing experimental and calculated $B(E2)$ values for the Sn isotopes	24
1.3	Existing experimental and calculated $B(E3)$ values for the Sn isotopes	25
2.1	Layout of the Pelletron-LINAC accelerator facility at Mumbai, India.	30
2.2	Schematic arrangement of a Si surface barrier detector	34
2.3	Schematic arrangement of a HPGe clover detector	35
2.4	Schematic experimental setup for ${}^7\text{Li}+{}^{112,116,118,120,122,124}\text{Sn}$ systems .	40
2.5	Schematic experimental setup for ${}^{12}\text{C}+{}^{112,116,118,120,122,124}\text{Sn}$ systems .	41
2.6	Schematic diagram of analog signal processing for heavy-ion scatter- ing measurements	42
2.7	Schematic experimental setup for γ -decay measurements in ${}^{32}\text{S}+{}^{120}\text{Sn}$ system	43
2.8	Schematic diagram of digital signal processing for γ -decay measure- ments	44
3.1	Radial coordinates in a nucleon/cluster transfer reaction	56
3.2	Interaction potential (representative) in nuclear collisions	61
3.3	Radial coordinates in a breakup reaction	72
4.1	Raw data showing outgoing projectile-like fragments in ${}^7\text{Li} + {}^{122}\text{Sn}$ reaction	78

4.2	Differential cross sections (experiment and CRC calculations) for ${}^7\text{Li}$ - induced $\lambda = 2$ excitation in Sn isotopes	80
4.3	Differential cross sections (experiment and CRC calculations) for ${}^7\text{Li}$ - induced $\lambda = 3$ excitation in Sn isotopes	81
4.4	Coupling scheme of the ${}^7\text{Li}+{}^{120}\text{Sn}$ system for the CRC framework . .	82
4.5	Projectile excitation ($E_x = 0.478$ MeV) in the ${}^7\text{Li}+{}^{120}\text{Sn}$ system . . .	84
4.6	Minimum $-\chi^2$ estimates of $\delta_\lambda^{ch,m}$	86
4.7	CDCC + CRC calculations for $\lambda = 2$ target excitations in ${}^7\text{Li}+{}^{112,116,118,120,122,124}\text{Sn}$ systems	92
4.8	CDCC + CRC calculations for $\lambda = 3$ target excitations in ${}^7\text{Li}+{}^{112,116,118,120,122,124}\text{Sn}$ systems	93
4.9	Raw data showing outgoing projectile-like fragments in ${}^{12}\text{C} + {}^{112}\text{Sn}$ reaction	96
4.10	Differential cross sections (experiment and CRC calculations) for ${}^{12}\text{C}$ - induced $\lambda = 2,3$ excitations in Sn isotopes	97
4.11	Coupling scheme of the ${}^{12}\text{C}+{}^{122}\text{Sn}$ system for the CRC framework . .	98
4.12	Projectile excitation ($E_x = 4.438$ MeV) in the ${}^{12}\text{C}+{}^{118,122}\text{Sn}$ reactions	101
4.13	Probe-dependent M_n/M_p ratios for $\lambda = 2, 3$ excitations in Sn isotopes	107
4.14	Effect of probe-size on target structural parameters	109
4.15	Intrinsic $\lambda = 2, 3$ matter deformation lengths for the Sn isotopes . . .	111
4.16	Intrinsic M_n/M_p for $\lambda = 2, 3$ excitations in Sn isotopes	113
5.1	Schematic diagram showing the principle of DSAM	120
5.2	Raw γ -ray spectra showing decay of 2_1^+ excited state in ${}^{120}\text{Sn}$	123
5.3	Relative population distribution with energy-angular correlation for the scattered ${}^{120}\text{Sn}$ recoils in their 2_1^+ excited state	125
5.4	Comparison of stopping powers of ${}^{120}\text{Sn}$ recoils in the 2_1^+ state, as calculated by different models	128

5.5	Schematic representation of evolving yield of recoils along the target depth	129
5.6	Lineshape modelling of experimental Doppler-broadened γ spectra for the $2_1^+ \rightarrow 0_{g.s.}^+$ decay in ^{120}Sn	130
5.7	Low-lying levels in ^{120}Sn	132
5.8	Systematic trends of $B(E2)$ values for the stable Sn isotopes compared with existing measurements	133
5.9	$4_1^+ \rightarrow 2_1^+$ transition in ^{120}Sn , in coincidence with $2_1^+ \rightarrow 0_{g.s.}^+$ transition	135
5.10	Spin-dependent moment of inertia for the 2_1^+ state in ^{120}Sn	139
6.1	States populated in inelastic scattering, 1-n transfer and 1-p transfer processes in $^7\text{Li}+^{120}\text{Sn}$ reaction	143
6.2	Elastic-to-Rutherford ratio in $^7\text{Li}+^{120}\text{Sn}$ system	147
6.3	Dominant inelastic scattering channels in $^7\text{Li}+^{120}\text{Sn}$ system	148
6.4	Dominant 1-n transfer ($^7\text{Li}, ^6\text{He}$) channels in $^7\text{Li}+^{120}\text{Sn}$ system	149
6.5	Dominant 1-p transfer ($^7\text{Li}, ^6\text{He}$) channels in $^7\text{Li}+^{120}\text{Sn}$ system	150
6.6	Available data for elastic and inelastic scattering in the $^7\text{Li}+^{120}\text{Sn}$ system compared with the present set of calculations	153
6.7	Experimental fusion functions using the results of FRESKO and CCFULL for reactions involving projectiles $^6,^7\text{Li}$	158
6.8	Same as Fig. 6.7, but plotted in logarithmic scale.	159
6.9	Uncoupled and coupled fusion cross sections calculated by CCFULL and FRESKO	160
6.10	Effect of inelastic channel couplings on fusion calculations	161
6.11	Comparison between fusion calculations of CCFULL and FRESKO for the $^{16}\text{O}+^{148}\text{Sm}$ system	163

List of Tables

1.1	Weisskopf estimates of the $B(E2)$ and $B(E3)$ values for the Sn isotopes	22
4.1	Nuclear potential (WS) parameters used in CRC calculations for ${}^7\text{Li}$ + ${}^{112,116,118,120,122,124}\text{Sn}$ systems	83
4.2	δ_λ^{ch} and δ_λ^m values obtained from ${}^7\text{Li}$ -induced excitations	86
4.3	Bound and unbound excitations for ${}^7\text{Li}$ included in the CDCC-CRC calculations	90
4.4	Binding potentials for the α - t cluster in the ${}^7\text{Li}$ nucleus	94
4.5	Nuclear potential (WS) parameters used in CRC calculations for ${}^{12}\text{C}$ + ${}^{112,116,118,120,122,124}\text{Sn}$ systems	100
4.6	δ_λ^{ch} and δ_λ^m values obtained from ${}^{12}\text{C}$ -induced excitations	102
4.7	Microscopic proton and neutron transition parameters for $\lambda = 2, 3$ target excitations in ${}^7\text{Li} + {}^{112,116,118,120,122,124}\text{Sn}$ reactions	105
4.8	Microscopic proton and neutron transition parameters for $\lambda = 2, 3$ target excitations in ${}^{12}\text{C} + {}^{112,116,118,120,122,124}\text{Sn}$ reactions	105
4.9	Intrinsic deformation lengths and M_n/M_p ratios for the Sn isotopes	112
5.1	Lifetime and electric transition probability for the 2_1^+ state in ${}^{120}\text{Sn}$	134
6.1	Particle-core spectroscopic factors for the 1-n and 1-p stripping in ${}^7\text{Li} + {}^{120}\text{Sn}$ reaction	151
6.2	Systems studied for probing model dependence of fusion calculations	155

Chapter 1

Introduction

The nucleus is a mesoscopic system that exhibits features from both quantum and macroscopic domains, consisting of $\sim 1 - 300$ constituents (nucleons), namely protons and neutrons. It can be regarded as a quantum many-body system with strong interactions between the constituents, with pronounced statistical regularities. At the same time, individual quantum states can be also studied, both experimentally and theoretically. Recent attempts try to model the interactions between the nucleons based on their respective fundamental internal quark compositions [1] and involve different degrees of many-body terms. Given these considerations, one would expect the structure and interactions of the nucleus to be chaotic and complicated. However, empirical data on level schemes of stable even-even nuclei reveal a different observation : the low-lying states are often found to exhibit a pattern that repeats in different regions of the nuclear chart. Owing to nucleon pairing, there is no uncompensated intrinsic angular momentum in the ground state of an even-even system, and a $J = 0^+$ ground state is expected for such nuclei. A survey of the spin-parity of first excited states in a vast majority of even-even nuclei shows that they are predominantly 2^+ [2]. Also, the first negative parity state is often found to be 3^- . Transitions to excited states in nuclei can be of electric, magnetic, isoscalar, isovector, or mixed character. The study of nuclear properties, such as energies and

nature of excitation of the various states, is an exploration of the symmetries and degrees of freedom that define such a system, and is one of the principal pursuits in nuclear physics measurements. Different approaches have been established for the same. One model of the nucleus, the liquid drop model, likens the forces acting between the nucleons to those between molecules of a low-viscosity liquid. Another model, based on the shell structure of the nucleus, likens the forces to those between particles in an elastic solid. For nuclei near closed shells, the shell model is capable of a good description, provided that the underlying single-particle energies and interactions are known. However, no single model could accurately predict all the excitation modes in a nucleus. Nuclei farther from closed shells exhibit characteristic features that can be described by the phenomenon of collectivity, or a coherent motion of the nucleons, a phenomenon that can be observed in numerous even-even nuclei across the nuclear chart. A very successful theoretical framework for the description of collectivity was introduced by Bohr and Mottelson [3], treating the nucleus as a shaped geometric object that can be subjected to excitations of vibrational or rotational character. Transitions to excited states are commonly expressed in terms of dynamic deformation of the equilibrium shape - such as an irrotational flow motion for statically deformed nuclei with cylindrical symmetry, or as surface oscillations for nuclei with spherical symmetry. For axially-symmetric shape deformations, one thinks of a neutron-proton fluid undergoing homogeneous isoscalar excitations about the equilibrium, with their respective transition densities in the ratio of N/Z . The measurement of the neutron and proton contributions provides one of the most important tools for understanding the relative importance of valence and core contributions to the low-lying collective transitions. The competition between valence and core configurations is of particular interest in single-closed-shell nuclei, where the low-lying excitations can be expected to be composed exclusively of the valence neutrons and/or protons, if the closed core were truly inert. The

ratio of the neutron and proton transition matrix elements, M_n/M_p , is a measure of their relative contributions, and has often been used to identify any inhomogeneity between their respective transition strengths, in comparison with the homogeneous collective model prediction of $M_n/M_p \sim N/Z$ [4].

Collective modes play an important role in a number of nuclear phenomena, the best known of which is the need for effective charges [5] for valence nucleons in shell model calculations of nuclear moments and transition rates. These effective charges account for polarization and virtual excitations of the core nucleons, the transitions of which are excluded in the shell-model space. The study of such structural characteristics of excited states requires knowledge about dynamic deformations, induced by an external field, of both neutron and proton distributions within the nuclei. Quantum mechanics describes the arrangement and motion of nucleons by means of the wave function. A nucleus has a stationary wave function in its ground state, with an equilibrium density distribution. When excited to higher energy states, the relative configurations of the nucleons in the nucleus give rise to distinctive deformations in the equilibrium shape. The arbitrary deformed shapes are commonly characterized by a multipole expansion of the nuclear density, with the different excitation modes characterized in terms of the number of units of orbital angular momentum, λ , transferred in the process, namely monopole ($\lambda = 0$), dipole ($\lambda = 1$), quadrupole ($\lambda = 2$), octupole ($\lambda = 3$), and so on. The nomenclature represents the shape of the nuclear density distribution during a particular transition. For example, the distribution of protons in a nucleus undergoing quadrupole electric (magnetic) transitions give rise to an oscillating electric (magnetic) field that represents the field generated by four point charges (poles). The validity and applicability of theoretical models rely largely on experimental signatures of accessible quantities that are characteristic of the collective excitations in nuclei. Such observables can be relative quantities like decay branching ratios or γ -ray multipole mixing ratios. How-

ever, absolute quantities, such as transition probabilities and deformation lengths, allow for more substantial interpretations of experimental data. Investigation of such observables involves placing the nucleus in an excited state and detecting the corresponding scattered energy, or the particle and γ emissions released in the process. The measurement of characteristics of excited states, specifically spin, parity, and level-lifetime, combined with their interpretation through theoretical models, allows for the reconstruction of the nuclear shape and the underlying microscopic configurations of the corresponding states.

1.1 Transition Probabilities

The transition probability, for a transition of multipolarity λ , is proportional to the square of the nuclear matrix element, $\mathcal{M}(M_f, M_i) = \langle J_f M_f | \hat{\mathcal{O}}_{\lambda\mu} | J_i M_i \rangle$, where $\hat{\mathcal{O}}_{\lambda\mu}$ is the quantum mechanical operator describing the mode of the transition. Here, J_f and J_i are the total spins of the final and initial states, respectively, which define the matrix element for the $\hat{\mathcal{O}}_{\lambda\mu}$ operator, with $\vec{J}_f = \lambda + \vec{J}_i$. The dependence of $\mathcal{M}(M_f, M_i)$ on the projections, M_i and M_f , of the initial and final total angular momenta on the quantization axis, can be factored out using the Wigner-Eckart theorem [6], leading to,

$$\mathcal{M}(M_f, M_i) = (J_i \lambda M_i \mu | J_f M_f) \langle J_f || \hat{\mathcal{O}}_{\lambda} || J_i \rangle \quad (1.1)$$

where the quantity $\langle J_f || \hat{\mathcal{O}}_{\lambda} || J_i \rangle$ defines the reduced matrix element, and is invariant under a rotation of the coordinate system. For transitions in nuclei induced by an electromagnetic field with vector potential \vec{A} and current density \mathcal{J} , the operator $\hat{\mathcal{O}}_{\lambda\mu}$ is either an electric multipole operator ($\hat{E}_{\lambda\mu}$), or a magnetic multipole operator ($\hat{M}_{\lambda\mu}$). An electric transition is said to have occurred when the charge/proton density undergoes dynamic deformations under the effect of an electric (Coulomb)

field. A magnetic transition takes place when the intrinsic spin is flipped. The nucleonic spins possess a natural frequency, ν_0 ; when a nucleus is excited at this frequency by an external magnetic field, spin-flip transitions are induced, with $h\nu_0$ as the energy difference between the spin-up and spin-down states. The average behaviour of many spins results in a net magnetization of the nucleus (nuclear spin).

The transitions are characterized by investigating the electromagnetic transition probabilities, $B(E\lambda)$ and $B(M\lambda)$, which are commonly obtained from rates of γ -decay in nuclei. A γ -photon emitted by a nucleus carries with it an oscillating electromagnetic field, with decay energy typically of the order of MeV, and typical de-Broglie wavelength ~ 100 fm. Although the wavelength of a γ -ray is smaller than the other forms of electromagnetic radiation, namely, visible or ultraviolet light, it is large with respect to nuclear dimensions. As a result, the field associated with a γ -photon is nearly uniform across the nucleus. Hence, there is little overlap between the wave functions of the photon and the nucleon(s) responsible for the emission. Consequently, γ -decay is a slow process in nuclear timescales ($\sim 10^{-12} - 10^{-14}$ s). Other contributing factors are the relatively weak strength of the electromagnetic force compared to that of the strong force between the nucleons, and the requirement that the photon carries away at least one unit of angular momentum ($\lambda \geq 1$). The transition, thus, involves some degree of nuclear reorientation, and the γ -rays are not sensitive to the details of the nuclear radial wave functions. A connection between the electromagnetic transition probability and the transition matrix element can be established using time-dependent perturbation theory [7], wherein, for a system in the state $\chi_0(r)$ at time $t = 0$, the transition probability per unit time to a state $\chi_f(r)$, under the effect of a Hamiltonian $H' = -\frac{1}{c}\vec{A} \cdot \mathcal{J}$, is given by the Fermi golden rule [7],

$$T = \frac{2\pi}{\hbar} |\langle \chi_f(r) | H' | \chi_0(r) \rangle|^2 \rho_{E_f} \quad (1.2)$$

where the constant ρ_{E_f} is known as the density of states at energy E_f . The perturbation H' comes from coupling between the nuclear and electromagnetic fields, and the density of final states is a product of the number of nuclear and electromagnetic states per energy interval at E_f . A suitable multipole expansion of the radiation field, $A(\vec{r}, t) \equiv \sum_k A_k(r)e^{-i\omega t} = \sum_{\lambda\mu} A_{\lambda\mu}(\vec{r}, t)$ defines two different component fields,

$$A_{\lambda\mu}(E\lambda, r) = -\frac{i}{k} \nabla \times (r \times \nabla) (j_\lambda(kr)Y_{\lambda\mu}(\theta, \phi)) \quad (1.3)$$

$$A_{\lambda\mu}(M\lambda, r) = (r \times \nabla) (j_\lambda(kr)Y_{\lambda\mu}(\theta, \phi)) \quad (1.4)$$

In the long-wavelength limit of γ -decay, the spherical Bessel function reduces to $j_\lambda(kr) \approx (kr)^\lambda$. Since the electric charge in a nucleus primarily consists of point charges carried by individual protons, and the magnetization currents are due to the magnetic moments of individual nucleonic spins and the orbital motion of proton, one obtains the electric and magnetic components of the Hamiltonian H' as,

$$H_{\lambda\mu}^{IE} \equiv \hat{E}_{\lambda\mu} = \sum_{i=1}^Z e r_i^\lambda Y_{\lambda\mu}(\theta_i, \phi_i) \quad (1.5)$$

$$H_{\lambda\mu}^{IM} \equiv \hat{M}_{\lambda\mu} = \sum_{i=1}^A \left[g_s(i) s_i + g_l(i) \frac{2l_i}{\lambda+1} \right] \cdot \nabla_i (r_i^\lambda Y_{\lambda\mu}(\theta_i, \phi_i)) \quad (1.6)$$

with e as the electronic charge of the proton, and g_s and g_l as the spin and orbital gyromagnetic ratios of the nucleons (defined in terms of the nuclear magneton, μ_N). The transition rate in Eqn. 1.2 can be expressed as,

$$T = \frac{8\pi(\lambda+1)}{\hbar\lambda[(2\lambda+1)!!]^2} \left(\frac{E_\gamma}{\hbar c} \right)^{2\lambda+1} B(\mathcal{O}\lambda; J_i \rightarrow J_f) \equiv \frac{1}{\tau} \quad (1.7)$$

with τ as the mean lifetime of the decaying state. The rate is observed to reduce with an increase in the multipolarity. The transition probability, $B(\mathcal{O}\lambda; J_i \rightarrow J_f)$, is

written in terms of the reduced matrix element of the multipole operator, for either electric or magnetic transition,

$$B(\mathcal{O}\lambda; J_i \rightarrow J_f) = \sum_{\mu M_f} |\langle J_f M_f | \hat{\mathcal{O}}_{\lambda\mu} | J_i M_i \rangle|^2 = \frac{1}{2J_i + 1} \langle J_f || \hat{\mathcal{O}}_{\lambda} || J_i \rangle \quad (1.8)$$

$$B(\hat{\mathcal{O}}\lambda, J_i \rightarrow J_f) = \frac{2J_f + 1}{2J_i + 1} B(\hat{\mathcal{O}}\lambda, J_f \rightarrow J_i) \quad (1.9)$$

in units of $e^2 \text{fm}^\lambda$ for $\mathcal{O}\lambda \equiv E\lambda$, and of $\mu_N^2 \text{fm}^{2\lambda-2}$ for $\mathcal{O}\lambda \equiv M\lambda$. Here, it may be emphasized that for the same decay energy and multipolarity, the magnetic transition rates are weaker than the electric transition rates by a factor of ~ 100 ($\frac{e^2}{\mu_N^2} \approx 10^2$). For the reduced matrix element to remain invariant under the inversion of coordinates, the forms of the electric and magnetic transition operators define the parity selection rules as $\Pi_i \Pi_f = (-1)^\lambda$ for the electric transitions, and $\Pi_i \Pi_f = (-1)^{\lambda+1}$ for the magnetic transitions. Thus, electric and magnetic transitions of the same multipolarity cannot both occur between a given pair of nuclear states. However, if both $E\lambda$ and $M(\lambda+1)$, or, $M\lambda$ and $E(\lambda+1)$, modes are allowed for a given pair of nuclear states, the transition is largely dominated by the electric component for the former case, while the latter transition is often found to have a mixed character.

A calculation of transition probability requires a knowledge of both the initial and final wave functions. As the first step toward establishing an average, some assumptions can be made about these wave functions so that a reasonable estimate can be made without reference to the specific states involved in a transition [7]. For this purpose, an extreme independent particle picture is adopted where nuclear transitions are considered to be taking place when a nucleon moves from one single particle orbit to another, without affecting the rest of the nucleus. This approach facilitates to (i) make an estimate of the sizes of $B(\mathcal{O}\lambda)$ that can be expected on an average, and (ii) have a basis with which some conclusion could be drawn on experimentally observed values. A deformation of nuclear shape is commonly described

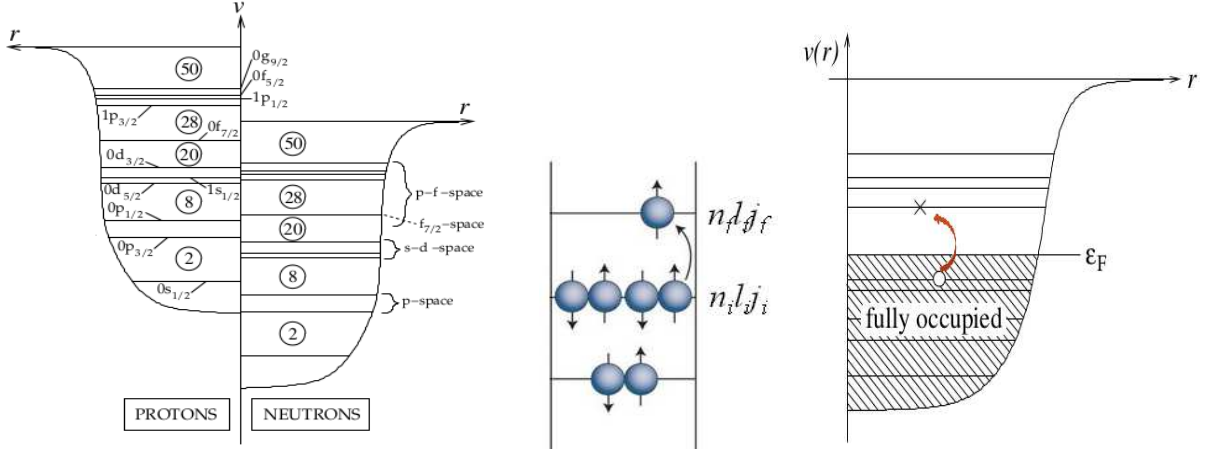


Figure 1.1: Schematic [8] of single particle transitions in a nucleus from the completely filled particle-hole valence space to the empty orbitals across the Fermi level.

as a coherent superposition of several single particle-hole states, forming a collective (vibrational or rotational) excitation.

1.1.1 The single-particle model

A nucleus is said to be in its ground state when energy levels are filled up to the proton and neutron Fermi levels - the particle-hole ground state. If a particle in the state $|\phi_{j_i}\rangle = |n_i l_i j_i\rangle$, of the closed shell, is excited to the state $|\phi_{j_f}\rangle = |n_f l_f j_f\rangle$ of the next shell, a particle-hole state, $|\psi^{\text{ph}}\rangle = |\phi_{j_f} \phi_{j_i}^{-1}\rangle$, is said to have been created. Thus, transitions can be viewed as exciting a particle from the particle-hole valence space into the empty orbitals across the Fermi level. These single particle estimates are commonly known as the Weisskopf estimates [9], given by,

$$B_{\text{Sp}}(\mathcal{O}\lambda; J_i \rightarrow J_f) = \frac{1}{2J_i + 1} \left| \langle n_f l_f j_f \left\| \hat{\mathcal{O}}\lambda \right\| n_i l_i j_i \rangle \right|^2 \quad (1.10)$$

where the single particle wave function of a spherically-symmetric potential for a nucleon with spin 1/2, in a shell with orbital angular momentum l , can be expressed as $|nljm\rangle = R_{nl}(r)\{Y_l(\theta, \phi) \times \chi_{1/2}\}_{jm}$. For electric transitions, the multipole operator

of Eqn. 1.5 leads to the single particle matrix element,

$$\begin{aligned} \langle n_f l_f j_f m_f | e r^\lambda Y_\lambda | n_i l_i j_i m_i \rangle &= e \int_0^\infty R_{n_f l_f}^*(r) r^{\lambda+2} R_{n_i l_i}(r) dr \\ &\times \langle \{Y_{l_f}(\theta, \phi) \times \chi_{1/2}\}_{j_f m_f} | Y_{\lambda \mu} | \{Y_{l_i}(\theta, \phi) \times \chi_{1/2}\}_{j_i m_i} \rangle \end{aligned} \quad (1.11)$$

For an approximation, the nucleus is assumed to be a sphere of uniform charge density, with radius $R_{ch} = 1.2A^{1/3}$. Also, the matrix element involving the angular momenta is evaluated as an average over the angular dependence around the value $\frac{1}{4\pi}$. Thus, the reduced transition probability becomes,

$$B_{sp}(E\lambda; J_i \rightarrow J_f) = e^2 \left(\frac{2\lambda + 1}{4\pi} \right) \left(\frac{3}{\lambda + 3} \right)^2 R_{ch}^{2\lambda} \quad (1.12)$$

The single particle picture works well if shells are nearly full or empty. A demerit of this approach is that the states of different J , excited between a pair of shell model orbitals involved in proton or neutron excitations, are considered to be degenerate, with the excitation energy given by the shell gap. Additionally, existing measurements of electric transition probabilities show enhancement over the Weisskopf estimates by multiple times across the nuclear chart for even-even nuclei. In a microscopic description, although γ -decay only involves the transition of a single nucleon, since a photon only interacts with one nucleon, a transition matrix element can be considerably larger than the single particle estimate through a superposition of terms in the matrix element [10]. This could be qualitatively explained if several particle-hole components participate in a transition, which manifests as a shape oscillation or deformation of the nucleus. This leads to a quantitative description of nuclear shape in terms of collective variables, beyond the realm of the shell model.

1.1.2 The collective model

As a consequence of the Pauli principle, the $2j + 1$ nucleons of a completely filled orbit nlj in even-even nuclei couple to a total angular momentum of $J = 0$. Therefore, the properties of the nuclear structure are determined by the nucleons in partially filled orbits, called valence nucleons and the residual interactions among them. Valence nucleons of the same kind in the same orbit nlj undergo coherent superposition, and can couple to different total angular momenta J , whose degeneracy is broken by the residual interaction between them. A figurative example of such an interaction is the surface delta interaction [8], which essentially models the short-range part of the nucleon-nucleon interaction. With an increase in the number of valence nucleons, the long-range part of the pairing forces become more important. This manifests as a shape oscillation, or in the formation of an increasingly deformed shape, which cannot be described by shell model, whose wave functions were obtained using a spherically symmetric potential. Such a configuration mixing of states, or coupling, leads to a collective state. Collective excitations of many body systems can be phenomenologically understood as fluctuations around a state of equilibrium. These may be fluctuations in the density or shape. The type of collective excitation strongly depends upon the composition of the system and the manner in which its components interact with each other. For example, particle-hole states, with 1^- spin and parity can be generated by transitions between different pairs of single particle states, $|\phi_{j_i}\rangle$ and $|\phi_{j_f}\rangle$, with $|j_i - j_f| \leq 1 \leq |j_i + j_f|$. Between the $0p$ and $0d - 1s$ shells as seen in Fig. 1.1, the possible particle-hole states are $|(0d_{5/2})(0p_{3/2})^{-1}\rangle$, $|(1s_{1/2})(0p_{3/2})^{-1}\rangle$, $|(0d_{3/2})(0p_{3/2})^{-1}\rangle$, $|(1s_{1/2})(0p_{1/2})^{-1}\rangle$ and $|(0d_{3/2})(0p_{1/2})^{-1}\rangle$, and such states can exist for both proton and neutron excitations. The number of nucleons per shell is larger in heavy nuclei, and the number of particle-hole states is accordingly greater. The ψ^{ph} states, N in number, are eigenstates of the unperturbed shell model Hamiltonian H_0 , and the residual interactions

among them, either attractive or repulsive, are given by $V_{if} = \langle \psi_f^{\text{ph}} | V_{\text{res}} | \psi_i^{\text{ph}} \rangle$. The pairing correlations for the full Hamiltonian, $H_0 + V_{\text{res}}$, define N new states, one of which manifests itself as a coherent sum of all the (allowed) particle-hole states. This is commonly known as the collective state,

$$|\psi_C\rangle = \frac{1}{\sqrt{N}} \sum_k^N c_k |\psi_k^{\text{ph}}\rangle \quad (1.13)$$

The coherent superposition of the amplitudes implies that the transition probability is enhanced for the collective state, and otherwise small, for the additional $N - 1$ states, which will add incoherently. The eigenenergy of the collective state is found to be shifted w.r.t. the unperturbed shell model energies [11]. In the case of attractive residual forces ($V_{\text{res}} < 0$), a low-lying collective state is formed, which, as experiments show, is either vibrational or rotational. In the case of repulsive forces ($V_{\text{res}} > 0$), a high-energy collective state is formed, usually called a giant resonance. In addition, the residual interactions also break the degeneracy between the $N - 1$ single particle orbitals.

1.1.3 Vibrational & Rotational excitations

Despite the very complex interplay of nucleons and forces present in the nucleus, a geometrical picture of the nucleus explains in a simple way the basic features of the collective behavior. Near closed shells, nuclei preferentially have a spherical shape, and can be excited to perform oscillations around this equilibrium shape, while in mid-shell regions, deformed shapes develop, which allow the nucleus to undergo rotational motion. The deformed shapes are expressed as a change in the nuclear radius, the change depending on the relative orientations of the radius vector to the intrinsic orientation of the nucleus.

The vibrational modes and frequencies observed in a system reveal about the na-

ture of forces acting within. In the early years of the study of atoms, an analysis of vibrational motion was notably important in the understanding of atomic structure. Similarly, on a far smaller scale, a richly varied spectrum of vibrations exists for the nucleus of an atom, which is a major source of information on nuclear structure and coupling effects of channels present in a reaction system [12]. The most accurate and sophisticated description of nuclear vibrations is given by the time-dependent mean field theory, wherein, the forces acting on the nucleons are calculated from the quantum-mechanical motion of the particles themselves. In general, nuclear vibrations are excited by bombarding target nuclei with high-energy γ -photons or other high-energy nuclei (projectiles with virtual photons). The vibrations are detected by observing how the projectile is absorbed or diffracted by the nucleus. The first vibration to be reported via such a measurement was the dipole vibration that could be excited by simply bombarding the target nuclei with photons having energy equal to that of the dipole mode. In this scenario, the field around the photon exerts a force on the positively charged protons, moving them away from the electrically neutral neutrons. However, to maintain the centre of mass of the nucleus at rest, the neutrons get displaced in the opposite direction. The restoring force of the vibration arises from the attraction between the protons and neutrons, mediated by the charge-independent strong nuclear force. The discovery of the dipole mode depended only on the availability of sources of mono-energetic high-energy photons, of the likes of bremsstrahlung from electron accelerators. However, unlike the dipole vibration, it was difficult to excite the higher modes with absorption of γ -rays as they interact with the nucleus through the electromagnetic force, and given their wavelength, can accelerate protons in only one direction. The next vibration to be reported, by means of nuclear scattering, was the quadrupole vibration which is a shape oscillation. A nucleus vibrating in the quadrupole mode is distorted to have ellipsoidal oscillations about the mean spherical shape.

Vibrational modes of multipolarity λ are expressed in terms of a departure from the equilibrium radius R_0 . The distance from the center of the nucleus to the surface at angles (θ, ϕ) and time t is given by,

$$R(\theta, \phi, t) = R_0 \left[1 + \sum_{\lambda=2}^{\infty} \sum_{\mu=-\lambda}^{\lambda} \beta_{\lambda\mu}(t) Y_{\lambda\mu}^*(\theta, \phi) \right] \quad (1.14)$$

with $\beta_{\lambda\mu}$ being the collective shape coordinates, and $Y_{\lambda\mu}$ being the spherical harmonics characterizing the shape of the nucleus. In Eqn. 1.18, the term corresponding to $\lambda = 0$ has been neglected since it describes a nucleus that changes its volume while retaining the basic spherical shape. Such an excitation, called the breathing mode, often occurs at very large energies (unlike the low-lying collective states). Also, the $\lambda = 1$ mode is excluded since it corresponds to a translation of the nucleus as a whole (without any changes in the internal structure), and not a shape deformation. The modes for $\lambda \geq 2$ are described in terms of a quantum harmonic oscillator model, for small-amplitude vibrations, with the Hamiltonian [7],

$$H_{\lambda}^{\text{vib}} = \frac{B_{\lambda}}{2} \sum_{\mu} \left| \frac{d\beta_{\lambda\mu}}{dt} \right|^2 + \frac{C_{\lambda}}{2} \sum_{\mu} |\beta_{\lambda\mu}|^2 \quad (1.15)$$

with oscillation frequency $\omega_{\lambda} = C_{\lambda}/B_{\lambda}$. Therefore, excitations can be imagined as mediated by phonons of angular momentum λ , with $\hbar\omega$ as the quantum of vibrational energy. Vibrational modes can be of one-phonon, or multiphonon nature.

With increasing distance to the closed shells, nuclei start to exhibit increasingly non-spherical or deformed equilibrium shapes, on account of the interplay between the short-range nuclear force, long-range repulsive Coulomb force, and centrifugal stretching. The residual interactions among the valence nuclei become dominant and determine the nuclear properties. In particular, the long-range component of the nucleon-nucleon interaction favours non-spherical configurations even in the ground state of several even-even nuclei [13]. In classical mechanics, one can distinguish

whether a spherically symmetric body rotates or not, but in quantum mechanics, all directions are equivalent and the body appears to be at rest. For a sphere, the square of its wave function is, by definition, independent of angles - it appears to be the same from all directions. As a result, the wave functions before and after a rotation cannot be distinguished. Therefore there is no rotational energy associated with degrees of freedom corresponding to a spherical symmetry. In contrast, rotational motion of a deformed object, such as an ellipsoid, may be detected, for example, by observing the changes in the orientation of the axis of symmetry with time. For rotational excitations, the nuclei have to have a preferred axis - not a signature of nuclei with 0^+ spin. The physical $J = 0^+$ state is, therefore, interpreted as the deformed intrinsic state averaged over all directions. In other words, nuclei which are intrinsically deformed in their ground state exhibit rotational excitations, wherein, the nucleus is described in terms of a deformed object with moment of inertia, \mathcal{I} . It has been observed that the effect of the rotational motion seems to be different for different ground-state structure; highly deformed, stable nuclei simply rotate, so that the moment of inertia is almost independent of angular velocity. Unstable and less deformed nuclei show a tendency to become more deformed as they rotate faster. One of the earliest models assumed the nucleus to be analogous to a rigid rotor, with the Hamiltonian given by [7],

$$H_J^{\text{rot}} = \frac{\hbar^2}{2\mathcal{I}}(J^2 - J_z^2) + \frac{\hbar^2}{2\mathcal{I}_z}J_z^2 \quad (1.16)$$

If K represents the projection of J along the symmetry (z) axis in the intrinsic frame, the expectation value of the Hamiltonian in the body-fixed system is then a function of $J(J + 1)$ and K , which are the expectation values of J^2 and J_z . A nucleus in a given intrinsic state can rotate with different angular velocities in the laboratory. A group of states, each with a different total angular momentum J but sharing the same intrinsic state, forms a rotational band, i.e., transitions between

two members of a band can take place by a change in the rotational frequency and, hence, the spin J , without any modifications to the intrinsic state. Since the only difference between these states is in their rotational motion, members of a band are related to each other in energy, static moments, and electromagnetic transition rates. For $K = 0$ in an even-even nucleus, parity transformation rules for the rotational wave function define the ground state rotational band as $J = 0^+, 2^+, 4^+, 6^+, 8^+$ and so on, connected by a cascade of electric quadrupole ($E2$) transitions, with quantum mechanical rotational energy given by,

$$E_J^{\text{rot}} = \frac{\hbar^2}{2\mathcal{I}} J(J+1) \quad (1.17)$$

The nuclear deformation can again be described by using the parametrization of the nuclear surface as,

$$R(\theta, \phi) = R_0 \left[1 + \sum_{\mu} \beta_{2\mu} Y_{2\mu}^*(\theta, \phi) + \beta_{4\mu} Y_{4\mu}^*(\theta, \phi) + \dots \right] \quad (1.18)$$

With the onset of deformation, the charge distribution in the nucleus exhibits a quadrupole moment, Q_0 . The size of the $E2$ transition matrix element is also related to the deformation of the intrinsic state, characterized by Q_0 , with,

$$B(E2; J_i \rightarrow J_f) = \frac{5}{16\pi} e^2 Q_0^2 \langle J_i K 20 | J_f K \rangle^2 \quad (1.19)$$

For axially symmetric collective vibrational/rotational deformations in a nucleus, an adequate parametrisation of the radius, $R(\theta) = R_0 [1 + \sum_{\lambda} \beta_{\lambda 0} Y_{\lambda 0}^*(\theta)]$, defines a quantity $\delta_{\lambda} = \beta_{\lambda 0} R_0$, known as the intrinsic deformation length, characterizing the degree of deformation. Such a shape parametrisation is often a starting point for theoretical calculations.

The experimental identification of characteristic features of collectivity has often been subject to investigating the same nucleus under different experimental probes and techniques to combine the results for conclusive information. The experiments can be classified into two major categories, (i) those that measure the shape of the nuclear potential and (ii) those that measure the shape of the charge distribution in the nucleus. The experiments all measure transition probabilities between excited states and the ground state, or between two excited states, since these probabilities are sensitively predicted by the nuclear shape in the vibrational/rotational model. One of the most common experimental techniques is measurement of Coulomb excitation cross section, when a nucleus is excited from the ground state solely via the time-dependent electromagnetic field generated by an interaction with another nucleus. A complementary approach involves measurement of mean lifetimes of nuclear excited states, which are related to the underlying microscopic configurations of the corresponding states. As the rate of the decay of an excited nuclear state is proportional to the square of the matrix element of the transition operator between the initial and final state wavefunction, measured lifetimes provide a very sensitive fingerprint of the relevant nuclear models. Another approach, though not widely used, is nuclear resonance fluorescence/resonance scattering that involves absorption/scattering of photons from nuclei. This method eliminates the need to know the usual geometrical and yield factors common to scattering experiments and is therefore inherently free of several sources of systematic errors. However, the fraction of γ -rays that possess the correct energy for nuclear excitation, is in most cases very small, and the difficulties of achieving reasonable statistics offset the advantages of the method. From such a variety of measurements employing electromagnetic interactions, a large volume of information is present about the distribution of charge (primarily, protons) in nuclei. Estimates of the neutron distribution require nuclear interactions. A suitable approach to probe nuclear excited states is inelastic scat-

tering in nucleon-nucleus and nucleus-nucleus collisions (light-ion/heavy-ion scattering), under the combined influence of both Coulomb and nuclear forces. Different shape modes can be selectively excited, and the scattering process is governed by two-body kinematics, leading to accurate determination of excitation energies and states of both the species.

1.2 Heavy-ion inelastic scattering

Heavy-ion scattering offers a spectroscopic tool for the excitation of high spin states of stable as well as unstable nuclei. The dominant feature which provides the key to understand such scattering phenomena is the strong surface absorption of heavy-ions; most of the elastically or inelastically scattered projectiles are predominantly involved in a direct peripheral interaction and are generally insensitive to the interaction in the interior region. In events of high-energy nuclear collisions involving hadrons/light-ions, the principal interaction is mediated by the strong nuclear force, and scattering phenomena can be understood by considering the wave nature of the incident particles. A collimated beam (thickness \sim few mm = $10^{12} \times$ nuclear size), passing through the target material, can be thought of as a plane wave enveloping a target nucleus. Depending on how the wave interacts with the nucleus, the outcome is a characteristic diffraction pattern [12]. After such an interaction, each small area of the nuclear surface acts as the origin of secondary wavelets, which propagate outward and undergo interference, either constructively or destructively, depending on their relative phase values at that point. Wavelets that originate from outward-moving surface areas have the same phase, whereas wavelets that arise from inward-moving surface areas have the opposite phase. The nature of the diffraction pattern can be understood by considering a plane downstream from the target nucleus and perpendicular to the beam axis. The wavelets diffracted to the centre of the plane along the beam axis would all travel the same distance, and hence,

arrive in phase. The resulting constructive interference would create a region of large wave amplitude in the center of the plane (analogous to a bright central spot formed during diffraction of a light wave by a black sphere). When the incident wave stimulates, say a quadrupole vibration, the wavelets originating from the elongating sides are initially 180° out of phase with the wavelets originating from the contracting sides. As a consequence, there is destructive interference in the centre of the plane. At some other points in the plane, where the distances to an elongating region and a contracting region differ by half-a-wavelength, the wavelets arrive in phase, interfering constructively. This leads to an angular distribution with an oscillatory pattern. In heavy-ion collisions, the diffractive (near-side and far-side) scattering from Coulomb and nuclear fields often become comparable at energies above the Coulomb barrier. The secondary wavelets emanating from the deformed nuclear surface are generated by a combined effect of the repulsive Coulomb and absorptive nuclear interactions at each point. At large distances between incoming projectile and target nucleus, Coulomb scattering to forward angles connects theory and experiment. As smaller distances are approached, the nuclear amplitude changes (and increases) rapidly causing scattering to backward angles. The oscillatory structure is gradually attenuated due to increasing opacity of the nuclear surface (surface absorption of heavy-ions), and thus, the differential scattering cross sections are commonly found to exhibit distinct patterns that are best described solely on account of Coulomb-nuclear interference (CNI) [14] effects.

The scattering amplitude for inelastic scattering depends on the multipolarity of the transition, with demarcated regions where (i) the Coulomb field dominates, (ii) the nuclear field dominates, and (iii) the Coulomb and nuclear fields interfere. Their combined effect, and individual strengths, govern the overall shape of the angular distribution for a particular λ and reveals important structural information about the nucleus. Therefore, it is possible to determine Coulomb and nuclear deformation

characteristics separately by measuring the distribution of scattered nuclei over a wide angular range. In the semi-classical approximation, the inelastic scattering cross section can be expressed as [15],

$$\left(\frac{d\sigma_{\text{inel}}}{d\Omega}\right) = \left(\frac{d\sigma_{\text{el}}}{d\Omega}\right) \cdot P_{\text{ex}}(\theta) \quad (1.20)$$

where, $P_{\text{ex}}(\theta) \propto |C + N|^2$ is the probability for a nucleus to be excited when the incoming particle is scattered into the angle θ , and C and N are the scattering amplitudes due to Coulomb and nuclear potentials, respectively. Using this method in combination with contemporary accelerators and improved charged-particle and γ detector arrays opens new possibilities of pursuit in the field of nuclear research. Complicated avenues of excitation are included by means of theoretical calculations in the coupled-channels framework.

Heavy-ion inelastic scattering is also closely analogous to an electric multipole radiative transition, and will show similar collective enhancement, which varies with the scattering angle [16]. However, magnetic transitions are not affected, the enhancement being found exclusively in the spin-independent electric transition amplitudes. For inelastic scattering of a nuclear projectile from a target, the transition amplitude on a direct interaction model, for excitation of the target from the ground state i to an excited state f , when the relative motion before and after excitation is described by waves χ , is given by $T_{fi} = \langle f | \hat{N} | i \rangle$, with the nuclear transition operator as,

$$N = \int d\vec{r}_0 \chi^{*(-)}(k_f, r_0) V(\vec{r} - \vec{r}_0) \chi^{(+)}(k_i, r_0) \quad (1.21)$$

A multipole expansion of the waves corresponding to asymptotic initial and final momenta, k_i and k_f , as well as of the interaction potential V , leads to a general form of the operator,

$$N_\lambda \propto j_\lambda(qr) Y_{\lambda\mu}(\Omega) \quad (1.22)$$

with $q = |k_i - k_f|$ as the recoil momentum. For low-lying transitions, $j_\lambda \sim r^\lambda$, and Eqn. 1.22 has a form analogous to the electric multipole operator (see Eqn. 1.5), except that the sum here is over all nucleons, whereas in the electric radiative transition operator, the sum is only over the protons. Correspondingly, the angular distribution of the inelastic scattering is given by $|T_{fi}|^2 \propto |\langle j_\lambda(qr) \rangle|^2$. It is expected that this condition will be satisfied by all projectiles inelastically scattered into the first (forward) peak of the differential cross section, and the structural characteristics of the target excited states obtained from scattering of the nuclear projectiles should be in compliance with those obtained from radiative decay of the state. Scattering through angles much larger than this may show significant variance compared to an electric transition, when nuclear field comes into the picture.

The understanding of peripheral heavy-ion collision processes in general, and elastic and inelastic scattering in particular, is an important part of an overall understanding of heavy-ion reactions. It is the purpose of this thesis work to demonstrate (i) the ability of this approach to systematically address crucial aspects of nuclear collectivity on an absolute scale along an isotopic chain of stable even-even nuclei within single experiments, (ii) the compliance between the results of heavy-ion scattering and conventional techniques, such as level-lifetime measurement, and (iii) the effects of dynamic structural couplings in heavy-ion collisions that influence the cross sections of all reaction channels in a system. In the course of this work, different experiments focusing on the signatures of vibrational collectivity have been performed on the stable even-mass Sn nuclei, which constitute the longest chain of semi-magic stable isotopes.

1.3 The Sn isotopic chain

The tin isotopes, with a closed proton shell of $Z = 50$, constitute the longest chain of single-shell-closed nuclei with 15 even-even isotopes between the ^{100}Sn ($N = 50$) and ^{132}Sn ($N = 82$) double-shell closures, each with intrinsic g.s. spin 0^+ . Seven of these isotopes, $^{112,114,116,118,120,122,124}\text{Sn}$, are stable and the rest are unstable. These features have made the tin isotopes a prototypical benchmark of extensive microscopic theory and experiment and a rich arena for investigating residual nucleon-nucleon interactions. This is reflected in the large number of studies, both experimental and theoretical, of the transitions populating the low-lying 2_1^+ (see Fig. 1.2) and 3_1^- (see Fig. 1.3) states of the stable isotopes in the past few decades. These levels are normally classified as 1-phonon quadrupole and octupole vibrational states, which is also supported by quasiparticle calculations [17]. From electromagnetic measurements, these excitations are known to possess electric character and the transition characteristics are usually inferred only through the $B(E\lambda)$ values, which, in principle, are related to the charge (proton) contributions to the excitation (the core is not truly inert), and do not include the contributions due to the matter (proton + neutron) densities that are known to have extended distributions for the neutron-excess Sn nuclei [18]. The Weisskopf estimates for the $B(E2)$ and $B(E3)$ values for the stable Sn isotopes are listed in Table 1.1.

Measurements of electric transition strengths only determine the proton transition matrix element, M_p , and are oblivious to the neutron transition matrix element, M_n , which is particularly of significance for the Sn isotopes that have only neutrons as the valence particles. The existing $B(E2)$ and $B(E3)$ values for the Sn isotopes, measured by means of Coulomb excitation, level-lifetime determination, and inelastic scattering of electron, proton, α and heavy-ions, are found to be substantially enhanced compared to the values given in Table 1.1, and are consequences of virtual excitations of the proton core, polarized by the valence neutrons. However, these ex-

Table 1.1: Weisskopf single particle estimates of the $B(E2)$ and $B(E3)$ values for low-lying $\lambda = 2$ and $\lambda = 3$ excitations in the Sn isotopes.

Nucleus	$B(E2; 0_{g.s.}^+ \rightarrow 2_1^+)_{sp}$ ($e^2 \text{fm}^2$)	$B(E3; 0_{g.s.}^+ \rightarrow 3_1^-)_{sp}$ ($e^2 \text{fm}^3$)
^{112}Sn	160.05	5204.56
^{114}Sn	163.89	5390.85
^{116}Sn	167.94	5594.11
^{118}Sn	171.64	5780.12
^{120}Sn	175.52	5977.29
^{122}Sn	179.47	6180.05
^{124}Sn	183.36	6382.11

isting estimates have a wide range and there are inconsistencies leading to different conclusions on the strength of collectivity of the excitation modes. Large inconsistencies also exist among measurements with the same probe at different incident energies [19–24]. Older theoretical estimates for excitations in $^{102-130}\text{Sn}$ based on single j -shell exact seniority model [25], as well as large-scale shell model calculations involving proton-core excitations for an $N = Z = 50$ core [26] suggest highly collective $\lambda = 2$ transitions in the Sn isotopes, with a symmetric decrease in $B(E2)$ as the neutron number varies from the midshell ^{116}Sn nucleus on either side, following a parabolic behaviour. This trend has been verified for the isotopes with mass $A > 116$ by exclusive Coulomb excitation measurements [27]. However, for $A < 116$, the measured $B(E2)$ values are found to increase first from ^{116}Sn to ^{112}Sn and stay nearly similar upto ^{106}Sn within experimental uncertainties, thereafter decreasing towards ^{104}Sn [28, 29]. Ref. [30] has shown that the interaction between nucleons in spin-orbit partner orbits, $\ell \uparrow (\downarrow) = \ell + (-)\frac{1}{2}$, could strongly modify the effective single particle energies. For any two nucleons, 1 and 2, the $\ell_1 \uparrow - \ell_2 \downarrow$ interaction is found to be strongly attractive, particularly between neutrons and protons, while the $\ell_1 \uparrow - \ell_2 \uparrow$ and $\ell_1 \downarrow - \ell_2 \downarrow$ interactions are repulsive. In measurements of single particle energies of ^{47}Ar ($Z = 18$) and ^{49}Ca ($Z = 20$) [31], the location of the $2p_{3/2}$ and $2p_{1/2}$ orbits were found to be at higher energies ($\sim 875\text{-keV}$ larger) in ^{49}Ca com-

pared to ^{47}Ar . This was suggested to be due to removal of two protons from $1d_{3/2}$ and $2s_{1/2}$, causing a weakening of the $N = 28$ shell closure. An analogous argument has been drawn for the Sn-isotopes [32], where the proton $1g_{9/2}$ orbit is expected to become less bound with decrease in the number of neutrons in the $1g_{7/2}$ orbit, towards the proton-rich side of the Sn chain. This would enhance the probability for core-proton excitations across the $Z = 50$ shell gap, leading to an increase in the $B(E2)$ values for the neutron-deficient isotopes. A seniority truncated shell-model calculation using ^{90}Zr as an inert core [26] predicts such an increase in transition probability as proton-core excitations are included. Newer relativistic quasiparticle random phase approximation (RQRPA) calculations [33] have been successful in justifying the observed $B(E2)$ trend for both the neutron-deficient as well as neutron-rich isotopes. However, the RQRPA results are suppressed by up to 30% for the stable $^{112-124}\text{Sn}$ isotopes compared to the adopted values.

Lately, a series of Coulomb excitation experiments on $^{112-124}\text{Sn}$, based on either direct estimation of $\tau_{2_1^+}$ [34,35], or direct measurement of $B(E2; 0_{\text{g.s.}}^+ \rightarrow 2_1^+)$ [36,37], have been reported with discrepant results. The $B(E2)$ values deduced from the level lifetimes reported by Jungclauss *et al.* [34] are considerably lower than the adopted values across the Sn isotopic chain, showing a departure from collectivity and with a shallow minimum at ^{116}Sn . These results have been much disputed later by Allmond *et al.* [37] and Kumar *et al.* [36]. Though the overall mass dependence of the $B(E2)$ values is similar in both these measurements, they report markedly different absolute values for the neutron-rich $^{120,122,124}\text{Sn}$ isotopes. The $B(E2)$ results of Kumar *et al.* [36] are apparently prone to normalization uncertainties as these quantities have been estimated relative to the $B(E2)$ value of the excited ^{58}Ni projectile used in this measurement, chosen to be equal to $0.065 \text{ e}^2\text{b}^2$, which is less than both the adopted value [38] as well as the average value from a recent compilation [39] of results of Coulomb excitation and electron scattering measurements

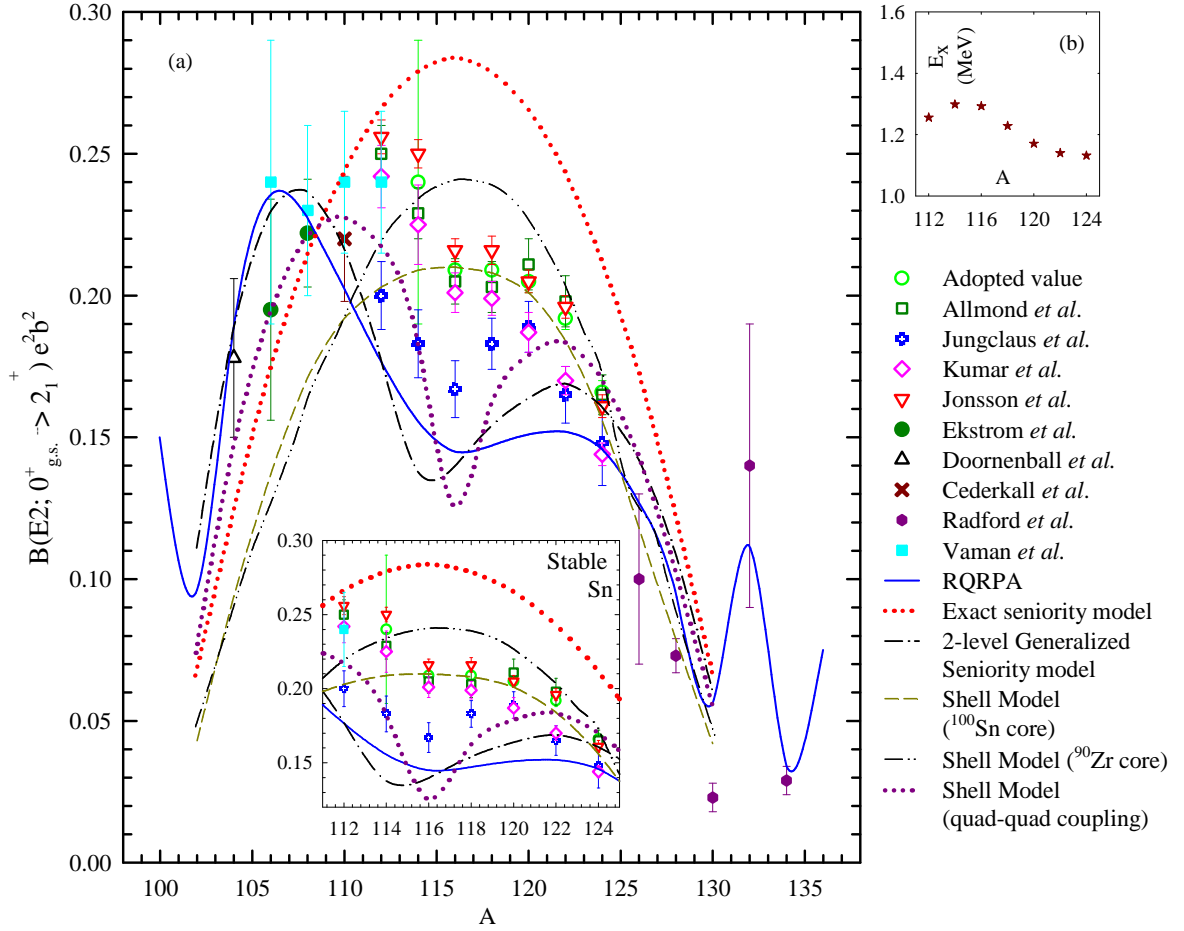


Figure 1.2: (a) Existing experimental (Coulomb excitation) and theoretical estimates of the $B(E2)$ values for the Sn isotopic chain. The inset shows the estimates for the stable isotopes. (b) $E2$ excitation energies for the stable isotopes.

on ^{58}Ni . On the other hand, Allmond *et al.* [37] report a robust measurement of the $B(E2)$ values, along with the static electric quadrupole moments and the magnetic dipole moments for all the stable Sn isotopes, to a high degree of precision in an inverse kinematics experiment. The $B(E2)$ results are in good agreement with the adopted values and predict an overall enhancement of collectivity.

There have been theoretical studies directed towards explaining the trend of low $B(E2)$ values, with a shallow minimum at ^{116}Sn , from the lifetime results reported by Jungclaus *et al.*, (i) employing two sets of effective charges across the Sn isotopic chain (for $A > 116$ and $A < 116$) for a shell model Hamiltonian with quadrupole-

quadrupole interaction between valence neutrons [40], and (ii) a schematic two-level, generalized seniority scheme concerned with the order of filling of the j -orbits in the Sn isotopes [25]. However, to reproduce the aforementioned trend, these calculations predict $B(E2)$ values further smaller by $\approx 15 - 25\%$, particularly for the $^{114-120}\text{Sn}$ isotopes.

Similar discrepancies exist for the $E3$ ($\lambda = 3$) transition probabilities of $^{112-124}\text{Sn}$, where, existing measurements form a wide range of the $B(E3)$ values with large uncertainties, and disagreements among theoretical estimates as well. The $B(E3)$ values obtained by the Coulomb excitation method (with less uncertainties) by N. G. Jonsson *et al.* [23] are much smaller than the ones obtained by D. G. Alkhazov *et al.* [24] by the same method, thereby causing an apparent discrepancy. Moreover, it has also been observed that the values obtained by inelastic scattering of α particles are much less compared to the ones obtained by scattering of protons [41, 42] or electrons [22]. Different sets of theoretical estimates [43, 44] based on quasiparti-

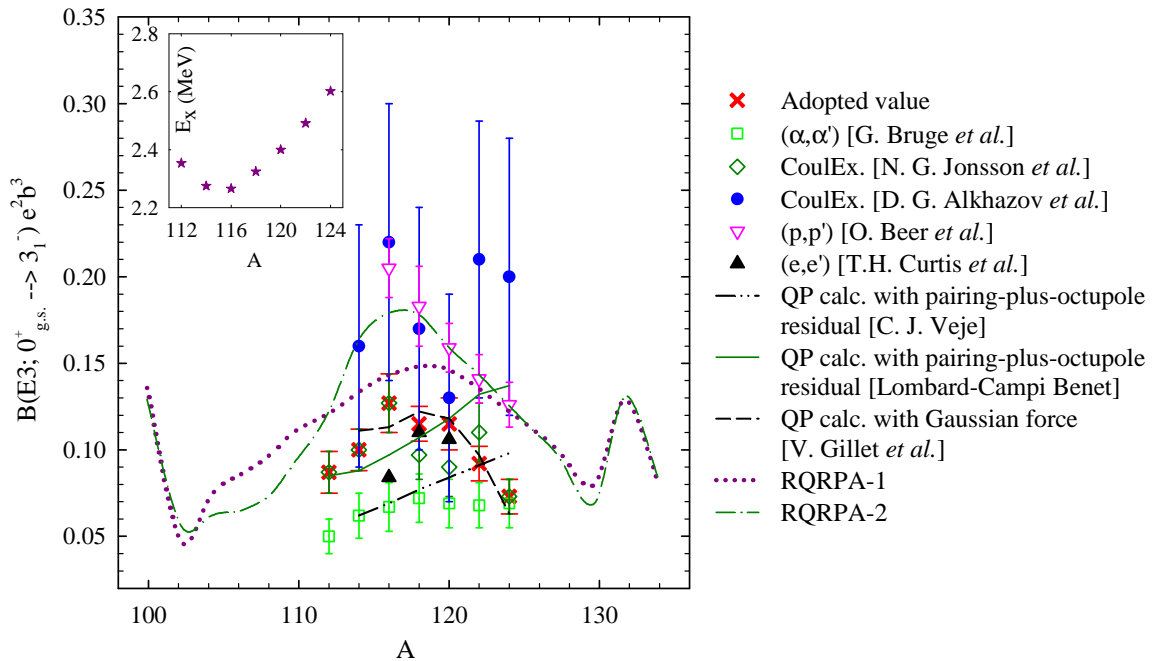


Figure 1.3: Existing experimental and theoretical estimates of the $B(E3)$ values for the Sn isotopes. The inset shows the $E3$ excitation energies for the stable Sn isotopes.

cle calculations with an octupole pairing force predict significantly different values among each other, and also contradict the trend of the results from a quasiparticle calculation involving a Gaussian force [45]. However, these results are at variance with a newer set of RQRPA calculations [17] that predict enhanced collectivity. In the light of such discrepancies, unambiguous quantitative assessments of collective properties for the 2_1^+ and 3_1^- states, particularly in the stable Sn isotopes, is necessitated. Extensive measurements and understanding of the basic collective phenomena in low-lying transitions along an isotopic chain of stable neutron-excess nuclei, with better understood structures, could act as a reference for improved studies with unstable isotopic chains, that are expected to be of similar complexity.

1.4 General motivation of the thesis

In light of the above discussions, the present thesis work has several key motivations. The primary motivation is to measure the transition probabilities, $B(E\lambda)$, of the dominant low-lying $\lambda = 2, 3$ excitations by means of heavy-ion scattering on the $^{112,116,118,120,122,124}\text{Sn}$ isotopes, compare them with existing estimates and understand the underlying contributions from the neutron and proton densities. Since descriptions of heavy-ion reaction mechanisms are sensitive to the choice the nuclear potential, such measurements are known to be dependent on the choice of the projectile used as the probe. To conclude about the existence of probe dependence, and effects thereof, measurements are carried out with a tightly-bound projectile with zero spin and isospin (^{12}C), as well as another weakly-bound projectile with non-zero spin and isospin (^7Li). An analogy is also expected between the excitation spectra of nuclei obtained by pure electric decay from the excited states, and by direct interactions such as the inelastic scattering of nuclear particles (as discussed in §1.2). However, the number of configurations which take part in the excitation and the total interaction operator are expected to be different in the two cases, on

account of the spin and isospin dependence of the nuclear interaction. An important difference also arises in the form of the (short) wavelengths of the colliding nuclei compared to the (longer) photon wavelength. Thus one would expect some quantitative differences. In this context, the $B(E2)$ value for the most-abundant ^{120}Sn isotope has been determined by a measurement of the γ -decay lifetime of the 2_1^+ state, using updated methodologies. The result has been compared with the values deduced from heavy-ion scattering measurements, as well as with existing lifetime measurements. The importance of realistic estimation of structural parameters and deformation characteristics of the dominant low-lying states in nuclei is realised through investigation of their effects on reaction dynamics in nuclear collisions, specifically by demonstrating a simultaneous description of the elastic scattering channel along with the inelastic scattering and one-nucleon transfer channels in the $^7\text{Li} + ^{120}\text{Sn}$ reaction system, at two bombarding energies. Further, as an extension of this work, it has been shown that inelastic channels can couple to the relative motion between colliding nuclei and significantly affect predictions of fusion cross sections, particularly in systems involving weakly-bound projectiles, where different model calculations lead to different conclusions about suppression/enhancement of complete fusion, compared to measured data.

The experimental details and outcomes of the above measurements and subsequent analyses, as well as the theoretical formalisms for investigating reaction dynamics, are discussed in the following chapters.

Chapter 2

Experimental methods

The experiments associated with the present thesis involve the detection and identification of charged particles and γ rays, and their energies emitted during the events of heavy ion collisions, over wide angular ranges. These are some of the major fundamental tools to study different aspects of nuclear reactions. The identification corresponds to the details of (i) the mass, charge, kinetic energy and emission angle of the charged particles, and (ii) the energy, angle of emission, multipolarity, nature of decay (electric or magnetic character), and Doppler shift/broadening, if any, for the γ -rays. In a typical binary heavy-ion collision measurement, where the outgoing channel consists of two broad categories of particles - the projectile-like fragment and the recoiling target-like particle, such as in inelastic scattering or nucleon/cluster transfer processes, one can reconstruct the kinematic details of the reaction by detecting and identifying one of the particles. Such two-body reactions are often accompanied by γ -decay events from excited states of either or both the participating nuclei. The study of the reaction kinematics in such scenarios conventionally involves a particle- γ coincidence technique to identify the direction of emission of radiation w.r.t. the source of the decay. The angular distribution of γ -rays is known to be sensitive to the spin and parity of the excited state. In the absence of coincidence techniques, one obtains an inclusive γ -yield from all possi-

ble directions of emission. The principal goals of this thesis are to investigate the structural properties (i) of the low-lying 2_1^+ and 3_1^- excited states in the stable Sn isotopes by means of heavy-ion scattering with ^7Li and ^{12}C projectiles, and (ii) of the 2_1^+ state in ^{120}Sn by means of level-lifetime measurement from radiative transitions. So, it is important to detect and identify, with precision, the scattered charged particles as well as γ -rays, using dedicated setups. Study of these reactions involves the generation and acceleration of the projectile, followed by the experimental arrangement of the relevant detector systems, associated electronic equipments and a data acquisition system. The details of each of the components are described hereafter.

2.1 Generation and acceleration of the projectile

The study of low/intermediate energy nuclear reactions generally involves projectiles having energies of the order of few MeV/nucleon. This can be obtained by accelerating the projectiles under an electric potential. All the measurements reported in this thesis have been carried out using the 14UD BARC-TIFR Pelletron-LINAC accelerator facility at Mumbai, a schematic of which is shown in Fig. 2.1.

An indigenously developed ion source, named MC-SNICS (Multi-Cathode Source of Negative Ions by Cesium Sputtering) is connected to the top of the accelerator, which produces negative ions of the desired projectile, with high intensity and low emittance. The negative ions are initially accelerated to low energies (150-250 keV) in a short horizontal section until they reach the injector magnet. Here, the ions are mass-analyzed by the 90° bending magnet to remove any impurities before transport into the vertical accelerating tube. The injected singly-charged negative ions are then accelerated towards the high voltage terminal situated at the center of the column, and thus gain an energy equal to the amount of eV_T , with V_T as the operational terminal voltage. The high voltage at the terminal is attained by a continuous transfer of positive charge, through electromagnetic induction, by virtue

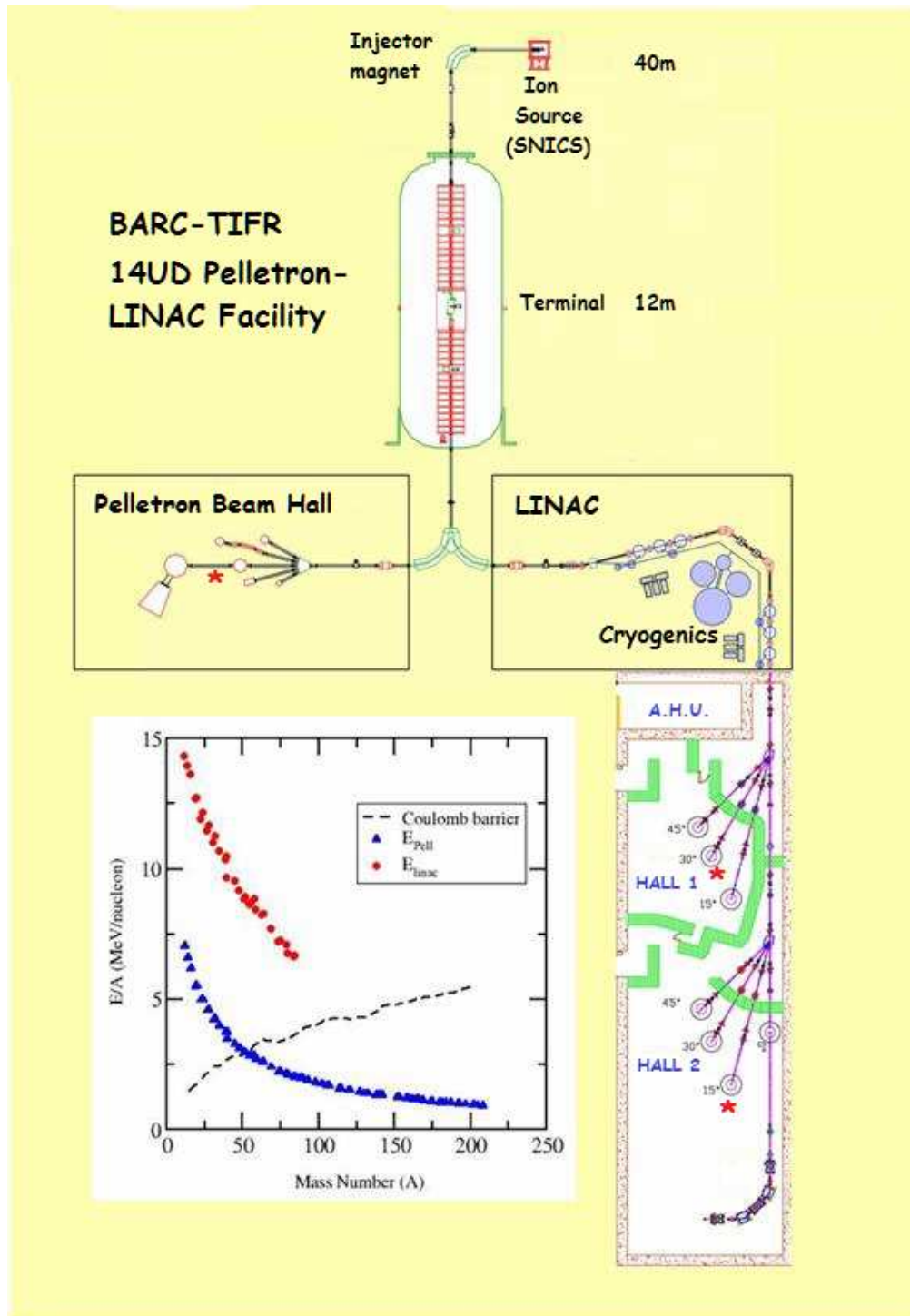


Figure 2.1: A schematic layout of the 14UD Pelletron-LINAC accelerator facility at Mumbai, India. The plot shows the available energy from Pelletron (red, circles) and LINAC (blue, triangles) as a function of mass number of ion. The different experiments pertaining to this thesis work have been carried out at the beam-lines marked with red asterisks.

of a chain of steel pellets; hence the name Pelletron accelerator. Inside the terminal, the singly-charged negative ions are passed through Carbon stripper foils, of thickness $\sim 5 \mu\text{g}/\text{cm}^2$, or a small volume of a gas, where they lose, say Z , electrons due to the charge exchange collision with the stripper material. Consequently, a positive charge state, Ze , is obtained for the ions after passing through this section. These positive ions are then subsequently repelled by the high voltage positive terminal and accelerated with energy ZeV_T , until they reach the analyzing magnet. Thus, the energy gained by the ions in the two stage tandem acceleration is $E_{\text{pell}} = (Z + 1)eV_T$. Though positive ions of different charged states arrive up to the analyzing magnet, ions of only a particular charged state are selected and extracted. The desired charged state of the ion can be transported to the LINAC stage for a further boost in the kinetic energy, based on requirement. Thereafter, the ion beam, with energy spread $\leq 2 \text{ keV}$, can be taken to one of the several beam-lines by using a switching magnet.

The desirability of having higher energy heavy-ion beams for certain experiments requires energy boosters. Most of the boosters already in operation at some laboratories are based on the technique of radio-frequency acceleration using cavity resonators made of both normal and superconducting materials. For the Pelletron at Mumbai, a superconducting linear accelerator is employed as the booster; the accelerating elements being lead plated quarter wave resonators [46]. The LINAC booster has a modular design with seven cryostat modules connected by a magnet system, each accommodating four quarter wave resonators, operating at 150 MHz. The optimum velocity acceptance for the cavities is $v/c=0.1$. Operational characteristics provide an average energy gain of $\sim 0.4 \text{ MV}$ per charge state per cavity, corresponding to 80% of the design value. Typically, beam transmission at target after collimation is known to be $\sim 50\%$ of that at the entry to the LINAC.

There are five beam-lines in the Pelletron beam hall, namely 0° , 15°N , 15°S , 30°N , and 30°S , three beam-lines in LINAC Hall-1, namely 15° , 30° , and 45° , and three beam-lines in LINAC Hall-2, namely 15° , 30° , and 45° . The heavy-ion scattering measurements on the Sn isotopes, reported in this thesis work, have been carried out in the region of the Pelletron energies for ^7Li and ^{12}C probes, at the 0° Pelletron and the 30° LINAC Hall-1 beam-lines, respectively. The level lifetime measurements on ^{120}Sn have been carried out with ^{32}S projectile at a LINAC-boosted bombarding energy, at the 30° LINAC Hall-2 beam-line. These measurements primarily aim at the detection of energetic heavy charged particles scattered from the g.s. as well as excited states of the Sn targets, or γ -rays emitted from the decay of excited states in ^{120}Sn . Different experimental arrangements and associated tools are used for these purposes, which are elaborated in the following sections.

2.2 Semiconductor radiation detectors

One of the most important advancements in nuclear instrumentation has been the development of semiconductor radiation detectors. Single crystals of semiconductor materials, such as Silicon (Si) and Germanium (Ge), are extensively used in nuclear reaction and structure studies. The small gap between their valence band and conduction band (~ 1.1 eV for Si and ~ 0.72 eV for Ge) facilitates the generation of a large number of electron-hole pairs, which improves signal quality. The energy required to produce electron-hole-pairs is also very low (~ 3 eV), compared to that required to generate charge carriers in gas detectors (~ 30 eV). As a result, the statistical variation of the pulse height is smaller and the energy resolution is higher. A semiconductor detector is basically a reversed biased p-n junction diode, wherein, the important characteristic which is of consideration is the active volume of the detector, determined by the thickness of the depletion region. Characteristics of ionizing incident particle/radiation is measured by virtue of the number of

charge carriers liberated in this active detector volume that is arranged between two electrodes. If Si or Ge of normal semiconductor purity is employed, the maximum achievable depletion depth is of a few mm, even at bias voltages close to the breakdown level. Therefore, the intrinsic crystal lattice of the material is generally doped with controlled amounts of suitable impurities (n-type/p-type) that enhance the overall conductivity of the material. The depletion width across the junction is known to increase with an increase in the reverse bias voltage, and a decrease in the doping concentration. At sufficiently high, and safe, operating voltages, the detector can be fully depleted of free charge carriers. The impurity concentration should be of the order of 10^{10} atoms/cm³ in order to realize wide depletion depths. Based on experimental requirements, the detectors are available in different configurations and geometries. The variants used in this thesis work are Si surface barrier (SSB) detectors and high-purity/hyperpure Ge (HPGe) clover detectors ($\leq 2 \times 10^{-4}$ ppb doping impurity). While detector-grade Si cannot be thicker than a few mm for bias voltages within safe limits of breakdown, HPGe can have a depleted, sensitive thickness of few cm at operating voltages of 2-3 kV, and therefore present a larger volume for total absorption of incident radiation. Hence, Si is mainly used for detecting charged particle, while Ge is widely used for γ -ray spectroscopy.

2.2.1 SSB detector for charged particles

Typical SSB detector is commonly made of n-type silicon on which one surface has been etched prior to coating with a thin layer of gold ($\sim 40 \mu\text{g}/\text{cm}^2$) that acts as the p-layer, and the other surface is coated with a thin layer of aluminum ($\sim 40 \mu\text{g}/\text{cm}^2$) to provide electrical contact. The barrier is thus formed at the surface of the crystal, and extends over the full thickness of silicon wafer, making the detector efficient in measuring the energy deposition by the incident particle. SSBs can be made with varying thickness and depletion widths, ranging from $10 \mu\text{m}$ to few mm.

A typical detector with a sensitive area of 300 mm² and 300 μm depletion depth operates at 100 V reverse bias. The schematic configuration of a SSB detector is shown in Fig. 2.2.

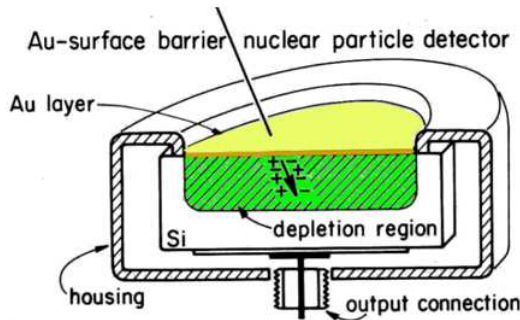


Figure 2.2: Schematic configuration of a typical Si surface barrier detector.

When an energetic charged particle penetrates into the semiconductor detector, it loses energy by means of electronic (and atomic) collisions and leads to ionization in the depletion region, generating electron-hole pairs. Since the Coulombic interaction with the orbital electrons has long range, it is not necessary for the light or heavy charged particle to always make a direct collision with an atom. While passing through the detector, the particle will transfer its energy to the atom. The drift motion of the liberated charge carriers under the external field produces an electrical signal with amplitude proportional to the energy deposited by the incident particle. The energy loss of the incident particle varies with its total energy E_{tot} , mass M , and atomic number Z . In a region of detector thickness Δx , the energy loss, ΔE is commonly expressed in terms of the Bethe-Bloch formula [47], given by $\frac{\Delta E}{\Delta x} = K \frac{MZ^2}{E_{\text{tot}}}$, where K is a constant. A plot between the quantities ΔE and E_{tot} aids in particle identification; different species of charged particle lie on different hyperboles proportional to the product MZ^2 . This principle of energy loss is employed in nuclear reaction studies, with a $\Delta E - E_{\text{res}}$ configuration, commonly known as a telescope, composed of two SSB detectors - a thinner ΔE where partial energy is deposited, and a comparatively thicker E_{res} where the residual energy is deposited,

and the particle comes to rest.

2.2.2 HPGe clover detector for γ -radiation

HPGe detector is commonly used as a total absorption detector for γ -rays, with energy up to a few MeV, which have multiple interactions with matter, unlike charged particles. However, in order to achieve maximum efficiency, the detector must be operated at liquid nitrogen temperature (77 K) to prevent thermal excitation of charge carriers at the room temperature, owing to the low band gap. A clover configuration consists of four coaxial n-type HPGe crystals, mounted in a common cryostat. This geometry further enhances the active volume of the detector. The schematic configuration of a HPGe clover detector is shown in Fig. 2.3. There are three key interaction mechanisms of γ -rays with the detector material, (i) photoelectric effect, (ii) Compton scattering, and (iii) pair production. The predominant mode of interaction depends on the energy of incident photons and the atomic number of the detector material. At low energies and with high Z materials, the photoelectric effect is main interaction process. At intermediate energies and in low Z materials, Compton scattering dominates. At sufficiently high energies ($E_\gamma > 1.022$ MeV), pair production becomes an important interaction process. When the photon col-

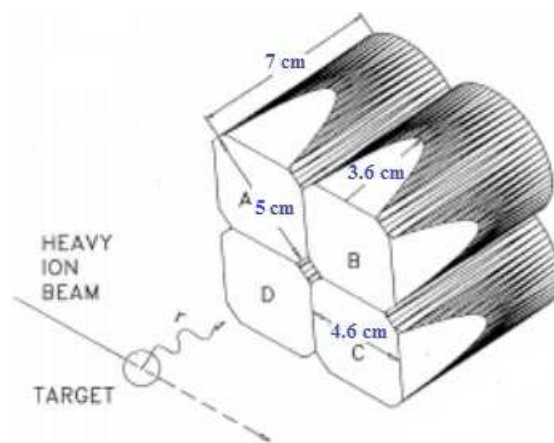


Figure 2.3: Schematic arrangement of a typical HPGe clover detector, with four crystals.

lides with an atom in the detector, it may impinge upon an orbital electron and transfer all of its energy to it, thereby ejecting it from the atom. The kinetic energy the ejected photo-electron receives equals the photon energy less its binding energy in the atomic shell, and the spectrum is thus populated by discrete photopeaks. The nucleus undergoes a recoil motion to conserve linear momentum carried by the incoming photon, and hence, this mechanism of interaction primarily involves the K or L shell electrons, and is dominant in high- Z materials. Once ejected, the photo-electron can ionize other atoms along its path, further leading to secondary/tertiary ionizations.

As incident γ -energy increases, inelastic/Compton scattering of a photon from a free electron becomes competitive. The momentum carried by the incoming photon is distributed between the recoil electron and the scattered photon. This leads to a continuous distribution of recoil energy for the scattered electron, which has a short range and deposits its energy into the detector material, while the scattered photon is most likely to escape. The signal from the recoil electron is recorded as a contribution to the baseline, since its energy is lower than the γ -energy. HPGe detectors are commonly used with associated components for Compton suppression, to improve precision and accuracy for isotope identification and reduce spectral interferences. In a Compton-suppressed arrangement, the scattered photons are detected by surrounding the clover with shields, commonly made of Bismuth-Germanate (BGO) detectors. If both the HPGe and the BGO detectors record an event within a specific time interval, that event is rejected, and correspondingly, the baseline of the Compton continuum being recorded by the HPGe gets drastically reduced. If the scattered photon, however, is detected by another crystal of the HPGe clover, the signals are then added to enhance photopeak efficiency. This process is known as add-back, where the charge collected by each of the crystals is summed, and used to determine the energy of the incident γ -ray.

As incident γ -energy further increases, spontaneous annihilation of radiation leads to the production of an electron-positron pair. Transformation of energy into mass occurs in presence of the electric field of the nucleus. The incident energy is divided into the rest mass energy and kinetic energy of the pair.

Another interaction mode, though not dominant in aspects of radiation detection, is coherent elastic scattering of photons. The incident photon is scattered by an atom in the detector material and is diverged from its original direction of motion, without any change in its energy. The electrons in the atom oscillate under the effect of the electromagnetic field carried by the photon, and radiate energy at the same frequency as the incident wave. Such a scattering event occurs primarily with very low energy photons and in materials with high atomic number. This effect can only be detected in narrow beam geometry.

2.3 Experimental setup & associated electronics

An electrical signal generated from a radiation detector has two branches - the energy branch and the timing branch. These need to be processed through suitable electronic circuits in order to extract the desired information for particle/ γ energies and timing correlations. The energy branch of the signal is processed through,

- a charge-sensitive preamplifier (CSP), to integrate the current signal from the detector and generate a voltage pulse with an amplitude proportional to the incoming input charge. It also acts as an impedance bridging network to prevent loss of signal voltage from the detector, with low output impedance, to the next stage, which is
- a gain amplifier/shaper, with high input impedance. The voltage signal is amplified to optimize the signal-to-noise ratio, and processed through pulse shaping filters. This stage is followed by

- an analog-to-digital converter (ADC) that converts, by sampling, the continuous-time and continuous-amplitude analog voltage signal to a discrete-time and discrete-amplitude digital signal/number representing the magnitude of the voltage. ADCs are generally sensitive to the peak of the voltage pulse, which characterizes the energy of the incident particle.

In order to extract the timing information of the signal, one needs

- a timing filter amplifier (TFA), which is a fast (rise time \sim few ns), variable RC filter that generates amplified, filtered outputs for optimal timing. Pulses are generally measured by their arrival time, when the signal exceeds a specified threshold. Consequently, the time resolution in such scenarios is compromised on account of a spread in the measured times (timing jitter) due to pulse height variations. This can affect the instrument response function. The contribution of pulse height distribution can be minimized with the use of
- a constant fraction discriminator (CFD), which essentially splits the signal into two parts - one part is delayed by half the pulse width and the other is inverted. When the two parts are recombined, the zero-crossing point is nearly independent of the pulse height, with a jitter of ≤ 50 ps. Additionally, one may use
- a time-to-digital converter (TDC), which assigns timestamps to the processed signals with fast rising edges. The pulses are also processed through
- logic units, where the signals are ORed or ANDed, to decide event multiplicity and trigger rates, and
- a gate and delay generator (GDG) that generates logic pulses with precise widths and delays (to compensate for intrinsic delays elsewhere in the system, such as cable delay or electronics delay) for triggering, syncing, delaying and

gating events. It provides electronic timing of a single event or multiple events w.r.t. a common timing reference/window.

Each of the aforementioned components can be used either in an analog data acquisition system (DAQ), or a digital data acquisition system (DDAQ).

2.3.1 Heavy-ion scattering measurements

In the heavy-ion scattering experiments relevant to the thesis, the main focus has been to measure the electric transition probability to the low-lying collective states in the Sn isotopes. Self-supporting enriched (>95%) targets of $^{112,116,118,120,122,124}\text{Sn}$ of thicknesses $\approx 540 \mu\text{g}/\text{cm}^2$, $1.45 \text{ mg}/\text{cm}^2$, $320 \mu\text{g}/\text{cm}^2$, $280 \mu\text{g}/\text{cm}^2$, $85 \mu\text{g}/\text{cm}^2$ and $290 \mu\text{g}/\text{cm}^2$, respectively, have been used for the measurements, mounted sequentially on a movable ladder inside an high-vacuum scattering chamber. The prerequisite for choosing each target foil was to identify well-resolved excited states of the nuclei involved in the collision, without compromising on the counting statistics. However, foils of different thickness have been used in this work since they were prepared at different laboratories, which had certain limitations at their respective fabrication facilities. The targets have been bombarded with projectile beams of ^7Li and ^{12}C ions at kinetic energy $E_{\text{lab}} = 28 \text{ MeV}$ and 60 MeV , respectively, sufficiently above the Coulomb barrier for each system. The measurements have been carried out in two sets, using arrays of telescopes ($\Delta E - E_{\text{res}}$), distributed on two arms of the scattering chamber, each placed 10° apart from its neighbouring telescope, at a distance of $\approx 21 \text{ cm}$ each from the target centre. The scattered projectile-like particles (ejectiles) are emitted over a wide angular range as permitted by two-body kinematics for elastic and inelastic scattering, with a change in kinetic energy corresponding to the Q -value of the process. The angular distribution for inelastic scattering is sensitive to the structural information of the excited state of the recoiling target. In addition, projectile-like fragments formed as a result of reactions

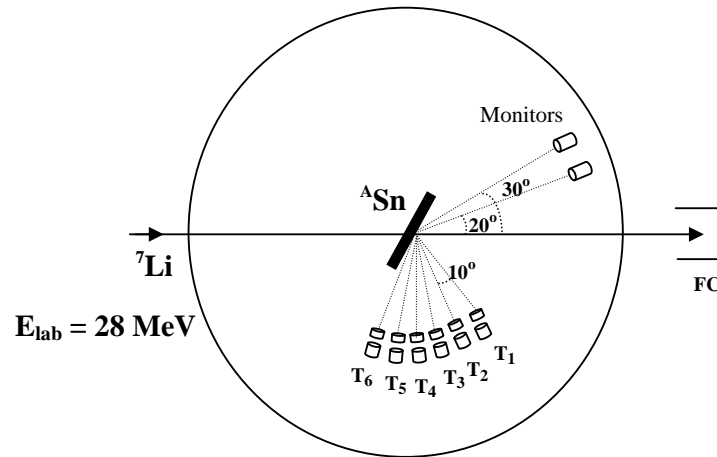


Figure 2.4: Schematic diagram of the experimental setup for the study of ${}^7\text{Li} + {}^{112,116,118,120,122,124}\text{Sn}$ reactions.

involving transfer of one or more nucleons, or light-charged particles originating from the projectile/ejectile breakup or fusion evaporation processes, are also detected. For the reactions induced by the ${}^7\text{Li}$ probe, six such telescopes (T_1 - T_6) have been used to detect reaction fragments in the angular range of 25° to 140° . The detector thicknesses were 25 to 50 μm for ΔE and ≈ 1000 μm for the E_{res} detectors. Two single Si-surface barrier (monitor) detectors fixed at 20° and 30° with respect to the beam at a distance of ≈ 39 cm from the centre, have been used to measure the Rutherford scattering cross section for flux normalization. A schematic diagram of the setup is shown in Fig. 2.4.

For the measurements with the ${}^{12}\text{C}$ probe, ten telescopes (T_1 - T_{10}), have been used to detect projectile-like fragments in the angular range of 20° to 110° . The detector thicknesses were 15 to 25 μm for ΔE and ≈ 300 to 1000 μm for the E_{res} detectors. Two monitor detectors are mounted on the chamber wall at $\pm 20^\circ$ with respect to the beam at a distance of ≈ 72 cm from the center. A schematic diagram of the setup is shown in Fig. 2.5.

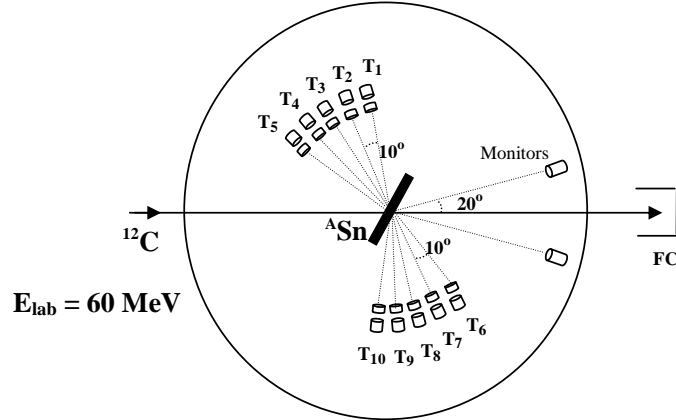


Figure 2.5: Schematic diagram of the experimental setup for the study of $^{12}\text{C} + ^{112,116,118,120,122,124}\text{Sn}$ reactions.

Signal Processing

Electrical connections from ΔE and E_{res} are taken from each telescope to identify the different charged particles, along with the current pulses generated by the monitor detectors. For signal processing, compact 8-channel modules, Mesytec MSI-8, are used, which have CSPs, gain amplifiers, shapers, with integrated TFA units. The shaper voltage signals, containing energy information from the ΔE and E detectors, were then fed to CAEN V785 peak-sensing ADC units for pulse digitization. The ADCs modules are set to an active BUSY state during the conversion process to prevent accumulation of data and reduce the dead-time for the DAQ system. The trigger/timing signals, from the E detector of each telescope, as well as the monitor detectors, were processed through ORTEC 935 CFD modules, and the outputs were ORed in a Phillips 755 logic unit. This ORed trigger signal was stretched to $\sim 4 \mu\text{s}$ by using Phillips 794 GDG module. This signal is known as raw-master/trigger signal. The BUSY signals from ADCs were used to veto the raw-master, and generate the gate for triggering the acquisition system. A schematic of the analog signal processing system is shown in Fig. 2.6. A LINUX based advanced multi-parameter data acquisition system, LAMPS [48], was used to acquire on-line list mode data.

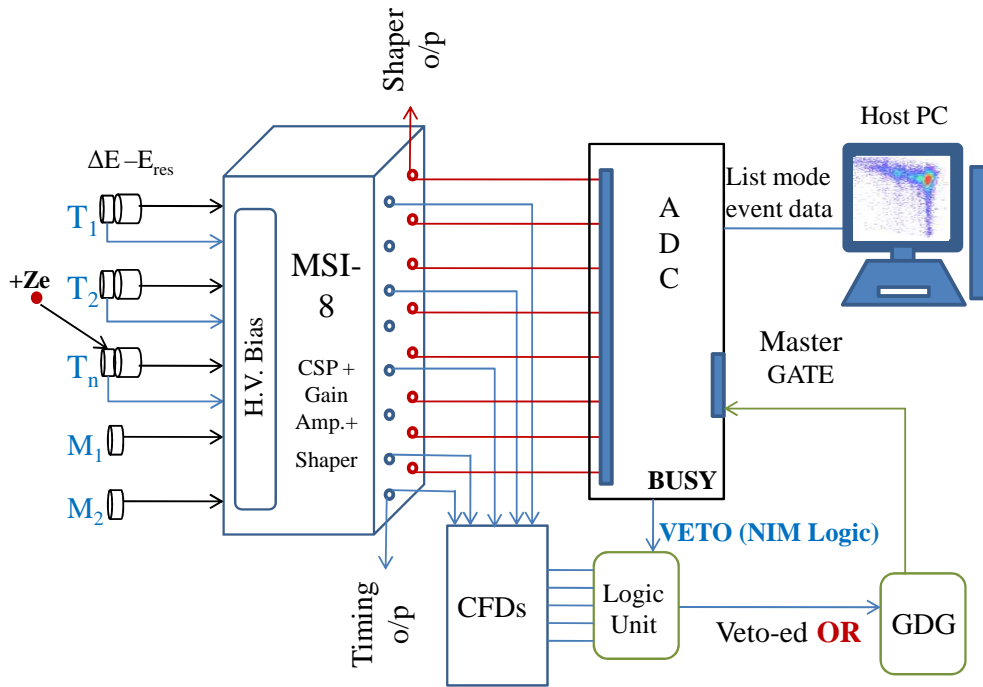


Figure 2.6: Schematic diagram of the analog signal processing-based data acquisition system for the Si surface barrier detectors.

2.3.2 Level-lifetime measurements

For level-lifetime measurements on the ^{120}Sn nucleus, low-lying excited states have been populated with the heaviest-available spherical projectile at the facility, ^{32}S , by means of the $^{120}\text{Sn}(^{32}\text{S}, ^{32}\text{S}')^{120}\text{Sn}^*$ reaction at kinetic energy $E_{\text{lab}} = 120$ MeV (to ensure larger recoil momentum; see Chapter 5). The target comprised of an enriched ^{120}Sn foil of thickness ≈ 6.4 mg/cm², with a ^{197}Au backing of thickness ≈ 6.2 mg/cm². Emitted γ -rays from the recoiling ^{120}Sn nuclei were detected using a segment of the Indian National Gamma Array (INGA) [49] spectrometer setup, then consisting of eleven Compton-suppressed segmented clover HPGe detectors, mounted at a distance of 25 cm from the target placed inside a small evacuated chamber. The anti-Compton shield of BGO material was placed in an aluminium housing, to prevent direct hit of γ -rays from the source/reaction centre to the BGO shield. Each clover also comprises of a heavy metal collimator, composed of tungsten

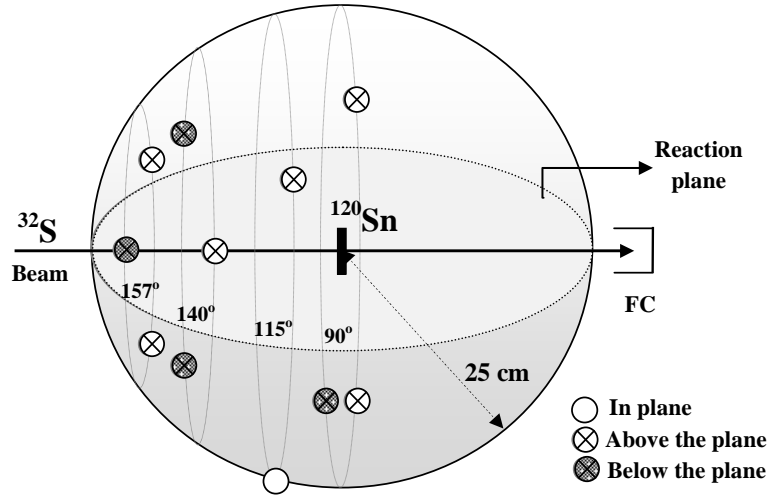


Figure 2.7: Schematic diagram of the experimental setup showing arrangement of the HPGe clover detectors.

material. The clovers were distributed in the backward hemisphere w.r.t. the beam direction at different angles, namely $\theta = 90^\circ$ (three at $\phi = 60^\circ, 120^\circ, 300^\circ$), $\theta = 115^\circ$ (two at $\phi = 90^\circ, 330^\circ$), $\theta = 140^\circ$ (three at $\phi = 0^\circ, 120^\circ, 240^\circ$) and $\theta = 157^\circ$ (three at $\phi = 60^\circ, 180^\circ, 300^\circ$). A schematic diagram of the setup with the arrangement of the clovers w.r.t the reaction plane is shown in Fig. 2.7.

Signal Processing

The decay events were recorded with a DDAQ system, consisting of Pixie-16 digitizer modules, developed by XIA LLC [50], each able to support four clover detectors. A 12-bit 100 MHz flash ADC (FADC) was used to digitize the preamplifier (CSP) signal produced by the crystals of each clover detector. The BGO signals were used for veto-ing the individual channels. A valid fast trigger was generated in the absence of the veto pulse in a specific time window. A typical schematic of the digital signal processing is shown in Fig. 2.8. Each analog input from the detector has its own signal conditioning unit that functions to adapt the incoming signals to the input voltage range of the FADC, which spans 2 V. The processing applies digital filter-

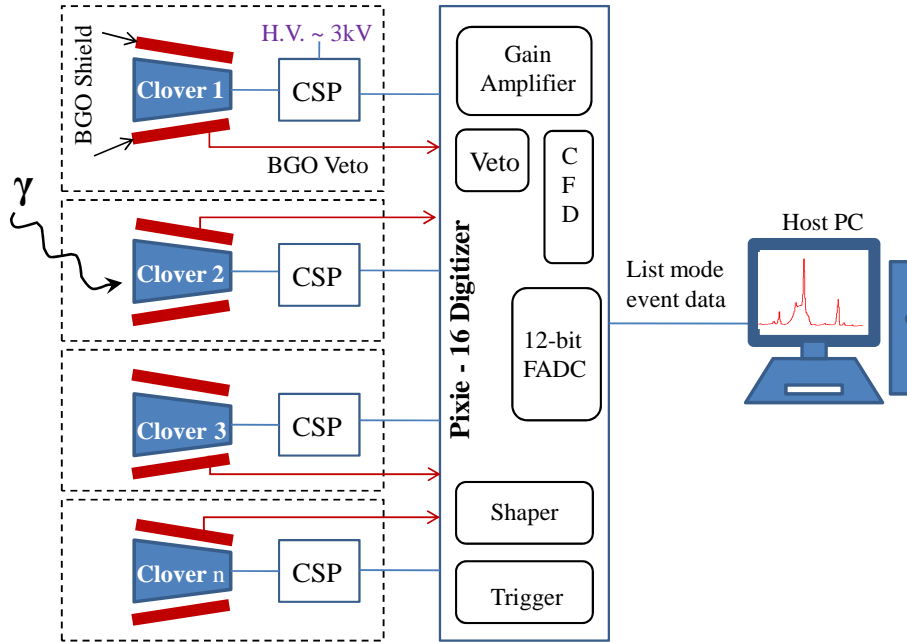


Figure 2.8: Schematic diagram of the digital signal processing-based data acquisition system for the HPGe clover detectors.

ing to perform essentially the same action as a shaping amplifier. The important difference is in the type of filter used; in DDAQ, trapezoidal filters are commonly used. The FADC is not peak sensing, rather acts as a waveform digitizer. The pulse processing runs independently in every channel. For a given channel, fast trigger validation is done and the time-stamped event header information was written. The resulting time-stamped spectroscopic data was sorted into spectra and E_γ - E_γ matrices using the multiparameter coincidence search program MARCOS [51], based on the mapping of DDAQ channels to different crystals of the detectors in the array. The matrices were both symmetric as well as angle dependent asymmetric ones for lifetime analysis. The latter had the 90° detectors on the X-axis, with detectors at one of the other angles (157° , 140° , 115°) on the Y-axis.

The detailed analyses and results of the different measurements are presented in the following chapters.

Chapter 3

Theoretical Framework : Coupled Channels Method

Heavy-ion collision processes are typically characterized by the presence of many open reaction channels. Depending upon the time-scale of interaction, the reaction modes are classified into (i) direct reaction processes and (ii) compound nuclear processes. When a reaction proceeds directly from the initial state to the final state without the formation of an intermediate nucleus, a direct reaction is said to have occurred (faster). A reaction that proceeds through the formation of intermediary nucleus is referred to as a compound nuclear reaction (slower). Many features of low-energy heavy-ion collisions are well understood by considering classical orbits of projectiles in the field of the targets, for various impact parameters. When the impact parameter is large, minimum interaction occurs and the projectile is only slightly deflected from its path. As impact parameter reduces with increase in bombarding energy, the orbit approaches the target more closely; the force of interaction increases, and so does the scattering angle. Consequently, the differential cross section for heavy-ion reactions progressively increases with increase in scattering angle. At energies around the Coulomb barrier, the dominant channels are elastic

scattering, inelastic excitations of directly populated low-lying states of projectile and/or target, transfer of nucleon(s), and the fusion process. When the projectile orbit intersects the target nuclear surface (grazing configuration), the cross sections for direct peripheral reactions like inelastic scattering and one/few nucleon transfer channels attain their maxima. If the projectile is weakly bound, then additional channels due to breakup of the projectile into two or more fragments also play an important role. If impact parameter reduces further, the projectile penetrates the target surface and complex processes of absorption come into the picture, thereby reducing the cross sections for surface reactions. A competition thus ensues among the several possible reaction modes, and a semi-classical approximation may not be realistic. Over several years, a comprehensive outlook in the form of the coupled channels (CC) framework [52] has evolved in which one seeks to describe all the main reaction processes simultaneously. The CC model calculations take into account the effect of dynamic coupling of different direct reaction channels on the two extremes - fusion and elastic scattering. Some of the CC calculations can also describe the cross sections of the different intermediate non-elastic channels, in concurrence with those of the elastic scattering and fusion channels.

In this chapter, the main focus is to understand the direct reaction processes involved in nuclear collisions and to portray the method of determination of cross-sections associated with each process in the realm of nuclear models. As this thesis work deals with the collision of heavy ions around the Coulomb barrier energy, the kinetic energy of the projectile is expectedly negligible as compared to its rest mass energy, leading to a non-relativistic approach to describe the nuclear reaction modes. However, the estimated velocity of the nucleons is $\sim 0.3c$, and the corresponding de Broglie wavelength ~ 4 fm, which is comparable to the nuclear radius parameter. This emphasizes the need to incorporate quantum effects into the nuclear interactions. Consequently, the framework of the theoretical CC models are based on the

effective solutions of the Schrödinger equation for the different channels belonging to the reaction system.

3.1 Generalized CC Model

When two nuclei approach each other in a collision process, they are deflected by the field generated from the mutual interactions of all nucleons in one nucleus with those of the other, both before and after any specific interaction leads to exchange of energy or nucleons between them. This amounts to a quantum many-body scattering problem, whose solutions are tedious. An alternative approach is to introduce an effective potential that depends only on the relative coordinate between the two nuclei participating in the reaction.

In a nuclear collision, all possible reaction channels are affected by couplings among the various degrees of freedom available to the collision partners. Various CC models are available that predict the cross sections of different reaction channels. There are several uncertainties in such analyses, in the nuclear interaction between the ions, the structural parameters of the participating nuclei, and in truncation of the CC calculations. A consistent set of coupling parameters is of utmost importance to be able to give realistic estimates for elastic scattering, fusion, as well as all channels in between, over a wide energy range. But this is prohibitive for some models that are unable to include all major channels that have an effect on fusion as well as the scattering observables of interest. While elastic scattering and other direct reaction channels are sensitive mostly to interaction form factors at peripheral distances (large radial separations), fusion is primarily sensitive to these quantities inside and around the barrier region. the choice of nucleus-nucleus potential is highly crucial. When the relative motion in the entrance channel couples to the intrinsic degrees of freedom, such as nuclear intrinsic excitations, static deformations, particle transfers and so on, the single one dimensional barrier for the system is split to form a

multidimensional distribution of barriers. The entrance flux is split among all such channels, each of which confronts a different barrier, depending upon its coupling strength [52].

For a pair of interacting nuclei, let r be the coordinate of relative motion and ξ define the intrinsic motion coordinate. The total Hamiltonian for the system can be written as a sum of the Hamiltonians of relative motion, $K(r) + V(r)$, intrinsic motion, $H_0(\xi)$, as well as the coupling interactions, $V_{\text{coup}}(r, \xi)$, of the internal degrees of motion with the relative coordinate.

$$H(r, \xi) = H_0(\xi) + K(r) + V(r) + V_{\text{coup}}(r, \xi) \quad (3.1)$$

The intrinsic wave-function, for an arbitrary internal degree of freedom α' , is the solution of the equation, $H_0(\xi)\Phi_{\alpha'}(\xi) = \epsilon_{\alpha'}\Phi_{\alpha'}(\xi)$, where $\epsilon_{\alpha'}$ represents the internal energy of the nucleus. The collision between the two partners can open up a multitude of reaction channels, each described by a wave function, $\psi_{\alpha'}(r, \xi) = \Phi_{\alpha'}(\xi)\chi_{\alpha'}(r)$. The total wave function is a linear combination of all such square-integrable basis states. Therefore, one may write the set of coupled equations for this system as,

$$\sum_{\alpha'} [H_0(\xi) + K(r) + V(r) + V_{\text{coup}}(r, \xi) - E] \psi_{\alpha'}(r, \xi) = 0 \quad (3.2)$$

This set of infinite equations can be decoupled by projecting on a particular channel α , and subsequently, integrating over ξ ,

$$[\langle \Phi_{\alpha} | H_0(\xi) | \Phi_{\alpha} \rangle + K(r) \langle \Phi_{\alpha} | \Phi_{\alpha} \rangle + \langle \Phi_{\alpha} | V(r) + V_{\text{coup}}(r, \xi) | \Phi_{\alpha} \rangle - E \langle \Phi_{\alpha} | \Phi_{\alpha} \rangle \chi_{\alpha}(r) + \sum_{\alpha \neq \alpha'} \langle \Phi_{\alpha} | V(r) + V_{\text{coup}}(r, \xi) | \Phi_{\alpha'} \rangle \chi_{\alpha'}(r) = 0 \quad (3.3)$$

$$\implies [\epsilon_{\alpha} + K(r) + V_{\alpha\alpha}(r) - E] \chi_{\alpha}(r) + \sum_{\alpha \neq \alpha'} V_{\alpha\alpha'}(r) \chi_{\alpha'}(r) = 0 \quad (3.4)$$

Eqn. 3.4 is the basic CC equation. The matrix element of the bare potential, $V_{\alpha\alpha}(r)$,

depends only on the relative coordinate between the collision partners. In general, it is chosen such as to describe the elastic scattering process accurately. The direct reactions are thought of as perturbations on the elastic scattering, as their typically observed cross sections are comparatively much smaller. An underlying assumption here is that the bare potential in every exit channel (that which accounts for the elastic scattering cross section in each channel) is same as the entrance channel potential, $V_{\alpha\alpha}(r)$, and is expressed as a sum of the nuclear, Coulomb and centrifugal terms as,

$$V_{\alpha\alpha}(r) = V_N^0(r) + \frac{Z_P Z_T e^2}{r} + \frac{\ell(\ell+1)\hbar^2}{2\mu r^2} \quad (3.5)$$

The matrix element of the coupling interaction is $V_{\alpha\alpha'}(r) = \langle \Phi_\alpha | V(r) + V_{\text{coup}}(r, \xi) | \Phi_{\alpha'} \rangle$. For dynamic couplings to the intrinsic degrees of freedom that usually have finite spin, the coupling interaction can be expanded into multipoles,

$$V_{\text{coup}}(r, \xi) = \sum_{\lambda>0} f_\lambda(r) Y_{\lambda\mu}(\hat{r}) T_{\lambda\mu}(\xi) \quad (3.6)$$

On decomposing each basis state into its constituent orbital (ℓ), intrinsic (I) and total (J) angular momentum components, one arrives at

$$V_{\alpha\alpha'}(r) \equiv V_{\ell I, \ell' I'}^J(r) = \sum_{\lambda>0} f_\lambda(r) \langle \ell I m_\ell m_I J M | Y_{\lambda\mu}(\hat{r}) T_{\lambda\mu}(\xi) | \ell' I' m_{\ell'} m_{I'} J M \rangle \quad (3.7)$$

Here $f_\lambda(r)$ defines the coupling form factor corresponding to multipolarity λ . With the aid of the well known Wigner-Eckart theorem [6], the matrix elements of spherical tensor operators acting on a basis of angular momentum eigenstates, Y_λ^μ and T_λ^μ , can be factorized into an angular momentum addition coefficient (Clebsch-Gordan/Wigner 3-j) and a reduced matrix element independent of the angular momentum orientation. With the addition properties of spherical harmonics, one

arrives at the explicit form of the coupling matrix element,

$$V_{\ell I, \ell' I'}^J(r) = (-1)^{\ell' + I' + m_I} \sum_{\lambda > 0} f_{\lambda}(r) \sqrt{2I + 1} \begin{pmatrix} I' & \lambda & I \\ m_{I'} & \mu & -m_I \end{pmatrix} \langle I || T_{\lambda} || I' \rangle \times \sqrt{\frac{(2\lambda + 1)(2\ell + 1)(2\ell' + 1)}{4\pi}} \begin{pmatrix} \ell' & \lambda & \ell \\ 0 & 0 & 0 \end{pmatrix}^2 \quad (3.8)$$

This formalism defines an effective (barrier) potential encountered by the flux in every channel coupled to the incoming channel.

At very low bombarding energies, charged nuclei can only scatter elastically. As the energy is raised, other reaction channels (both direct and compound) open and consequently, some flux is removed from the elastic scattering channel. At sufficiently high energies, the direct reaction mechanism dominates and the compound nucleus formed at that energy will decay with vanishing probability to the low-lying levels of the product nuclei, owing to the competition among the various open channels. This leads to a large removal of flux from the entrance channel. Different CC models simulate these effects in varied ways. In some simplified models (e.g. CC-FUS [53], CCDEF [54], CCMOD [55]), the interaction matrix for the set of decoupled equations (eigenchannels) is diagonalized to yield a spectrum of barriers across the different channels. However, these approaches are plagued by demerits such as (i) only two channels are solved at a time, (ii) structures of the colliding nuclei are not disturbed until fusion occurs inside the barrier region, (iii) influence of deformed nuclear shapes is taken into account within the sudden-limit approximation, where orientations in space are regarded as frozen throughout the collision (relative motion of the nuclei is fast and densities of the colliding nuclei remain constant), and (iv) under the assumption that incident relative energy is much higher than intrinsic energies and coupling strengths, the coupling form factors are assumed to have

same spatial dependence for all channels. Some exact CC models (e.g. CCFULL [56]) employ rigorous numerical solution of the coupled equations subject to an Incoming Wave Boundary Condition (IWBC) to simulate fusion. In others (e.g. FRESCO [57]), $V_{\alpha\alpha}(r)$ is taken to be a complex potential, since a real potential conserves flux. The addition of a negative imaginary potential leads to absorption of flux from the entrance channel, which is attributed as the fusion process. These reaction models are largely sensitive to the dynamic coupling interactions incorporated into the model space.

3.2 Coupling Interactions

Along with scalar nuclear attractions and scalar Coulomb repulsions, if either nucleus has spin $J \neq 0$ in its intrinsic state, then there exist higher order interactions that couple the spin and orbital motion, giving rise to interaction potentials of non-central character, such as those pertaining to (i) inelastic excitations, or (ii) particle/cluster transfers. Inelastic excitations populate the higher-energy states of nuclei. Single-particle excitations are another kind of inelastic process, when a particle in one of the nuclei is excited during the reaction from its initial bound state to another state which may be bound or unbound. Inelastic excitation of a weakly bound projectile, to an unbound state above the breakup threshold, leads to its dissociation into cluster components. Nucleons may likewise be transferred/exchanged between the two nuclei, either independently, or as the concurrent exchange of nucleons as a particle cluster.

3.2.1 Inelastic excitations

Inelastic potentials arise when nuclei have either permanent deformations, or are vibrationally deformable, or when one of the nuclei can be decomposed into core

+ valence structure, where the ground state of the composite can get reoriented, or the valence particle can be excited into higher energy eigenstates. Satchler [58] had performed perturbative calculations on the effects of ground state reorientation, showing that the nuclear level couples to itself, except that the magnetic substate is changed in the transition. The torque due to the long range Coulomb force reorients the deformed nuclei and subsequently alters the barrier distribution. The static/dynamic deformations of mass and charge distributions in nuclei modifies both the nuclear and Coulomb interaction potentials in events of nuclear collisions. In the geometrical collective model [3], the radius of a deformed nucleus is parametrized as $R(\theta, \phi) = R_0 \left[1 + \sum_{\lambda\mu} \beta_{\lambda\mu} Y_{\lambda\mu}^*(\theta, \phi) \right]$. The deformed charge and mass densities can be approximated by this expansion, with respective radii $R_0 = R_{ch}$ and $R_0 = R_m$.

Coulomb deformations :

Inelastic excitations in a nucleus (say, target, with charge density ρ_t) under the influence of the Coulomb interaction with another nucleus (projectile) are governed by the interaction potential of the form,

$$\begin{aligned} V_C(r) &= \int d^3 r' \frac{Z_p Z_t e^2}{|\vec{r} - \vec{r}'|} \rho_t(r') \\ &= \frac{Z_p Z_t e^2}{r} + \int d^3 \vec{r}' Z_p Z_t e^2 \rho_t(r') \sum_{\substack{\lambda' \neq 0 \\ \mu'}} \frac{4\pi}{2\lambda' + 1} \frac{r_{\leq}^{\lambda'}}{r_{>}^{\lambda'+1}} Y_{\lambda'\mu'}(\hat{r}') Y_{\lambda'\mu'}^*(\hat{r}) \end{aligned} \quad (3.9)$$

For a sharp density distribution, the electric multipole operator (see Eqn. 1.5), upto first order, for the deformed nucleus with charge radius R_{ch} is defined as [59]:

$$\hat{E}_{\lambda'\mu'} = \int d^3 \vec{r}' Z_t e \rho_t(r') r'^{\lambda'} Y_{\lambda'\mu'}(\hat{r}') \equiv \frac{3e}{4\pi} Z_t R_{ch}^{\lambda'} \beta_{\lambda\mu} \delta_{\lambda\mu, \lambda'\mu'} \quad (3.10)$$

The diagonal matrix elements of the $\hat{E}_{\lambda'\mu'}$ operator define the electric multipole moments, such as the static quadrupole moment, for statically deformed states in

nuclei (expectation value of $\hat{E}_{\lambda\mu}$ in those states), with $\lambda = 2, 4, \dots$. This is commonly known as the reorientation coupling, i.e., coupling to magnetic substates, m_J , for a state J . The off-diagonal matrix elements define the dynamic/transition rates and moments.

The Coulomb potential can then be written in the form,

$$V_C(r, \beta_{\lambda\mu}) = \frac{Z_p Z_T e^2}{r} + \sum_{\lambda\mu} \frac{3Z_p Z_T e^2}{2\lambda + 1} \beta_{\lambda\mu} Y_{\lambda\mu}^*(\hat{r}) \frac{R_{ch}^\lambda}{r^{\lambda+1}} \quad (3.11)$$

The first term on the right side is the bare Coulomb interaction, and the second term is the Coulomb component of the coupling Hamiltonian.

Nuclear deformations :

The nuclear interaction is sensitive to the matter distribution of the nucleus as a whole. In the collective model, the nuclear interaction is assumed to be a function of the separation distance between the surfaces of the colliding nuclei. For small deformations, the linear coupling approximation leads to,

$$V_N(r, \beta_{\lambda\mu}) = V_N(r - R_m \sum_{\mu} \beta_{\lambda\mu} Y_{\lambda\mu}^*(\hat{r})) \quad (3.12)$$

$$= V_N(r) - R_m \frac{dV_N}{dr} \sum_{\lambda,\mu} \beta_{\lambda\mu} Y_{\lambda\mu}^*(\hat{r}) \quad (3.13)$$

The first term of the right-hand side is the bare nuclear potential in the absence of the coupling, while the second term is the nuclear component of the coupling Hamiltonian.

For an axially symmetric dynamic deformation, the dependence on the orientation of angular momentum vanishes, and only $\mu = 0$ survives, leading to the effective

coupling potential,

$$V_{\text{coup}}(r, \lambda) = \left(-R_m \frac{dV_N}{dr} + \frac{3Z_p Z_T e^2 R_{ch}^\lambda}{2\lambda + 1 r^{\lambda+1}} \right) \sum_{\lambda} \beta_{\lambda 0} Y_{\lambda 0}^*(\hat{r}) \quad (3.14)$$

In analogy with Eqn. 3.6, one obtains $T_{\lambda 0}(\xi) \equiv \beta_{\lambda 0}$, and the term within the brackets represents the form factor for the inelastic excitation. The corresponding coupling matrix element for the cumulative effect of the the Coulomb and nuclear interactions, $V_{\alpha\alpha'}$, is expressed as,

$$V_{\alpha\alpha'}(r) = -\beta_{\lambda} R_m \frac{dV_N}{dr} + \frac{4\pi Z_p e}{2\lambda + 1} \sqrt{B(E\lambda)} \frac{1}{r^{\lambda+1}} \quad (3.15)$$

The matrix element is related to the well-known deformation parameters, $\beta_{\lambda} = \langle J_f 0 | \beta_{\lambda 0} | J_i 0 \rangle$. The quantity $B(E\lambda) = \left(\frac{3Z_T \beta_{\lambda} R_{ch}^\lambda}{4\pi} \right)^2$ is commonly defined as the electric transition probability (as introduced in Chapter 1), and is the primary observable in scattering measurements. The charge and mass distributions are often found to have different deformation characteristics, leading to,

$$V_{\alpha\alpha'}(r) = -\delta_{\lambda}^m \frac{dV_N}{dr} + \delta_{\lambda}^{ch} \frac{3Z_p Z_T e^2 R_{ch}^{\lambda-1}}{2\lambda + 1 r^{\lambda+1}} \quad (3.16)$$

where $\delta_{\lambda}^m = \beta_{\lambda}^m R_m$ and $\delta_{\lambda}^{ch} = \beta_{\lambda}^{ch} R_{ch}$ are the multipole transition parameters, known as the mass and charge deformation lengths, respectively, and they characterize the changes in the charge and mass radii of the nucleus at which the coupling potentials are evaluated. In the scope of this discussion, the couplings are demonstrated only upto the (dominant) first order in order to illustrate the coupling scheme. However, higher order terms in the coupling matrix are often found to be important.

3.2.2 Transfer processes

Transfer interactions have different particles in the incoming and outgoing channels and correct treatment of the effect of recoil and finite range of the binding potentials is of utmost importance. The dynamical details of the transfer processes, $c'(a, c)B$, arise from matrix elements of the Hamiltonian for the three bodies involved - the initial and final cores, c and c' , and the valence particle, x , with $a = c + x$ and $B = c' + x$. The Hamiltonian is expressed as,

$$H = K_{\vec{r}_{ac'}} + K_{\vec{r}_{cx}} + V_a(\vec{r}_{cx}) + V_B(\vec{r}_{xc'}) + U_{cc'}(\vec{r}_{cc'}) \quad (3.17)$$

Here, $V_a(\vec{r}_{cx})$ and $V_B(\vec{r}_{xc'})$ are the binding potentials of the valence particle/cluster with the cores c and c' , and $U_{cc'}(\vec{r}_{cc'})$ is the core-core optical potential. The binding potentials are usually fitted so that the eigenenergies agree with the experimental separation energies. If the interaction is weak, it is sufficiently accurate to define a first-order matrix element between entrance and exit channel wave functions, to evaluate the reaction amplitude, given by

$$T_{ca} = \int \int \chi_c^{*(-)}(\vec{r}_{cB}) \langle Bc|V|c'a \rangle \chi_a^{(+)}(\vec{r}_{ac'}) d\vec{r}_1 d\vec{r}_2 \quad (3.18)$$

where $\chi_a^{(+)}, \chi_c^{(-)}$ are the wave functions that describe the relative motion of the pair of nuclei $c' - a$ before the interaction, and of $B - c$ after the interaction, with associated angular momenta ℓ_a and ℓ_c , and asymptotic wave numbers k_a and k_c , respectively. The non-local coupling matrix element between the internal states for the transition is expressed as,

$$\langle Bc|V|c'a \rangle = \langle \psi_B(\xi_c \xi_x r_2) \psi_c(\xi_c) | V(\vec{r}_1) | \psi_{c'}(\xi_{c'}) \psi_a(\xi_c \xi_x r_1) \rangle \quad (3.19)$$

Here, the form of $V(\vec{r}_1)$ is analogous to that defined in Eqn. 3.6, with the orbital

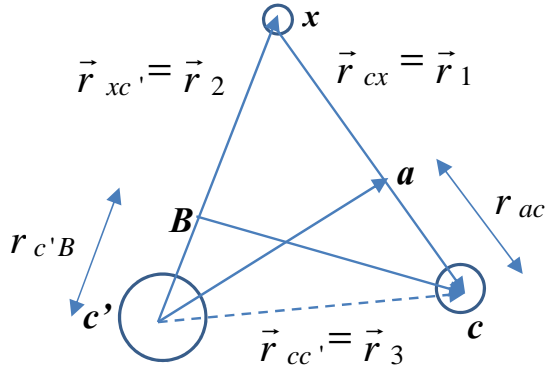


Figure 3.1: Radial coordinates showing arrangement of nuclei in a transfer process for the $c'(a, c)B$ reaction, where x is the transferred particle/cluster.

angular momentum of relative motion, λ , transferred from the entrance channel to the exit channel governed by a Clebsch Gordan coefficient, $\langle \ell_c m_c \lambda \mu | \ell_a m_a \rangle$. The interaction is assumed to depend only on the separation between c and x , and not on any internal coordinate. Eqn. 3.19 defines the effective interaction/form factor, as a function of r_1 and r_2 , for the transition between the states $\chi_a^{(+)}$ and $\chi_c^{(-)}$. It contains all information on nuclear structure, angular momentum selection rules and the type of reaction being considered. A single nucleon transfer reaction can populate certain category of states in a very selective manner that have a structure predominantly given by the parent nucleus as a bound core, with the transferred nucleon in an orbit around it, populating any of its vacant higher levels to give rise to corresponding states of the residual nucleus, by coupling to the core ground state. The residual interactions between valence nucleons, of c and c' with x , will produce multiple configurations and the final nucleus will have the single particle overlap amplitude split between all the contributing component states. Each state of the composite nucleus is a superposition of many single particle states of x , coupled to all possible core states of c and c' , each with a definite coefficient of fractional parentage, called the spectroscopic amplitude, \sqrt{S} . The internal coordinates can

thus be eliminated by,

$$\psi_B(\xi_{c'}\xi_x r_2) = \sqrt{S_B} \psi_{c'}(\xi_{c'})\psi_x(\xi_x r_2) \quad (3.20)$$

$$\psi_a(\xi_c\xi_x r_1) = \sqrt{S_a} \psi_c(\xi_c)\psi_x(\xi_x r_1) \quad (3.21)$$

The intensity of each single particle component, known as the spectroscopic factor, $S_{\ell s j}^{J_i J_f}$, defines the probability of finding the nucleon in a single particle state ℓ, s, j (spin J_f) coupled to the core with spin J_i . Experimentally, it is extracted by taking the angular distribution of differential cross section that is calculated for a pure single particle state and comparing it to the angular distribution that is measured. For the transfer of a nucleon with isospin quantum numbers t, t_z , the initial target and final recoil states have definite isospin associated with them (T_i and T_f). Consequently, the spectroscopic amplitude is multiplied by an isospin Clebsch-Gordon coefficient [57], $C = \langle T_i T_{zi} t t_z | T_f T_{zf} \rangle$.

From the coordinate diagram of the transfer process shown in Fig. 3.1, $\vec{r}_{ac'} = \vec{r}_2 + \frac{m_c}{m_a}\vec{r}_1$ and $\vec{r}_{c'B} = \vec{r}_1 + \frac{m_{c'}}{m_B}\vec{r}_2$. These relations can be used to express the wave functions as a function of any pair of these vectors. In order to simplify the evaluation of the reaction amplitudes, either the vector dependence of the integrand in Eqn. 3.18 may be expanded, or the wave functions may be expanded in a basis that permits separation of variables. This gives rise to several approximations :

I. No-recoil approximation : The transferred particle is restricted to a line between c and c' (local interaction), with no change in its linear momentum, and the distances \vec{r}_{ac} and $\vec{r}_{c'B}$ are neglected. This may hold good only for some light-ion reactions. Under the assumption $\vec{r}_{cB} \sim \vec{r}_{ac'} \sim \vec{r}_3$, the reaction amplitude is reduced to,

$$T_{ca}^{\text{NR}} = \int \chi_c^{*(-)} \left(\frac{m_{c'}}{m_B} \vec{r}_3 \right) \psi_x^*(\vec{r}_3 - \vec{r}_1) V(\vec{r}_1) \psi_x(\vec{r}_1) \chi_a^{(+)}(\vec{r}_3) d\vec{r}_1 d\vec{r}_3 \quad (3.22)$$

The transferred orbital angular momentum of relative motion is restricted by the condition $\langle \ell_c 0 \lambda 0 | \ell_a 0 \rangle$. This approximation breaks down as the energy increases and the two cores approach each other.

II. Zero-range approximation : The vector dependence of the integrand is neglected, with $V(\vec{r}_1)\psi_x(\vec{r}_1) = V_0\delta(r_1)$, leading to,

$$T_{ca}^{\text{ZR}} = \int \chi_c^{*(-)} \left(\frac{m_{c'}}{m_B} \vec{r}_3 \right) \psi_x^*(\vec{r}_3) V_0 \chi_a^{(+)}(\vec{r}_3) d\vec{r}_3 \quad (3.23)$$

This approximation is justified only when the potential is very short-ranged (nearly zero), and the projectile is in an s -state, leading to the generation of c at the same point at which a is absorbed.

III. Local energy approximation : For interactions of small range (non-zero) and projectile in s -state, a first-order Taylor expansion of the wave functions, $\chi_a^{*+}(\vec{r}_{ac'})$ and $\chi_c^{*-}(\vec{r}_{cB})$, leads to a reaction amplitude of the form,

$$T_{ca}^{\text{LE}} = \int \langle Bc | V | c'a \rangle \exp(\vec{r}_1 \cdot \hat{O}) \chi_c^{*(-)} \left(\frac{m_{c'}}{m_B} \vec{r}_2 \right) \chi_a^{(+)}(\vec{r}_2) d\vec{r}_1 d\vec{r}_2 \quad (3.24)$$

The amplitude is determined from the local energy in the entrance ($a \rightarrow c + x$) and exit ($c' + x \rightarrow B$) channels, with the gradient operator, $\hat{O} = \nabla_c + \frac{m_c}{m_a} \nabla_a$. The convergence becomes rapid if \vec{r}_1 is of short range.

IV. Finite-range transfer : The finite range of the interaction, as well as exact treatment of the recoil effects are taken into account. The form factor, given by Eqn. 3.19, is expanded into multipole terms that correspond to the transfer to a nuclear orbit of definite angular momentum, j . If a and c have spins s_a and s_c , and the target and residual nuclear spins are $J_{c'}$ and J_B , then, the form factor of the interaction depends on the nuclear quantum numbers for the transferred particle,

defined by $j = J_B - J_{c'}$, $s = s_a - s_c$, $\ell = j - s$ and $m = m_b + m_c - m_{c'} - m_a$ [60].

$$T_{ca}^{\text{FR}} = \sum_{\ell s j} \sqrt{2\ell + 1} \sqrt{S_a S_B} (-1)^{s_c - m_c} \langle J_{c'} j m_{c'} m_B - m_{c'} | J_B m_B \rangle \quad (3.25)$$

$$\times \langle \ell s m m_a - m_c | j m_B - m_{c'} \rangle \langle s_a s_c m_a - m_c | s_a - m_c \rangle \beta_{sj}^{\ell m}$$

The expansion given above has the convenience that the different values of ℓ, s, j contribute incoherently to the reaction amplitude, and often, only one value is allowed, thereby simplifying the calculation. Here, $\beta_{sj}^{\ell m}$ defines the partial/reduced amplitude given by,

$$\sqrt{2\ell + 1} \beta_{sj}^{\ell m} = \int d\vec{r}_1 d\vec{r}_2 \chi_c^{*(-)}(\vec{k}_c, \vec{r}_{cB}) f_{\ell s j m}(\vec{r}_{ac'}, \vec{r}_{cB}) \chi_a^{*(+)}(\vec{k}_a, \vec{r}_{ac'}) \quad (3.26)$$

where $f_{\ell s j m}(\vec{r}_{ac'}, \vec{r}_{cB}) \propto \langle \ell_c \ell_a M m - M | \ell m \rangle Y_{\ell_c, M}^*(\hat{r}_{cB}) Y_{\ell_a, m-M}^*(\hat{r}_{ac'})$ is the radial form factor for the transfer of the $\ell s j$ multipoles. The problem of finite range interaction is thus reduced to evaluating $\beta_{sj}^{\ell m}$, which describes the dynamics of the reaction.

All current approaches to the extraction of realistic structural information, like deformation parameters from inelastic excitations and spectroscopic information on overlaps from transfer reactions, are based on the different variations of the generalized CC model. In most CC calculations of fusion, a real and energy-independent potential is used, and all couplings are explicitly included to solve for the channel wave functions. For analysing scattering data, one couples the dominant reaction channels and employs complex optical potentials (energy-dependent polarization potentials), where the imaginary part is used to simulate the effect of absorption into the excluded channels. However, incorporating a multitude of coupling interactions is prohibitive for some nuclear models.

3.3 CCFULL Model

When many channels are coupled in an interacting intrinsic system, a spectrum of barriers (a multidimensional potential barrier) is generated for the incident flux; some of these values may be higher than the uncoupled barrier and some may be lower [61, 62], decided by the coupling mechanism. CCFULL exclusively couples the relative motion of the colliding nuclei to the nuclear intrinsic motions like inelastic excitations, and relies on the assumption that fusion occurs due to quantum tunneling across the barriers [56, 63]. Nuclear coupling matrix elements are evaluated by using the matrix diagonalisation method once the physical space has been defined. The couplings are considered to act only when nuclei overcome the barrier and inter-penetrate. The coupled Schrödinger equations (Eqn. 3.4) are rigorously solved by means of numerical integration upto full order. The model employs an incoming wave boundary condition (IWBC) that corresponds to the case where there is a strong absorption in the interior region of the barrier, at a suitable position where the Coulomb pocket has a minimum, so that the incoming flux never returns. It relies on the assumption that the fusion process is predominantly governed by quantum tunneling over the Coulomb barrier. The corresponding radial solutions of the coupled wave equations are expressed as:

$$\chi_\alpha(r) \rightarrow T_\alpha^\ell \exp\left(-i \int_{r_{min}}^r k_\alpha(r') dr'\right), \quad r \leq r_{min} \quad (3.27)$$

$$\chi_\alpha(r) \rightarrow H_\ell^{(in)}(k_\alpha r) \delta_{\alpha,0} + R_\alpha H_\ell^{(out)}(k_\alpha r), \quad r > r_{max} \quad (3.28)$$

where T_α^ℓ is the transmission coefficient for the ℓ^{th} partial wave across the barrier, and $k_\alpha(r') = \sqrt{\frac{2\mu}{\hbar^2} (E - \varepsilon_\alpha - V_{\alpha\alpha}(r')) - \ell(\ell + 1) \frac{\hbar^2}{2\mu r'^2}}$ is the local wave number for the channel α . In order to ensure only incoming waves at $r \rightarrow r_{min}$, CCFULL solves

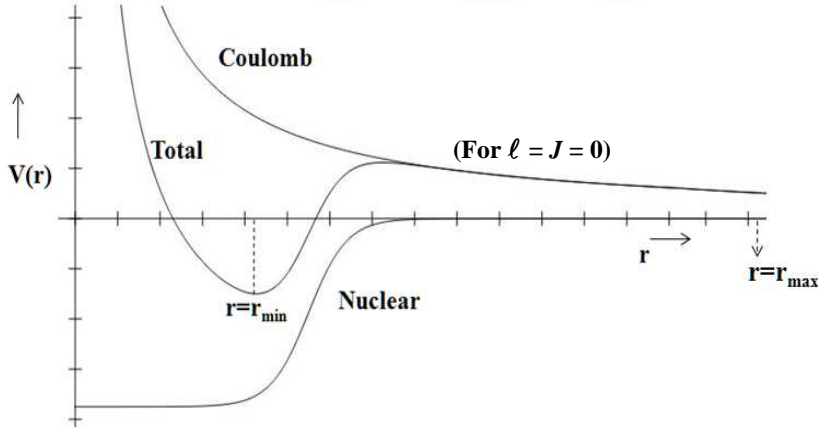


Figure 3.2: Interaction potential (representative) in nuclear collisions. The potential-pocket vanishes at high ℓ values.

the CC equations outward from r_{min} by imposing the conditions

$$\chi_{\alpha}(r_{min}) = 1, \quad \frac{d}{dr}\chi_{\alpha}(r_{min}) = -ik_{\alpha}(r_{min}) \quad (3.29)$$

$$\chi_{\alpha'}(r_{min}) = 0, \quad \frac{d}{dr}\chi_{\alpha'}(r_{min}) = 0, \quad \forall \alpha \neq \alpha' \quad (3.30)$$

Since the first derivative at r_{min} is specified, the wave functions, $\chi_{\alpha}(r_{min} + h)$, with h being the radial mesh to integrate the equations, are obtained numerically, and the full CC set is solved numerically from $r_{min} + h$ to r_{max} , to obtain the inclusive penetrability (where the intrinsic degree of freedom emerges in any final state) of each partial wave, given by $P_{\ell}(E) = \sum_{\alpha} \frac{k_{\alpha}(r_{min})}{k_0} |T_{\alpha}^{\ell}|^2$. The fusion cross section then depends on the tunneling coefficient for each partial wave across the barriers [56]. However, this model is best-suited for systems with a small number of channels that couple to the ground state/entrance channels. Loss of potential pocket at high ℓ values limits fusion as it applies IWBC at r_{min} . For deeper nuclear potentials, the pocket remains upto high ℓ values, and high energy fusion data can be represented by CCFULL. However, such potentials may be unrealistic if they do not reproduce scattering data and related observables.

3.3.1 Isocentrifugal approximation

For a nucleus with intrinsic spin I , the total angular momentum is written as $\vec{J} = \vec{\ell} + \vec{I}$, with $\ell = |J - I|, \dots, |J + I|$. Since relative motion does not destroy intrinsic parity, hence, for every I , there are $I + 1$ allowed values of ℓ , i.e., allowed sub-channels. The dimension of the full CC physical space becomes intricate and is reduced under the assumption that the orbital angular momentum of relative motion, ℓ , is conserved during intrinsic excitations. The isocentrifugal approximation considers all the ℓ sub-channels to be equally affected by couplings of roughly the same strengths. Consequently, an average centrifugal potential is defined with $\ell(\ell + 1) \rightarrow J(J + 1)$. Thus, only one value of $\ell = J$ (one partial wave) is considered per I channel. This is effectively analogous to solving the CC equations for a spin-less intrinsic system, with $V_{\alpha\alpha}(r) = V_N^0(r) + \frac{Z_P Z_T e^2}{r} + \frac{J(J+1)\hbar^2}{2\mu r^2}$. Under this approximation, CCFULL considers all nuclei to have zero spin ($I = 0$) in their ground state. The assumption of spin-zero intrinsic systems allows one to choose the z -axis along the centre-of-mass distance, \vec{r} , with $\hat{r} = \hat{z}$. This conserves the magnetic quantum number of the intrinsic spin, and only the components of the coupling interaction with $\mu = 0$ survive, leading to,

$$V_{\text{coup}}(r, \xi) = \sum_{\lambda > 0} f_{\lambda}(r) Y_{\lambda}^0(\hat{r}) T_{\lambda}^0(\xi) = \sum_{\lambda > 0} \sqrt{\frac{2\lambda + 1}{4\pi}} f_{\lambda}(r) T_{\lambda}^0(\xi) \quad (3.31)$$

The net fusion cross section through the coupled multidimensional barrier is then expressed as:

$$\sigma_F^{\text{CCFULL}}(E) = \frac{\pi}{k_0^2} \sum_J (2J + 1) P_J(E) \quad (3.32)$$

This approximation is unrealistic for several nuclei with finite g.s. spin. The calculations are truncated at the angular momentum, J , whose contribution to the cross section is less than 10^{-4} times the total fusion cross section. Another demerit of this model is the limited number of inelastic channels that can be coupled to the incoming channel. Also, the transfer channels can be coupled only in an approximate

way, without incorporating finite range and recoil effects.

3.4 FRESCO Model

This model constructs a comprehensive theory for fusion that is consistent with the major direct reactions, particularly, elastic scattering. It is essentially based on the Feshback framework of direct reaction theory. FRESCO explicitly solves the Schrödinger equation (Eqn. 3.4) for all the included channels, and involves imaginary potentials to model how flux is lost from the physical space to other channels. The fusion cross sections are calculated by imposing specific boundary conditions on the incoming channel and outgoing coupled wave functions of each channel, governed by an imaginary potential and accounts for the bulk of the flux which is lost from both entrance channel and direct reaction channels to the fusion channel. The flux that is lost from the entrance channel goes to either direct reaction channels or fusion channel giving rise to total reaction cross section [57]. So, the fusion cross section is taken as the difference between the total reaction cross section and the sum of all direct reaction cross sections.

3.4.1 Effective Interaction

The manifestation of the fact that one deals with a many-body scattering problem is seen from a straightforward derivation of the coupled equations that leads to an infinite set. A generalization involves a reformulation of the problem of solving an infinite set of equations to one which involves solving a finite set with a modified/effective interaction - the dynamic polarization potential, added to the bare potential. A model of the system wave function is constructed by projecting the complete wave function, $|\psi_{\text{tot}}\rangle$, onto a product of accessible projectile and target states (either bound states or discrete representations of continuum levels)

$\Phi_\alpha = \phi_{\alpha p} \times \phi_{\alpha t}$, with $\chi_\alpha(r_\alpha)$ describing their relative motion. This projection can be defined as the action of an operator P , that represents the set of open channels that can be well-resolved - a portion of the available Hilbert space known as the model space, such that $\hat{P}|\psi_{\text{tot}}\rangle$ asymptotically contains only the P channels. Thus,

$$\hat{P}|\psi_{\text{tot}}\rangle \approx |\psi_{\text{model}}\rangle = \sum_{\alpha}^N \Phi_{\alpha} \chi_{\alpha}(R_{\alpha}) \quad (3.33)$$

Similarly, from the Hamiltonian, H , of the entire system, one obtains the effective Hamiltonian, $\tilde{\mathcal{H}}$, satisfying $\hat{P}[H - E]|\psi_{\text{tot}}\rangle = [\tilde{\mathcal{H}} - E]|\psi_{\text{model}}\rangle = 0$. Introducing a complementary operator, Q , where $\hat{Q}|\psi_{\text{tot}}\rangle$ projects onto the subspace of the excluded and/or closed channels, with $\hat{Q} = 1 - \hat{P}$, leads to

$$\hat{P}H\hat{P}(\hat{P}|\psi_{\text{tot}}\rangle) + \hat{P}H\hat{Q}(\hat{Q}|\psi_{\text{tot}}\rangle) = E\hat{P}|\psi_{\text{tot}}\rangle \quad (3.34)$$

Here, $\hat{P}H\hat{P}$ defines the matrix element connecting model space wave functions and $\hat{P}H\hat{Q}(\hat{Q}|\psi_{\text{tot}}\rangle)$ introduces effects of the excluded channels into the model space. Similar to Eqn. 3.34, one can write

$$\hat{Q}H\hat{P}(\hat{P}|\psi_{\text{tot}}\rangle) + \hat{Q}H\hat{Q}(\hat{Q}|\psi_{\text{tot}}\rangle) = E\hat{Q}|\psi_{\text{tot}}\rangle \quad (3.35)$$

$$\implies \hat{Q}|\psi_{\text{tot}}\rangle = \frac{1}{E - \hat{Q}H\hat{Q} + i\epsilon} \hat{Q}H\hat{P}(\hat{P}|\psi_{\text{tot}}\rangle) \quad (3.36)$$

where ϵ is a positive infinitesimal quantity which is purportedly introduced to ensure that the excluded channels only remove flux from the model space. Substituting $\hat{Q}|\psi_{\text{tot}}\rangle$ into Eqn. 3.34, the effective Hamiltonian is constructed as,

$$\tilde{\mathcal{H}} = \hat{P}H\hat{P} + \hat{P}H\hat{Q} \frac{1}{E - \hat{Q}H\hat{Q} + i\epsilon} \hat{Q}H\hat{P} \equiv \hat{P}H\hat{P} + \hat{O} \quad (3.37)$$

The Hamiltonian involves an effective interaction, \hat{O} , taking into account the dy-

dynamic couplings between the P and Q subspaces. The arbitrary matrix \hat{O} can be decomposed into Hermitian and anti-Hermitian components, and Eqn. 3.37 can be written as,

$$\langle \Phi_\alpha | \tilde{\mathcal{H}} | \Phi_\alpha \rangle = \langle \Phi_\alpha | \hat{P}H\hat{P} | \Phi_\alpha \rangle + \frac{1}{2} \langle \Phi_\alpha | (\hat{O} + \hat{O}^\dagger) | \Phi_\alpha \rangle + \frac{1}{2} \langle \Phi_\alpha | (\hat{O} - \hat{O}^\dagger) | \Phi_\alpha \rangle \quad (3.38)$$

The second term on the right side contributes a small correction term, say V_0 , to the matrix element of the Hermitian operator, $\hat{P}H\hat{P}$ (that also includes the kinetic energy operator), while the expectation value in the third term leads to a negative imaginary potential, denoted by W_0 , that accounts for loss/outflow of flux from the incident channel (probability density is not conserved). This defines the optical model equation, $[\tilde{\mathcal{H}} - E]|\psi_{\text{model}}\rangle = 0$, for the system, with $V_0 + iW_0$ as the optical potential. The basis states in $|\psi_{\text{model}}\rangle$ do not form an orthogonal set. Transitions from non-fusion channels into fusion channels, via an intermediate compound stage, occur only when two nuclei overlap and interact strongly. So, the absorptive imaginary potential should ideally have a short range (such as a surface potential). However, due to computational limitation, several direct reaction channels could be excluded from the model space. To account for effects of such peripheral channels onto the P space, a long range (volume) imaginary potential is often employed. It is widely recognized that the cross sections to only few of the many open channels in a typical cyclotron/tandem accelerator experiment can be effectively resolved. This limits the amount of information that can be extracted. For a large number of such competing channels, it becomes cumbersome to solve the CC equation exactly. A reasonable approximation is to truncate the infinite number of channels to a few major channels (the P -space) those which are expected/known to be (either theoretically or experimentally) strongly coupled, and represent/simulate the effect of the others (the Q -space) by the complex optical potential.

An important remark should be made at this point : IWBC is not the limit of $W_0 \rightarrow \infty$, as there would also be some finite reflection due to W_0 , which will then have to be neglected. The concepts of IWBC and W_0 belong to the realm of completely different models. In FRESKO, the choice of the strength of the imaginary potential should be such that the mean-free path of the projectile inside the barrier is much smaller than the dimensions of the potential [64], and the flux entering into the chosen short range (within the Coulomb pocket) spherical region must get absorbed satisfying the boundary condition.

Couplings deform the real and imaginary optical potentials. It can be said that the imaginary couplings only redistribute the flux, already penetrated through the barrier, among the elastic and non-elastic channels. The distribution of flux, before and during barrier penetration, among the several channels is determined largely by the longer ranged real couplings. Each pair of projectile and target excited states is a distinct channel with its own scattering wave function and boundary conditions. The entrance channel specifies an incident plane wave; all exit channels have outgoing (scattered) spherical waves. For systems with tightly bound nuclei, the calculation is done by means of the Coupled Reaction Channels (CRC) approach, while for those involving a weakly bound partner, the approach of Continuum Discretized Coupled Channels (CDCC) is employed.

Common approximations :

The solutions of the CC equations often employ some approximation techniques that neglect higher order effects for weaker couplings, which can be treated perturbatively. During the collision, the incident (plane) wave will be distorted due to interactions with the target nucleus and, after the collision, at sufficiently large distances, the projectile and target emerge in any of their (kinematically allowed) eigenstates. For

the entrance channel α , one can write,

$$\psi_\alpha(r_\alpha, \xi_\alpha) = \Phi_\alpha(\xi_\alpha)e^{ik_\alpha \cdot r_\alpha} + \Phi_\alpha(\xi_\alpha) \mathcal{F}_{\alpha\alpha}(r_\alpha, k_\alpha) \frac{e^{ik_\alpha \cdot r_\alpha}}{r_\alpha} + \sum_{\alpha' \neq \alpha} \Phi_{\alpha'}(\xi_{\alpha'}) \mathcal{F}_{\alpha\alpha'}(r_{\alpha'}, k_\alpha) \frac{e^{ik_{\alpha'} \cdot r_{\alpha'}}}{r_{\alpha'}} \quad (3.39)$$

where the coefficient $\mathcal{F}_{\alpha\alpha}$ defines the elastic scattering amplitude of the outgoing wave, and $\mathcal{F}_{\alpha\alpha'}$ define the inelastic scattering/reaction amplitudes. For a particular channel, α' , the solution of Eqn. 3.4 for the scattered wave function $\chi_{\alpha'}(r_{\alpha'})$, in the asymptotic limit, integrated over the internal coordinates $\xi_{\alpha'}$, is expressed as,

$$\langle \Phi_{\alpha'}(\xi_{\alpha'}) | \psi_{\alpha'}(r_{\alpha'}, \xi_{\alpha'}) \rangle \equiv \chi_{\alpha'}(r_{\alpha'}) \sim e^{ik_{\alpha'} \cdot r_{\alpha'}} \delta_{\alpha\alpha'} + \mathcal{F}_{\alpha\alpha'}(r_{\alpha'}, k_\alpha) \frac{e^{ik_{\alpha'} \cdot r_{\alpha'}}}{r_{\alpha'}} \quad (3.40)$$

For the outgoing wave in the reaction plane, $\mathcal{F}_{\alpha\alpha'}(r_{\alpha'}, k_\alpha) \equiv \mathcal{F}(\theta)$ is given by,

$$\mathcal{F}_{\alpha\alpha'}(\theta) = -\frac{\mu_{\alpha'}}{2\pi\hbar^2} \langle e^{ik_{\alpha'} \cdot r_{\alpha'}} \Phi_{\alpha'}(\xi_{\alpha'}) | V_{\text{coup}}(r_{\alpha'}, \xi_{\alpha'}) | \psi_\alpha(r_\alpha, \xi_\alpha) \rangle \quad (3.41)$$

where $\mu_{\alpha'}$ is the reduced mass in the channel α' . From a knowledge of the exact form of ψ_α , one can extract the scattering amplitude from the asymptotics of $\chi_{\alpha'}$. An approximation commonly used, known as the Born approximation, treats all interactions as weak perturbations to the incident wave, and the relative motion before and after collision is assumed to be described by plane waves, i.e., $\psi_\alpha(r_\alpha, \xi_\alpha) \approx \Phi_\alpha(\xi_\alpha)e^{ik_\alpha \cdot r_\alpha}$. The motion at large radii is considered to be described by undisturbed plane waves. However, since elastic scattering and absorption can both occur in a reaction system, a plane wave is not an ideal solution for Schrödinger equation. In an alternative approach, if some local/non-local couplings to the entrance channel are weak, they can be treated as successive perturbations to the elastic channel, iteratively. The relative motion between the nuclei is described by waves distorted by elastic scattering, and such an approach is known as the Distorted Wave Born Approximation (DWBA). These distorted waves are generated from optical model

potentials that are chosen to explain the elastic scattering in the entrance and exit channels, and the reaction channels are treated as weak transitions between the elastic states, with,

$$\mathcal{F}_{\alpha\alpha'}^{\text{DWBA}}(\theta) = -\frac{\mu_{\alpha'}}{2\pi\hbar^2} \left\langle e^{ik_{\alpha'} \cdot r_{\alpha'}} \Phi_{\alpha'} \left| V_{\text{coup}} \right| \Phi_{\alpha} e^{ik_{\alpha} \cdot r_{\alpha}} + \Phi_{\alpha} \mathcal{F}_{\alpha\alpha}(\theta) \frac{e^{ik_{\alpha} \cdot r_{\alpha}}}{r_{\alpha}} \right\rangle \quad (3.42)$$

DWBA is most useful for reactions that probe the surface region of nuclei, i.e., reactions that probe only the asymptotic tails of the wave function in transfer/inelastic scattering processes.

When inelastic scattering channels are strongly coupled (i.e., when the iterative scheme fails to converge), an exact solution for elastic and inelastic scattering states becomes imperative for convergence of the solution set. These channels are blocked together and treated as a single unit during iterations, while solving the couplings within the block by the exact method. The distorted elastic waves in Eqn. 3.42 are replaced by the solutions of a CC problem that includes both elastic as well as the inelastic waves. The transfer channels are still treated to first order. Such an approximation is known as the Coupled Channels Born Approximation (CCBA). With the dominant β inelastic channels coupled to the entrance channel, the scattering amplitude for a weakly-coupled channel α' becomes,

$$\mathcal{F}_{\alpha\alpha'}^{\text{CCBA}}(\theta) = -\frac{\mu_{\alpha'}}{2\pi\hbar^2} \left\langle e^{ik_{\alpha'} \cdot r_{\alpha'}} \Phi_{\alpha'} \left| V_{\text{coup}} \right| \Phi_{\alpha} e^{ik_{\alpha} \cdot r_{\alpha}} + \Phi_{\alpha} \mathcal{F}_{\alpha\alpha}(\theta) \frac{e^{ik_{\alpha} \cdot r_{\alpha}}}{r_{\alpha}} + \sum_{\beta \neq \alpha} \Phi_{\alpha} \mathcal{F}_{\alpha\beta}(\theta) \frac{e^{ik_{\beta} \cdot r_{\beta}}}{r_{\beta}} \right\rangle \quad (3.43)$$

where $\mathcal{F}_{\alpha\alpha}$, $\mathcal{F}_{\alpha\beta}$ are determined by numerically solving the CC equations for the corresponding channels exactly.

The approximations discussed above are often employed in the different nuclear models, and significantly reduce computation time for attaining convergence.

3.4.2 Coupled Reaction Channels (CRC) Formalism

In the CRC framework, elastic scattering is described using a complex optical potential, where the imaginary part implicitly accounts for the flux lost to other reaction channels. Transfer reactions and directly populated inelastic excitations are then often considered to be perturbations on the elastic scattering in the DWBA limit (for weak excitations). The estimated total reaction cross section, σ_{reac} , is usually identified with the expectation value of the imaginary potential in the entrance channel. The fusion process, at an energy E , is described as the multi-step absorption through the potential barrier in each channel,

$$\sigma_F^{\text{FRESKO}}(E) = \sigma_{\text{abs}}^{\text{el}} + \sigma_{\text{abs}}^{\text{inel}} + \sigma_{\text{abs}}^{\text{tr}} + \dots \equiv \sigma_{\text{reac}} - \sum_{\alpha} \sigma_{\alpha}^{\text{dir}} \quad (3.44)$$

where $\sigma_{\alpha}^{\text{dir}}$ corresponds to the cross section for α^{th} reaction channel. For a reaction system with n mass-partitions, a channel α is abbreviated as $\alpha = \{npt, (\ell J_p) J J_t; J_{\text{tot}}\}$. With diagonal optical potential $V_{\alpha\alpha,n}$ and centrifugal potential $U_{n\ell,\alpha}$, the full CRC equation is expressed as,

$$\begin{aligned} [E_{\alpha,n} - K_{\alpha,n} - V_{\alpha\alpha,n} - U_{n\ell,\alpha}] \chi_{\alpha,n}(r_n) &= \sum_{\alpha'} i^{\ell' - \ell} V_{\alpha\alpha',n}(r_n) \chi_{\alpha',n}(r_n) \\ &+ \sum_{\alpha', n \neq n'} i^{\ell' - \ell} \int^{r_n'} V_{\alpha\alpha',nn'}(r_n, r_{n'}) \chi_{\alpha'}(r_{n'}) dr_{n'} \end{aligned} \quad (3.45)$$

where $V_{\alpha\alpha',n}(r_n)$ governs local coupling interactions within a partition (such as inelastic excitations), and $V_{\alpha\alpha',nn'}(r_n, r_{n'})$ defines non-local coupling interactions that arise from particle transfers. Once all coupling matrices are specified, the equation set is solved, either exactly (CCBA) or iteratively (DWBA), depending upon the local/non-local coupling strengths, satisfying specific boundary conditions for each

$J_{\text{tot}} (= (\ell + J_p) + J_t)$, given by,

$$\chi_\alpha(r_n) \sim r_n^{\ell+1}, \quad r_n \rightarrow 0 \quad (3.46)$$

$$\chi_\alpha(r_n) = H_{J_{\text{tot}}}^{(+)}(k_\alpha r_n) \delta_{\alpha\alpha'} + S_{\alpha\alpha'}^{J_{\text{tot}}} H_{J_{\text{tot}}}^{(-)}(k_\alpha r_n), \quad r_n \rightarrow \infty \quad (3.47)$$

with $H_{J_{\text{tot}}}^{(+)}$ and $H_{J_{\text{tot}}}^{(-)}$ as the incoming and outgoing Coulomb waves, and $S_{\alpha\alpha'}^{J_{\text{tot}}}$ as the asymptotic S -matrix element. The factor $i^{\ell'-\ell}$ ensures that the wave functions revert to the Coulomb functions in the absence of a nuclear potential in the model. The scattering amplitude for the outgoing waves in a reaction channel, such as inelastic excitation or particle rearrangement, is commonly defined as $\mathcal{F}_{\alpha\alpha',n}(\theta) \propto \sum_{\substack{\ell_\alpha \ell_{\alpha'} J_{p\alpha} J_{p\alpha'} \\ m_\alpha m_{\alpha'} J J_{\text{tot}}}} Y_{\ell_\alpha m_\alpha}(r_\alpha) Y_{\ell_{\alpha'} m_{\alpha'}}(r'_\alpha) S_{\alpha\alpha'}^{J_{\text{tot}}}$, which governs the differential cross section for a channel α as,

$$\sigma_{\alpha,n}(\theta) = \frac{1}{(2J_{p\alpha} + 1)(2J_{t\alpha} + 1)} \sum_{\substack{m_{p\alpha} m_{t\alpha} \\ m_{p\alpha'} m_{t\alpha'}}} |\mathcal{F}_{\alpha\alpha',n}(\theta)|^2 \quad (3.48)$$

$$\Rightarrow \sigma_{\alpha,n} = \frac{\pi}{k_\alpha^2} \frac{1}{(2J_{p\alpha} + 1)(2J_{t\alpha} + 1)} \sum_{\substack{\ell J_{\text{tot}} J \\ \alpha'}} (2J_{\text{tot}} + 1) |S_{\alpha\alpha'}^{J_{\text{tot}}}|^2 \quad (3.49)$$

If a large number of partial waves are involved, the CRC equations are solved for every J_{tot} at fixed intervals (small intervals for grazing partial waves, and larger for Coulomb-dominated peripheral processes), and the intermediate ones are interpolated.

3.4.3 Continuum Discretized Coupled Channels (CDCC)

Formalism

For nuclei with low binding energies, additional dynamic channels are introduced into the reaction system on account of their breakup into fragments/clusters. Because of multi-step effects involved, the phenomenon of breakup is not treated as

a perturbation to the elastic scattering waves. The CDCC framework is a non-perturbative approach that treats the breakup (into two fragments) process as inelastic excitation to unbound states (continuum), upto all orders, and includes Coulomb and nuclear effects on equal footing. However, the continuum wave functions do not decay to zero as $r \rightarrow \infty$ sufficiently fast as to have square norms. For the infinite unbound non-normalizable continuum excitations, the range of energies/momenta is, therefore, discretized into a finite number of square-integrable bin states (continuum states averaged over a range of energies), constructed from the scattering states.

For a projectile composed of two loosely-bound particles/clusters, c (the core cluster) and v (the valence cluster), the scattering event from a target (t) can be described by the $c + v + t$ three-body system. Fig. 3.3 is an illustration of the three-body system and coordinates among the three nuclei. The vector, \vec{r}_ζ ($\zeta = c, v$) defines the relative coordinate between ζ and t , while \vec{r} is a vector that connects the centres of mass of v and c , and \vec{R} connects the centre of mass of t to the $(c + v)$ subsystem. The Hamiltonian for the system is expressed as,

$$H_{3\text{body}} = K(r) + K(R) + U_{cv}(r) + V_{ct}(r_c) + V_{vt}(r_v) \quad (3.50)$$

Here, U_{cv} represents the binding/interaction potential between v and c that defines the different bound and unbound states of the projectile, while $V_{ct}(V_{vt})$ is the fragment-target optical potential of the scattering of $c(v)$ on t . The total three body wave function ψ is expanded by the complete set of eigenfunctions of the internal Hamiltonian of the projectile, $K(r) + U_{cv}(r)$ of the $(c + v)$ subsystem, and the eigenfunctions are written in terms of both bound and continuum states, $\phi_i(r)$. The continuum states are characterized by the orbital angular momentum, L , and the linear momentum, k , of the $(c + v)$ subsystem, and they are suitably truncated as $L \ll L_{\text{max}}$ and $k \ll k_{\text{max}}$ [65]. In terms of the bound states and the infinite

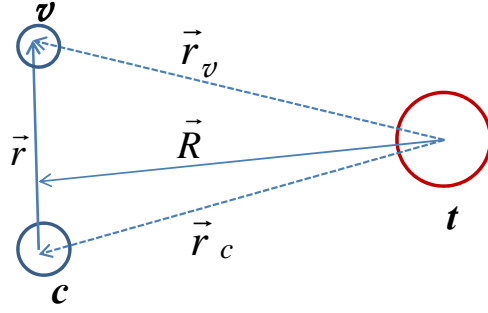


Figure 3.3: Radial coordinates showing three-body system of the core (c), valence (v) and target (t) nuclei in the event of a projectile breakup process.

k -continuum,

$$\psi(r, R) = \phi_b(r)\chi_b(R) + \int_0^\infty dk \sum_L \phi_k(r)\chi_K(R) \quad (3.51)$$

where the coefficients $\chi(R)$ describe relative motion between the projectile in state ϕ , and the target t , with relative momentum, K .

As Eqn. 3.51 involves an integral over a continuous variable to infinity, summed over L , attempting to arrive at a solution of the Schrödinger equation becomes impractical. A discretization of the k -continuum into a finite set of square integrable basis states is required, where the radial functions for the continuum bins are defined as a superposition of the scattering eigenstates within a bin $k_{i-1} \leq k \leq k_i$, given as,

$$\tilde{\phi}_i(r) = \sqrt{\frac{2}{\pi N_i}} \int_{k_{i-1}}^{k_i} w_i(k)\phi_k(r)dk \quad (3.52)$$

with $w_i(k)$ as a weight function and $N_i = \int_{k_{i-1}}^{k_i} |w_i|^2 dk$ as the normalization constant so chosen that $\tilde{\phi}_i(r)$ form an orthonormal set.

A model space, P' , thus constructed is described as $P' = \sum_{i=0}^N |\tilde{\phi}_i\rangle\langle\tilde{\phi}_i|$, with $\psi_{\text{CDCC}} \equiv P'\psi = \sum_{i=0}^N \tilde{\phi}_i(r)\chi_i(R)$. Here, $i = 0$ refers to the ground state and $i \geq 1$ represents the scattering states. This construction can be easily generalised to give coupled-channels bin wave functions for the model space equation

$\hat{P}' H_{3\text{body}} |\psi\rangle = E \hat{P}' |\psi\rangle$. This leads to a set of coupled equations,

$$[E - K_R - \varepsilon_i] \chi_i(R) = \sum_J^N \langle \tilde{\phi}_i | V_{ct}(r_c) + V_{vt}(r_v) | \tilde{\phi}_j \rangle \chi_j(R) \quad (3.53)$$

where ε_i are the energies of the $(c+v)$ subsystem. Solving the CDCC equations with the regular boundary condition, one can get the S-matrix elements of the elastic scattering and the projectile-breakup reactions. Additional couplings to the entrance channel due to the excitations of the target nucleus, or exchange of nucleons with the projectile (prior to breakup) can also be incorporated into the framework. Such an interplay of different reaction modes is commonly defined as the CDCC + CRC formalism.

The various nuclear models described in this chapter have been used for the theoretical calculations and subsequent analyses in this thesis work.

Chapter 4

Low-lying collective excitations in $^{112,116,118,120,122,124}\text{Sn}$ isotopes

A transparent approach to probe collective properties of dynamic nuclear deformations would involve independent excitations of the proton and neutron densities, at the same energy. Inelastic transitions triggered by nucleus-nucleus collisions, such as heavy-ion scattering, occur under the combined influence of Coulomb and nuclear interactions, and could be a reliable alternative for a simultaneous study of deformations of charge and mass densities in nuclei during excitations. The electromagnetic forces are principally the Coulomb forces coupling to the charges of the protons, while the nuclear forces may be central, or couple to individual spins of the nucleons. However, such measurements are subject to the choice of the probe/projectile that induces the excitations. The intrinsic deformations of nuclei can be deduced by removing the effects of probe-size and nature of probe-target interaction in the extraction of intrinsic deformed nuclear shapes.

4.1 Probe-dependence in heavy-ion scattering

Excitations in heavy-ion scattering are often induced at bombarding energies not too far above the Coulomb barrier; contributions from Coulomb and nuclear processes become comparable. An experimental analogy between the inelastic excitation probabilities obtained by pure Coulombic interactions and by nuclear interactions is thus expected. This can be qualitatively observed when the $0_{\text{g.s.}}^+ \rightarrow 2_1^+$ ($\lambda = 2$) and $0_{\text{g.s.}}^+ \rightarrow 3_1^-$ ($\lambda = 3$) excitations of doubly even spherical nuclei are studied in the framework of a collective vibrational model - the charge and mass deformation lengths are of the same order of magnitude. However, the number of configurations which take part in the excitation and the explicit interaction operator may be different in the two cases, thus one would expect some quantitative differences. One of the most widespread approaches to this problem is based upon the use of an optical potential for the description of the elastic scattering of two heavy ions [59]. In addition to the Coulomb potential, V_C , between the colliding nuclei, scattering phenomena are described in terms of an optical potential, V_N , whose shape, owing to the short range of the nuclear force, is of the same general form as that of the nuclear density distribution. The CNI effect allows a simultaneous determination of charge and mass deformation lengths, δ_λ^{ch} and δ_λ^m from the angular distribution of the measured scattering cross section. These are sensitive to deviations in charge and mass distributions from the equilibrium shape of the nucleus. Since the deformed nuclear shapes and transition amplitudes depend sensitively on the chosen matter (or, potential) radius and rely on the interaction potential $V_N(r)$, it is not surprising that these quantities extracted from scattering of different projectiles are systematically different and indicate discrepant transition rates. A scaling relation proposed by Blair [66], $\delta_\lambda^m \equiv \delta_\lambda^{\text{pot}}$. However, this prescription does not remove all discrepancies. A long-standing difficulty in the comparison between δ_λ^{ch} and δ_λ^m has been due to the different radii that characterize the two types of interactions. The

mechanism of Coulomb excitation is well understood and the charge radius has been accurately measured by electron scattering to be about $1.2A^{1/3}$ fm for a suitably diffuse radial charge distribution, where A is the atomic mass of the target nucleus. On the contrary, the optical potential radius characterizing the matter distribution may vary from $1.25A^{1/3}$ for collisions with tightly bound probes, to $1.55A^{1/3}$ fm with weakly bound probes.

The characteristics of the low-lying $0_{\text{g.s.}}^+ \rightarrow 2_1^+$ and $0_{\text{g.s.}}^+ \rightarrow 3_1^-$ transitions in the stable even-mass Sn isotopes have been extensively studied with a variety of probes, with contrasting results. Additional information about the structure of the 2_1^+ and 3_1^- states can be extracted by studying the ratio of the multipole neutron and proton transition matrix elements, M_n/M_p . Bernstein *et al.* [4, 67] have reviewed various methods for determining proton and neutron matrix elements. Since M_p can be accessed through electromagnetic measurements, isospin conservation is a convenient approach to deduce M_n , with $M_n(N, Z) = M_p(Z, N)$ [4]. However, this is predominantly applicable for light nuclei and their mirrors. Similar studies for heavier nuclei generally involve the comparison of measurements of a transition using two experimental probes with different sensitivities to proton and neutron contributions. In such scenarios, the question of the relative participation of neutron and proton densities is of considerable interest. Comparing pure Coulomb scattering with heavy-ion scattering data is considered as one of the most transparent approaches. However, to avoid large experimental uncertainties of M_n/M_p due to normalization error of heavy-ion cross sections, a simultaneous determination of charge and mass transition probabilities, for which M_n/M_p is not affected by normalization uncertainties, may be achieved by heavy-ion scattering across the CNI region.

The present work focusses on the extraction and interpretation of nuclear size and shape information for the excited 2_1^+ and 3_1^- levels in the stable $^{112,116,118,120,122,124}\text{Sn}$

isotopes from the study of heavy-ion inelastic scattering using two different probes, ${}^7\text{Li}$ and ${}^{12}\text{C}$, separately at bombarding energies $E_{\text{c.m.}}/V_{\text{B}} \approx 1.3$. The shape of the differential cross section across a wide angular range allows simultaneous quantitative assessments of $\delta_{\lambda}^{\text{ch}}$ and $\delta_{\lambda}^{\text{m}}$, from which, the ratio of M_n/M_p is deduced uniquely for a given probe. The complex reaction mechanisms are expected to be reflected in probe-dependent characteristics. This is particularly important for exciting discrete collective states with an isoscalar ($N = Z = \text{even}$) nucleus such as ${}^{12}\text{C}$, as the projectile-target interaction is devoid of any isospin dependence. As a result, such ions probe the matter distribution of the nucleus as a whole. On the other hand, the complementary probe ${}^7\text{Li}$ is a weakly-bound nucleus with unpaired nucleons, and the projectile-target interaction is expected to show spin and isospin dependence. The objective is to investigate the probe dependence and subtract its effect, if any, to conclude about intrinsic M_n/M_p ratios for the low-lying $\lambda = 2, 3$ excitations in the Sn isotopes. To understand the inelastic scattering mechanism, model calculations have been attempted by simultaneously coupling several major direct reaction channels to the entrance channel, in the framework of explicit CDCC and CRC formalisms, the success of which is well documented for energies above Coulomb barrier.

4.2 ${}^7\text{Li}$ -induced excitations

A schematic diagram of the experimental setup is shown in Fig. 2.4 of Chapter 2. From a typical gain-matched spectrum of ΔE versus $E_{\text{total}} (= E_{\text{res}} + \Delta E)$ shown for the ${}^7\text{Li} + {}^{122}\text{Sn}$ system in Fig. 4.1, fragments with different Z ($=1-3$) and A ($=1-7$) are clearly identified. Typical energy resolution of a telescope was ≈ 65 keV. Along with the elastic scattering peak, the yields of projectile and target excited states corresponding to first quadrupolar rotational state of ${}^7\text{Li}$ (0.478 MeV), and the 2_1^+ and 3_1^- vibrational states of ${}^{112,116,118,120,122,124}\text{Sn}$ were found to be dominant (shown

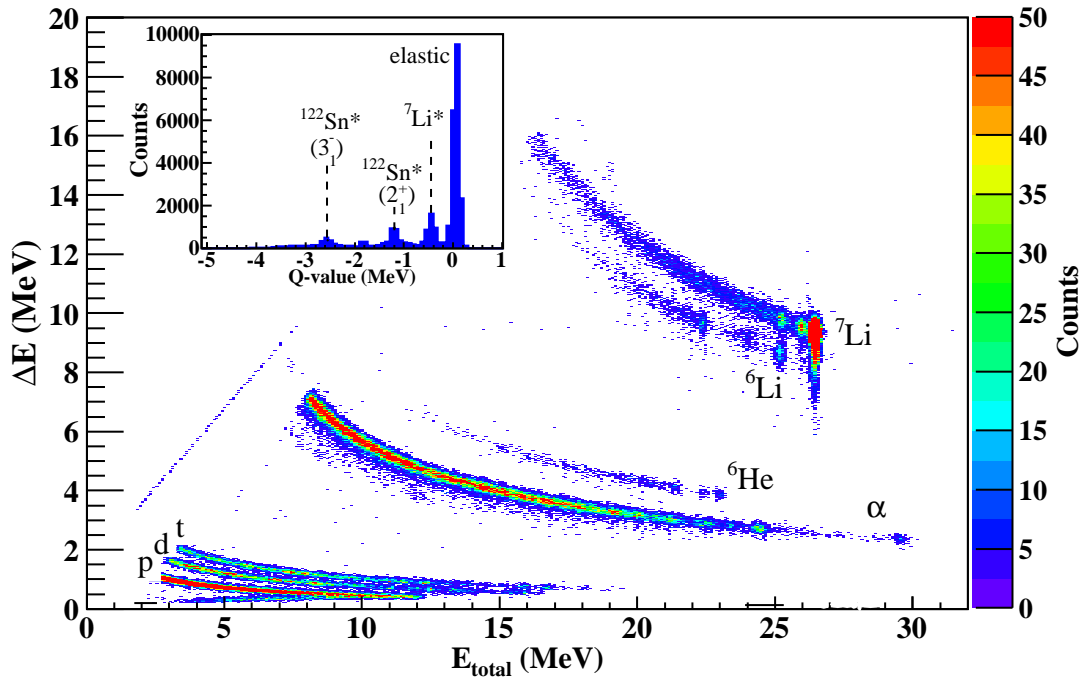


Figure 4.1: Typical (ΔE versus E_{total}) gain-matched spectrum showing the outgoing projectile-like fragments at $\theta_{\text{lab}}=60^\circ$ in the ${}^7\text{Li} + {}^{122}\text{Sn}$ system. Inset: 1D spectrum showing Q-value distribution of states identified in elastic and inelastic scattering.

in inset of Fig. 4.1). In addition, several states corresponding to 1-neutron stripping (${}^7\text{Li}$, ${}^6\text{Li}$) as well as 1-proton stripping (${}^7\text{Li}$, ${}^6\text{He}$), with subsequent excitation of the respective residual nuclei could be identified. The background-subtracted yields for the elastic scattering and excited (2_1^+ and 3_1^-) states of target were extracted separately for evaluating their differential cross sections. They were then translated to the centre of mass frame, where the experimental cross sections retain little information about any experimental constraints or impacts of the laboratory angles. Since the same number of particles get scattered into the solid angles $d\Omega_{\text{lab}}$ and $d\Omega_{\text{c.m.}}$, with $d\phi_{\text{lab}} = d\phi_{\text{c.m.}}$, this leads to

$$\frac{d\sigma}{d\Omega_{\text{c.m.}}} = \frac{|1 + \gamma \cos \theta_{\text{c.m.}}|}{(1 + \gamma^2 + 2\gamma \cos \theta_{\text{c.m.}})^{3/2}} \frac{d\sigma}{d\Omega_{\text{lab}}} \quad (4.1)$$

where $\gamma = \sqrt{\frac{m_p m_e}{m_t m_r} \left(\frac{E_{c.m.}}{E_{c.m.} + Q} \right)}$, for a reaction involving projectile p and target t , leading to an ejectile e and residual r , of masses m_p, m_t, m_e, m_r respectively. $E_{c.m.}$ and Q represent the energy available for the reaction and the Q -value for each excitation channel. The experimental cross sections for scattering to the 2_1^+ excited state for each Sn isotope are shown as open squares in Fig. 4.2(a)-4.2(f), with the elastic scattering angular distributions in the inset (open circles). The average statistical errors on the elastic scattering cross sections are typically 1-2% over the entire angular range, except for extreme backward angles where it is 4-5%. The $\lambda = 2$ transition is found to be dominant in the forward region where Coulomb field is expected to have greater influence than nuclear field. Fig. 4.3(a)-4.3(f) shows the experimental differential cross sections for excitation to the 3_1^- state (triangles). The lines in all figures represent the results of the calculations described in §4.2.1 and §4.2.2, carried out in the CRC as well as CDCC-CRC formalisms.

4.2.1 CRC Calculations

CRC calculations were performed by coupling the major direct reaction channels to the entrance channel in the DWBA limit, (since the couplings to the direct channels were not found to significantly alter the calculation of the elastic scattering cross section). The target excited states were treated as collective vibrational states. To constrain the set of potential and target structural parameters, inelastic excitation of ${}^7\text{Li}$ to its only bound excited state $\frac{1}{2}^-$ at 478-keV was coupled into the model space. In addition, some of the dominant low-lying states corresponding to one-nucleon stripping processes with residual excitation, upto ≈ 1.5 MeV, were included with available spectroscopic factors (C^2S). The states for which the spectroscopic factors were not available were included with $C^2S = 1.0$. The coupling scheme for one of the systems is shown in Fig. 4.4. The distorted waves were generated from a phenomenological optical potential of Woods-Saxon (WS) volume type, whose

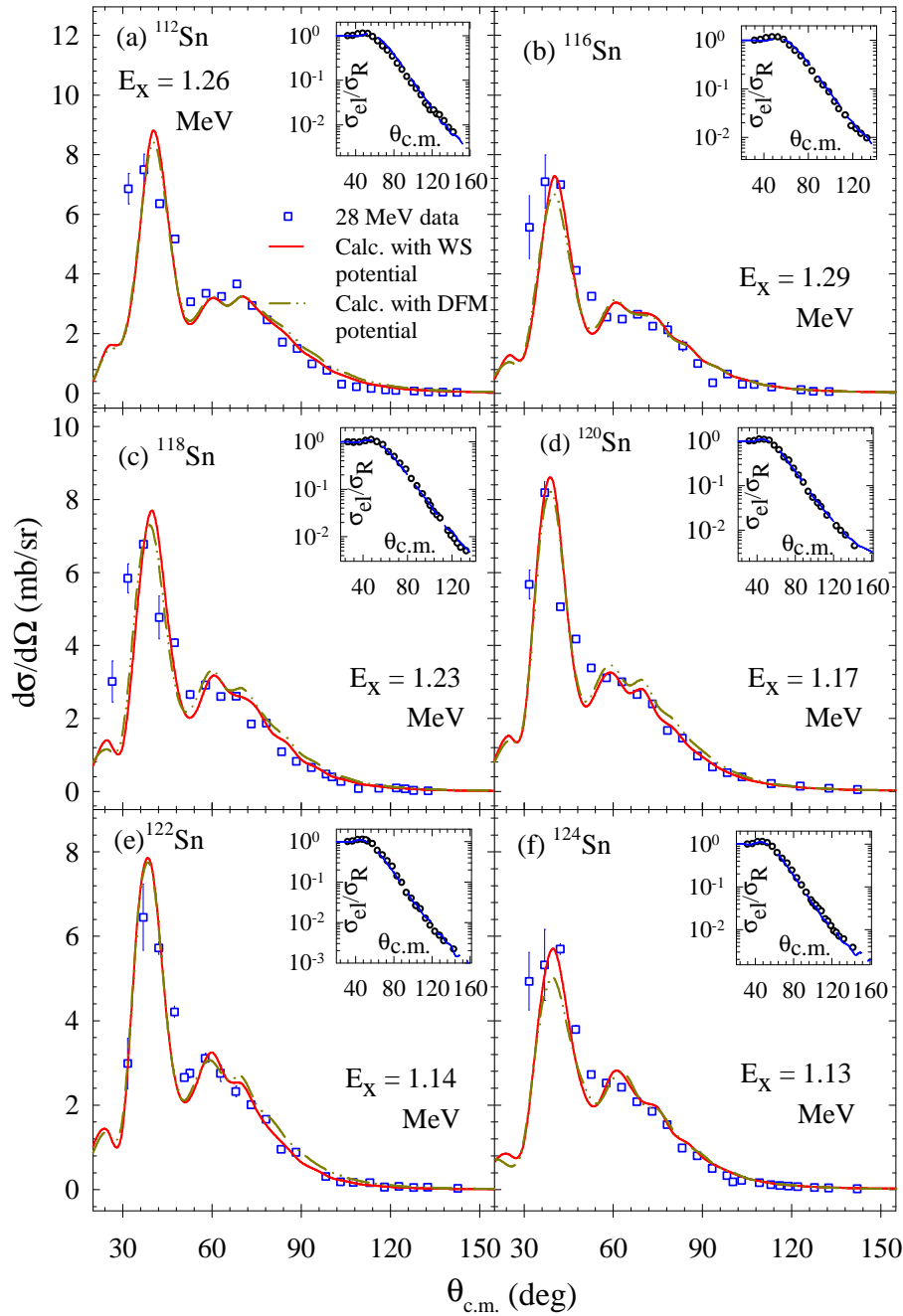


Figure 4.2: Experimental cross sections (open squares) and the results of the CRC calculations (solid lines for WS potential, dash-dot-dot lines for DFM potential) for $\lambda = 2$ inelastic scattering processes corresponding to the target excitations in $^{7}\text{Li} + ^{112,116,118,120,122,124}\text{Sn}$ systems. Inset: Experimental elastic scattering angular distributions (circles) with calculation using WS potential (dashed lines).

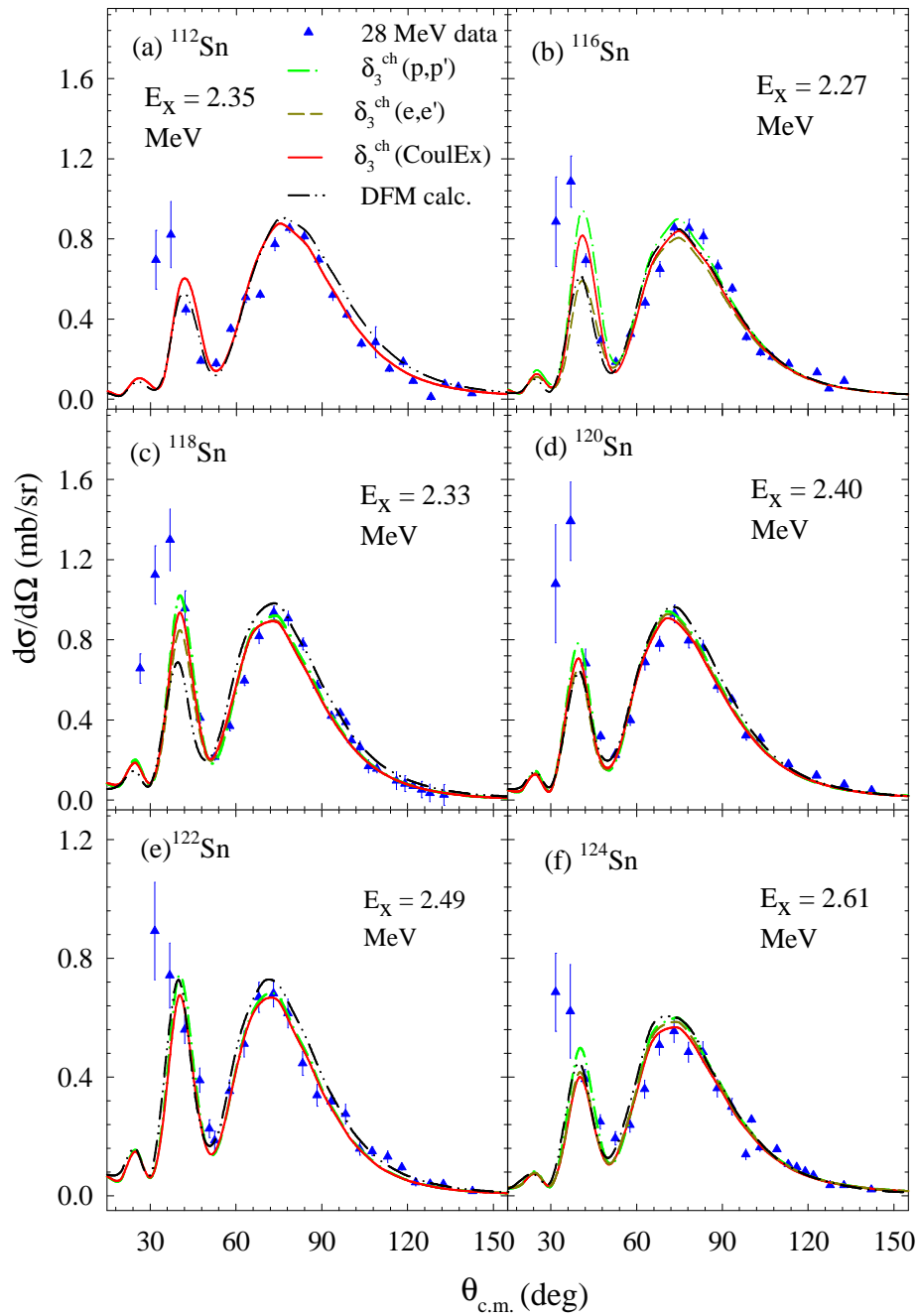


Figure 4.3: Experimental cross sections (filled triangles up) and the results of the CRC calculations (lines) for $\lambda = 3$ inelastic scattering processes corresponding to the target excitations in ${}^7\text{Li}+{}^{112,116,118,120,122,124}\text{Sn}$ systems. Calculations using WS potential with δ_3^{ch} values from existing Coulomb excitation measurement [23] (solid lines), electron scattering [21,22] (dashed lines) and proton scattering [41] (dash-dot lines) are shown. Also shown are calculations using DFM potential with δ_3^{ch} from Coulomb excitation (dash-dot-dot lines).

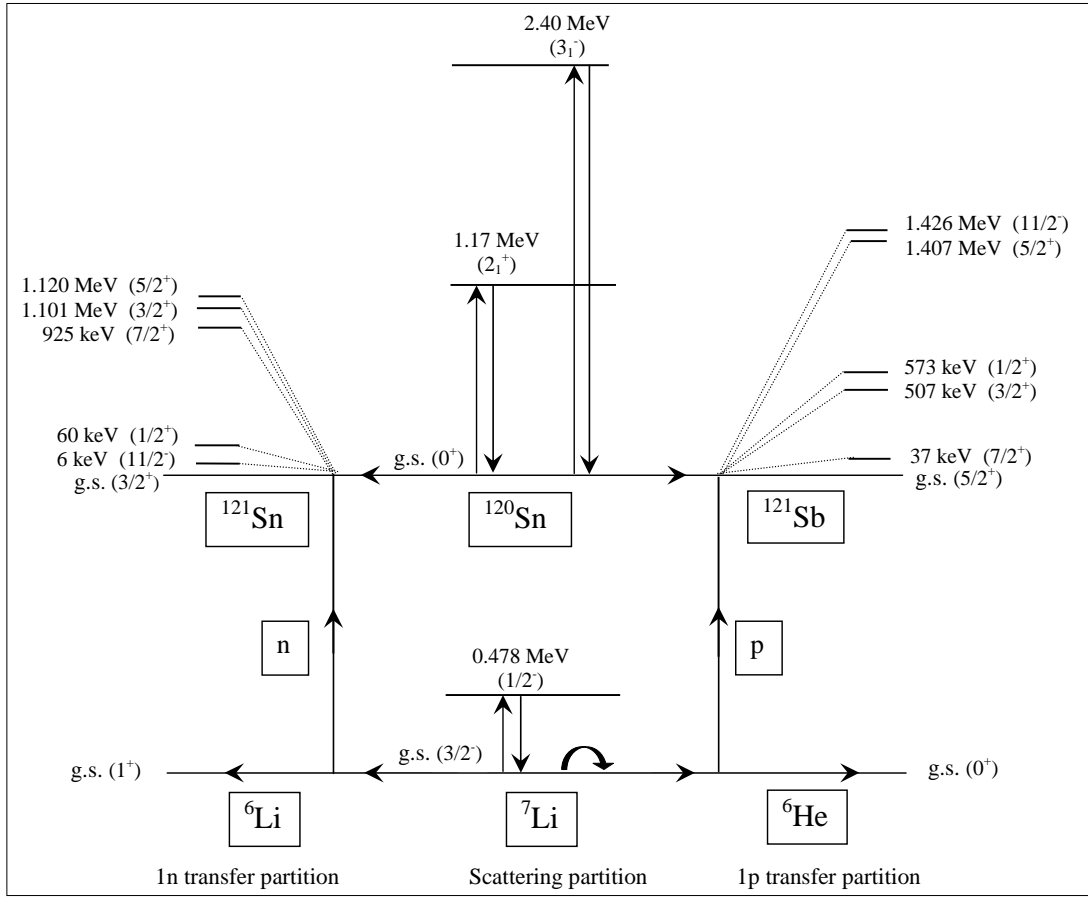


Figure 4.4: Coupling scheme of the ${}^7\text{Li} + {}^{120}\text{Sn}$ system used for the CRC calculations in FRESKO.

parameters were determined by reproducing the measured elastic scattering data for each system. This may be considered as the local equivalent potential (i.e., bare + polarization potential) that has taken care of the effect of couplings of breakup and other excluded reaction channels on the elastic channel. The total potential in the entrance channel is defined as:

$$V_{\text{total}}(r) = V_c(r, r_c) - \frac{V_0}{1 + \exp(\frac{r-r_a}{a_0})} - \frac{iW_0}{1 + \exp(\frac{r-r_w}{a_w})} \quad (4.2)$$

Here, $V_c(r, r_c)$ is the Coulomb potential due to a uniformly charged sphere of radius $R_c = r_c(A_P^{1/3} + A_T^{1/3})$, with charge radius r_c fixed at 1.20 fm and A_P and A_T are the mass numbers of projectile and target, respectively. The mass radius is calculated

Table 4.1: WS potential parameters for entrance channel used in CRC calculations for ${}^7\text{Li}+{}^{112,116,118,120,122,124}\text{Sn}$ systems at $E_{\text{lab}} = 28$ MeV. Values of r_0 and a_0 have been kept fixed at 1.243 fm and 0.695 fm respectively.

Target	V_0 (MeV)	W_0 (MeV)	r_w (fm)	a_w (fm)
${}^{112}\text{Sn}$	26.05	55.30	1.134	0.620
${}^{116}\text{Sn}$	29.25	59.50	1.166	0.575
${}^{118}\text{Sn}$	33.66	54.20	1.147	0.605
${}^{120}\text{Sn}$	35.06	57.71	1.138	0.678
${}^{122}\text{Sn}$	32.05	59.20	1.157	0.571
${}^{124}\text{Sn}$	31.45	58.70	1.165	0.605

as an average of r_0 and r_w . The depth of the real part was adjusted to optimize the simultaneous fit to elastic and inelastic scattering cross sections in each system. The volume absorptive imaginary part accounted for flux lost into the excluded nonelastic channels, as well as compound reaction in the entrance channel. To arrive at a consistent set of nuclear potential parameters across the Sn isotopic chain, two of the six parameters (r_0 and a_0) were kept fixed and the ranges of the others were restricted. The exit channel real potential was kept to be same as that of the entrance channel, with a short range imaginary potential of WS squared form. The final potential parameters are listed in Table 4.1. Integrating the radial wave functions up to 50 fm in steps of 0.25 fm and summing over 100 partial waves are found to be adequate to attain numerical convergence.

4.2.1.1 Effect of projectile excitation

The calculation for projectile excitation has been done assuming that the ground state and 478-keV states are members of the $K = 1/2$ rotational band and the transition is of quadrupole nature, with $\delta^{ch} = 3.944$ fm (obtained using ground state spectroscopic quadrupole moment -4.06 efm² and $B(E2; 3/2^- \rightarrow 1/2^-) = 8.3$ e²fm⁴) and $\delta^m = 1.993$ fm. This mass deformation length is consistent with the one obtained from an earlier measurement on ${}^7\text{Li}+{}^{11}\text{B}, {}^{13}\text{C}$ systems [68]. However, it may

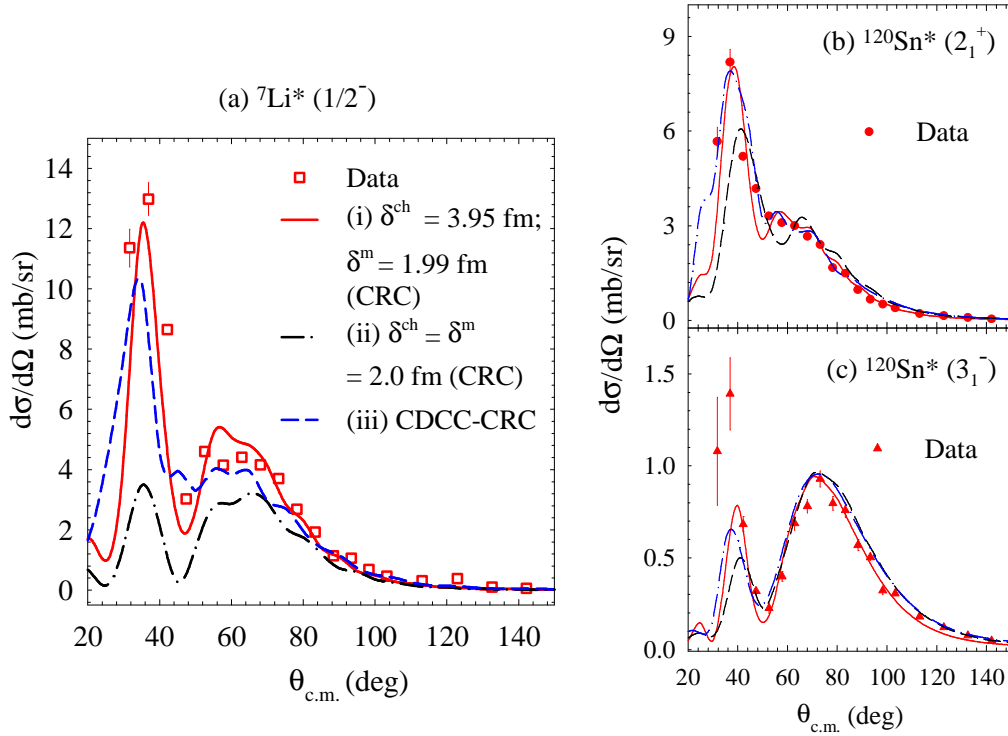


Figure 4.5: Experimental cross sections for inelastic scattering in ${}^7\text{Li}+{}^{120}\text{Sn}$ system corresponding to (a) bound excited state of ${}^7\text{Li}$, and target excited states (b) 2_1^+ and (c) 3_1^- . The lines show CRC calculations for different pairs of δ^{ch} and δ^m values : (i) $\delta^{ch} = 3.944$ fm , $\delta^m = 1.993$ fm (solid), (ii) $\delta^{ch} = \delta^m = 2.0$ fm (dash-dotted) and (iii) CDCC-CRC calculations (dashed) with $B(E2; (3/2^- \rightarrow 1/2^-)) = 8.39 e^2 fm^4$. Calculations for (i) and (iii) are found to suitably agree with the data and these parameters are used for complete theoretical modelling in the CRC and CDCC-CRC frameworks.

be important to note that in the work of Ref. [68] the relative heights of the maxima observed in the differential cross section could not be reproduced with the parameters $\delta^m = \delta^{ch} = 2.0$ fm. In the present work, the nuclear contribution to the inelastic excitation of this state is found to be smaller compared to the Coulomb contribution, i.e., $\delta^m < \delta^{ch}$. A similar feature of larger Coulomb amplitude is also observed in [69]. To find the suitability of the values of δ^{ch} and δ^m for the bound excited state of ${}^7\text{Li}$, different sets of calculations with unequal as well as similar charge and mass deformation lengths are compared with experimental data (symbols) in for the ${}^7\text{Li}+{}^{120}\text{Sn}$ system in Fig. 4.5(a). The solid line represents the CRC calculation with unequal deformation lengths for mass and charge densities, whereas, the dashed

line corresponds to the CRC calculations using equal deformation lengths. The dash-dotted line corresponds to the result of CDCC calculations described later in §4.2.2. The effects of such a variety in projectile couplings on the target excited states are also shown in the adjoining Figs. 4.5(b)-4.5(c) for each set of projectile coupling factors. Since the solid and dashed-dotted lines reasonably reproduce the experimental data, the respective parameters for ${}^7\text{Li}$ excitation have been used for CRC and CDCC calculations. The results indicate that the effect of projectile excitation is not much pronounced, particularly for the 3_1^- target excitation.

4.2.1.2 Target structural parameters

The calculations made use of independent adjustments of δ_λ^{ch} and δ_λ^m to reproduce the first and second peak respectively, in Figs. 4.2(a)-4.2(f) and Figs. 4.3(a)-4.3(f), as well as angular position of the minimum between them. For the $\lambda = 2$ transition in each isotope, δ_2^{ch} is consistent with existing Coulomb excitation measurements of $B(E2)$ by Allmond *et al.* (shown as circles in Fig.1.2) while δ_2^m differs by $\approx 5\%$. For the $\lambda = 3$ transition, however, existing $\delta_3^{ch,m}$ values measured with different probes, employing either pure Coulomb or nuclear fields, could not reproduce the data throughout the angular range. Also, the calculations beyond the minimum between the two major peaks in the CNI pattern were found to be less sensitive to δ_3^{ch} . Modest fits for ${}^{112,118,120,124}\text{Sn}$ are obtained by using δ_3^{ch} values from an existing systematic measurement of Coulomb excitation by Jonsson *et al.* (shown as circles in Fig.1.3), which are fairly closer to the data compared to other $B(E3)$ estimates. The δ_3^{ch} values for ${}^{116,122}\text{Sn}$ are suitably adjusted for a better reproduction of the experimental data and to obtain a uniform set across the isotopic chain, as Ref. [23] reports much larger values for these two isotopes compared to their neighbours. The charge deformation lengths, however, were found to overestimate the cross section beyond the CNI region. For obtaining the best fit, this was remedied

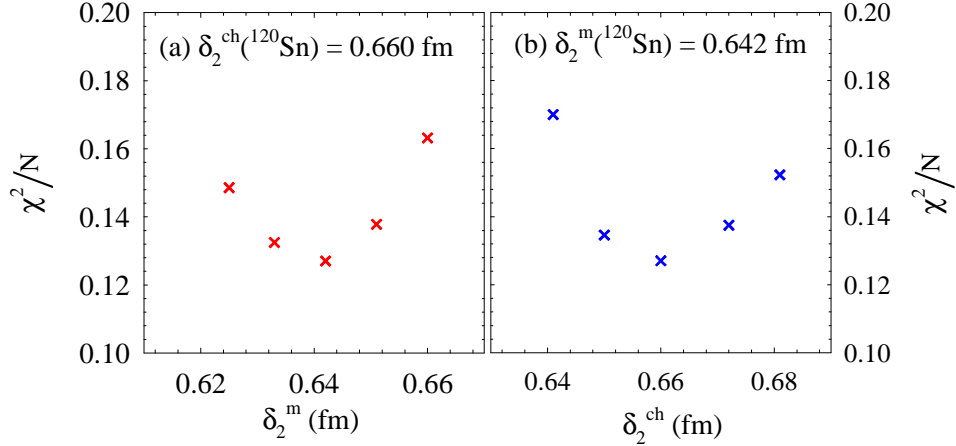


Figure 4.6: Minimum- χ^2 estimates of δ_2^{ch} and δ_2^m for the ^{120}Sn isotope.

Table 4.2: Experimental deformation lengths for the low-lying $\lambda = 2, 3$ target excitations in $^7\text{Li} + ^{112,116,118,120,122,124}\text{Sn}$ systems.

Target	$\lambda = 2$		$\lambda = 3$	
	δ_2^{ch} (fm)	δ_2^m (fm)	$^\dagger\delta_3^{ch}$ (fm)	δ_3^m (fm)
^{112}Sn	0.702(35)	0.698(35)	0.738(103)	0.581(51)
^{116}Sn	0.651(41)	0.656(38)	*0.745(101)	0.542(52)
^{118}Sn	0.645(33)	0.651(33)	0.753(108)	0.570(48)
^{120}Sn	0.660(29)	0.642(41)	0.717(129)	0.556(30)
^{122}Sn	0.615(31)	0.611(42)	*0.655(103)	0.477(41)
^{124}Sn	0.569(26)	0.563(41)	0.632(087)	0.458(33)

† From Coulomb excitation measurement [23]

* Modified

by keeping $\delta_3^m \ll \delta_3^{ch}$ in the present calculations. The CRC calculations reflected a strong correlation between δ_2^m and δ_2^{ch} (i.e. a small reduction in δ_2^{ch} had to be compensated by a similar increase in δ_2^m), whereas δ_3^m was found to be nearly independent of fluctuations in δ_3^{ch} . However, these values are lower than the range of those previously observed over the years. The first maximum of the differential cross section could not be well reproduced, and different sets of calculations are shown in Figs. 4.3(a)-4.3(f) keeping δ_3^m fixed and using δ_3^{ch} measured via Coulomb excitation (solid lines) [23], electron scattering (dashed lines) [21, 22] and proton scattering (dash-dotted lines) [41], wherever available.

To test the parametric fit of the deformation lengths, a χ^2 test has been carried out. The minimum- χ^2 estimate of δ_λ^m for each isotope is arrived at by keeping the value of δ_λ^{ch} unchanged, and vice-versa, as typically shown in Fig. 4.6 for the $\lambda = 2$ excitation of the ${}^{120}\text{Sn}$ nucleus. The extracted $\delta_\lambda^{ch,m}$ values for the different isotopes are presented in Table 4.2.

The chosen parameter set for the nuclear potential governing these interactions, given in Table 4.1, is not unique. There are various such sets which reproduce the data equally well. However, once a consistent description of elastic and inelastic scattering channels is attained, it is observed that the combination of real and imaginary radii required to explain the data always led to δ_λ^m similar to those reported in Table 4.2.

4.2.1.3 Sensitivity of interaction potential

The traditional interpretation of elastic (inelastic) scattering in the framework of the usual optical model (deformed optical model) is highly phenomenological and does not incorporate the more microscopic aspects of the reaction and excitation mechanism, where one seeks to describe the scattering of the projectile from a nucleus in terms of fundamental interactions between the nucleons. The basic justification for using potentials of the Woods-Saxon shape for nucleus-nucleus scattering, for example, is the knowledge that a nuclear density distribution is effectively constant in the nuclear interior with a diffuse surface. When this distribution is folded with a short-range nucleon-nucleon interaction, the result is a similar shape with a more diffuse surface. In order to compare the calculations using the phenomenological potential with a universal potential, the CRC calculations were repeated with density dependent double folding model (DFM) nucleus-nucleus potential calculated for systems with at least one spin-less nucleus, as a function of centre-to-centre separation,

\mathbf{r} , as

$$V_{DFM}(\mathbf{r}) = \int d\mathbf{r}_1 \int d\mathbf{r}_2 [v_{IS}(\rho, \mathbf{r} + \mathbf{r}_2 - \mathbf{r}_1) \cdot (\rho_{1n}^{g.s.} + \rho_{1p}^{g.s.}) \cdot (\rho_{2n}^{g.s.} + \rho_{2p}^{g.s.}) + v_{IV}(\rho, \mathbf{r} + \mathbf{r}_2 - \mathbf{r}_1) \cdot (\rho_{1n}^{g.s.} - \rho_{1p}^{g.s.}) \cdot (\rho_{2n}^{g.s.} - \rho_{2p}^{g.s.})] \quad (4.3)$$

with \mathbf{r}_1 and \mathbf{r}_2 as the radial vectors of the projectile (1) and target (2). Here, v_{IS} and v_{IV} are the effective isoscalar (spin and isospin independent) and isovector (isospin-dependent) components of the fundamental microscopic nucleon-nucleon interaction.

The radial dependence is parametrized in the M3Y-Paris forms [70], as

$$v_{IS}(r) = 11061.625 \frac{e^{-4r}}{4r} - 2537.5 \frac{e^{-2.5r}}{2.5r} \quad (4.4)$$

$$v_{IV}(r) = 313.625 \frac{e^{-4r}}{4r} + 223.5 \frac{e^{-2.5r}}{2.5r} \quad (4.5)$$

The associated density dependence is chosen to be of the DDM3Y1-type [70], with $\rho = \rho_1(\mathbf{r}_1) + \rho_2(\mathbf{r}_2)$. The shapes of the proton and neutron ground state densities $\rho_{(p,n)}^{g.s.}$ of ⁷Li and each Sn isotope were taken to be analogous to their ground state charge density distributions obtained from existing electron scattering measurements, with their r.m.s. radii consistent with the measured neutron skin thickness of the ⁷Li [71] and Sn nuclei [18, 72]. The r.m.s. radii for the point-matter distributions for all nuclei are deduced from their measured charge r.m.s. radii, by unfolding the charge distribution of the proton as well as a minor, but important, contribution from the charge distribution of the neutron, with $\langle r_m^2 \rangle = \langle r_{ch}^2 \rangle - 0.722 + \left(\frac{N}{Z}\right) 0.115 \text{ fm}^2$. Here, the mean square charge radius of the proton is 0.722 fm² (consistent with electron scattering [73] and muonic hydrogen Lamb-shift measurements [74]) and mean square charge radius of the neutron is -0.115 fm² (from measurements of neutron-electron scattering length [75]). The contribution to the r.m.s. radius of the point-matter distribution from the neutron form factor is of the order of 0.02–0.03 fm. A complex form of the bare DFM potential has been used in the full CRC calcu-

lations with adjustable normalization factors for the imaginary part. This potential is suitably deformed by introducing structural parameters that govern the inelastic excitations of the collision partners. Interestingly, the analysis using DFM potential generates optimum description of elastic scattering and target excited states with the same set of deformation lengths as given in Table 4.2, and the calculations are in good agreement with those of the WS potential. This implies that the extracted structural parameters are independent of the method of scattering analysis. The calculations have been shown by dash-dot-dot lines for the 2_1^+ state in Figs. 4.2(a)-4.2(f) as well as for the 3_1^- state in Figs. 4.3(a)-4.3(f).

4.2.2 CDCC-CRC Calculations

To further investigate the role of the weakly bound nature of the projectile (if any), another set of calculations in the CDCC-plus-CRC framework that include a simultaneous analysis of projectile breakup (into $\alpha + t$), target collective excitations and transfer processes, have also been carried out. The coupling of direct and resonant breakup channels of ${}^7\text{Li}$, which is known to affect the elastic scattering, may in turn affect the target excitation channels of interest. In addition, direct coupling of the projectile breakup channels with the target excitations may also affect the inelastic scattering cross sections. Simultaneous inclusion of both projectile breakup and target inelastic channels has been made by first calculating the cluster folded (CF) bare potential [76] from the fragment-target interaction potentials. Then, this CF potential has been read in to calculate the additional potentials contributed by the target deformations corresponding to different excitations.

The projectile excitations corresponding to the bound excited state (0.478 MeV, $1/2^-$), unbound resonant states at 4.63 MeV ($7/2^-$), 6.67 MeV ($5/2^-$) and non-resonant continuum above the α - t breakup threshold ($E_{\text{th}} = 2.468$ MeV) up to an excitation energy of about 8 MeV of ${}^7\text{Li}$ were included, where it has been assumed

Table 4.3: The states of the projectile ^7Li included in the model space of the CDCC-CRC calculations. E_x , E_{\min} and E_{\max} represent the mean, minimum and maximum excitation energies, respectively, of a particular bin above the α - t breakup threshold, E_{th} .

L	J^π	E_x (MeV)	E_{\min} (MeV)	E_{\max} (MeV)
0	$1/2^+$	0.2421	0.0021	0.4821
0	$1/2^+$	1.2103	0.4841	1.9365
0	$1/2^+$	3.1470	1.9365	4.3570
0	$1/2^+$	6.0520	4.3570	7.7460
1	$3/2^-$	-2.468 (E_{th})	-	-
1	$3/2^-$	0.2421	0.0021	0.4821
1	$3/2^-$	1.2103	0.4841	1.9365
1	$3/2^-$	3.1470	1.9365	4.3570
1	$3/2^-$	6.0520	4.3570	7.7460
1	$1/2^-$	-1.990 (bound inelastic)	-	-
1	$1/2^-$	0.2421	0.0021	0.4821
1	$1/2^-$	1.2103	0.4841	1.9365
1	$1/2^-$	3.1470	1.9365	4.3570
1	$1/2^-$	6.0520	4.3570	7.7460
2	$5/2^+$	0.2421	0.0021	0.4821
2	$5/2^+$	1.2103	0.4841	1.9365
2	$5/2^+$	3.1470	1.9365	4.3570
2	$5/2^+$	6.0520	4.3570	7.7460
2	$3/2^+$	0.2421	0.0021	0.4821
2	$3/2^+$	1.2103	0.4841	1.9365
2	$3/2^+$	3.1470	1.9365	4.3570
2	$3/2^+$	6.0520	4.3570	7.7460
3	$7/2^-$	0.2421	0.0021	0.4821
3	$7/2^-$	1.2720	0.4840	2.0600
3	$7/2^-$	2.1600	2.0600	2.2600
3	$7/2^-$	3.3080	2.2600	4.3200
3	$5/2^-$	0.2421	0.0021	0.4821
3	$5/2^-$	1.2103	0.4841	1.9365
3	$5/2^-$	2.3200	1.9370	2.7100
3	$5/2^-$	4.2100	2.7100	5.7100

to have a cluster structure of $\alpha + t$. The Watanabe-type folding model is assumed for the structure of ${}^7\text{Li}$ as an $\alpha + t$ two-body cluster. This calculates the Coulomb as well as nuclear transition strengths among the excited states of ${}^7\text{Li}$ from the resulting wave functions. The transition potentials are calculated by folding the α and t optical potentials over the ${}^7\text{Li}$ cluster wave functions for the initial and final states, in a similar way to the deformed diagonal potentials as in a conventional collective model calculation. This narrows down to the target structural factors as the only adjustable parameters in the model. The corresponding calculation for excitation to the 0.478 MeV state of ${}^7\text{Li}$ with established $B\left(E2; 3/2_{\text{g.s.}}^- \rightarrow 1/2_{0.478\text{MeV}}^- \right) = 8.39 \text{ e}^2\text{fm}^4$, is shown as dashed lines in Fig.4.5. The continuum of the α - t cluster of ${}^7\text{Li}$ at excitation E_x (w.r.t. E_{th}) has been discretized with respect to the α - t relative momentum of $\hbar k$ into several momentum bins, in steps of $\Delta k = 0.2 \text{ fm}^{-1}$, up to $k = 0.8 \text{ fm}^{-1}$ [77]. Each bin beyond E_{th} has been treated as an excited state of the α - t cluster with excitation energy equal to the mean excitation value for that bin (shown in Table 4.3). The spin of each excited state, J^π , has been obtained as the vector sum of the α - t relative angular momentum L and the spin of the triton S . All possible states with $L = 0,1,2,3$ have been included. The binning of the continuum with $L = 3$ has been suitably modified to include the resonances $7/2^-$ and $5/2^-$ with average excitation energies (above E_{th}) of $E_x = 2.16$ and $E_x = 4.21$ MeV, and widths of 0.2 and 3.0 MeV respectively. The α - t binding potentials are of Gaussian form as given in [78], but suitably adjusted (shown in Table 4.4) to reproduce the ground state quadrupole moment and $B\left(E2; 3/2_{\text{g.s.}}^- \rightarrow 1/2_{0.478\text{MeV}}^- \right)$ for ${}^7\text{Li}$, as well as generate resonance criteria (phase shift) at correct excitation energies.

A standard entrance channel projectile-target cluster-folded (CF) interaction was generated, where São Paulo potentials [79] were used as the real parts of the fragment-target, $\alpha+\text{Sn}$ and $t+\text{Sn}$ potentials, evaluated at $E_\alpha = \frac{4}{7}E_{\text{lab}}$ and $E_t = \frac{3}{7}E_{\text{lab}}$. The imaginary potentials were of Woods-Saxon form with short ranged vol-

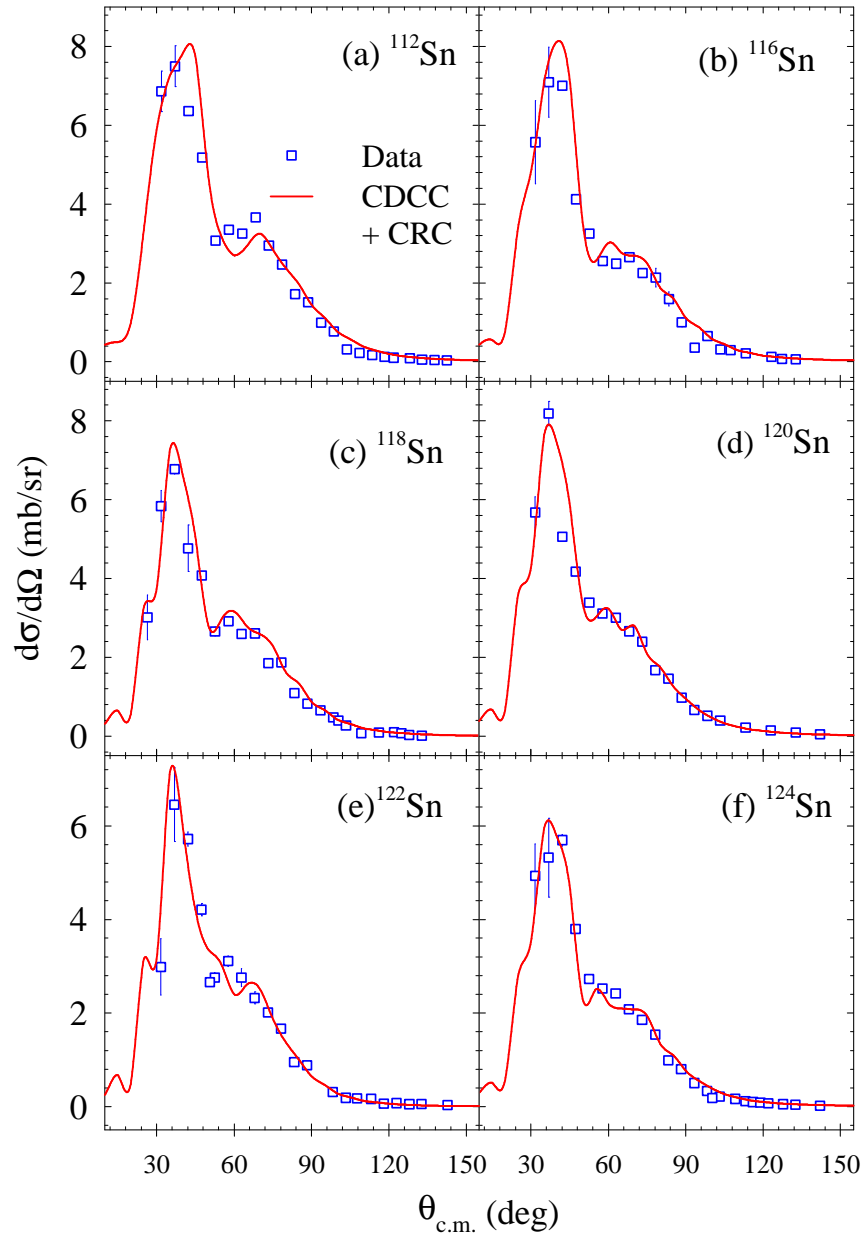


Figure 4.7: Experimental cross sections (filled triangles up) and the results of the CDCC-plus-CRC calculations (solid lines) for $\lambda = 2$ inelastic scattering processes corresponding to target excitations in $^7\text{Li} + ^{112,116,118,120,122,124}\text{Sn}$ systems.

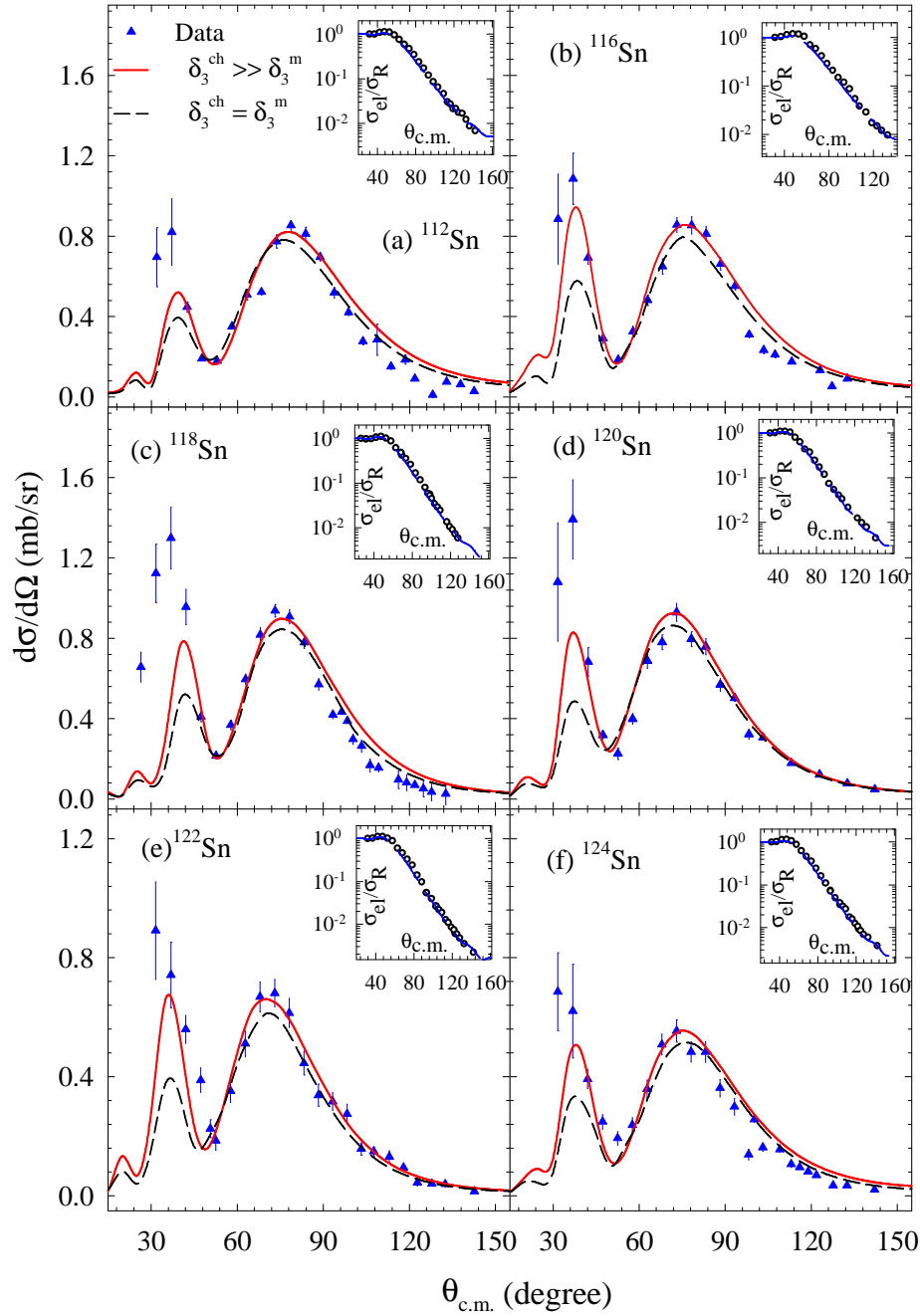


Figure 4.8: Experimental cross sections (filled triangles up) and the results of the CDCC-plus-CRC calculations (solid lines) for $\lambda = 3$ inelastic scattering processes corresponding to target excitations in ${}^7\text{Li}+{}^{112,116,118,120,122,124}\text{Sn}$ systems. Inset: Experimental elastic scattering angular distribution (circles) with calculation under CDCC-CRC formalism (dashed lines). The calculations for inelastic scattering with reduced values of δ_3^{ch} but equal to δ_3^{m} are also shown (dashed lines).

Table 4.4: α - t binding potentials of the form $V = -V_0e^{-r^2/a_0^2} + V_{so}e^{-r^2/a_{so}^2}$ for the ^7Li projectile used in CDCC+CRC calculations.

State(s)	V_0 (MeV)	a_0 (fm)	V_{so} (MeV)	a_{so} (fm)
g.s.+non-resonant	83.780	2.590	2.006	2.590
bound inelastic	83.557	2.570	2.006	2.570
7/2 ⁻	83.404	2.520	4.012	2.520
5/2 ⁻	78.810	2.520	4.012	2.520

ume and surface terms. The quadrupole and octupole target excitations were then coupled to the bound and unbound excitations of the projectile by deforming the entrance channel Coulomb and CF interactions with the δ_λ^{ch} and δ_λ^m parameters, respectively, from Table 4.2. Few dominant 1-nucleon transfer channels have also been coupled. The strongly coupled elastic, breakup and inelastic scattering channels were solved exactly and blocked together to be treated as a single unit during iterations. The weaker transfer couplings were treated as successive perturbations iteratively, with the same exit channel potentials and couplings as mentioned in Sec. 4.2.1. The fragment-target São Paulo potentials were normalized suitably to reproduce the elastic scattering angular distribution for each system.

The inelastic scattering data and resulting calculations for the 2_1^+ and 3_1^- excitations are shown in Figs. 4.7 and 4.8 with a good agreement between them in the regions of the valley and the second maximum. The fit to elastic scattering data has also been reproduced for each system (insets of Fig. 4.8). Interestingly, the data could again be well reproduced with the same set of $\delta_\lambda^{ch,m}$ as obtained from the CRC analysis described earlier in section 4.2.1. It may be safely surmised that the explicit effect of projectile breakup channels on the target excitations is inconsequential. In addition, calculations were also performed with lower values of δ_3^{ch} but equal to the respective values of δ_3^m as shown by dashed lines in Fig. 4.8(a)-4.8(f). However, the latter calculations lead to larger disagreement between experiment and theory in the region of the first maximum. These tests put emphasis on the validity of the realis-

tic coupling parameters and structural information, particularly mass deformation length, extracted using the model calculations for the present systems.

To establish the existence of probe-dependence in extracting target structural information, another set of measurements have been carried out with a different projectile, ^{12}C . Intermediate energy scattering using an isoscalar probe like ^{12}C can be a useful spectroscopic tool for exciting discrete collective states as such nuclei are sensitive to nuclear matter distributions and the projectile-target interaction is devoid of any spin and isospin dependence. Such probes are complementary to those with unpaired proton(s) or neutron(s).

4.3 ^{12}C -induced excitations

A schematic diagram of the experimental setup is shown in Fig. 2.5 of Chapter 2. A typical gain-matched spectrum of ΔE versus $E_{\text{total}} (= E + \Delta E)$ is shown for the $^{12}\text{C} + ^{112}\text{Sn}$ system in Fig. 4.9(a), where projectile-like fragments with different $Z (= 2-7)$ and $A (= 4-14)$ are identified. Energy resolution of a telescope is in the range $\approx 75-100$ keV ($\approx 170-200$ keV for the thicker foil of ^{116}Sn), sufficient to resolve the different excited states of interest. Along with the elastic scattered peak, the yields of projectile and target excited states corresponding to the 2_1^+ and 3_1^- vibrational states of $^{112,116,118,120,122,124}\text{Sn}$ as well as the first excited state of ^{12}C (4.438 MeV), are found to be dominant (Fig. 4.9(b)). In addition, few states corresponding to one-neutron pickup ($^{12}\text{C}, ^{13}\text{C}$) as well as one-proton stripping ($^{12}\text{C}, ^{11}\text{B}$), with subsequent excitation of the respective residual nuclei, could be identified. All these channels are included into the theoretical modelling of the reaction system to constrain the calculations and lead to realistic potential and coupling parameters.

Similar to the analysis procedure described in §4.2, the differential cross sections for the elastic scattering and transitions to the excited 2_1^+ and 3_1^- states of the targets

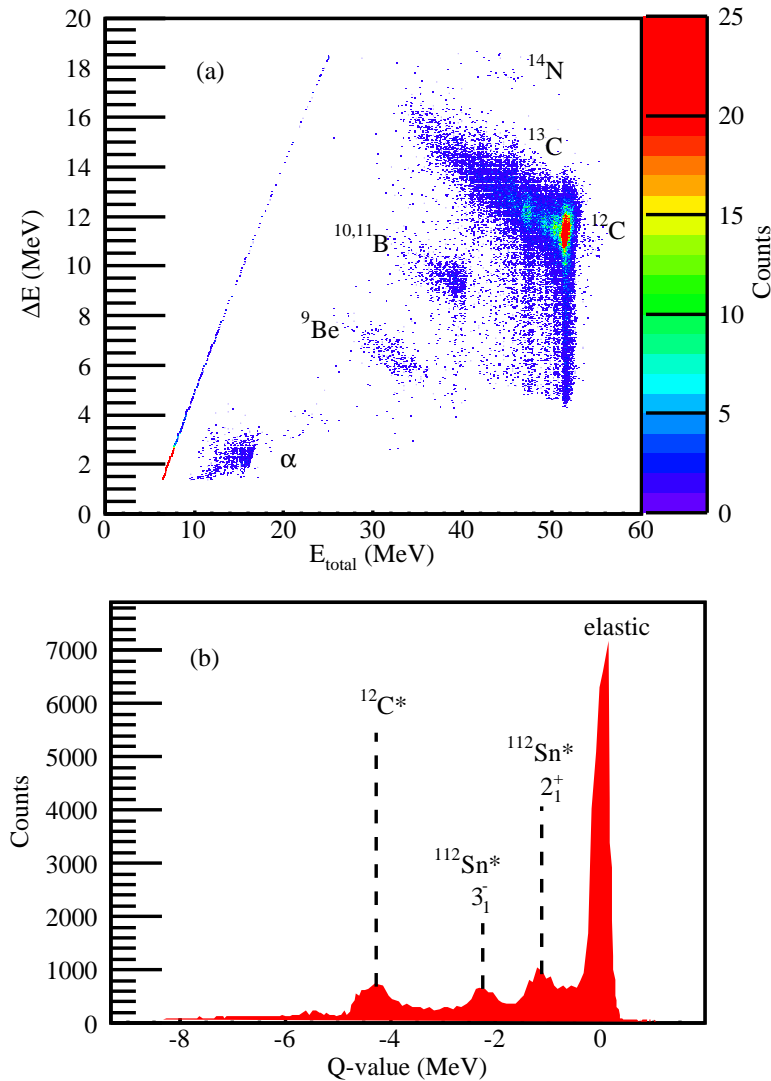


Figure 4.9: (a) Typical two-dimensional (ΔE versus E_{total}) gain-matched spectrum showing the outgoing projectilelike fragments at $\theta_{\text{lab}}=70^\circ$ in the $^{12}\text{C} + ^{112}\text{Sn}$ reaction. (b) One-dimensional spectrum showing Q -value distribution of elastic and inelastic scattering.

are extracted in the centre of mass frame. The elastic-to-Rutherford ratio angular distributions are shown as hollow circles in Fig. 4.10(a)-4.10(f). The experimental cross sections for the $\lambda = 2$ transition in each Sn isotope are shown as squares in Figs. 4.10(g)-4.10(l), and, for the $\lambda = 3$ transition are shown as triangles in Figs. 4.10(m)-4.10(r). The lines in all figures represent the results of theoretical calculations described in §4.3.1.

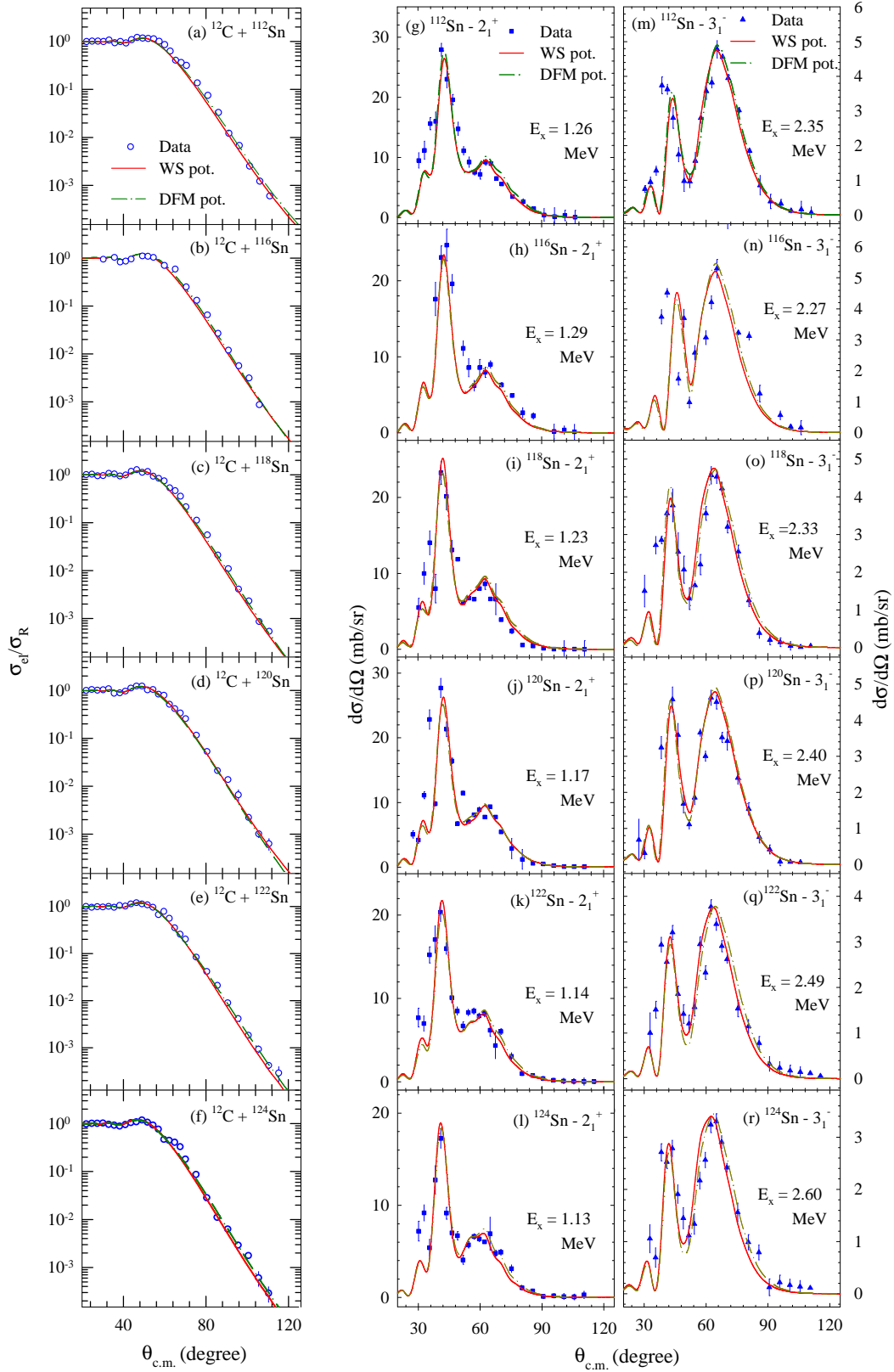


Figure 4.10: Experimental angular distributions and results of CRC calculations (solid lines for WS potential, dash-dotted lines for DFM potential) for (a-f) elastic-to-Rutherford cross section ratio, and (g-l) target inelastic scattering to 2_1^+ (squares) and (m-r) 3_1^- (triangles up) states in $^{12}\text{C} + ^{112,116,118,120,122,124}\text{Sn}$ systems at $E_{lab} = 60$ MeV.

4.3.1 CRC Calculations

CRC model calculations for elastic and inelastic scattering angular distributions have been performed by coupling the major direct reaction channels to the entrance channel, in the CCBA limit. For the ^{12}C -induced excitations, the DWBA formalism was found to be inadequate to explain the strongly-coupled excited states. In addition, the first excited state of the ^{12}C projectile at 4.438 MeV, and a few dominant channels identified in the one-neutron pickup and one-proton stripping processes, corresponding to low-lying states of the respective residual nuclei, are also included with available spectroscopic factors. The coupling scheme for one of the systems is shown in Fig. 4.11. Since the coupling effect of all open reaction channels to

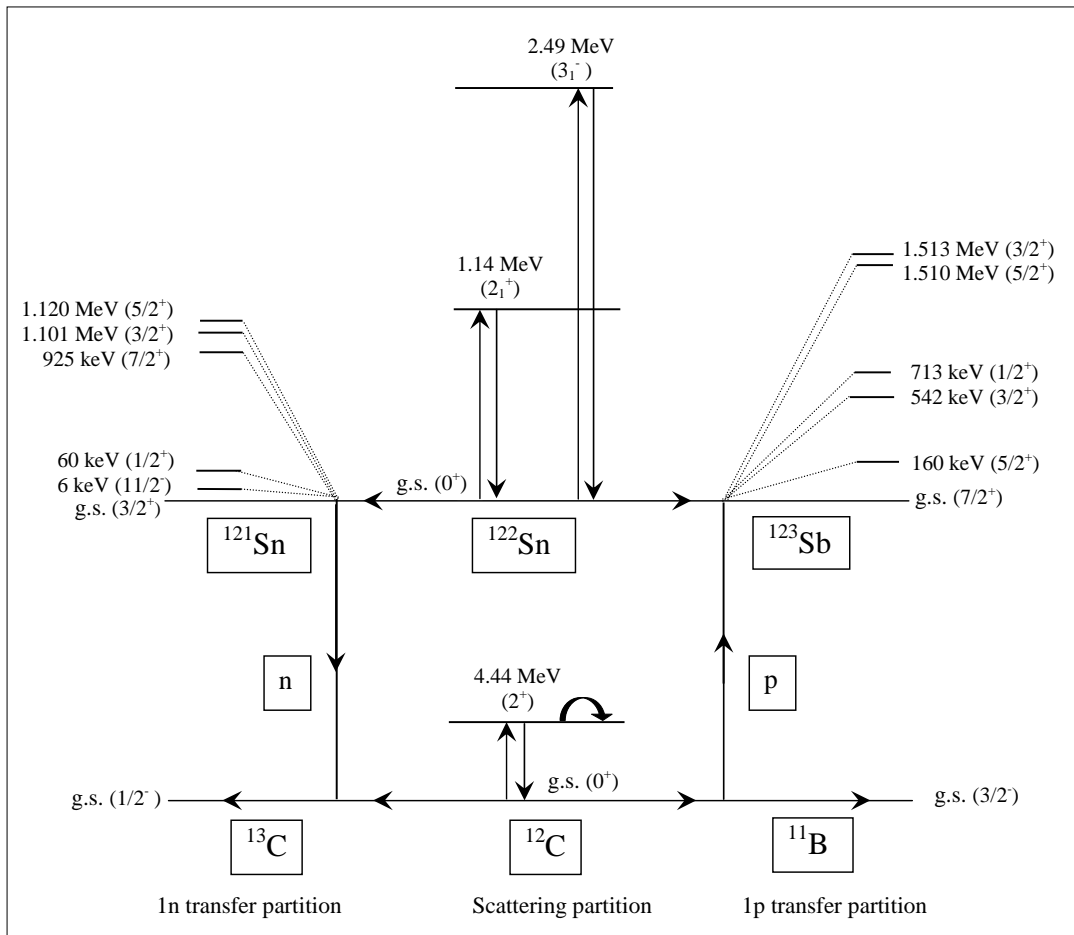


Figure 4.11: Coupling scheme of the $^{12}\text{C} + ^{122}\text{Sn}$ system used for the CRC calculations in FRESKO.

the entrance channel is manifested in the elastic scattering cross section, the wave functions for the different model space channels are generated from a phenomenological optical potential of Woods-Saxon (WS) form, whose parameters are determined by reproducing the measured elastic scattering data for each system. Generally, if all dominant reaction channels are coupled in a heavy-ion collision involving stable, tightly-bound nuclei, only a short range imaginary potential in the entrance as well as all outgoing channels would suffice to calculate the net fusion cross section and simultaneously predict proper elastic scattering cross section. Accordingly, the present calculations included the dominant projectile and target inelastic states and few low-lying one-nucleon transfer channels as seen in Fig. 4.9(a), which were coupled by an optical potential with long range real part and an imaginary part of shorter range (WS square form). These couplings, however, failed to adequately explain the elastic scattering data, even with variations of the potential depths (not shown in the plots). This could be the consequence of non-inclusion of some of the higher excitations in the projectile or target, as well as some multinucleon/cluster transfer channels in the couplings, due to computational limitation. To account for the loss of the incident flux, associated with the population of the channels excluded from the model space, a volume absorptive optical potential of WS type with a long range imaginary part is finally used. The total potential is defined by Eqn. 4.2. The final potential parameters used in the CRC calculations that provide optimum simultaneous description of elastic as well as non-elastic channels are listed in Table 4.5.

The exit channel real potential is kept to be same as that of the entrance channel, with a short ranged imaginary potential of WS square form, given by $W_0 = 10.00$ MeV, $r_w = 1.00$ fm and $a_w = 0.40$ fm. Integrating the radial wave functions up to 20 fm in steps of 0.10 fm and summing over 100 partial waves are found to be adequate to attain numerical convergence.

Table 4.5: Entrance channel WS potential parameters used in CRC calculations for $^{12}\text{C} + ^{112,116,118,120,122,124}\text{Sn}$ systems at $E_{\text{lab}} = 60$ MeV. Values of r_0 and r_w were fixed at 1.175 fm and 1.150 fm, respectively.

Target	V_0 (MeV)	a_0 (fm)	W_0 (MeV)	a_w (fm)
^{112}Sn	49.70	0.725	23.13	0.670
^{116}Sn	52.85	0.702	26.50	0.613
^{118}Sn	63.75	0.705	38.32	0.620
^{120}Sn	56.65	0.675	37.81	0.551
^{122}Sn	50.45	0.712	39.60	0.595
^{124}Sn	58.85	0.702	40.44	0.612

4.3.1.1 Effect of projectile excitation

Among the various nonelastic channels, the coupling of the first excited 2^+ state of ^{12}C is found to have considerable influence on the elastic scattering angular distribution. Several studies in the past report an oblate nature of the deformation of ^{12}C nucleus in its 2^+ state, confirmed by exclusive measurements [80, 81] of the spectroscopic quadrupole moment (reorientation coupling), $Q_S(2^+)$, in the range of 0.06-0.07 eb. This translates to an intrinsic quadrupole moment of -0.21 eb in the body-fixed frame, which supports a substantial oblate deformation. A compilation [82] of the deformation length for this excitation in ^{12}C obtained from several existing measurements with a variety of probes shows scattered values, ranging from -1.42 fm to -1.76 fm. The values extracted from $^{12}\text{C}+^{12}\text{C}$ inelastic scattering at energies above 100 MeV vary from -1.15 fm [83] up to -2.1 fm [84].

In the present work, the deformation lengths are suitably adjusted, and kept same for the Coulomb potential and the real and imaginary parts of the nuclear potential. The reorientation coupling is also defined, which is found to be crucial in order to reproduce the elastic data at the extreme backward angles. The extracted values, $\delta^{ch} = \delta^m = -1.38$ fm, $B(E2; 0^+ \rightarrow 2^+) = 29.5$ e 2 fm 4 and $Q_S(2^+) = 0.05$ eb (intrinsic quadrupole moment of -0.17 eb), lead to an optimum agreement between the calcu-

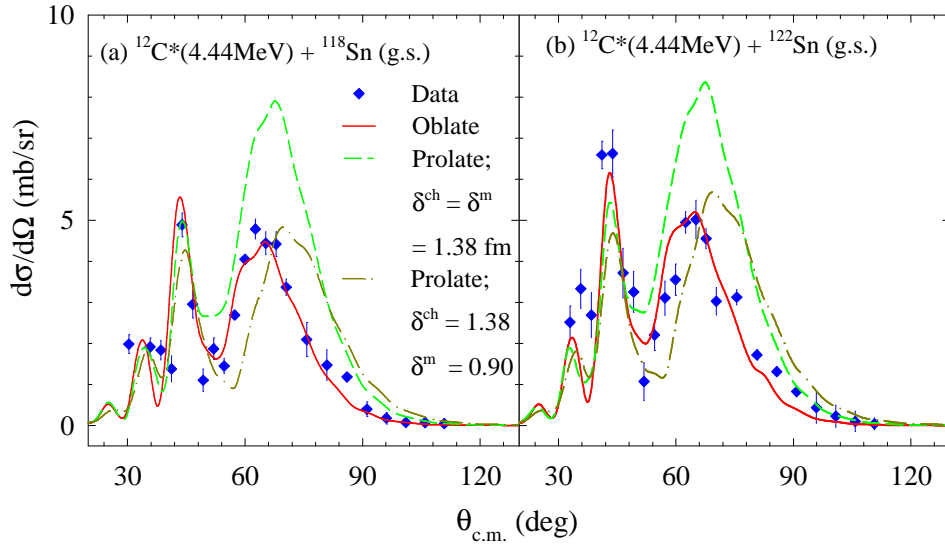


Figure 4.12: Experimental differential cross sections (diamonds) for inelastic excitation of ^{12}C in (a) $^{12}\text{C}+^{118}\text{Sn}$ and (b) $^{12}\text{C}+^{122}\text{Sn}$ systems. The lines show CRC calculations for : (i) $\delta^{ch} = \delta^m = -1.38$ fm; $Q_S = +0.05$ eb (solid), (ii) $\delta^{ch} = \delta^m = +1.38$ fm (dashed), and (iii) $\delta^{ch} = +1.38$ fm and $\delta^m = +0.90$ fm (dash-dotted). Calculation with parameter set (i) is found to suitably agree with the data and these parameters are used for complete theoretical modelling in the present systems.

lated (solid lines) and measured (symbols) cross sections as shown in Fig. 4.12(a,b) for the $^{12}\text{C}^*$ (4.44 MeV)+ $^{118,122}\text{Sn}$ systems. The results are in good agreement with existing value of $B(\text{E}2; 0^+ \rightarrow 2^+) = 38.6 \text{ e}^2\text{fm}^4$ [85]. The calculated cross sections are found to be highly sensitive to the sign of the deformation lengths for the ^{12}C excitation. One fails to reproduce the angular positions of the maxima by considering prolate deformations, with $\delta^{ch} = \delta^m = 1.38$ fm, or with unequal values, $\delta^{ch} = 1.38$ fm, $\delta^m = 0.90$ fm (as shown with dashed and dash-dotted lines in Fig. 4.12). The angular distribution obtained from heavy ion inelastic scattering is, therefore, a sensitive tool for identifying prolate or oblate nature of an excitation.

4.3.1.2 Target structural parameters

The calculations require independent adjustments of δ_λ^{ch} and δ_λ^m . For the $\lambda = 2$ and 3 transitions in each isotope, values of δ_2^{ch} and δ_3^{ch} are nearly consistent with the results reported from ^7Li -induced excitations (given in Table 4.2). However, δ_2^m

and δ_3^m values measured with the ^7Li probe could not satisfactorily reproduce the data throughout the angular range. The mass deformation lengths, thus, remain free parameters for each target nucleus, and a characteristic probe-dependence is evidenced. New values are determined from the present data. While δ_2^m is found to be correlated to and larger by about $\approx 5\text{-}7\%$ than δ_2^{ch} , the δ_3^m values are completely independent of δ_3^{ch} , and are slightly lower, with the calculations beyond the minimum region less sensitive to the δ_3^{ch} parameter. The calculations for $\lambda = 2$ and $\lambda = 3$ excitations are shown by solid lines in Figs. 4.10(g)-4.10(l), and Figs. 4.10(m)-4.10(r), respectively. The minimum- χ^2 estimates of $\delta_\lambda^{ch,m}$ are reported in Table 4.6.

Table 4.6: Experimental deformation lengths for the low lying $\lambda = 2, 3$ excitations in Sn isotopes in the $^{12}\text{C} + ^{112,116,118,120,122,124}\text{Sn}$ systems.

Target	$\lambda = 2$		$\lambda = 3$	
	δ_2^{ch} (fm)	δ_2^m (fm)	δ_3^{ch} (fm)	δ_3^m (fm)
^{112}Sn	0.709(39)	0.760(45)	0.742(109)	0.707(46)
^{116}Sn	0.651(33)	0.687(42)	0.763(083)	0.720(62)
^{118}Sn	0.649(25)	0.715(37)	0.757(092)	0.692(51)
^{120}Sn	0.665(39)	0.697(47)	0.720(115)	0.665(41)
^{122}Sn	0.615(28)	0.655(36)	0.677(076)	0.621(49)
^{124}Sn	0.572(36)	0.614(41)	0.655(107)	0.610(43)

The values reported in Table 4.6 are independent of the choice of potential parameters once a consistent description of elastic and inelastic scattering channels is attained.

4.3.1.3 Sensitivity of interaction potential

In order to compare the results with those using a microscopic potential, the CRC calculations are repeated with the DFM potential calculated as a function of centre to centre separation, r , as

$$V_{DFM}(\mathbf{r}) = \int d\mathbf{r}_1 \int d\mathbf{r}_2 [v_{00}(\mathbf{r} + \mathbf{r}_2 - \mathbf{r}_1) \cdot (\rho_{1n}^{g.s.} + \rho_{1p}^{g.s.}) \cdot (\rho_{2n}^{g.s.} + \rho_{2p}^{g.s.})] \quad (4.6)$$

Here, v_{00} is the fundamental isoscalar interaction parametrized in the DDM3Y1-Paris form given by Eqn. 4.4. The shapes of the proton and neutron ground state densities for ^{12}C and ^ASn are calculated following the prescription in §4.2.1.3. For the ^{12}C nucleus, the neutron and proton distributions are considered to be equal [86]. A complex form of the bare DFM potential is used in the full CRC calculations to generate optimum description of elastic scattering, with adjustable normalization coefficient for the imaginary part. DFM analysis using the deformation lengths given in Table 4.6 leads to adequate representation of elastic and inelastic scattering data for all states concerned. The calculations have been shown by dash-dotted lines for the 2_1^+ state in Figs. 4.10(g)-4.10(l) as well as for the 3_1^- state in Figs. 4.10(m)-4.10(r), and are in good agreement with the results of the WS potential.

4.4 Neutron & proton transition matrix elements

From the study of ^7Li - and ^{12}C -induced excitations in the Sn isotopes, the probe-dependence of structural parameters, particularly mass deformation lengths, is established. However, the results obtained using the phenomenological potential are in excellent agreement with those of the microscopic potential for all the aforementioned reaction systems. It can be seen from the basic folding formulas that this model generates the first-order term of the microscopic optical potential that is derived from Feshbach's theory of nuclear reactions [87]. This draws attention to the need for exploring the root cause of the probe-dependence. From the experimental information of δ_λ^m and δ_λ^{ch} , as reported in Tables 4.2 and 4.6, the microscopic neutron and proton deformation lengths, $\delta_\lambda^{(n,p)}$, can be disentangled as described in Refs. [4]. The corresponding neutron and proton multipole transition matrix elements are

commonly written as [88],

$$M_{(n,p)} = \int_0^\infty r^{\lambda+2} \rho_{tr,\lambda}^{(n,p)} dr \quad (4.7)$$

where the phenomenological transition densities are derived using Bohr-Mottelson prescription [3], given by $\rho_{tr,\lambda}^{(n,p)} = -\delta_\lambda^{(n,p)} \frac{d\rho_{g.s.}^{(n,p)}}{dr}$. This leads to the collective model ratio, $M_n/M_p = \frac{N\langle r^{\lambda-1} \rangle \delta_\lambda^n}{Z\langle r^{\lambda-1} \rangle \delta_\lambda^p}$, which acts as a tool for identifying the relative participation of neutrons and protons in a surface vibration. Here, the underlying assumption is that proton and neutron densities are proportional to each other with Z and N factors, and the radial moments $\langle r^{\lambda-1} \rangle_{n,p}$ are taken over the g.s. densities. If the transitions are homogeneous mass vibrations, neutron and proton densities are expected to have the same radial shape and one would obtain $\delta_\lambda^n = \delta_\lambda^p$. Any deviation may imply inhomogeneity in a transition. Empirically, it is assumed that $\delta_\lambda^p \approx \delta_\lambda^{ch}$ and $\delta_\lambda^m \approx \frac{Zb_p\delta_\lambda^p + Nb_n\delta_\lambda^n}{Zb_p + Nb_n}$, where $b_{n(p)}$ are microscopic bare interactions of the external field/probe with the neutrons (protons) of the target. The net transition matrix element for an excitation can be commonly defined as $M = b_n M_n + b_p M_p$. The quantity b_n/b_p defines the ratio of the neutron and proton field strengths. As different probes have different sensitivities to proton and neutron contributions in the target nuclei, the b_n/b_p ratio is expected to be the source of discrepancy between the mass deformation lengths extracted using different probes.

For the interactions with the ⁷Li probe, the ratio b_n/b_p is deduced from the DFM calculations for the isoscalar and isovector parts of the effective nucleus-nucleus potential (defined in Eqn. 4.3), as $\frac{b_n}{b_p} = \frac{v_{IS} - v_{IV}}{v_{IS} + v_{IV}}$. This ratio is found to be ≈ 1 for the present case, with a much smaller isospin-dependent interaction compared to the isoscalar part. Using the results of $\delta_\lambda^{ch,m}$ from Table 4.2, the $\delta_\lambda^{n,p}$ and M_n/M_p values have been determined for the different Sn isotopes, as summarized in Table 4.7.

For the interactions with the ¹²C probe, the ratio b_n/b_p is taken to be unity (no

Table 4.7: Experimental values of δ_λ^n , δ_λ^p and M_n/M_p corresponding to $\lambda = 2, 3$ excitations in Sn isotopes, for the ${}^7\text{Li} + {}^{112,116,118,120,122,124}\text{Sn}$ systems.

Target	$\lambda = 2$					$\lambda = 3$				
	δ_2^p (fm)	δ_2^n (fm)	M_n/M_p	$B(E2)$ (e^2b^2)	$B(IS2)$ (e^2b^2)	δ_3^p (fm)	δ_3^n (fm)	M_n/M_p	$\dagger B(E3)$ (e^2b^3)	$B(IS3)$ (e^2b^3)
${}^{112}\text{Sn}$	0.702(35)	0.694(69)	1.25(12)	0.239(9)	0.241(28)	0.738(103)	0.453(93)	0.79(13)	0.087(12)	0.058(11)
${}^{116}\text{Sn}$	0.651(41)	0.659(70)	1.36(15)	0.207(6)	0.211(18)	*0.745(101)	0.392(71)	0.73(10)	*0.095(11)	0.053(08)
${}^{118}\text{Sn}$	0.645(33)	0.655(65)	1.41(09)	0.205(7)	0.214(18)	0.753(108)	0.434(95)	0.82(15)	0.097(14)	0.059(10)
${}^{120}\text{Sn}$	0.660(29)	0.629(73)	1.38(10)	0.215(9)	0.209(21)	0.717(129)	0.439(99)	0.91(15)	0.090(17)	0.057(11)
${}^{122}\text{Sn}$	0.615(31)	0.606(73)	1.46(11)	0.191(4)	0.189(15)	*0.655(103)	0.353(66)	0.82(11)	*0.077(12)	0.043(08)
${}^{124}\text{Sn}$	0.569(26)	0.558(68)	1.51(08)	0.165(4)	0.166(14)	0.632(087)	0.338(65)	0.85(13)	0.073(10)	0.040(07)

\dagger From Coulomb excitation measurement [23]

* Modified

isospin dependence in the probe-target interactions). Using the results of $\delta_\lambda^{ch,m}$ from Table 4.6, the corresponding $\delta_\lambda^{n,p}$ and M_n/M_p values have been determined for the different Sn isotopes and are summarized in Table 4.8.

Owing to the negligible differences between the b_n/b_p ratios for the ${}^7\text{Li}$ - and ${}^{12}\text{C}$ -induced excitations in the Sn isotopes, it may be said that the effect of probe-target interactions are effectively inconsequential on the extracted deformation lengths from inelastic scattering analysis. The origin of probe-dependence lies elsewhere.

Table 4.8: Experimental values of δ_λ^n , δ_λ^p and M_n/M_p corresponding to $\lambda = 2, 3$ excitations in Sn isotopes, for the ${}^{12}\text{C} + {}^{112,116,118,120,122,124}\text{Sn}$ systems.

Target	$\lambda = 2$					$\lambda = 3$				
	δ_2^p (fm)	δ_2^n (fm)	M_n/M_p	$B(E2)$ (e^2b^2)	$B(IS2)$ (e^2b^2)	δ_3^p (fm)	δ_3^n (fm)	M_n/M_p	$B(E3)$ (e^2b^3)	$B(IS3)$ (e^2b^3)
${}^{112}\text{Sn}$	0.709(39)	0.804(69)	1.41(18)	0.242(23)	0.251(25)	0.742(109)	0.684(093)	1.19(17)	0.087(12)	0.081(17)
${}^{116}\text{Sn}$	0.651(33)	0.693(72)	1.45(19)	0.206(20)	0.211(28)	0.763(083)	0.662(101)	1.21(21)	0.098(13)	0.090(19)
${}^{118}\text{Sn}$	0.649(25)	0.744(65)	1.58(16)	0.208(16)	0.246(31)	0.757(092)	0.617(095)	1.16(24)	0.097(17)	0.087(19)
${}^{120}\text{Sn}$	0.665(39)	0.718(63)	1.56(22)	0.217(28)	0.242(38)	0.720(115)	0.625(094)	1.29(28)	0.090(14)	0.082(16)
${}^{122}\text{Sn}$	0.615(28)	0.682(67)	1.63(18)	0.191(17)	0.216(30)	0.677(076)	0.584(085)	1.33(23)	0.082(14)	0.074(18)
${}^{124}\text{Sn}$	0.572(36)	0.621(71)	1.67(22)	0.167(20)	0.185(29)	0.655(107)	0.541(102)	1.31(32)	0.073(11)	0.067(14)

For strongly absorbed heavy-ion probes, only the surface region of the Sn nuclei contributes to the direct reaction processes so that the scattering cross section in the

regions of the Coulomb and nuclear fields is proportional to the respective matrix elements. The electric transition probability is directly related to the charge deformation, and in turn, the proton transition matrix element as $B(E\lambda)=|M_p|^2$. An analogous quantity related to homogeneous mass deformation of the nucleus is often defined, known as the isoscalar transition probability [67], assuming that neutrons and protons maintain their equilibrium density ratio of N/Z ,

$$B(IS\lambda) = \left(\frac{Z}{A}\right)^2 |M_n + M_p|^2 \quad (4.8)$$

Using the present results of M_n/M_p , the $B(E\lambda)$ and $B(IS\lambda)$ values have been determined for the Sn isotopes and are reported in Table 4.7 for the ⁷Li-induced transitions and in Table 4.8 for the ¹²C-induced transitions. It is noteworthy that the $B(E2)$ and $B(E3)$ values are found to be enhanced, by factors of $\sim 9-15$, and $\sim 11-18$, respectively, over the standard Weisskopf single-particle estimates for the Sn isotopes (see Table 1.1), thereby indicating collective excitations. The probe-dependence of the M_n/M_p values is also shown in Fig. 4.13. The errors on all the above quantities are assigned by propagating the errors on the corresponding δ_λ^{ch} and δ_λ^m values extracted from the model calculations. Since the Sn isotopes are proton-shell-closed and the $\lambda = 2, 3$ transition probabilities are found to be substantially enhanced over the single-particle estimates, it is conventionally expected that the excitations would be strongly dominated by the neutron collectivity and its consequent polarization of the proton core, thereby leading to large M_n/M_p ratios, at variance with the phenomenological homogeneous N/Z trend (represented by the solid line in Fig. 4.13). With the ¹²C probe [90], both the $\lambda = 2$ and $\lambda = 3$ transitions are observed to closely follow, within errors, the N/Z trend with nearly similar $B(E\lambda)$ and $B(IS\lambda)$ values. For $\lambda = 2$, the M_n/M_p ratios (triangles up) are slightly enhanced over N/Z - an enhancement in neutron collectivity is observed. For transition to the 3_1^- state in each Sn isotope, the ratios are found to be sup-

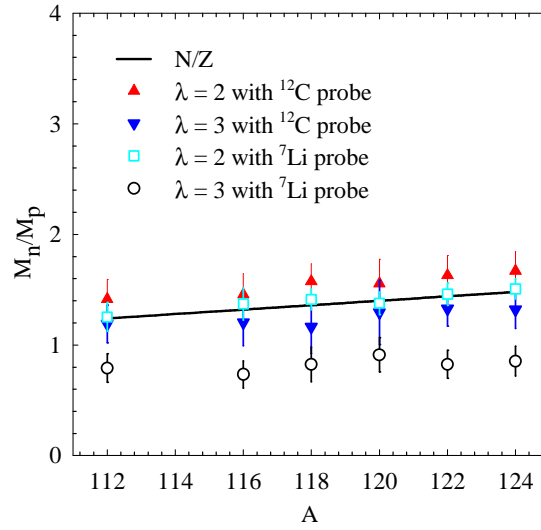


Figure 4.13: The M_n/M_p ratios for low-lying $\lambda = 2$ (triangles up) and $\lambda = 3$ (triangles down) excitations in Sn isotopes probed by ^{12}C nucleus. The hollow squares and circles represent the corresponding results with the ^7Li projectile [89]. The solid line shows the homogeneous value of N/Z .

pressed compared to the N/Z line, shown as triangles down. Results obtained using the complementary probe having an unpaired nucleon, ^7Li [89], show a significant deviation in M_n/M_p from N/Z for the $\lambda = 3$ transition (hollow circles) in all Sn isotopes. This hints at a possible inhomogeneity for the octupole excitation in Sn when probed using ^7Li . For the $\lambda = 2$ transition in each isotope, nearly similar neutron collectivity is observed with both the probes. In a nutshell, under the approximation that neutron and proton transition densities homogeneously scale as N/Z , the two sets of measurements predict different M_n/M_p ratios for all the Sn isotopes.

4.5 Intrinsic deformation lengths

In the previous section, it has been seen that the ratio $\frac{b_n}{b_p}$ for the Sn isotopes is not grossly different between the heavy-ion probes ^7Li and ^{12}C . Consequently, the spin and isospin dependence of probe-target interaction is expected to weakly affect the

structural information derived from heavy-ion scattering measurements. Since the net effects of all couplings are manifested in the optical potential, the size (radius parameter) and shape of which are the result of a convolution of projectile and target sizes and properties, the effect of probe-size is another factor that is expected to contribute towards the discrepant transition rates observed in Sn isotopes. The reduced value of δ_λ^m may reflect the finite size of the projectile smearing out the deformation of the target nucleus.

For nuclear inelastic scattering from statically-deformed nuclei, Hendrie [91] suggested a simple procedure for removing the effects of finite projectile size in the extraction of nuclear potential shapes. This model leads to geometric relationships that have immediate application. The prescription can also be extended to nuclei with vibrational modes of excitations. Here, the underlying assumption is that the probes and the targets interact only at their mutual sharply defined surfaces. With the centre of mass at the origin of the body-fixed frame and an axially symmetric shape, the edge of a spherical nucleus of radius R_0 deformed by quadrupole and octupole vibrations can be written as:

$$\begin{aligned} R(\theta) &= R_0 [1 + \beta_{20}Y_{20}(\theta) + \beta_{30}Y_{30}(\theta)] \\ &\equiv R_0[1 + \varepsilon(\theta)] \end{aligned} \tag{4.9}$$

When a projectile of size (radius) Δ probes the dynamically deformed target surface, the locus of the center of the projectile describes a surface with radius [82,91],

$$r(\theta) = r_0 + \delta_2(\Delta)Y_{20}(\theta) + \delta_3(\Delta)Y_{30}(\theta) \tag{4.10}$$

Here, r_0 characterizes the spatial extension of the optical potential, and defines the potential radius for the target nucleus in its ground state. The quantities $\delta_\lambda(\Delta)$ are the experimentally determined deformation lengths for target excitation of mul-

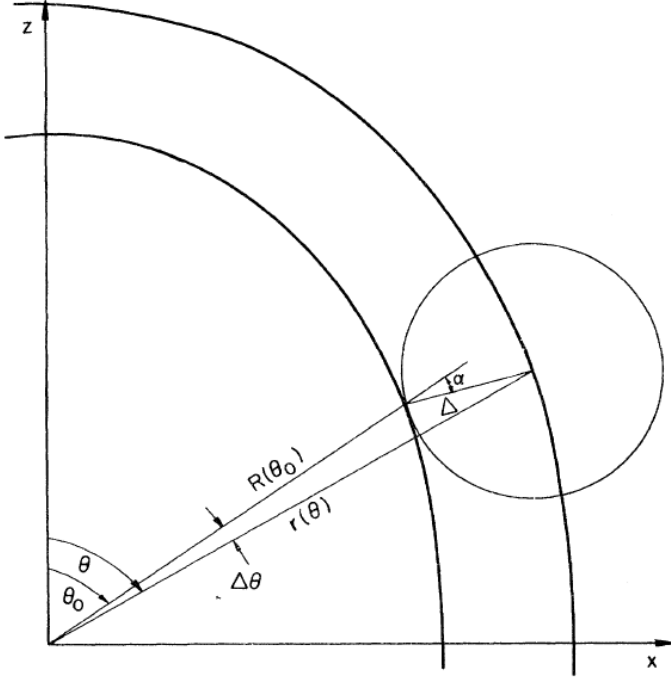


Figure 4.14: Geometric quantities as described in the text [91]. $R(\theta)$ defines the nuclear edge, and Δ is the radius of the probe.

tipolarity λ . From the construction of Fig. 4.14, differential geometry leads to $\tan \alpha = \frac{-R'(\theta_0)}{R(\theta_0)} = \frac{-\varepsilon'(\theta_0)}{1+\varepsilon(\theta_0)}$, where α defines the angular difference between the direction of $R(\theta_0)$ and the normal to the nuclear surface at θ_0 . Using trigonometric relations, $r^2(\theta) = R^2(\theta_0) + \Delta^2 + 2\Delta R(\theta_0) \cos \alpha$, and $\frac{\sin(\Delta\theta)}{\Delta} = \frac{\sin \alpha}{r(\theta)}$, and to lowest order in the deformation parameters, one obtains $\alpha \approx \varepsilon'(\theta_0) \equiv \varepsilon'(\theta)$ and $\Delta\theta \approx \frac{-\Delta}{R_0 + \Delta} \varepsilon'(\theta)$. This leads to

$$r(\theta) = R_0 + R_0 \varepsilon(\theta) + \Delta + \frac{1}{2} \frac{R_0 \Delta}{R_0 + \Delta} \varepsilon'(\theta)^2 \quad (4.11)$$

On comparing Eqns. 4.10 and 4.11,

$$\delta_\lambda(\Delta) = \delta_\lambda(0) + \frac{1}{2} \frac{R_0 \Delta}{R_0 + \Delta} \int Y_{\lambda 0} \varepsilon'(\theta)^2 d\Omega \quad (4.12)$$

where $\delta_\lambda(0) \equiv \beta_{\lambda 0} R_0$ defines the intrinsic nuclear deformation length. The quantities Δ and R_0 are considered to be measures of the point-matter radii for the probes and the targets, respectively.

For the vibrational Sn nuclei, the 2_1^+ and 3_1^- states have been studied with a variety of projectiles for which the deformation lengths can be written as functions of the probe size Δ ,

$$\delta_2(\Delta) = \delta_2(0) + \frac{R_0\Delta}{R_0 + \Delta} (0.270\beta_{20}^2 + 0.756\beta_{30}^2) \quad (4.13)$$

$$\delta_3(\Delta) = \delta_3(0) + \frac{R_0\Delta}{R_0 + \Delta} (0.505\beta_{20}\beta_{30}) \quad (4.14)$$

Combining the results for $\delta_\lambda(\Delta)$ of the present work using ^7Li , ^{12}C probes with the ones from the existing measurements using other probes such as p [41], d [92], ^3He [93], α [20], ^6Li [94] and ^{10}B [95], a systematic analysis has been made over a range of Δ values. Since the transition characteristics in the Sn isotopes usually have been inferred only by determining the $B(E\lambda)$ or δ_λ^{ch} values, for such measurements that do not explicitly report mass (or potential) deformation parameters, a value of $\delta_\lambda^m(\Delta) \approx \delta_\lambda^{ch}(\Delta)$ has been assumed. Using eqns. (4.13) and (4.14), the parameters $\delta_2(0)$ and $\delta_3(0)$ are obtained as the unweighted averages from the best-fit curves to the experimental values of $\delta_2(\Delta)$ and $\delta_3(\Delta)$, respectively, and provide probe-independent intrinsic $\lambda = 2$ and $\lambda = 3$ matter deformation lengths for the Sn isotopes. The results are summarized in Table 4.9 and in Fig. 4.15.

With same radial shape for the intrinsic neutron and proton density deformations, one can write the ratio of their corresponding transition matrix elements as:

$$\frac{M_n}{M_p} = \frac{\delta_\lambda(0)}{\delta_\lambda^{ch}} \left(1 + \frac{N}{Z}\right) - 1 \quad (4.15)$$

with δ_λ^{ch} taken from Table 4.2. The results are shown in Table 4.9 and also in Fig. 4.16 as circles and squares for the $\lambda = 2$ and $\lambda = 3$ transitions, respectively. This approach shows that neutron collectivity is the dominant contribution to the 2_1^+ and 3_1^- target excited states, as may be expected in proton-magic isotopes. Interestingly, the evolution of these ratios shows that the trend of core-proton collectivity (as given

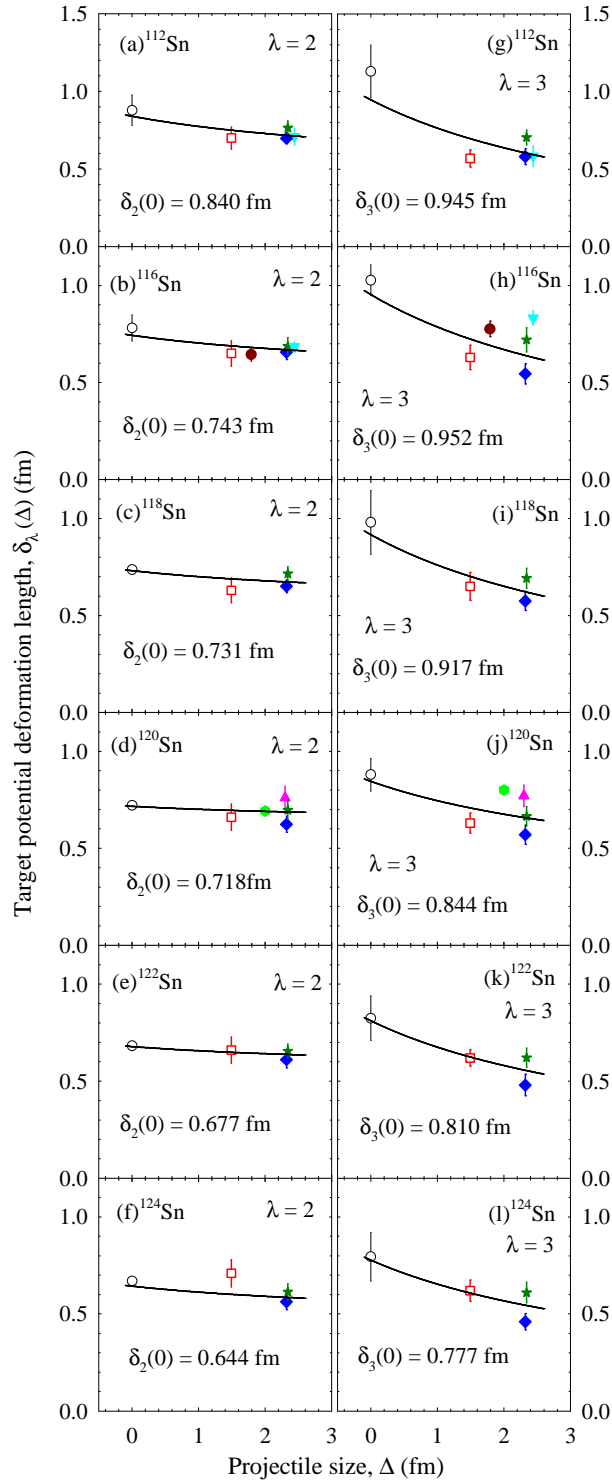


Figure 4.15: Nuclear inelastic scattering deformation lengths for the (a-f) $\lambda = 2$ and (g-l) $\lambda = 3$ excitations in Sn isotopes as a function of probe size Δ . The measurements are with a variety of probes such as p (hollow circles) [41, 42], d (hexagons) [92], ${}^3\text{He}$ (filled circles) [93], α (squares) [20], ${}^6\text{Li}$ (filled triangles down) [94], ${}^7\text{Li}$ (diamonds) [89], ${}^{10}\text{B}$ (filled triangles up) [95], and ${}^{12}\text{C}$ (stars; present work). The curves are best fits to eqns. (4.13) and (4.14).

by the $B(E2)$ and $B(E3)$ values in Tables 4.7 and 4.8) differs from the neutron one. Clearly, the two transition densities do not simply scale as N/Z as often assumed in the homogeneous collective model, and this has quantitative consequences as reflected in the much larger M_n/M_p ratios. It may be surmised that the effect of probe size is apparently the major factor leading to discrepant deformation lengths. The present results for the $\lambda = 2$ transition are found to be in good agreement with those obtained from a systematic study of M_n/M_p for single-closed-shell nuclei reported in Ref. [4].

Table 4.9: Intrinsic nuclear deformation lengths and M_n/M_p ratios for the $\lambda = 2, 3$ transitions in the Sn isotopes.

Nucleus	$\lambda = 2$		$\lambda = 3$	
	$\delta_2(0)$ (fm)	M_n/M_p	$\delta_3(0)$ (fm)	M_n/M_p
^{112}Sn	0.840(102)	1.67(24)	0.945(201)	1.84(38)
^{116}Sn	0.743(068)	1.69(17)	0.952(172)	1.88(31)
^{118}Sn	0.731(083)	1.67(20)	0.917(148)	1.85(29)
^{120}Sn	0.718(096)	1.62(22)	0.844(121)	1.82(25)
^{122}Sn	0.677(059)	1.68(14)	0.810(122)	1.91(28)
^{124}Sn	0.644(078)	1.76(18)	0.777(134)	1.92(30)

The results have been compared with microscopic calculations employing quasi-particle random phase approximation (QRPA) [96] within the quasiparticle-phonon model [97] (dashed and dash-dot-dotted lines in Fig. 4.16) that account for the collectivity in Sn isotopes as largely caused by the neutrons. In this approach, each orbit is treated a mixture of particle and hole degree of freedom, recognized by an occupation number : a quasiparticle state. Vibrational modes are treated as transitions between states generated via between coherent combinations of quasiparticle excitations. The QRPA approach leads to larger ratios for the $\lambda = 2$ transition as neutron number increases, while the trend is in decent agreement with the extracted intrinsic ratio for the $\lambda = 3$ transition.

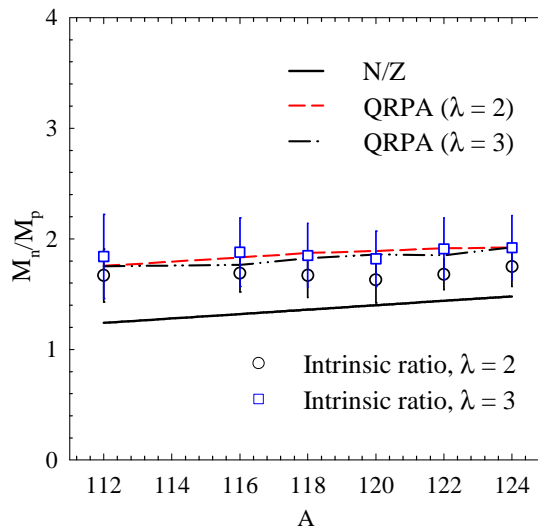


Figure 4.16: Intrinsic M_n/M_p ratios for low-lying excitations in Sn isotopes corresponding to $\lambda = 2$ (circles) and $\lambda = 3$ (squares) transitions. The solid line shows the homogeneous trend of N/Z . The dashed and dash-dot-dotted lines represent the results of QRPA calculations for 2_1^+ and 3_1^- transitions, respectively [96].

Effective charges for neutron and proton

A precise estimate of the intrinsic M_n/M_p ratio allows the determination of neutron and proton effective charges to be used in shell model calculations for transition rates and related observables. The value of the effective charges is dependent on the size of the shell model space describing the transitions and the type of effective interaction that operates within this space. In single-closed-shell nuclei such as the Sn isotopes, effective charges reflect the strength of the coupling between the motion of the valence nucleons and the virtual excitations of the core nucleons. The matrix elements M_n and M_p can be written in terms of valence-space matrix elements, M'_n and M'_p , and the core-polarization contributions, as [5]

$$M_n = M'_n(1 + \delta^{nn}) + M'_p\delta^{np} \quad (4.16)$$

$$M_p = M'_n\delta^{pn} + M'_p(1 + \delta^{pp}) \quad (4.17)$$

Here, δ_{xy} defines the core-polarization parameter corresponds to core x 's polarized by valence y 's. It essentially accounts for the coupling of nucleons y to the virtual excitations of the core nucleons x . By convention, $\delta^{pp} = \delta^{nn}$. These core-polarization parameters are connected to the electromagnetic effective charges as $e_n = \delta^{pn}$ and $e_p = 1 + \delta^{pp} = 1 + \delta^{nn}$. Since Sn isotopes have no valence protons, this leads to $M'_p = 0$, or

$$\frac{M_n}{M_p} = \frac{1 + \delta_{nn}}{\delta_{pn}} \equiv \frac{1 + \delta_{pp}}{\delta_{pn}} = \frac{e_p}{e_n} \quad (4.18)$$

From the results reported in Table 4.9, it may be surmised that a value of proton effective charge approximately a factor of nearly two larger than the neutron effective charge in shell model calculations is expected to satisfactorily accord for both $\lambda = 2, 3$ excitations along the Sn-isotopic chain. A recent work on Monte Carlo shell model calculations for the ^{100–138}Sn isotopes [98] gives an adequate reproduction of the measured $B(E2)$ trend with $e_p/e_n = 1.7$, in good agreement with the value proposed from the intrinsic M_n/M_p ratios above.

4.5.1 Quantifying the effect of probe-target interaction

The cumulative effect of probe-size and probe-target interaction is contained in the δ_λ^m values extracted in each measurement with a different projectile. Once the effect of the projectile size is eliminated, and the proton and neutron distributions are considered to have same radial shape in collective vibrations, the ratio $\frac{\delta_\lambda^m}{\delta_\lambda^{ch}} \approx \frac{1 + \frac{b_n}{b_p} \frac{M_n}{M_p}}{1 + \frac{b_n}{b_p} \frac{N}{Z}}$, defined in §4.4, is expected to accentuate the effect of solely the nature of interaction between the probe and the target, surmised by the corresponding b_n/b_p ratio. For the proton induced reactions, Ref. [4] puts $b_n/b_p = 3$, while for the isoscalar projectiles such as $\alpha, ^{12}\text{C}$, one obtains $b_n/b_p = 1$. Using the veritable M_n/M_p values for the Sn isotopes as reported in Table 4.9, one obtains a difference of mere $\approx 5\%$ between the $\frac{\delta_2^m}{\delta_2^{ch}}$ ratios, and a corresponding difference of $\approx 10\%$ between the $\frac{\delta_3^m}{\delta_3^{ch}}$ ratios, from the proton and heavy-ion induced excitations. Thus, for the projectiles considered in the

present study, the crucial factor for the extraction of intrinsic deformation lengths of the Sn isotopes is the removal of finite probe size. Thereafter, one observes that the effect of the nature of probe-target interaction is rendered insignificant.

4.6 Summary & Conclusions

A systematic study of the characteristics of the 2_1^+ and 3_1^- excited states in $^{112,116,118,120,122,124}\text{Sn}$ is presented, by means of heavy-ion inelastic scattering using two different probes ^7Li and ^{12}C , at $E_{\text{c.m.}}/V_{\text{B}} \approx 1.3$. The deformation lengths and transition probabilities are extracted via extensive CDCC as well as CRC calculations employing the collective model approach. Under the phenomenological approximation that neutron and proton transition densities scale as N/Z in collective excitations, disagreements are seen between the results of ^7Li - and ^{12}C -induced excitations in all the Sn isotopes. A prescription to remove the effects of projectile size is used to deduce the intrinsic mass deformation length for each isotope. The results indicate that neutron collectivity is the dominant contribution to the 2_1^+ and 3_1^- excited states in the Sn isotopes, as may be expected in proton-magic nuclei. The effect of size of the probe is the dominant factor that leads to discrepant transition rates; the effect of the nature of probe-target interaction is secondary (and meagre).

Chapter 5

Measurement of the 2_1^+ level lifetime in ^{120}Sn

In the previous chapter, systematic measurements of the low-lying quadrupole and octupole transitions in the $^{112,116,118,120,122,124}\text{Sn}$ isotopes, induced by heavy-ion inelastic collisions, have been discussed. The corresponding $B(E2)$ and $B(E3)$ values are found to be significantly enhanced over the single-particle estimates. Even though the Sn isotopes are proton-magic, the enhanced $B(E\lambda)$ values are suggestive of polarization and virtual excitations of the shell-closed proton core, induced by the valence neutrons. In a complementary approach, the $B(E\lambda)$ values can also be determined if the spin and parity of the states involved, the γ -decay branching ratio and the mean lifetime, τ , of the excited state are known.

It has been suggested that the matrix elements for excitation in a direct interaction model of heavy-ion scattering are closely analogous to those for electric multipole radiation between the same two states (see §1.2). In this regard, the transition probabilities reported in the previous chapter are in satisfactory accord with those measured by Allmond *et al.* [37] from Coulomb excitation cross sections. However, existing estimates for 2_1^+ level lifetime in the Sn isotopes indicate reduced collectivity,

with discrepant results, remarkably for the most abundant ^{120}Sn isotope. In addition to the measurements reported by Jungclaus *et al.* [34], few other measurements exist for the lifetime for ^{120}Sn . Sie *et al.* [99] measured γ -rays emitted from excited levels of ^{120}Sn in coincidence with backscattered ^{35}Cl projectiles, leading to $\tau_{2_1^+} \sim 1$ ps, and report that a comparison of their lifetime with values inferred from absolute Coulomb excitation cross sections indicated a discrepancy, with their value being longer. An older measurement of $\tau_{2_1^+} = 1.26$ ps by nuclear γ -ray resonance absorption method [100] also puts the $B(E2)$ value in the region of much lower collectivity. This result is in contrast to a complementary measurement [101] of angular distribution of photon scattering cross section that reports a very high $B(E2)$ for ^{120}Sn . To address the large disagreements among a series of existing measurements and at the same time, verify the validity of the electric transition probabilities deduced from heavy-ion induced scattering in this thesis work, a revisited measurement of level lifetime of the 2_1^+ state in ^{120}Sn with updated techniques is thus warranted. The exercise is expected to facilitate concluding on the lifetime of the 2_1^+ state and, thus, the $B(E2, 0_{g.s.}^+ \rightarrow 2_1^+)$ value determined therefrom. Existing estimates put the lifetime of the 2_1^+ state in the sub-picosecond region, and hence, needs to be probed with a suitable technique that optimizes the conditions required for accurate measurement.

5.1 The Doppler Shift Attenuation Method

Nuclear excited levels exhibit a range of lifetimes that can be probed by different experimental techniques. In the μs to ns range, or even higher, the lifetimes are usually measured with electronic-timing techniques. For short lifetimes in the range of $< \mu\text{s}$ to ps, Doppler-shift methods are commonly used. These techniques utilise the fact that after a nuclear reaction has occurred, the velocity of a recoiling nucleus in an excited state may be obtained, at the moment of the γ -ray decay of the state, by measuring the Doppler shift of the photopeak energy. For even shorter lifetimes, < 1

fs, x -ray coincidence techniques are commonly used, which compare the timescale of the nuclear decay process to the time taken by the nucleus to traverse an atomic spacing in a crystal. Over several years, the Doppler Shift Attenuation Method (DSAM) has been customarily adopted for measuring lifetimes of short-lived levels in the sub-picosecond regime [102, 103], and is one of the most prolific nuclear lifetime techniques. The level lifetime, τ , is compared with the slowing down/stopping time, τ_{stop} , of the recoiling nucleus in the backing media, typically of the order of 10^{-12} – 10^{-14} s over a range of materials. If the lifetime is long compared to the stopping time, the nucleus emits after coming to rest and one does not observe any Doppler effect. As the stopping time competes with the level lifetime, one typically measures an ‘attenuated’ Doppler shift characterized as either (i) a partial shift in the peak (centroid) energy (for $\tau < \tau_{\text{stop}}$), or (ii) a peak at the actual energy with an accompanying lineshape (for $\tau \sim \tau_{\text{stop}}$). This method has found extensive use in studies of light nuclei where the principal experimental goal has been the measurement of γ -ray centroid shifts. With heavy-ion induced reactions facilitating high recoil velocities, combined with usage of high resolution Ge-detectors with small instrumental linewidths, this method has been employed to investigate the detailed shapes of Doppler-broadened γ -ray lines in heavier nuclei.

In the present work, the 2_1^+ level in ^{120}Sn ($E_x = 1171$ -keV) has been populated by means of inelastic excitation by the ^{32}S projectile. Once populated, the state remains excited for a mean lifetime $\tau_{2_1^+}$. A more common decay process that competes with γ -decay of any multipolarity is emission of conversion electrons. The probability of this process is proportional to the density of electrons in the element, and thus, is more important for higher- Z nuclei. Further, since the process competes with γ -decay, levels in which the lifetime is long are more likely to decay by electron emission. Therefore, for low-energy or high-multipolarity transitions, the conversion process will be large and may be the dominant decay mode. The $2_1^+ \rightarrow 0_{\text{g.s.}}^+$ ($\lambda = 2$) decay is

known to have nearly 100% γ -branching [104]. A scattering event induced by a heavy beam facilitates a large momentum transfer, and substantial Doppler-broadening of the measured γ -energies. The broadening of the γ -rays emitted in-flight depends on the direction of emission of radiation, $\Phi_\gamma = (\theta_\gamma, \phi_\gamma)$, relative to the recoil direction, and on the instantaneous recoil velocity (β_{rec}) at the moment of emission as,

$$E_\gamma(\Phi_\gamma) = E_\gamma^0 (1 + \beta_{\text{rec}}(t) \cos \Phi_\gamma) \quad (5.1)$$

where E_γ^0 is the unshifted decay energy (1171-keV). The cardinal component of such an analysis is the simulation of the slowing down process for the recoils of interest in the target and/or the backing media. The trajectories and velocity profiles of the recoiling nuclei are used to reconstruct the observed Doppler shift/shape, which is sensitive to the interplay between the level-lifetime and the recoil stopping time. This requires calculation of the corresponding stopping powers and the same has been identified as one of the principal uncertainties in the extracted lifetime in DSAM. In fact, it may be stated that the level lifetimes can be determined only as accurately as the stopping powers; a precise estimation of the average value of τ_{stop} leads to reduced ambiguities in optimizing the value of the lifetime, τ , from the Doppler analysis method. Traditionally the method is pursued with a thin target for production of nuclei of interest, on a thick elemental backing material wherein the entire slowing down process is perceived to occur. The present work uses an aberrant thick target, which contributes both to the production of the recoils as well as their subsequent slowing down. All current approaches to the extraction of realistic lifetime information from inelastic excitation of ^{120}Sn ions recoiling in thick media are based on the framework of energy losses of ions in matter and the subsequent Doppler-broadened lineshape modelling and analysis, the success of which has been well documented, particularly for fusion-evaporation reactions in the domain of simulating the stopping process by incorporating the fine details of

nuclear reaction kinematics and energetics [105, 106].

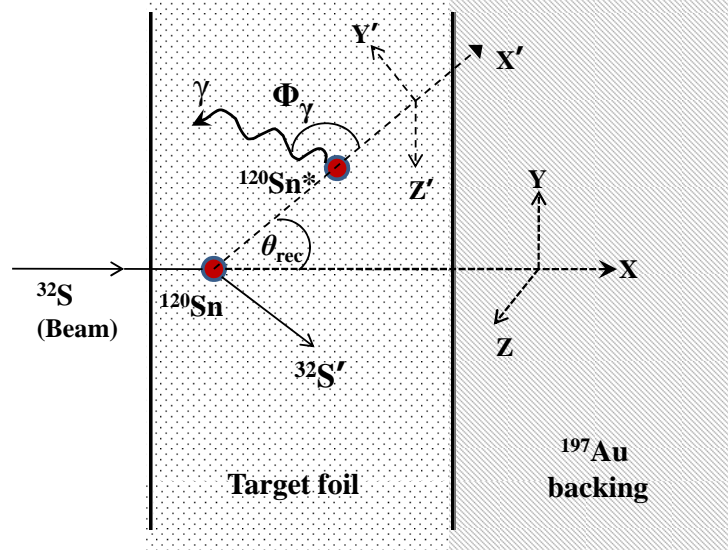


Figure 5.1: Schematic representation of inelastic scattering $^{120}\text{Sn}(^{32}\text{S}, ^{32}\text{S}')^{120}\text{Sn}^*$ producing ^{120}Sn recoils in their 2_1^+ excited state. The recoils emit in-flight during the slowing-down process, leading to Doppler-affected γ -rays.

5.2 γ -decay from excited levels in ^{120}Sn

A schematic diagram of the experimental setup is shown in Fig. 2.7 of Chapter 2. The detectors were calibrated in energy and efficiency using standardized ^{133}Ba - ^{152}Eu source. A resolution of ≈ 2.6 keV was obtained at an energy of 1408 keV. Beam energy ($E_{\text{lab}} = 120$ MeV) below the Coulomb barrier ($V_B \approx 123$ MeV) was chosen on the basis of coupled reaction channels calculations (i) to minimize the contribution of the nuclear field in the excitation process, (ii) to have substantial inelastic scattering cross section for the excitation of the 2_1^+ state in ^{120}Sn , (iii) to suppress the excitation of higher energy states (such as higher multiplicities and/or multiphonon excitations) that could feed the nuclear level of our interest, and (iv) to minimize contamination from other reaction channels such as transfer of nucleon(s) and fusion ($\sigma_F < 1$ mb). Thus, inelastic scattering process in a binary reaction system facilitates to optimize the conditions required for accurate measurements of

the transition characteristics. The excitation was governed by well defined two-body kinematics and energetics, and predominantly mediated by the Coulomb interaction between the collision partners.

5.2.1 Distribution of inelastically scattered ^{120}Sn nuclei

From kinematic considerations of an inelastic scattering event in a binary collision between a projectile, P , and stationary target, T , (see Fig. 5.1), momentum and energy conservation constraints lead to the laboratory kinetic energies of the scattered projectile, E' , and recoiling target nucleus, E_{rec} , as,

$$E' = \frac{M_P^2 E_{\text{lab}}}{(M_P + M_T)^2} \left(\cos \theta_P + \left[\left(\frac{M_T^2}{M_P^2} \right) \left(1 + \frac{M_P Q}{M_T (E_{\text{lab}} + Q)} \right) \left(\frac{E_{\text{lab}} + Q}{E_{\text{lab}}} \right) - \sin^2 \theta_P \right]^{\frac{1}{2}} \right)^2 \quad (5.2)$$

$$E_{\text{rec}} = \frac{M_P M_T E_{\text{lab}}}{(M_P + M_T)^2} \left(\cos \theta_{\text{rec}} + \left[\left(1 + \frac{M_P Q}{M_T (E_{\text{lab}} + Q)} \right) \left(\frac{E_{\text{lab}} + Q}{E_{\text{lab}}} \right) - \sin^2 \theta_{\text{rec}} \right]^{\frac{1}{2}} \right)^2 \quad (5.3)$$

Here, $\sin \theta_{\text{rec}} = \sqrt{\frac{M_P E'}{M_T E_{\text{rec}}}} \sin \theta_P$, with the scattered projectile covering the angular range $0^\circ < \theta_P < 180^\circ$. This restricts the angular distribution of the excited recoils to the range $0^\circ < \theta_{\text{rec}} < 90^\circ$ (extended range of γ -decay positions).

Ideally, one prefers that the nuclei recoil in one specified direction with a unique velocity (or in a narrow cone centred on the beam direction with a small spread in velocity). The average value of $\cos \theta_{\text{rec}}$ will be zero if the emission of outgoing particles is symmetric about 90° in the centre-of-mass system. Reactions which proceed via compound nucleus formation (a statistical process) satisfy this condition, but inelastic scattering does not. This is often remedied by detecting the outgoing projectile-like particle in coincidence with the emitted γ -rays, which fixes the recoil velocity in the laboratory frame. However, one must compromise on counting statistics in such an experimental setup, owing to the low detection efficiency of Ge-detectors. It is therefore desirable to design experiments that make use of direct (singles) spectra from Ge-detectors, without coincidence requirements. The present

work attempts to decipher the lifetime of the 2_1^+ level from the inclusive singles mode, by incorporating the complete spread in recoil velocity across a wide angular range. The relative number of recoils scattered in a particular direction and with particular kinetic energy depends on the probability of such a directional scattering event - expressed in terms of the differential inelastic scattering cross section. The analysis of Doppler shapes following γ -ray measurements in singles mode, where the angular distribution of the recoiling ions is given by inelastic scattering theory, bears the advantage of improved counting statistics when compared to a coincidence measurement for $E_{\text{lab}} < V_{\text{B}}$, where the spectra are less populated. Nordhagen *et al.* [107] and Stokstad *et al.* [108] have successfully demonstrated the measurement of lifetimes of several levels in ^{59}Co , ^{63}Cu , ^{150}Nd and ^{152}Sm by means of lineshape analysis on direct singles gamma radiation spectra, to be in good agreement with those from independent measurements.

In the direct singles spectra as shown in Fig. 5.2, a distinct structure of γ -ray lineshape for the E2 transition in ^{120}Sn was observed from the de-excitation of the 2_1^+ state, with photopeak energy 1171 keV. Owing to wide angular coverage of ^{120}Sn recoils as permitted by kinematics (see inset of Fig. 5.2), each HPGe detector recorded an inclusive decay spectrum for scattering at all possible recoil directions. The consequent Doppler-broadened lineshape extends to both higher and lower energies in the vicinity of the stopped peak, on account of a wide distribution in θ_γ (see Eqn. 5.1). The γ -rays are emitted in-flight, with the recoiling ^{120}Sn nuclei in relative motion with respect to the detectors in the array, and thus, exhibit Doppler effect as expected. The heavy ^{32}S beam facilitated large excitation probability of the target, and imparted substantial recoil velocity ($v_{\text{rec}}/c > 2\%$) to the scattered nuclei. This manifested into larger Doppler-broadening of the emitted gamma rays, thereby reducing the uncertainty in predicting the lifetime from lineshape analysis based on the modelling of the slowing-down process of the recoils in the target-plus-backing

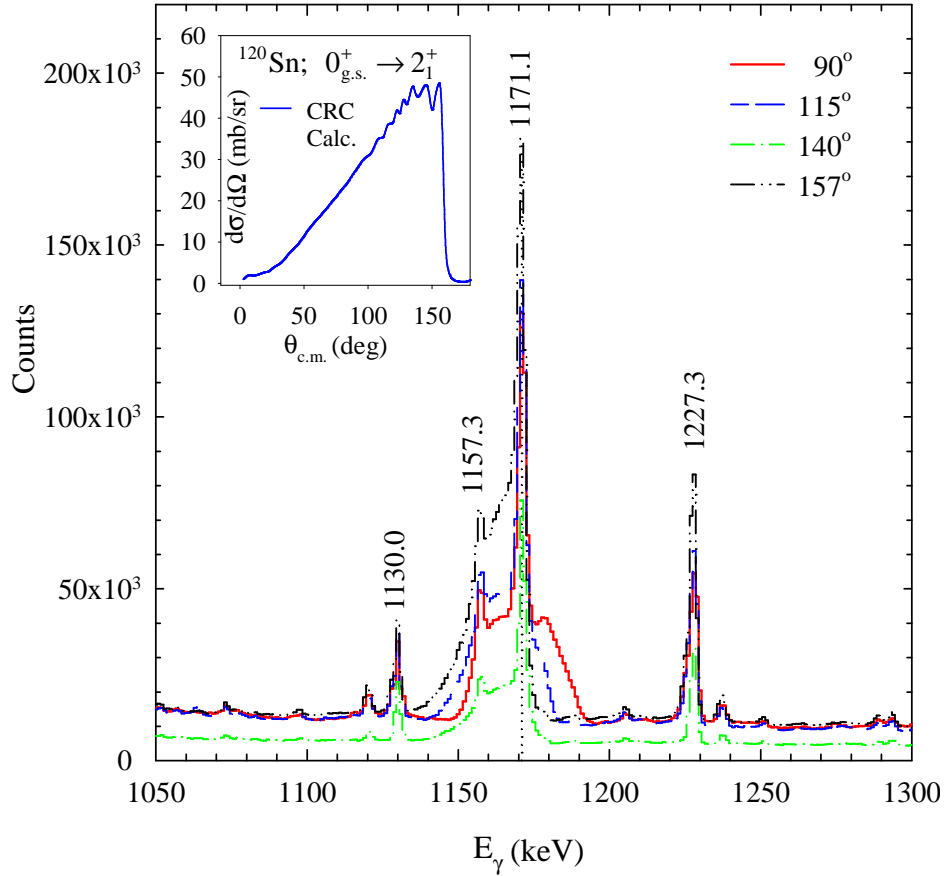


Figure 5.2: Raw γ -ray spectra recorded in HPGe clovers at different angular positions in the lab frame, for the $^{32}\text{S}+^{120}\text{Sn}$ system. The most dominant transition corresponds to the decay of the 2_1^+ excited state of ^{120}Sn at 1171 keV. Inset shows the calculated angular distribution of the scattered ^{120}Sn nuclei in the centre-of-mass frame (the moving source for the decay), at $E_{\text{lab}} = 120$ MeV.

material.

The decay peak had a stopped component at the actual energy and a pronounced accompanying shape, which confirms that the lifetime being probed is comparable with the slowing down time of the Sn recoils in the target/backing material. As ^{32}S is a spherical nucleus with well defined excited states beyond 2 MeV, any contaminant γ -energies in the spectra, arising from projectile excitation, are avoided.

The origin of the additional stopped peaks observed along with the E2 lineshape from ^{120}Sn (Fig. 5.2) are ascertained from coincidence analysis of a symmetric $E_\gamma - E_\gamma$ matrix for the detector array. These γ -energies could be ascribed to the de-exciting

residues produced in the fusion-evaporation reaction of the ^{32}S beam with oxygen present in the partially oxidized ^{120}Sn target. The dominant products of such a reaction include ^{39}K , ^{42}Ca , ^{43}Sc etc., as indicated in statistical model calculations with the PACE [109] code as well as in experimental data on the decay of the same compound nucleus (^{48}Cr) [110] at nearly overlapping excitation energies. The 1227 keV peak, for instance, is presumably from the decay of residual nuclei ^{42}Ca and ^{43}Sc , while the most probable source for the 1130 keV energy can be attributed to a long lived state ($\tau \sim 12$ ps [111]) in ^{39}K . Most importantly, the 1157.3 keV stopped peak riding on the lineshape of the E2 transition from ^{120}Sn is confirmed to be from the decay of a long-lived state ($\tau \approx 8.1$ ps [112]) of ^{43}Sc , with no contribution to the observed low energy tail of the shape corresponding to the E2 decay from in ^{120}Sn , and is not expected to affect the subsequent analysis or the results therefrom. The absence of any other rogue γ -peak under the lineshape is also verified.

5.3 Lineshape Modelling

Lifetime analysis of the 2_1^+ state in ^{120}Sn has been carried out using the developments by Das *et al.* [105] in conjunction with the LINESHAPE [113] package. The analysis principally incorporates the trajectories of the scattered (^{120}Sn) nuclei traversing in the target and the backing media wherein additional considerations consequent to the use of thick target are appropriately imbibed. This involves (i) the kinematics of the excitation process in the reaction plane, (ii) the structure of the thick target and backing foils, (iii) the evolving energy of the beam, and the consequent angular distribution of the inelastic scattering cross section along the target depth, and (iv) the energy-angle distribution of the recoiling nuclei.

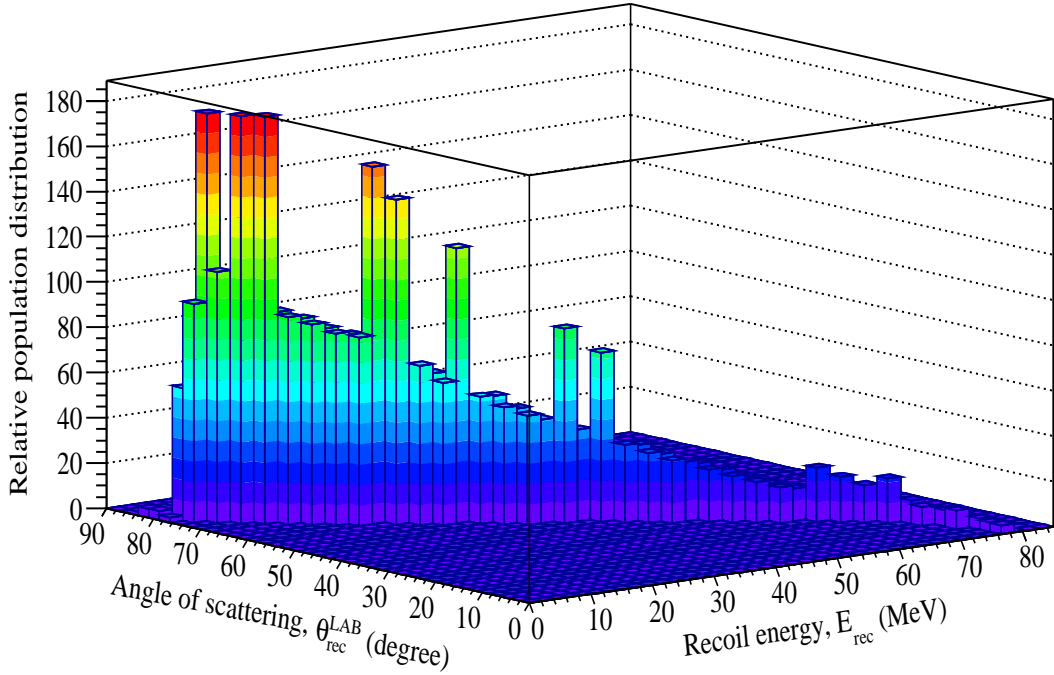


Figure 5.3: Typical calculated relative population distribution of the scattered ^{120}Sn recoils in their 2_1^+ excited state as a function of laboratory scattering angle $\theta_{\text{rec}}^{\text{LAB}}$ and kinetic energy E_{rec} , in the $^{32}\text{S} + ^{120}\text{Sn}$ system at $E_{\text{lab}} = 120$ MeV.

5.3.1 Evolution of the $0_{\text{g.s.}}^+ \rightarrow 2_1^+$ scattering cross section along the target depth

An estimate of the scattering cross section for inelastic excitation of ^{120}Sn nuclei to their 2_1^+ state in the $^{32}\text{S} + ^{120}\text{Sn}$ system is determined in the framework of the CRC model using FRESKO [57]. The calculations have been performed by coupling the major direct reaction channels to the entrance channel, such as (i) the low-lying 2_1^+ and 3_1^- states of ^{120}Sn at excitation energies 1.171 MeV and 2.401 MeV, respectively, treated as collective vibrational one-phonon states with $B(E2; 0_{\text{g.s.}}^+ \rightarrow 2_1^+) = 0.21 \text{ e}^2\text{b}^2$ [37, 89, 90] and $B(E3; 0_{\text{g.s.}}^+ \rightarrow 3_1^-) = 0.09 \text{ e}^2\text{b}^3$ [23, 89, 90], (ii) the first-excited 2^+ state of ^{32}S lying at 2.231 MeV, with $B(E2; 0_{\text{g.s.}}^+ \rightarrow 2_1^+) = 0.033 \text{ e}^2\text{b}^2$ and static quadrupole moment $Q_S(2_1^+) = -0.20 \text{ b}$ [114], and (iii) transfer channels corresponding to pickup of neutron(s), ($^{32}\text{S}, ^{33}\text{S}$) and ($^{32}\text{S}, ^{34}\text{S}$), with unit spectroscopic factors. The coupling effects of excited states of ^{120}Sn with higher

multipolarities or of multiphonon nature on the excitation probability of the 2_1^+ state are also found to be negligible. For instance, the excitation probability of the 4_1^+ state at $E_x = 2.194$ MeV, coupled as a double-quadrupole phonon state, is found to be very poor. The projectile-target interaction is governed by the Coulomb potential as well as an optical nuclear potential of Woods Saxon form, with a short ranged imaginary part to account for the fusion cross section. The effect of nuclear coupling on the excitation of the 2_1^+ state in ^{120}Sn is found to be inconsequential, and the angular distribution of the scattering cross section is primarily governed by the Coulomb interaction. Subject to the calculated differential scattering cross section, the relative population distribution of the recoils along the reaction plane is estimated, as shown in Fig. 5.3.

Given the substantial thickness of the ^{120}Sn foil that leads to appreciable energy loss of the incident beam, and the energy dependence of scattering cross sections in heavy ion collisions, the evolution of the cross section with decreasing beam energy along the thickness of the target has been calculated. The CRC model predicts a rapid decline of the $0_{\text{g.s.}}^+ \rightarrow 2_1^+$ cross section as the beam energy reduces beyond 95 MeV in the inner layers of the target foil. Hence, it may be safely surmised that ≈ 3.2 mg/cm² of the target foil facing the beam is the effective production thickness that contributes to the population of ^{120}Sn recoils in their 2_1^+ excited state. The remaining thickness of the target, along with the Au backing, operate only as stopping media for the energetic recoils.

5.3.2 Stopping simulations of recoiling nuclei

One of the key inputs, as well as a significant source of uncertainty, in DSAM analysis is the simulation of trajectories and the time-dependence of the velocities of the recoiling nuclei of interest, traversing the target and backing media. Strongly dependent on the stopping power of these media, obtained from a knowledge of the

interaction of the atoms and ions with the moving nucleus, the trajectories are typically represented by the velocity (β_{rec}) and the direction (direction cosines) of the recoiling nuclei, in uniform time steps. The slowing down is due to two physical processes : (i) electronic stopping (dominates for $\beta_{\text{rec}} \approx 2\text{-}2.5\%$, with no change in recoil flight direction), and (ii) nuclear stopping (becomes significant towards the end of the recoil path, when $\beta_{\text{rec}} < 0.5\%$, leading to large-angle deviations in flight direction) [115]. There have been several approaches for determining the stopping powers, principally through theoretical modeling based on available experimental data. One of the early developments in this domain to determine the time-dependent velocity of an ion in a multiple-scattering medium was put forth by Blaugrund [116], which makes use of the theory of electronic and atomic collisions proposed by Lindhard *et al.* [117], based on the Thomas-Fermi model of the atom, to calculate specific energy losses of recoiling ions. The accuracy of the Doppler-affected shapes calculated by this formalism relies on the accuracy of stopping power calculations, which is estimated to be accurate within 20-25% [117], with large over-estimations of nuclear stopping powers. This is of significance in the present context since the analysis of Sie *et al.*, leading to $\tau_{2^+} \sim 1$ ps, is entirely based on Blaugrund's formalism. Later developments in the stopping power modeling include those by Northcliffe and Schilling [118] as well as Ziegler [119], which are essentially based on the proton stopping data (under the assumption of smooth variations between the points measured for different stopping materials) and α stopping data (showing a pronounced shell structure which becomes weaker with increasing energy), respectively. These employ different semi-empirical scaling algorithms for heavy-ions, and the results therefrom have been identified as inadequate at low kinetic energies [120]. These models have been adopted in the lineshape analyses of Refs. [34, 35] as reported by Jungclauss *et al.*

A more rigorous approach incorporating Monte Carlo calculations in the treatment

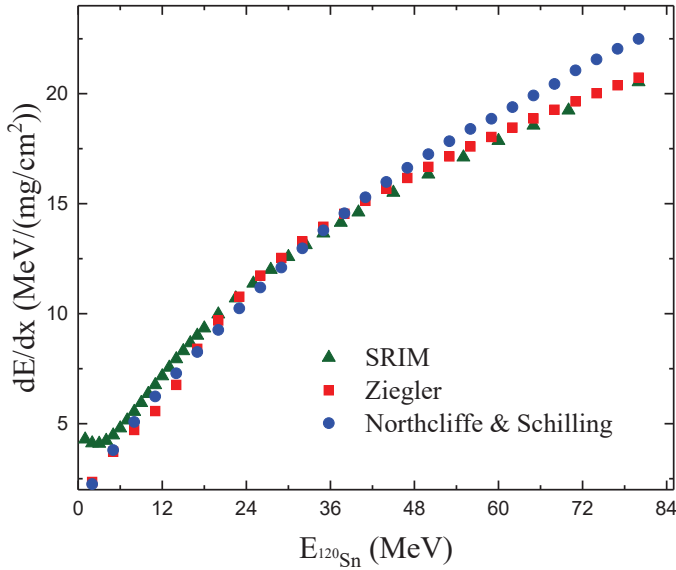


Figure 5.4: Comparison of stopping powers of ^{120}Sn recoils in the 2_1^+ state, in the ^{120}Sn medium, as calculated by different models, Ziegler [119], Northcliffe-Schilling [118] and SRIM [122]), at energies relevant in the current reaction.

of nuclear scattering was demonstrated by Currie [121] to be superior to an analysis using Blaugrund's formalism. The corresponding γ -ray shapes were accompanied by lower uncertainties. However, the weakest point continued to be the uncertainties in absolute stopping powers. This can be remedied with the use of the contemporary SRIM + TRIM [119] packages, involving a database of updated and experimentally-benchmarked electronic as well as atomic stopping powers for heavy-ions in a wide variety of media, with an uncertainty of a modest $\sim 5\%$ [122] and known to be highly reliable in the kinetic energy range of 0.001-1000 MeV/nucleon [120]. A comparison of the stopping powers of the ^{120}Sn recoils in the 2_1^+ state, as calculated by different models of the slowing-down process, is shown in Fig. 5.4. The difference is significant, particularly at lower kinetic energies of the recoiling ions, when atomic collisions become important for evaluating the trajectory.

For the description of the slowing-down process in the present work, the stopping simulations for a series of ^{120}Sn recoils have been carried out via simulations of recoil paths in TRIM, with stopping powers from SRIM, as implemented in the methodology developed by Das *et al.* [105]. The production thickness of the target has been binned into six divisions representing the changing beam energy, and the

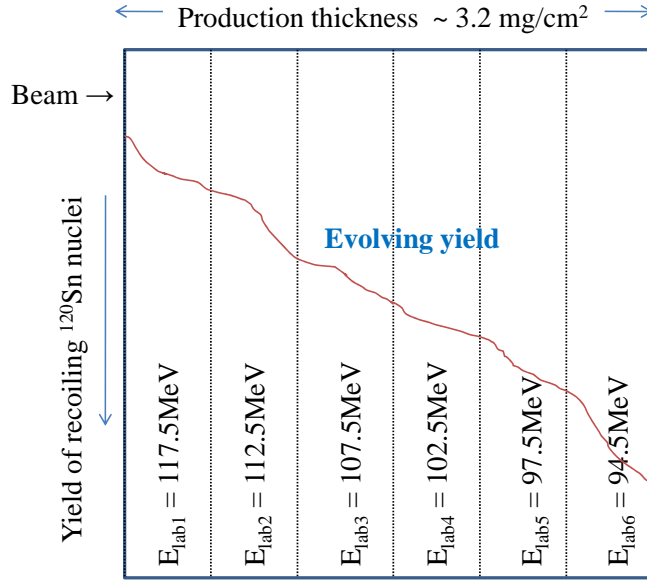


Figure 5.5: Schematic representation of the decreasing beam energy accompanied by evolving yield of the ^{120}Sn recoils along the target depth. The evolution is represented by up to six bins in the present analysis, as detailed in the text.

evolving excitation cross section of the scattered ^{120}Sn nuclei in the 2_1^+ state and corresponding energy-angle distribution therein (see Fig. 5.5). This changes the number of scattered recoiling nuclei produced at varying target depths, that would have different starting points as well as different initial energy-angle distributions for their respective trajectories. The default trajectories from the TRIM simulations in each bin are made to corroborate with the corresponding reactions kinematics and energetics by distributing the origin of the trajectories across the production thickness. For each recoil, the origin of the trajectory and the direction of entry into the stopping medium (following inelastic scattering) w.r.t. the beam axis is suitably modified in accordance with the energy-angle distribution of the respective bin. Subsequently, from the trajectory information in the form of energy and coordinates, the corresponding velocity profile, $\beta_{\text{rec}}(t)$, is extracted in uniform time steps of 0.002 ps. From the TRIM trajectory simulations, it is expected that the stopping power of the thick ^{120}Sn medium is most likely to keep a vast majority of the recoiling ions confined within itself, and only $\approx 20\%$ nuclei are expected to penetrate the

Au backing medium, where the slowing down process is expected to be faster. For this small fraction of recoils that escape the target foil, the TRIM calculations are separately executed in the region of the ^{197}Au backing to extract the corresponding velocity profiles. The resulting velocity profiles from both media are then combined.

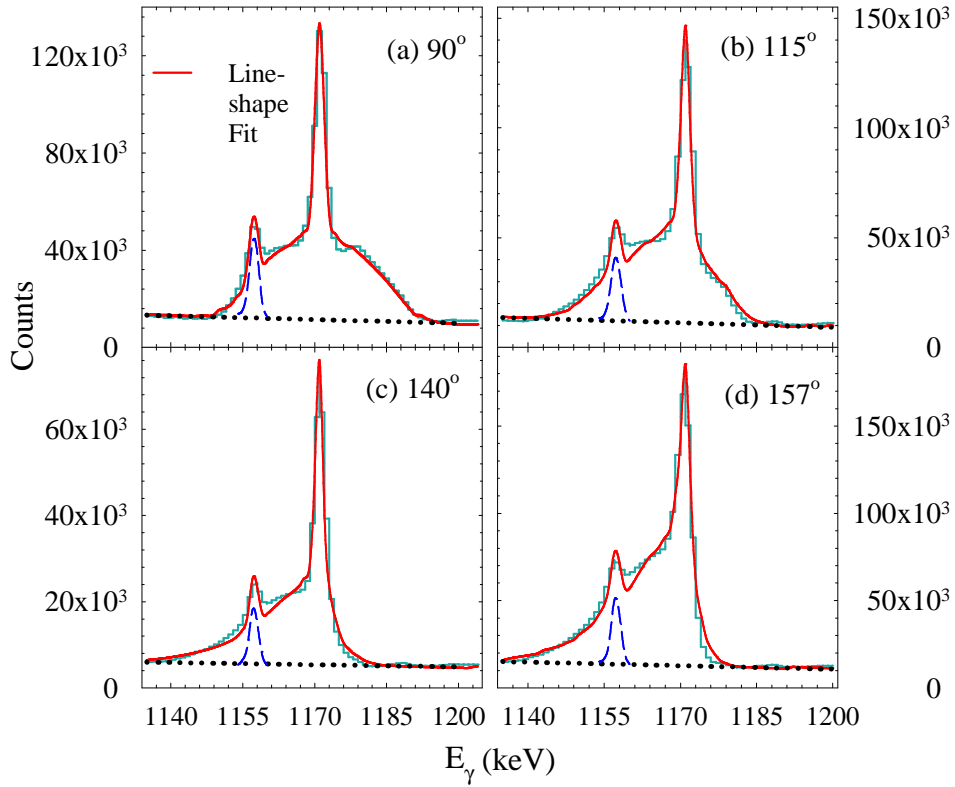


Figure 5.6: Experimental Doppler-broadened γ spectra and the results of the LINESHAPE calculations (solid lines) for the $2_1^+ \rightarrow 0_{g.s.}^+$ decay in ^{120}Sn , at $E_x = 1171$ keV. The dashed and dotted lines represent the deconvoluted fit of the additional stopped peak (from the decay of a long lived state in ^{43}Sc) and the linear fit of the background, respectively.

5.3.3 Generating Doppler-broadened lineshapes

For each time step, the simulated energy and direction histories of the recoiling nuclei, obtained using the prescription stated above, have been converted into the time-dependent velocity profile as seen by each clover detector at a certain angle

in the array, using the HISTAVER routine of the LINESHAPE package. This incorporates the target-detector distance, the detector radius, the detector positions - θ , ϕ , and, for each detector, its relative efficiency. The LINESHAPE code calculates the broadened shapes using these velocity profiles and assumed initial values for the lifetime, $\tau_{2_1^+}$, or the transition quadrupole moment, Q_{02} , for the observed transition and similarly, also for unobserved feeder transitions. These lifetimes (and other parameters such as normalizations, backgrounds, and impurity peak areas) are varied for each clover by several minimization routines to produce the best least-squares calculated fit to the data lineshapes [113]. In the current analysis, single detector (clover) spectra at the eleven different (θ, ϕ) angles were fitted simultaneously as per the standard procedure [106]. Figs. 5.6(a)-5.6(d) illustrate typical fits of the γ -ray peak of interest, 1171 keV from ^{120}Sn , represented by continuous curves. The calculation incorporated the 1157 keV peak riding on the Doppler shape of 1171 keV. The lifetime value of the 2_1^+ state in ^{120}Sn obtained from this analysis is $\tau_{2_1^+} = 0.863_{-0.036}^{+0.029}$ ps. The quoted uncertainties were derived from χ^2 analysis of the fitted values and do not include the systematic effect of the uncertainties on the stopping powers. However, given that these were from the SRIM code, it may be emphasized that the accompanying uncertainties are known to be $\sim 5\%$ [122] and significantly lesser than the earlier models ($\sim 20\%$) used in conventional analysis.

Another uncertainty in lifetime analysis, following DSAM, pertains to (side) feeding from states above the level of interest. If these cannot be accounted appropriately, the lifetime result on the state of interest is, at best, an upper limit of the same. As per the partial level scheme of ^{120}Sn (see Fig. 5.7), the 2_1^+ state can be fed by $E2$ decays from (i) the 4_1^+ state via 1023 keV, (ii) the 0_2^+ state via 704 keV, (iii) the 2_2^+ state via 926 keV, and by an $E1$ decay from (iv) the 3_1^- state via 1229 keV. These can be modelled in the LINESHAPE code by a set of transitions with independently variable lifetimes. They are, however, not expected to impact the aforementioned

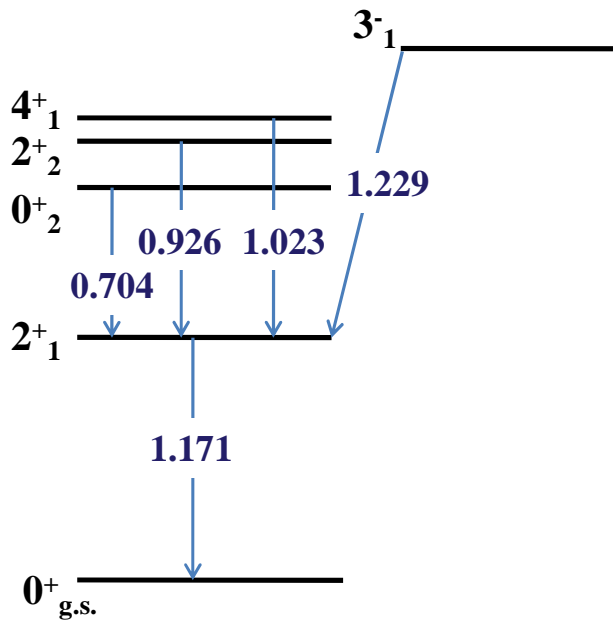


Figure 5.7: Level scheme of ^{120}Sn showing the low-lying excited states [123].

lifetime of the 2_1^+ state since the CRC calculations predict rather low excitation probabilities for these levels at the chosen below-barrier bombarding energy in this work. Also, most of these states are long lived ones [104] and feeding therefrom is expected to be insignificantly Doppler affected. The feedings were nevertheless incorporated into the analysis, with intensity $\sim 10\%$ for the expectedly strongest $4_1^+ \rightarrow 2_1^+$ branch at the chosen bombarding energy, and observed to cause a variation in the lifetime result of the 2_1^+ level within the quoted uncertainties. The side feeding from the 3_1^- state ($E_x = 2401$ keV), through 1228 keV transition, has been found to be insignificant in this case. In fact, the statistics on the 1171 keV peak, with gate on 1228 keV transition in the angle-dependent matrices, is rather sparse for any conclusive analysis.

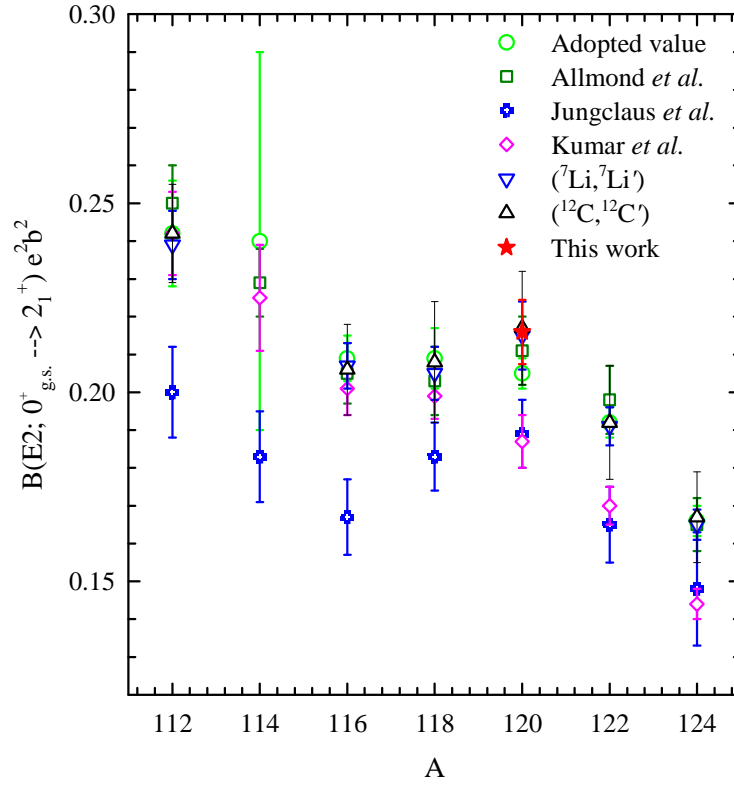


Figure 5.8: Systematic plot of $B(E2; 0_{g.s.}^+ \rightarrow 2_1^+)$ values for the stable even-mass Sn isotopes using the data obtained from measurements carried out in this thesis work, compared with values deduced from recent measurements of the 2_1^+ level lifetime [34, 89, 90].

5.4 Enhanced $B(E2; 0_{g.s.}^+ \rightarrow 2_1^+)$

From the measured lifetime, the transition probability for the $2_1^+ \rightarrow 0_{g.s.}^+$ decay with $E_\gamma^0 = 1.171$ MeV can be deduced, using Eqn. 1.7, as follows,

$$\frac{1}{B(E2; 2_1^+ \rightarrow 0_{g.s.}^+)} = 1.225 \times 10^9 (E_\gamma^0)^5 \tau_{2_1^+} \quad (5.4)$$

With $B(E2; 2_1^+ \rightarrow 0_{g.s.}^+) = \left(\frac{1}{5}\right) B(E2; 0_{g.s.}^+ \rightarrow 2_1^+)$, the results of the lifetime, transition quadrupole moment and the transition probability are summarized in Table 5.1. It may be emphasized here that the results of $\tau_{2_1^+}$ and $B(E2)$ are not grossly different from the existing values. This affirms that while the degree and nature of target oxidation could not be established, the partial oxidation of the production

thickness of the target foil may not have been veritable enough to significantly affect the stopping power (compared to that of elemental Sn), and a vast majority of the excited Sn recoils are slowed down in the enriched Sn medium. The consequent uncertainty, if any, is presumably covered within the statistical uncertainty of the lifetime result. As a case study, Ref. [106] reports a measurement on the level lifetimes in ^{32}P populated in a reaction involving an oxidized target. In the absence of absolute quantification of oxide phases in the target, a large deviation from the expected value is shown for the lifetime of the 1755 keV state in ^{32}P with variations in assumed density of the target foil. In comparison, the partial oxidation in the present work can be expected not to have affected the density of the thick target foil in the region where the slowing down occurs, thereby leading to a realistic lifetime numbers of worth and reason. Given the accuracy of the methodology adopted in the present work, with lower uncertainty on the stopping power, the present result is an improved estimate of the 2_1^+ level lifetime in ^{120}Sn by the DSAM method.

Table 5.1: Lifetime τ and transition probability $B(E2)$ for the $\lambda = 2$ excitation in ^{120}Sn .

E_γ^0 (MeV)	$\tau_{2_1^+}$ (ps)	Q_{02} (eb)	$B(E2; 0_{g.s.}^+ \rightarrow 2_1^+)$ (e^2b^2)
1.171	$0.863^{+0.029}_{-0.036}$	$1.468^{+0.024}_{-0.033}$	$0.215^{+0.008}_{-0.009}$

The result from lifetime analysis confirms enhanced collectivity in the 2_1^+ excitation in ^{120}Sn , with $B(E2)/B(E2)_{\text{sp}} \sim 12.3$, with $B(E2)_{\text{sp}}$ from Table 1.1. From Fig. 5.8, it is noteworthy that the present result, reported in Ref. [124], is in excellent agreement with the $B(E2)$ value measured by Allmond *et al.* [37], and also with the results from heavy-ion scattering measurements with ^7Li and ^{12}C projectiles, as reported in the previous chapter, as well as in Refs. [89, 90] as part of this thesis work.

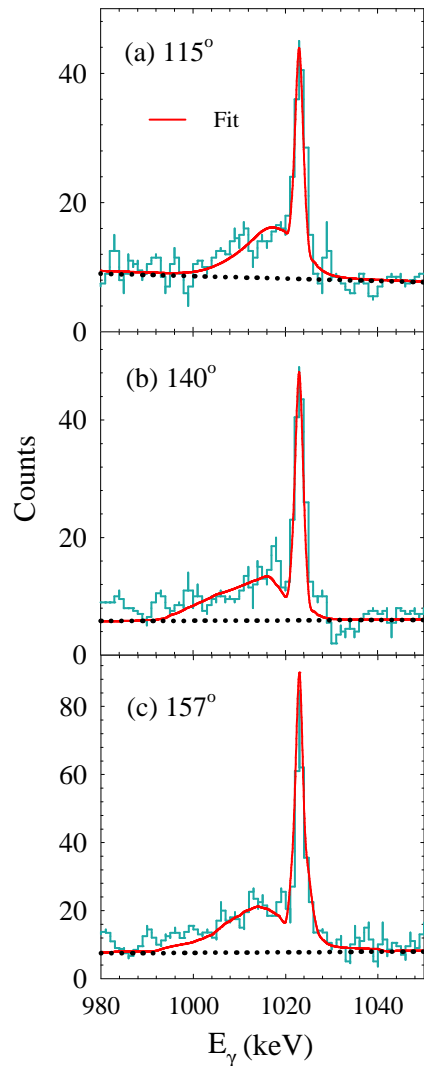


Figure 5.9: γ -ray spectra gated with the $2_1^+ \rightarrow 0_{\text{g.s.}}^+$ transition (1171 keV) in ^{120}Sn showing the coincident $4_1^+ \rightarrow 2_1^+$ transition (1023 keV). Asymmetric angular matrices, 90° versus (157° , 140° , 115°), have been used for generating the coincidence spectra with gate set on the 1171 keV transition at the 90° detectors. The fits to the accompanying weak structure of the $E2$ decay peak lead to the lifetime, $\tau_{4_1^+}$, of the decay.

5.4.1 The $4_1^+ \rightarrow 2_1^+$ feeding transition

Traditionally, the analysis of the Doppler shapes/shifts should preferably be carried out with coincident spectra corresponding to a gate set on a transition above the transition of interest in a cascade. Such an implementation eliminates the effects of any feeding, other than the gating one, and facilitates in improving the accuracy of the measurement. As far as the current measurement is concerned, the 1023 keV transition from the decay of the 4_1^+ state could have qualified for the purpose and the lifetime analysis of the 2_1^+ level could have been pursued with gated spectra of the 1023 keV transition. However, as it has been brought out in the preceding

text, the feeding from the 4_1^+ level is rather insignificant and the corresponding coincidence spectra, with gate set on 1023 keV transition, are plagued with dearth of sufficient statistics for reliable fitting. Also, it is worth noting that the 4_1^+ level, as per the existing literature [104], is long-lived ($\tau \sim 2$ ps) compared to the 2_1^+ state. Consequently, only a part of this feeding population will contribute to the Doppler shape of the 1171 keV transition, de-exciting the 2_1^+ state, further vexing the analysis in the top-gated spectra (contribution is primarily to the stopped component at 1171 keV).

To verify this claim, the Doppler shape analysis could be pursued for the 1023-keV transition in the coincident spectra with gate on 1171-keV and lifetime of the 4_1^+ state be extracted therefrom. Fig. 5.9(a)-5.9(c) illustrate the representative fits obtained from asymmetric angular matrices, with 90° detectors on one axis and one of the backward angles (157° , 140° , 115°) detectors on the other axis, with gate set on the 1171 keV transition at the 90° detectors. The corresponding lifetime, $\tau_{4_1^+} = 1.77_{-0.089}^{+0.084}$ ps, translates into a $B(E2; 4_1^+ \rightarrow 2_1^+) = 0.041_{-0.003}^{+0.002}$ e²b², in compliance with the previously published [23] value of $0.035(11)$ e²b². Since the lifetime analysis of the 4_1^+ state has been carried out with a gate set on a transition below the transition of interest, it may be argued that $\tau_{4_1^+}$ is actually an upper limit on the same. However, realistically speaking, the excitation reaction used herein, has tenuously populated the states that are still higher up in the excitation scheme of ^{120}Sn , following which the aforementioned value of $\tau_{4_1^+}$ can be perceived as its actual, at least within the purview of the present analysis. It may thus be concluded that the contributions from the dominant feeder levels to the broadened shape of the 1171 keV peak is insignificant and the result of $\tau_{2_1^+} = 0.863_{-0.036}^{+0.029}$ ps is equivalent to the mean lifetime of the 2_1^+ state.

5.5 Non-zero moment of inertia for the 2_1^+ state

In the course of this thesis work, the $B(E2)$ value for the 2_1^+ state in ^{120}Sn has been unambiguously measured and corroborated from measurements of heavy-ion inelastic scattering as well level lifetime. The corresponding Q_{02} is reported in Table 5.1. The comparison of experimental and theoretical values of structural parameters of excited states provides a test for the validity of nuclear models. The first excited 2^+ states in even-even nuclei are predominantly found to be of collective vibrational or rotational nature. The low-lying 2_1^+ states in rare earth even-even nuclei with cylindrical symmetry in their body-fixed frame, depopulated by enhanced $E2$ ($2_1^+ \rightarrow 0_{\text{g.s.}}^+$) transitions and with large intrinsic quadrupole moments, have been recognized by Bohr & Mottelson [125] as the missing levels of g.s. rotational bands with characteristic moments of inertia. On the other hand, such g.s. rotational bands are not found in even-even nuclei with spherical symmetry in their body-fixed frame. But theoretical estimates [126] as well as several measurements of non-zero static quadrupole moments for the 2_1^+ states in nuclei with spherical symmetry are at variance with the near-harmonic vibrational model of excitations. This provides evidence for anharmonic vibrations (rotational-vibrational coupling). Although the accuracy of determination of static quadrupole moments in nuclear excited states is not appreciable (50–100%) as that for transition quadrupole moments (2–10%) [127], a conclusion can be drawn about the existence of a nonvanishing moment of inertia, $\mathcal{I}_{2_1^+} \neq 0$, in excited 2_1^+ states of spherical nuclei. The static electric quadrupole moment of 2_1^+ state of ^{120}Sn has previously been determined by means of the reorientation effect [123, 128] and is found to be small, 0.09 ± 0.10 eb, but non-zero.

With the failure of the rigid rotor model [129] for describing rotational character in even-even nuclei (due to internal structure of nuclei, such as alignment of single-particle angular momentum), Bohr-Mottelson proposed a hydrodynamical

model [130] for the correlation between the transition quadrupole moment for the $E2$ excitation, Q_{02} , and the associated moment of inertia of the nucleus characteristic of an irrotational flow motion, \mathcal{I} , that is expected to reproduce the excitation spectra as,

$$E_J = \frac{\hbar^2}{2\mathcal{I}}J(J+1) - BJ^2(J+1)^2 \quad (5.5)$$

with the nucleus-specific constant B representing rotation-vibration coupling, in analogy with molecular spectroscopy. However, a detailed analysis of the measured energies and lifetimes of 2_1^+ states in several such nuclei by Sunyar [131] leads to the conclusion that the moments of inertia deduced from the $E_{2_1^+}$ values are 4 to 5 times larger than those predicted by the hydrodynamical model.

The characteristics of both the g.s. (intrinsic) deformed as well as g.s. spherical nuclei have been successfully unified with the idea of nuclear spin-dependent moment of inertia for a wide range of even-even nuclei by means of the semiclassical variable moment of inertia (VMI) model [132] that defines an energy spectrum of states exhibiting rotational character,

$$E_J(\mathcal{I}_J) = \frac{1}{2}C(\mathcal{I}_J^2 - \mathcal{I}_0^2) + \frac{1}{2\mathcal{I}_J}J(J+1) \quad (5.6)$$

The parameters C and \mathcal{I}_0 are the restoring force constant and the g.s. moment of inertia, respectively. The equilibrium condition $\partial E_J(\mathcal{I}_J)/\partial \mathcal{I}_J = 0$ determines \mathcal{I}_J as the moment of inertia (in units of \hbar^2) for a state J . For a nucleus with spherical ground state, the above prescription of Eqn. 5.6 can be rewritten in the limit of $\mathcal{I}_0 \rightarrow 0$ as,

$$E_J(\mathcal{I}_J) = \frac{3}{4} \frac{J(J+1)}{\mathcal{I}_J} \quad (5.7)$$

VMI model proposes an empirical relationship [132, 133] between the $2_1^+ \rightarrow 0_{g.s.}^+$ transition quadrupole moment, Q_{02} , and transition moment of inertia, \mathcal{I}_{02} , for nuclei

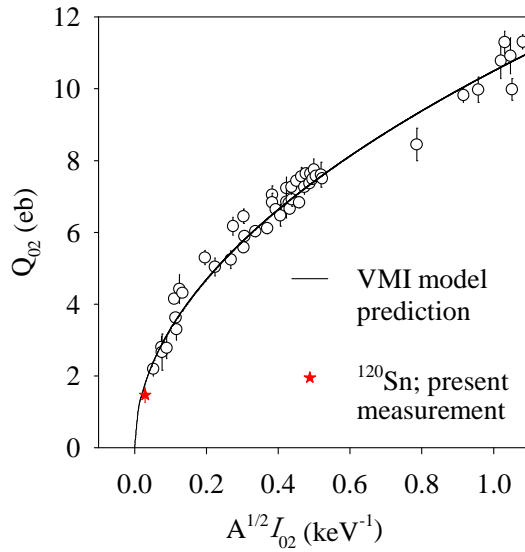


Figure 5.10: Plot of Q_{02} versus $A^{1/2}\mathcal{I}_{02}$ for a wide range of nuclei. The abscissae have been calculated by the VMI model in Ref. [132]. The data for Q_{02} (hollow circles) are taken from Ref. [134]. The solid curve gives the best-fit to Eqn. (5.8). The red solid symbol represents the result of the present work, with Q_{02} extracted from DSAM lifetime analysis and \mathcal{I}_{02} calculated using VMI model prescription.

in the mass range $12 \leq A \leq 252$ as:

$$Q_{02} = K A^{1/4} \sqrt{\mathcal{I}_{02}} \quad (5.8)$$

where $K=10.5$ eb keV $^{1/2}$ and $\mathcal{I}_{02}^2 = \frac{1}{2} \left(\mathcal{I}_{0_{g.s.}^+}^2 + \mathcal{I}_{2_1^+}^2 \right)$ [133]. The correlation between intrinsic transition quadrupole moments from Ref. [134] and moments of inertia given by the VMI model [132] is shown in Fig. 5.10 for several even-even nuclei with atleast some states of rotational character. The curve represents the best-fit to Eqn. (5.8).

With the 2_1^+ state at $E_{2_1^+} = 1171$ keV in ^{120}Sn , a value of $\mathcal{I}_{2_1^+} \approx 0.00384$ keV $^{-1}$ is obtained. The Q_{02} value from Table 5.1 is plotted against the VMI model-predicted \mathcal{I}_{02} , as shown by the filled symbol in Fig. 5.10. The symbol falls on the best-fit curve. This confirms presence of anharmonicity in the $0_{g.s.}^+ \rightarrow 2_1^+$ intrinsic excitation in ^{120}Sn , suitably explained by the existence of a nonvanishing angular momentum dependent moment of inertia. Measurements of level lifetimes and transition quadrupole moments can thus be an important tool to test nuclear models.

5.6 Summary & Conclusions

The mean lifetime of the 2_1^+ level in ^{120}Sn ($E_x = 1171$ keV) has been exclusively determined using DSAM implemented through updated methodologies, and the corresponding $B(E2; 0_{\text{g.s.}}^+ \rightarrow 2_1^+)$ value is deduced therefrom. An enhancement in collectivity for the 2_1^+ state is confirmed, following an improved determination of the level lifetime with reduced uncertainties. The present result is in excellent agreement with the results obtained from heavy-ion inelastic scattering [89,90] discussed in the previous chapter. The framework of analysis in this work relies on stopping simulations for the velocity profiles of recoils traversing a thick stopping medium, generated using the contemporary SRIM + TRIM packages. Such measurements are not limited to the conventional DSAM approach of a thin target backed by a high- Z element, in a particle- γ coincidence setup. As an additional test, the lifetime of the 4_1^+ level has also been estimated and is in compliance with existing estimate of $B(E2; 4_1^+ \rightarrow 2_1^+)$. This establishes the fact that the velocity profile is the most sensitive part of this analysis, and with lower uncertainties ($\sim 5\%$) on stopping powers, compared to the uncertainties with earlier calculations ($\sim 20\%$) for similar analyses, this methodology leads to modest fits of the inclusive decay spectra to arrive at veritable lifetime numbers (even with possible contaminations or unincorporated feeding statistics).

A precise measurement of level lifetime also reduces uncertainty in the estimation of the proton transition matrix element, which, in conjunction with the neutron transition matrix element obtained from light/heavy ion scattering experiments, would allow the determination of proton and neutron effective charges to be used in new shell model calculations for transition rates.

Chapter 6

Importance of inelastic couplings in reaction dynamics

In the previous two chapters, the focus has been directed towards determining transition probabilities/deformation lengths for the low-lying excited states in the Sn isotopes under study. The transition probability between two nuclear states depends sensitively on their structural paradigm. In binary heavy-ion interactions, the reaction dynamics are governed by the couplings between the relative motion coordinate and the internal degrees of freedom of the participating nuclei. Inelastic couplings pertaining to the low-lying surface modes are among the most dominant reaction channels in events of nucleus-nucleus collisions. Knowledge of accurate deformation/structural properties is of fundamental importance to determine the coupling effects on the entrance channel that influence the resulting cross sections of all channels between the extremities of elastic scattering and fusion. To that effect, the direct comparison of experimental and theoretical values of structural quantities, or of their effects on other observables, provides a test for nuclear models.

6.1 Elastic, inelastic and 1-nucleon transfer channels in ${}^7\text{Li}+{}^{120}\text{Sn}$ system

Heavy-ion peripheral reactions, like inelastic excitations and transfer processes, offer a spectroscopic tool for the excitation of high spin states of stable as well as unstable nuclei and complex nuclear configurations such as single-particle states coupled to core vibrational states. Simultaneous description of such dominant outgoing channels by the same coupled channels calculation, using a single set of potential and coupling parameters, is one of the difficult tasks in nuclear reaction studies, and is an important tool that reveals realistic structural parameters for that projectile-target system. Systematic analysis of elastic and inelastic scattering cross sections for ${}^7\text{Li}+{}^{120}\text{Sn}$ have been reported previously in Chapter 4 at 28 MeV bombarding energy. From optical model analysis of the elastic scattering data, the net reaction cross section, σ_{reac} , is predicted to be ~ 1200 mb at this energy. With respect to the CRC (§4.2.1) and CDCC-CRC (§4.2.2) calculations that explain the measured data for the different channels, the quadrupole and octupole excitations in ${}^{120}\text{Sn}$ constitute a total of ~ 26 mb of σ_{reac} . The CDCC-CRC calculations assign an additional ~ 21 mb to the breakup of ${}^7\text{Li}$ into $\alpha + t$. The remaining fraction is attributed the excitation of ${}^7\text{Li}$ to its bound inelastic state at 478-keV (21 mb), and to the small number of 1-nucleon transfer channels coupled into the model space, as well as the cumulative absorption due to the imaginary potential (~ 1120 mb) that includes the estimated cross sections for fusion along with those of the excluded channels. Such a calculation of fusion probability largely relies on the coupling effects of the dominant peripheral channels. The importance of realistic estimation of the structural parameters for the colliding nuclei is realized when the same parameters are used to explain the deformation properties at another bombarding energy, as well as simultaneously explain several other major direct reaction channels. In this context,

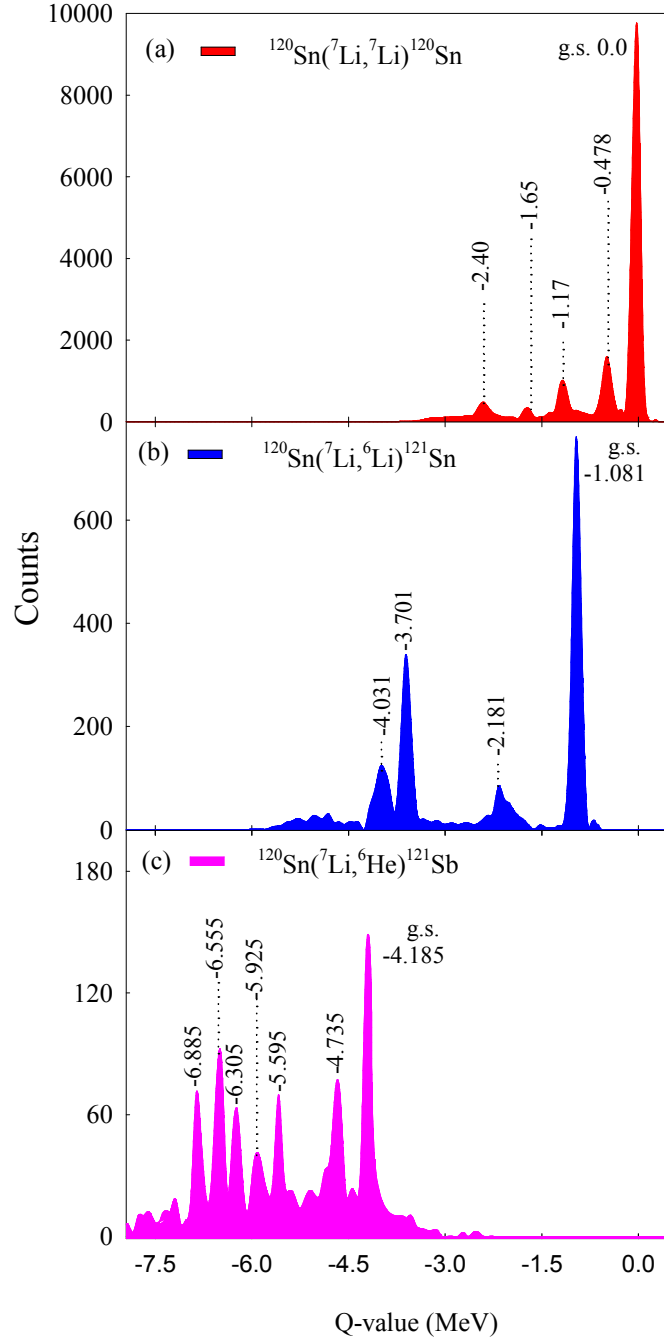


Figure 6.1: 1D spectrum showing Q -value distribution of states identified in (a) elastic and inelastic scattering, (b) 1-n transfer and (c) 1-p transfer processes at $\theta_{lab}=60^\circ$ for $E_{lab} = 30$ MeV.

differential cross sections for elastic and inelastic scattering for ${}^7\text{Li} + {}^{120}\text{Sn}$ system have been determined at $E_{\text{lab}} = 30$ MeV. In addition, experimental angular distributions for cross sections of one-nucleon transfer channels, ${}^{120}\text{Sn}({}^7\text{Li}, {}^6\text{Li}){}^{121}\text{Sn}$ and ${}^{120}\text{Sn}({}^7\text{Li}, {}^6\text{He}){}^{121}\text{Sb}$, have been determined at both 28 and 30 MeV beam energies for residual excitations up to ~ 3 MeV. A simultaneous description of all reaction channels has been attempted with a consistent set of potential parameters, as well as coupling parameters [135].

The schematic experimental arrangement is same as that shown in Fig. 2.4. Along with the channels studied in §4.2, the yields for the identified states of the one-nucleon transfer partitions were extracted separately for evaluating their respective experimental differential cross sections. While the inelastic peaks could be clearly distinguished, however, for the case of the densely populated transfer peaks, each centroid could contain contributions from more than one state, embedded within a background of other nuclear levels, owing to the existence of several closely spaced neighbouring states in the residual nuclei. Few groups of states are found to be enhanced over others (see Figs. 6.1(b,c)).

Studies of heavy-ion induced single nucleon transfer reactions reveal strong J and Q preferential selectivity in the relative cross sections, which primarily depends on the type of projectile and the orbit from which the transfer occurs [136–138]. Transfer reactions between heavy-ions at energies well above the Coulomb barrier have substantial cross-section when certain kinematical conditions are satisfied. These relate the Q -value of the reaction to the angular momentum of the transferred nucleon in the initial and final nuclei. In the present case as well, among the large number of known levels in the residual nuclei, up to ~ 17 MeV excitation energy each in ${}^{121}\text{Sn}$ and ${}^{121}\text{Sb}$, only some groups of levels are enhanced that are favoured by the selectivity conditions. Earlier measurements also exist on the population of states in ${}^{121}\text{Sn}$ and ${}^{121}\text{Sb}$ by means of light-ion bombardment, for instance ${}^{120}\text{Sn}[(t,d),(d,p)]$ [139–141]

and ${}^{120}\text{Sn}[({}^3\text{He},\text{d}),(\alpha,\text{t})]$ [142–144] reactions, respectively. In contrast to light-ion nucleon transfer reactions where the initial proton/neutron orbit has an s -state for its initial bound orbital, the initial nucleon orbit is $p_{3/2}$ ($j_i = l_i + 1/2$) each for the (${}^7\text{Li},{}^6\text{He}$) and (${}^7\text{Li},{}^6\text{Li}$) reactions. As a result, the present reactions populate states in residual nuclei with different strengths, based on the kinematic selection rules. These conditions govern whether the final nucleon orbital has $j_f = l_f + 1/2$ or $j_f = l_f - 1/2$, with l_f being the orbital angular momentum of the final shell the nucleon enters. Following the prescription given in Ref. [136],

$$l_f = l_{\text{c.m.}} - m_i \frac{R_2}{R_1} \quad (6.1)$$

$$k_i R_i + m_i = k_f R_f(Q) + m_f \quad (6.2)$$

where R_1 (R_2) is the radius of the heavy ion from which (to which) the transfer occurs, and m_i and m_f are projections of the initial and final orbital angular momenta of the transferred nucleon, l_i and l_f . The quantity $l_{\text{c.m.}}$ defines the angular momentum due to centre-of-mass motion, with $k_i R_i$ and $k_f R_f$ being the grazing angular momenta brought into the collision, ${}^7\text{Li}+{}^{120}\text{Sn}$, and that carried by the outgoing relative motion, ${}^6\text{Li}+{}^{121}\text{Sn}({}^6\text{He}+{}^{121}\text{Sb})$, with g.s. Q -value $-1.081(-4.185)$ MeV.

Even though all the aforementioned reactions (earlier as well as present) populating states in ${}^{121}\text{Sn}$ and ${}^{121}\text{Sb}$ have the nucleon originating from $j_i = l_i + 1/2$, but for the more negative Q -values of the present reactions, higher spin states are favoured that provide the best momentum matching conditions owing to a variety of l_f values possible, as compared to $(\text{t},\text{d}),(\text{d},\text{p})$ and $({}^3\text{He},\text{d})$ reactions. The difference, $\Delta L = |k_i R_i - k_f R_f(Q)|$, governs the final state spin values as given by $\Delta L = |j_i - 1/2 - j_f|$. The structure of the residuals are essentially dominated by these single-particle degrees of freedom coupled to vibrations of the spherical Sn core, i.e; by coupling the odd proton or odd neutron in the spherical shell model orbitals $2d_{5/2}, 1g_{7/2}, 3s_{1/2}$,

$2d_{3/2}$, and $1h_{11/2}$ to the low-lying excitations of the Sn cores. Thus, certain groups of states are enhanced over others. The yields for each group have been extracted to determine the differential cross section, then converted to the centre-of-mass frame. In this study, the experimentally observed centroid Q -value has been considered for computing the transformation factor (see Eqn. 4.1) for each case. The experimental and calculated cross sections are related as,

$$\left(\frac{d\sigma}{d\Omega}\right)_{\text{expt}} = \frac{2J_f + 1}{2J_i + 1} C^2 S_t C^2 S_p \left(\frac{d\sigma}{d\Omega}\right)_{\text{calc}} \quad (6.3)$$

where, $C^2 S_p$ and $C^2 S_t$ correspond, respectively, to the projectile-stripping and target-pickup spectroscopic overlap factors $\langle {}^7\text{Li} | {}^6\text{Li} + n \rangle$ and $\langle {}^{120}\text{Sn} + n | {}^{121}\text{Sn} \rangle$ for the (${}^7\text{Li}, {}^6\text{Li}$) reaction, and $\langle {}^7\text{Li} | {}^6\text{He} + p \rangle$ and $\langle {}^{120}\text{Sn} + p | {}^{121}\text{Sb} \rangle$ for the (${}^7\text{Li}, {}^6\text{He}$) reaction. As the coupling to the continuum demands a high computational capacity, a complete calculation including not only the continuum but also bound states of inelastic and several transfer channels becomes very difficult. Hence, the present calculations have been carried out within the CRC formalism. The coupling scheme is similar to that shown in Fig. 4.4, with residual excitations up to ~ 3 MeV for the 1-nucleon transfer processes.

CRC calculations in finite range DWBA (FRDWBA) limit have been performed by including as many as 30 significant channels that couple to the entrance channel, and the results are compared with the experimental data for both energies. The nuclear potential parameters as well as the coupling parameters for the inelastic states are kept equivalent to those reported in Tables 4.1 and 4.2, as well as in §4.2.1.1. The experimental angular distributions for normalized elastic scattering differential cross section, and the corresponding calculations are shown in Fig. 6.2. The dashed lines represent the results without any coupling. In order to compare the calculations using the above potential and coupling parameters with another generalized potential, the calculations have been repeated using the São Paulo Potential (SPP) [79]

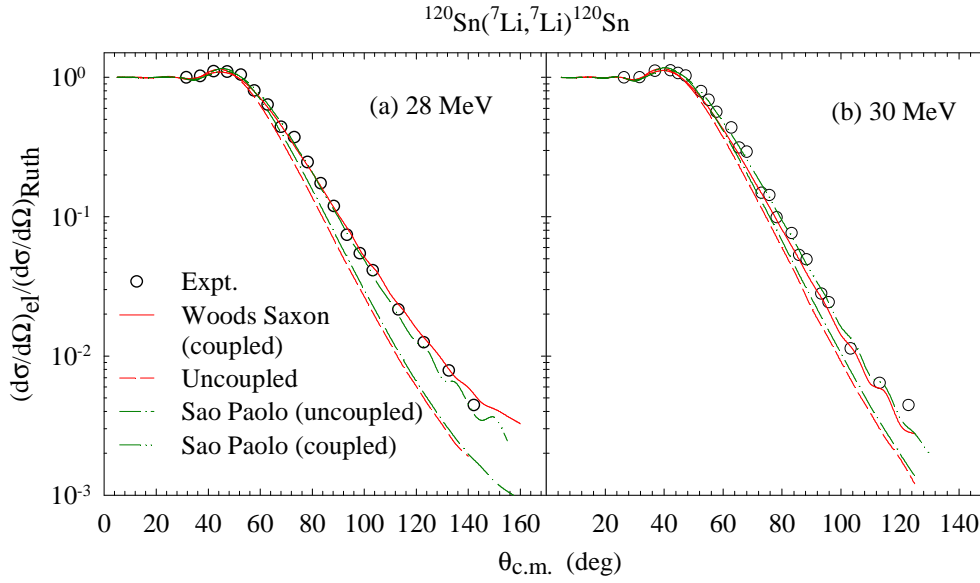


Figure 6.2: Experimental cross section and CRC calculation for the elastic channel (relative to Rutherford).

with both real and imaginary parts. The full CRC calculations including dominant inelastic and transfer channels requires the real part of the SPP to be increased by a factor of 1.4 in order to explain the measured elastic scattering. The experimental inelastic scattering angular distributions are shown as symbols in Fig. 6.3(a)-6.3(h). The data (symbols) for 1-n transfer are shown in Fig. 6.4(a)-6.4(h), and for 1-p transfer in Fig. 6.5(a)-6.5(n). The lines represent CRC calculations. Fusion in the exit channels of the transfer partitions was accounted for, by defining the total absorption due to a short-ranged imaginary potential of Woods-Saxon (WS) square form, given by $V_0 = 10.00$ MeV, $r_0 = 1.00$ fm and $a_0 = 0.40$ fm. The potentials binding the transferred particles were also of WS form, with radius $1.25A^{1/3}$ fm and diffuseness 0.650 fm, with A being the mass of the core nucleus. The depths were automatically adjusted to obtain the required binding eigen-energies (separation energies) of the particle-core composite system. The transfer angular distributions are peaked in the vicinity of the grazing angle for the collision at each energy. The amplitude for the overlaps $\langle {}^7\text{Li}|{}^6\text{Li} + n \rangle$ and $\langle {}^7\text{Li}|{}^6\text{He} + p \rangle$ are taken as 0.948 [145]

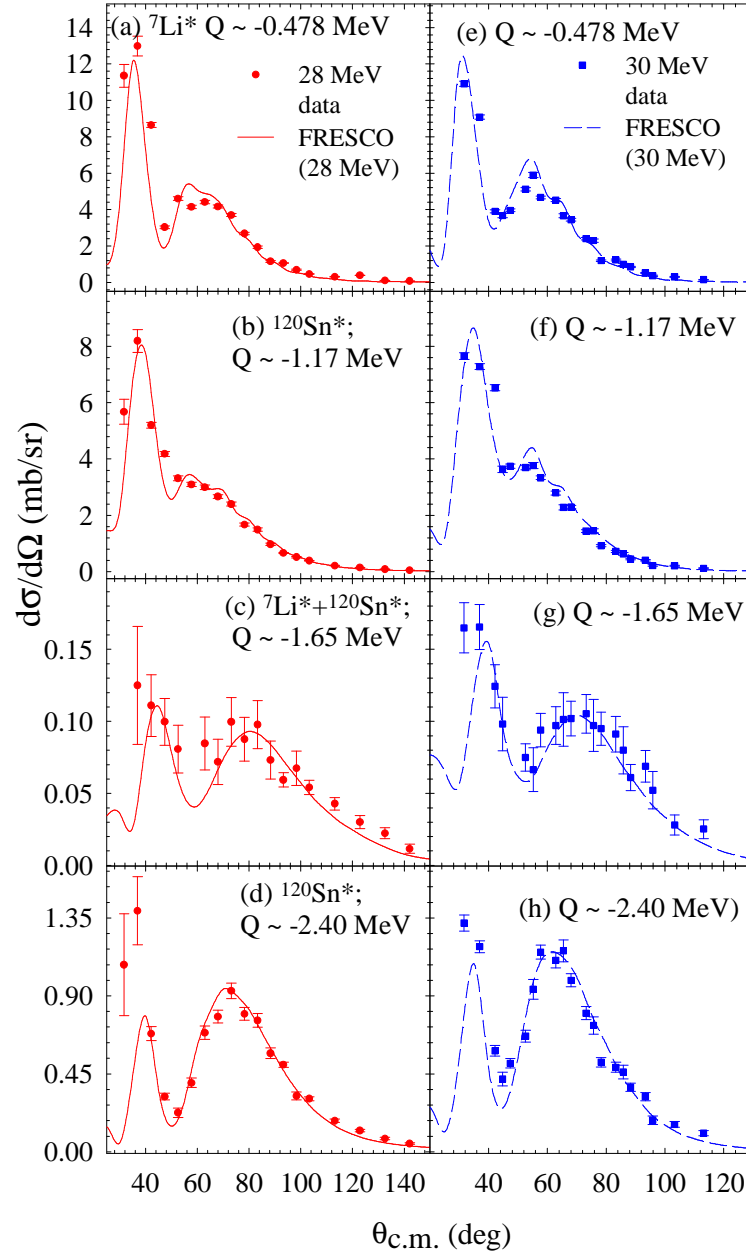


Figure 6.3: Experimental cross sections (open circles) and respective calculations (solid lines) for inelastic scattering processes in ${}^7\text{Li}+{}^{120}\text{Sn}$ system at 28 MeV for (a) quadrupole excitation in ${}^7\text{Li}$, (b) quadrupole excitation in ${}^{120}\text{Sn}$, (c) mutual quadrupolar transitions in ${}^7\text{Li}$ and ${}^{120}\text{Sn}$, and (d) octupole excitation in ${}^{120}\text{Sn}$. The corresponding experimental data (filled circles) and calculations (dashed lines) for 30 MeV are shown in (e), (f), (g) and (h), respectively.

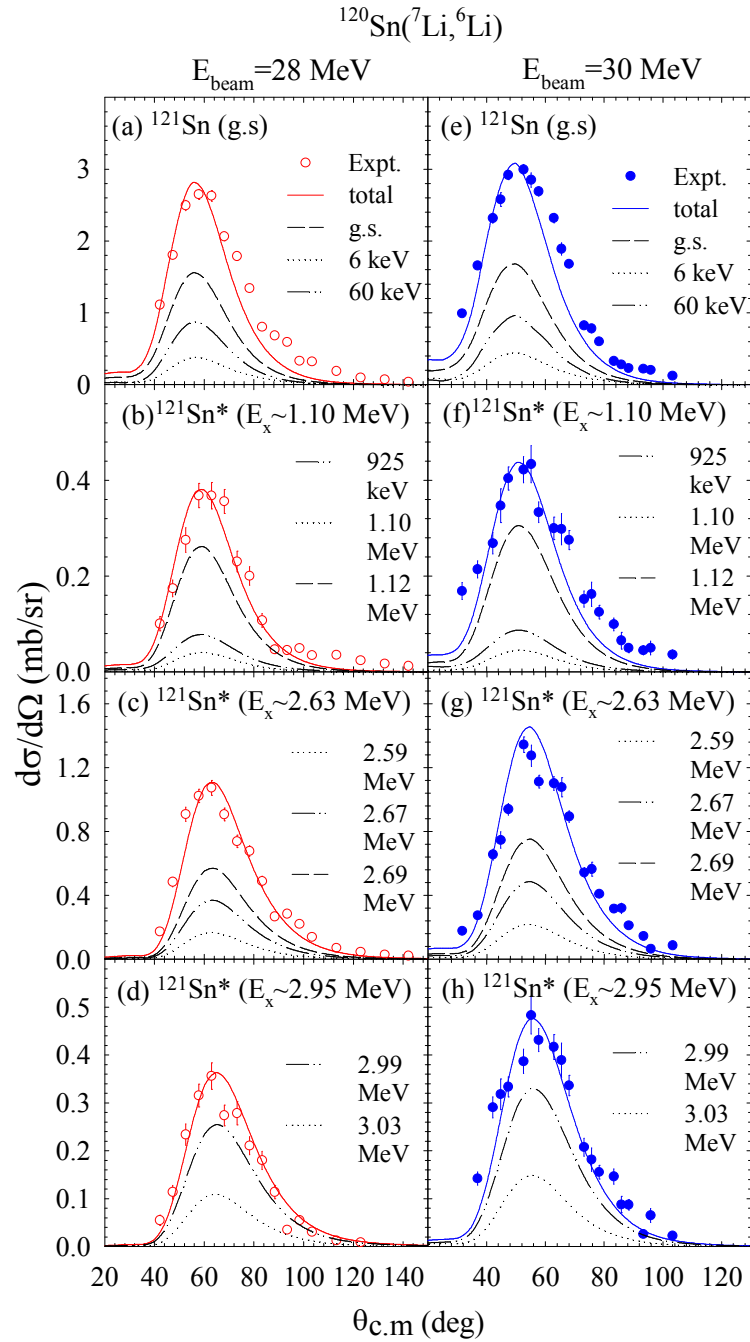


Figure 6.4: Experimental cross sections and respective calculations at 28 MeV for 1-n transfer process (${}^7\text{Li}, {}^6\text{Li}$) for different excitations of the recoil are shown in (a)-(d). The corresponding data and calculations for 30 MeV are shown in (e)-(h), respectively. The states included in the model calculations for each centroid energy are listed in Table 6.1 with respective structural information.

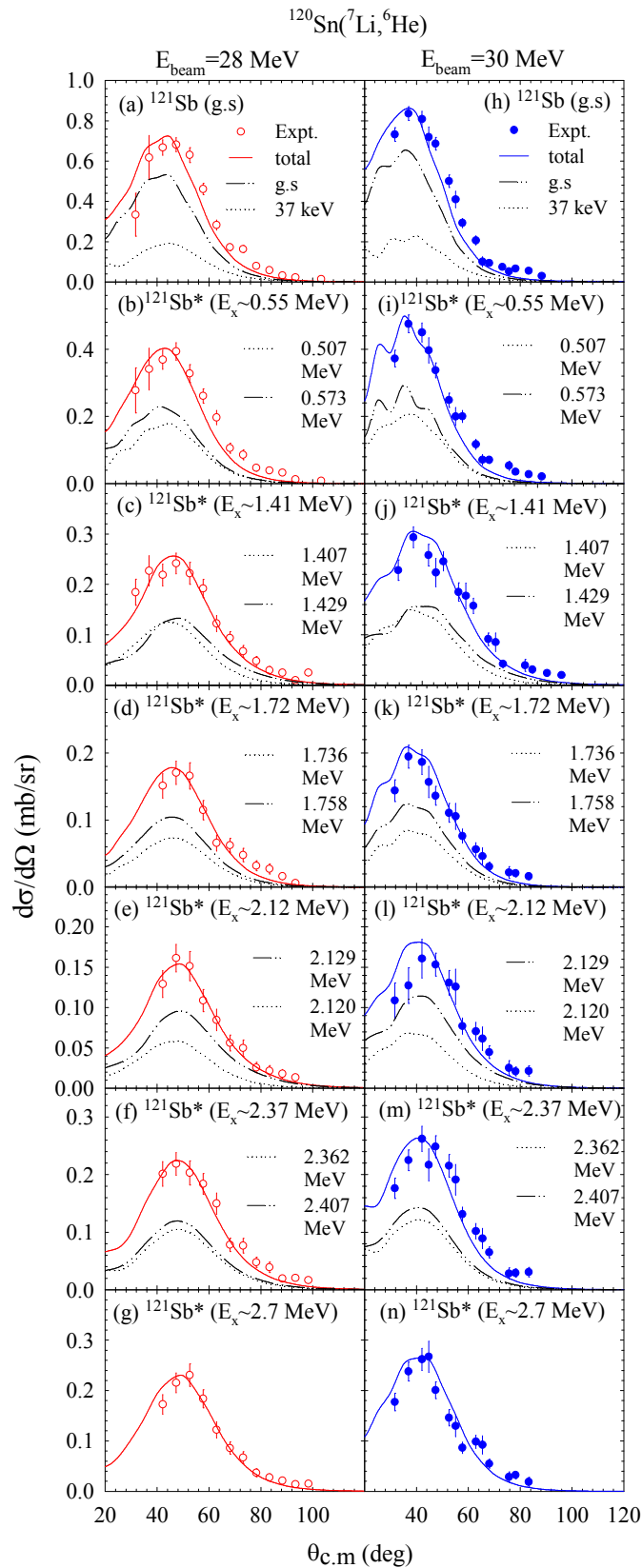


Figure 6.5: Experimental cross sections and CRC calculations for 1-p transfer process ($^7\text{Li}, ^6\text{He}$) at 28 MeV for different excitations of the recoil are shown in (a)-(g). The corresponding data and calculations for 30 MeV are shown in (h)-(n), respectively. The states included in the calculations for each centroid energy are listed in Table 6.1.

Table 6.1: Particle-core spectroscopic factors for the 1-n and 1-p transfer states in residual nuclei.

Nucleus	E_x (expt.) (MeV)	E_x (calc.) (MeV)	State ($n\ell j$)	$C^2S_{\ell j}$	[ref.]	$C^2S_{\ell j}$ (this work)
${}^{121}\text{Sn}$	g.s.	0.00	$2d_{3/2}$	0.439	[140]	
		0.006	$1h_{11/2}$	0.488	[140]	
		0.060	$3s_{1/2}$	0.315	[139]	
	1.10	0.925	$1g_{7/2}$	0.049	[139]	
		1.101	$2d_{3/2}$	0.0125	[139]	
		1.121	$2d_{5/2}$	0.066	[139, 141]	
	2.62	2.589	$2f_{7/2}$	0.052	[139]	
		2.666	$2f_{7/2}$	0.119	[139]	
		2.690	$2f_{7/2}$	0.185	[141]	
	2.95	2.999	$2d_{3/2}$	-		0.151(12)
3.028		$2f_{7/2}$	0.041	[140]		
${}^{121}\text{Sb}$	g.s.	0.00	$2d_{5/2}$	0.915	[143]	
"		0.037	$1g_{7/2}$	1.13	[144]	1.277(93)
0.55	0.507	$2d_{3/2}$	0.295	[143]	0.460(21)	
		$3s_{1/2}$	0.379	[143]	0.590(39)	
1.41	1.407	$2d_{5/2}$	0.183	[142, 143]	0.221(15)	
		$1h_{11/2}$	1.12	[144]	1.311(91)	
1.74	1.736	$2d_{3/2}$	-		0.143(10)	
		$2d_{5/2}$	-		0.152(12)	
2.12	2.120	$2d_{5/2}$	0.085	[143]		
		$1h_{11/2}$	-		0.684(56)	
2.37	2.362	$1g_{7/2}$	-		0.504(42)	
		$1g_{9/2}$	-		0.518(47)	
2.70	2.72	$2d_{5/2}$	0.185	[143]	0.414(39)	

and 0.768 [146], respectively. By coupling the dominant target inelastic states in the model space, the same phenomenological potential is expected to reproduce the experimental differential cross sections for the identified one-nucleon transfer channels. Comparisons between calculations and experimental data fixes the quantum numbers of the final states of the residual nuclei as well as the spectroscopic factors denoting the overlap between initial and final states. The attempt here was to utilize the existing information on spectroscopic factors for the transfer channels and predict the cross sections for all identified states, consistently at both energies.

However, for few of the channels, these structural parameters were either unavailable, or had to be varied (to within 20%-30% with the already measured values) to obtain optimum representation of experimental data. In the limit of detector resolution, due to mixing of indistinguishable closely spaced neighbouring states in both recoils, the angular distribution for each peak was represented by a group of kinematically allowed states in the calculations around that particular reaction Q -value. For some of the states included in the calculations, whose total angular momenta are unknown, they were assigned the highest spin possible for the known angular momentum transfer, in accordance with kinematic selection rules for this system. Extracted spectroscopic factors are estimated through χ^2 -minimization, primarily by normalization in the region of the grazing angle. For such an angular distribution represented by more than one constituent excited state of the residual nucleus, the state with the higher cross section is assigned a higher spectroscopic factor. The channels included in the calculations are listed in Table 6.1, with respective structural information. The solid lines in Figs. 6.4 and 6.5 represent sum of the theoretical cross sections corresponding to one or more closely spaced states which were experimentally unresolved. The individual cross sections of the constituent states have also been shown in the above figures by dotted, dash-dotted and dashed lines.

6.1.1 Calculations for existing data at 44 MeV

An attempt has been made to reproduce existing data, if any, on elastic/inelastic/transfer cross sections for the ${}^7\text{Li}+{}^{120}\text{Sn}$ system at different energies, with the same set of potential and structural parameters and coupling the same number of reaction channels as done for 28 and 30 MeV. There are only a few measurements available in the literature for this system. Tungate *et al.* [147] have measured the angular distributions, at 44 MeV beam energy, for elastic scattering,

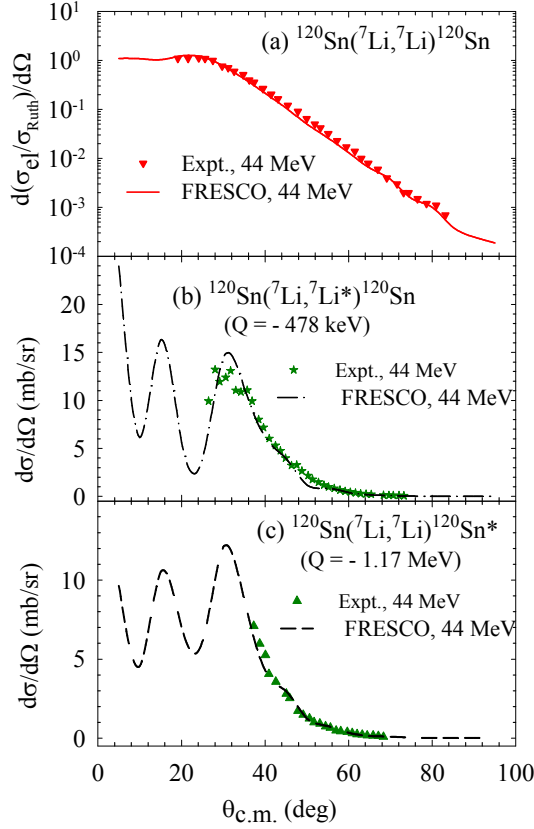


Figure 6.6: Available data at $E_{\text{beam}} = 44$ MeV, for (a,b) elastic scattering and inelastic scattering corresponding to the 478 keV excitation of ${}^7\text{Li}$ from Ref. [147] and (c) inelastic scattering corresponding to the 1.17 MeV state in ${}^{120}\text{Sn}$ taken from Ref. [148]. The lines represent the CRC model calculations.

and inelastic scattering corresponding to ${}^7\text{Li}^*(1/2^-, 0.478 \text{ MeV})$ excitation, while the inelastic data for excitation to the 2_1^+ state of ${}^{120}\text{Sn}$ ($E_x = 1.171 \text{ MeV}$) are available in Ref. [148], at the same beam energy, though with limited angular coverage. These measurements could be effectively reproduced. The results are depicted in Fig. 6.6(a)-6.6(c). This lays emphasis on the validity of the realistic coupling and structural parameters extracted in the present study, which essentially depends on the interplay among the dominant channels in reaction dynamics.

6.2 Systematic model-dependence of complete fusion cross section

For calculations of fusion cross sections, the coupling between the relative motion and internal degrees of freedom causes a splitting in energy of the uncoupled fu-

sion barrier. The resultant distribution of fusion barriers has a shape indicative of the relevant couplings, and is directly manifested as an enhancement of the fusion cross section at energies below the uncoupled barrier. For systems involving weakly bound projectiles, such as ${}^6,7\text{Li}$, presence of additional degrees of freedom owing to the low binding energies of these nuclei is commonly manifested as a suppression in the fusion cross section at above-barrier energies. Many measurements on complete fusion (CF) cross section involving ${}^6,7\text{Li}$ show suppression by various degrees when compared to theoretical CC calculations. However, there is no concrete picture at sub-barrier energies. Some authors have reported an enhancement in experimental CF cross sections at sub-barrier energies [149–152], while some have reported suppression in CF cross sections [153,154]. The discrepant conclusions can be attributed to different CC models that often lead to contrasting results. This difference can be best illustrated by coupling the dominant inelastic scattering channels to the entrance channel while computing fusion. For example, in a recent work on complete fusion in ${}^7\text{Li}+{}^{144,152}\text{Sm}$ system [155], it has been shown that the fusion cross sections calculated by the two most-commonly used codes, CCFULL and FRESKO, are different - with the inclusion of only inelastic couplings of target, the results of FRESKO are much closer to the experimental data in the above barrier region, while the CCFULL results show quite a large suppression in experimental CF cross section compared to theory. The conclusion about the enhancement or suppression of fusion cross sections, thus, becomes model-dependent.

To further explore the above observation in reactions involving ${}^6,7\text{Li}$ as projectiles with different target nuclei of medium to heavy mass, a systematic study [156] has been carried out by means of CC calculations using both FRESKO and CCFULL. Here, only those reactions have been considered whose CF cross sections are already measured, compared with calculations and available in literature. The aim is to analyze the differences in fusion predicted by the two models of calculations, under

Table 6.2: Projectile and target inelastic channels and their corresponding modes of excitations that are included in the CC calculations.

Reaction [Ref.]	Projectile excitations	Target excitations
${}^6\text{Li}+{}^{64}\text{Ni}$ [149]	none	2^+ (vib)
${}^6\text{Li}+{}^{90}\text{Zr}$ [157]	”	$2^+, 3^-$ (vib)
${}^6\text{Li}+{}^{144}\text{Sm}$ [150]	”	3^- (vib)
${}^6\text{Li}+{}^{152}\text{Sm}$ [151]	”	$2^+, 4^+$ (rot)
${}^6\text{Li}+{}^{159}\text{Tb}$ [158]	”	$2^+, 4^+$ (rot)
${}^6\text{Li}+{}^{197}\text{Au}$ [159]	”	$\frac{1}{2}^+$ (vib)
${}^6\text{Li}+{}^{209}\text{Bi}$ [153]	”	$3^-, 5^-$ (vib)
${}^7\text{Li}+{}^{64}\text{Ni}$ [160]	$\frac{1}{2}^-$ (rot)	2^+ (vib)
${}^7\text{Li}+{}^{144}\text{Sm}$ [155]	”	$2^+, 3^-$ (vib)
${}^7\text{Li}+{}^{152}\text{Sm}$ [155]	”	$2^+, 4^+$ (rot)
${}^7\text{Li}+{}^{159}\text{Tb}$ [161]	”	$2^+, 4^+$ (rot)
${}^7\text{Li}+{}^{197}\text{Au}$ [159]	”	$\frac{1}{2}^+$ (vib)
${}^7\text{Li}+{}^{209}\text{Bi}$ [153]	”	$3^-, 5^-$ (vib)

vib : vibrational coupling
rot : rotational coupling

the coupling effects of the dominant low-lying excitations in the target nuclei. For each system, the number of coupled inelastic channels, bare potentials and coupling parameters used are same as given in the original papers. The list of the reaction systems, inelastic channels and excitation modes are given in Table 6.2. Couplings with projectile excitations above the breakup threshold and transfer channels are not included.

6.2.1 Fusion Functions

To compare the fusion data of two different models, a novel reduction method [162] is used that eliminates the geometrical aspects of each system, such as heights and positions of the barriers, sizes and charges of participating nuclei as well as the static effects present in weakly bound nuclei due to their clustered structure, and expresses the differences only in terms of dynamic effects of channel couplings particularly around the barrier energy. This allows comparison of any kind of system in the

same graphic. In this prescription, a parabolic approximation of the fusion barrier is made, as had been done by Wong [163], and the fusion cross section, corresponding to capture of the trajectories of different angular momenta (below the critical angular momentum value, l_c), is given by:

$$\sigma_F^W = \frac{\pi \hbar^2}{2mE_{c.m.}} \sum_{l < l_c} (2l + 1) T_l(E_{c.m.}) \quad (6.4)$$

For the parabolic barrier, in the centre of mass frame, the transmission probability for l^{th} partial wave [163] is:

$$T_l(E_{c.m.}) = \frac{1}{1 + \exp \left[\frac{2\pi}{\hbar\omega} \left(V_B + \frac{l(l+1)\hbar^2}{2mR_B^2} - E_{c.m.} \right) \right]} \quad (6.5)$$

where V_B , R_B , $\hbar\omega$ are, respectively, the barrier height, position and curvature at R_B . This leads to,

$$\sigma_F^W = \frac{\hbar\omega R_B^2}{2E_{c.m.}} \ln \left[1 + \exp \left(\frac{2\pi(E_{c.m.} - V_B)}{\hbar\omega} \right) \right] \quad (6.6)$$

Canto *et al.* suggested reducing the incident energies to a dimensionless form, $x = \frac{E_{c.m.} - V_B}{\hbar\omega}$. When no couplings are involved in a reaction system, σ_F^W accurately predicts the fusion cross section and that leads to a general, system-independent fusion function of the dimensionless variable x , called the Universal Fusion Function (UFF) given by:

$$\text{UFF}(x) = \frac{2E_{c.m.}}{\hbar\omega R_B^2} \sigma_F^W = \ln [1 + \exp(2\pi x)] \quad (6.7)$$

Akin to this prescription, the corresponding experimental fusion cross section leads to a reaction fusion function, given by

$$F(x) = \frac{2E_{c.m.}}{\hbar\omega R_B^2} \sigma_F^{exp} * \left(\frac{\sigma_F^W}{\sigma_F^{CC}} \right) \quad (6.8)$$

Here, σ_F^{exp} incorporates the global effect of couplings to all bound as well as unbound channels. The term within the brackets is a normalization factor, with σ_F^{CC} as theoretical fusion cross section obtained from coupled-channels calculations. This formalism isolates the effect of relevant bound channel couplings included in the calculations, such as the directly populated inelastic excitations of the projectile and target, leading to $F(x) = UFF(x) * \frac{\sigma_F^{exp}}{\sigma_F^{CC}}$. Any deviation of $F(x)$ from $UFF(x)$ is attributed to dynamic channel coupling effects, and can be effectively used for pointing out model-dependent differences in fusion within a single system. In the absence of transfer channels with large, positive Q -values, Canto *et al.* have suggested that the deviation may be attributed predominantly to the breakup channels, that have not been explicitly included while computing σ_F^{CC} .

In this way, data for different systems (listed in Table 6.1) were compared between FRESKO and CCFULL directly by calculating function $F(x)$. Figures 6.7 and 6.8 show results obtained using FRESKO and CCFULL, plotted in linear and logarithmic scales, respectively. Fig. 6.7 particularly emphasizes the above barrier ($x > 0$) model-dependence of fusion, while Fig. 6.8 lays emphasis on the below barrier ($x < 0$) model-dependence. It is observed that the CCFULL results do not agree with those predicted by FRESKO, even though the CC calculations by both models include the same inelastic excitation channels and same bare potentials. Fig. 6.7 shows that the experimental fusion functions $F(x)$ (symbols) for all the reactions induced by both ${}^6\text{Li}$ as well as ${}^7\text{Li}$ projectiles are suppressed compared to $UFF(x)$ (solid line) at above barrier energies, showing a universal behavior independent of target nuclei. However, the degree of fusion suppression is not only different for different projectiles but also different for same projectile when $F(x)$ is calculated using two different CC models. The above barrier average suppression percentages for the ${}^6\text{Li}$ -induced reactions, obtained using FRESKO and CCFULL generated results, are $\sim 22\%$ and 29% respectively, and $\sim 13\%$ and 23% for the ${}^7\text{Li}$ -induced

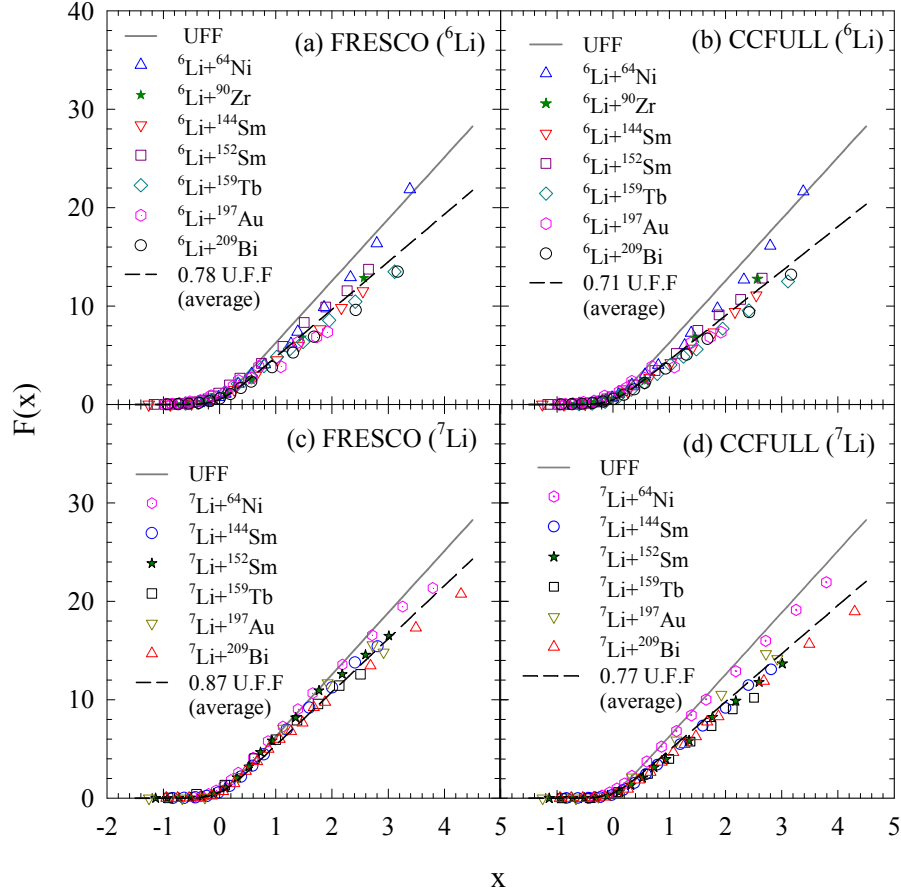


Figure 6.7: Experimental fusion functions using the results of FRESCO and CCFULL calculations for several reactions involving weakly bound projectiles ${}^6,{}^7\text{Li}$. The solid lines represent Universal Fusion Functions (UFFs) obtained from Eqn. 6.7, and dashed lines represent re-normalized UFFs to show the average suppression factors in experimental CF at above barrier energies.

reactions. The suppression is higher in case of CCFULL than FRESCO irrespective of the projectile. At sub-barrier energies, it can be observed from Fig. 6.8(a,b) that for all ${}^6\text{Li}$ -induced reactions, the experimental fusion functions are enhanced compared to the UFF irrespective of the model used for calculating σ_F^{CC} . But the degree of enhancement in $F(x)$ compared to $\text{UFF}(x)$ at sub-barrier energies is noticeably higher when FRESCO generated σ_F^{CC} is used to calculate $F(x)$. For ${}^7\text{Li}$ induced fusion reactions, FRESCO predicts a mixed result at below barrier region as seen in Fig. 6.8(c). For systems like ${}^7\text{Li}+{}^{152}\text{Sm}$, ${}^{159}\text{Tb}$, there is an enhancement while there is no enhancement/suppression for ${}^7\text{Li}+{}^{144}\text{Sm}$, ${}^{197}\text{Au}$, ${}^{209}\text{Bi}$ systems. On the other

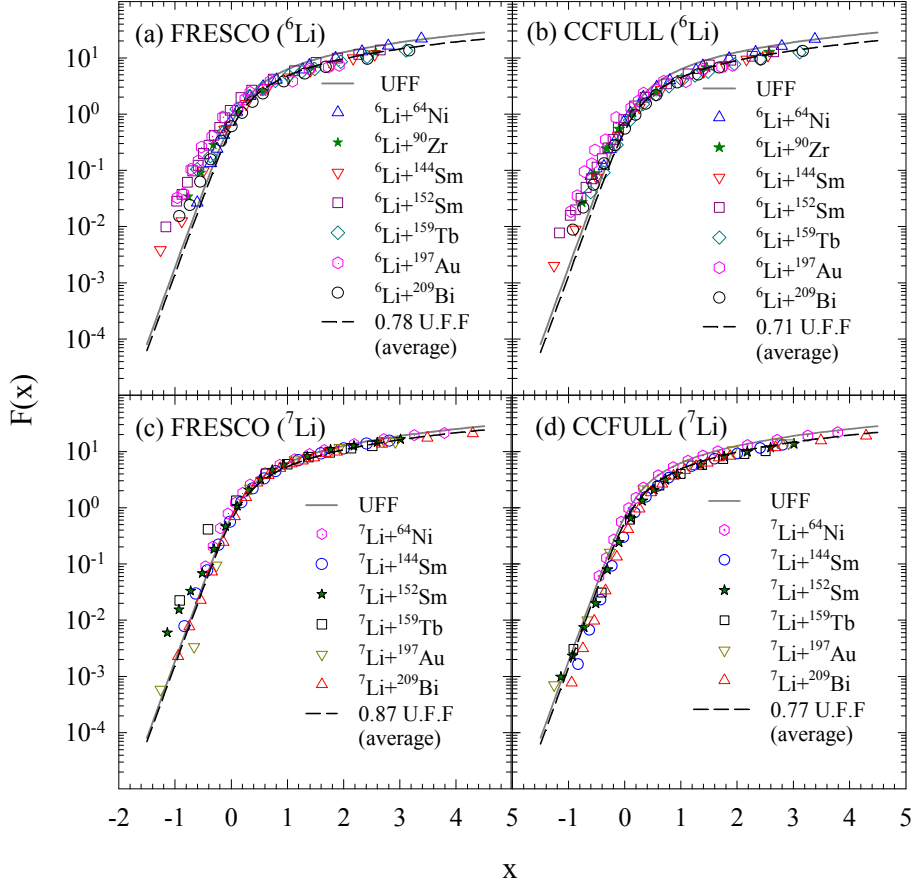


Figure 6.8: Same as Fig. 6.7, but plotted in logarithmic scale.

hand, according to CCFULL, there is a suppression over the entire energy range as shown in Fig. 6.8(d). The larger deviations of $F(x)$ from $UFF(x)$ at both sub- and above-barrier energies observed between the reactions induced by ${}^6\text{Li}$ and ${}^7\text{Li}$ projectiles can be understood in terms of the difference in breakup coupling related to the projectile breakup threshold energy - ${}^6\text{Li}$ has smaller breakup threshold energy (~ 1.48 MeV) compared to ${}^7\text{Li}$ (~ 2.47 MeV). However, the difference observed in the results for the same system but obtained from two models is more interesting. Fusion cross sections (σ_F^{CC}) calculated using two models are found to be different despite using same bare potentials, same coupling parameters and inclusion of same inelastic channels. As discussed in Chapter 3, the theoretical formalisms for two models are very different leading to a significant difference between the fusion functions calculated by them.

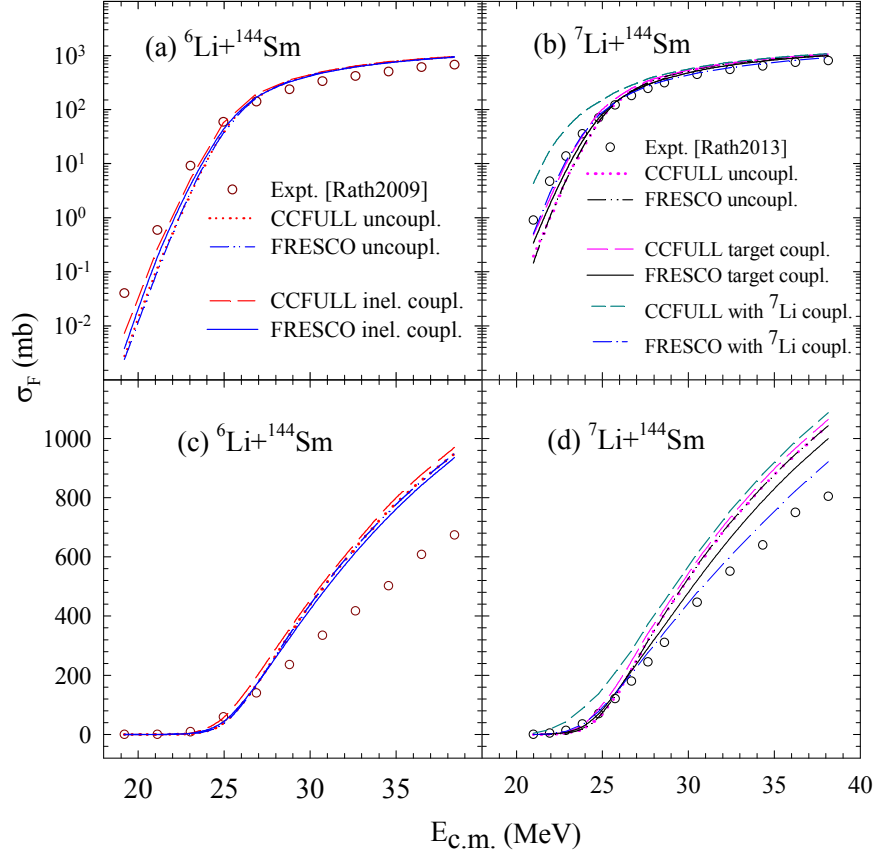


Figure 6.9: Differences in the effect of inelastic couplings between CCFULL and FRESKO for (a,c) ${}^6\text{Li}+{}^{144}\text{Sm}$ and (b,d) ${}^7\text{Li}+{}^{144}\text{Sm}$ reactions plotted in log and linear scale respectively. Calculated fusion cross sections are compared with experimental data taken from Refs.(Rath2009: [150]) and (Rath2013: [155]) respectively.

To investigate the origin of the above difference, fusion cross sections, σ_F^{CC} and $\sigma_F^{\text{uncoupl}}$, have been calculated by the two models with and without inelastic couplings, respectively. The results for two typical reactions e.g., ${}^6,7\text{Li}+{}^{144}\text{Sm}$, are shown in Fig. 6.9. The cross sections, $\sigma_F^{\text{uncoupl}}$, obtained from the two models, are found to be identical. This implies that their theoretical formalisms are equivalent when the fusion is calculated through a one-dimensional barrier. However, the results are different when inelastic channels are coupled i.e., when a multidimensional barrier is introduced. At above barrier energies the fusion cross section obtained from CCFULL are higher than the uncoupled cross sections. In contrast, the cross sections obtained from FRESKO with inelastic couplings are smaller than the ones

without any coupling.

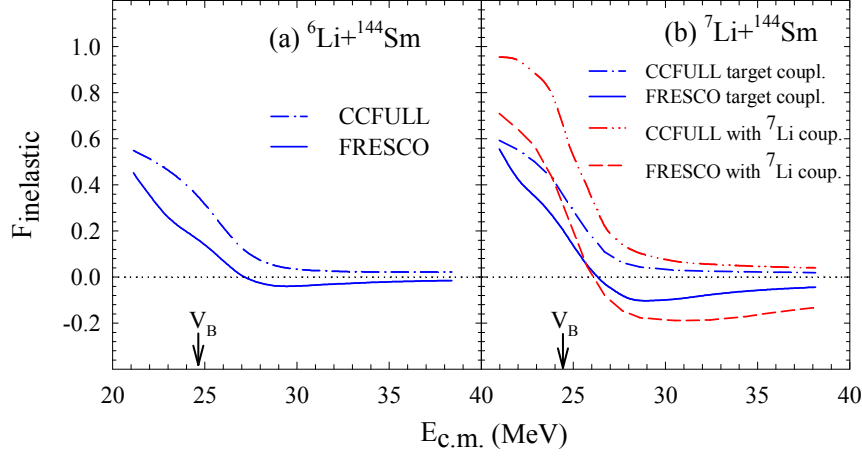


Figure 6.10: The quantity $F_{\text{inelastic}} \left(= 1 - \sigma_F^{\text{uncoupl}} / \sigma_F^{CC} \right)$ derived from the coupled and uncoupled fusion cross sections calculated using CCFULL and FRESCO.

Further, to amplify the above differences over the entire energy range, a quantity called $F_{\text{inelastic}} = \left(1 - \frac{\sigma_F^{\text{uncoupl}}}{\sigma_F^{CC}} \right)$ is derived as a function of energy, and shown in Fig. 6.10. The $F_{\text{inelastic}}$ obtained from CCFULL results was found to be a positive quantity throughout the energy range for both the systems, while it attains negative values for FRESCO in the high energy region. In particular, at barrier energies, the enhancement due to target inelastic couplings in ${}^6\text{Li}+{}^{144}\text{Sm}$ system is $\sim 33\%$ for CCFULL and $\sim 16\%$ for FRESCO, while in the ${}^7\text{Li}+{}^{144}\text{Sm}$ system, it is around 44% for CCFULL and 20% for FRESCO with only target couplings, and around 66% for CCFULL and 33% for FRESCO when projectile coupling is also included, as seen in Figs. 6.10(a) and 6.10(b), respectively. Couplings to the projectile bound excited state mainly redistribute the flux that has already penetrated the Coulomb barrier [64]. However, CCFULL, unlike FRESCO, considers the projectiles to be spin-less in their ground state. With such differences in calculated fusion cross sections and experimental fusion functions derived using two different models based on two different theoretical formalisms, one needs to be careful while concluding about enhancement or suppression of experimental fusion cross sections on comparison

with either of the two CC calculations.

6.2.2 The case of a tightly-bound projectile

It is often observed that the potential parameters used in simplified CC codes (e.g. CCFULL) to reproduce experimental fusion cross sections do not reproduce elastic and direct reaction channels when used as input to FRESKO or other codes that calculate these cross sections. To this effect, an exercise aimed at using realistic parameters for potentials and couplings that are capable of explaining simultaneously the measured cross sections of elastic scattering, inelastic scattering and fusion channels, and find the differences in the fusion cross sections calculated by two CC codes, is undertaken for a reaction system involving a tightly bound projectile, $^{16}\text{O} + ^{148}\text{Sm}$ [164–166]. The target ^{148}Sm being near spherical, the most important channels to be coupled with elastic channels are the inelastic excitations. In the coupled-channels calculations using FRESKO, two inelastic channels corresponding to the low-lying 2^+ (0.55 MeV) and 3^- (1.16 MeV) excitations of ^{148}Sm and one projectile inelastic state (3^- , 6.13 MeV) are included along with the elastic channel. A real potential of WS volume form with strength, radius and diffuseness parameters of 76.0 MeV, 1.18 fm and 0.67 fm respectively has been used for the entrance channel. With FRESKO, considering that all the relevant channels are explicitly included in the coupling, the fusion cross section is estimated from the absorption by a short range imaginary potential of WS square form, with strength, radius and diffuseness parameters equal to 10 MeV, 1.0 fm and 0.4 fm respectively. For inelastic couplings, the deformation parameters are obtained from Refs. [165, 167], assuming $\delta_\lambda^{ch} = \delta_\lambda^m$. The typical FRESKO results for elastic and inelastic scattering, at $E_{\text{lab}} = 66$ MeV, have been compared with the experimental cross sections in Figs. 6.11(a) and 6.11(b) respectively. Using the same potential and coupling parameters, fusion cross sections have been calculated at different beam energies and shown as a solid line in

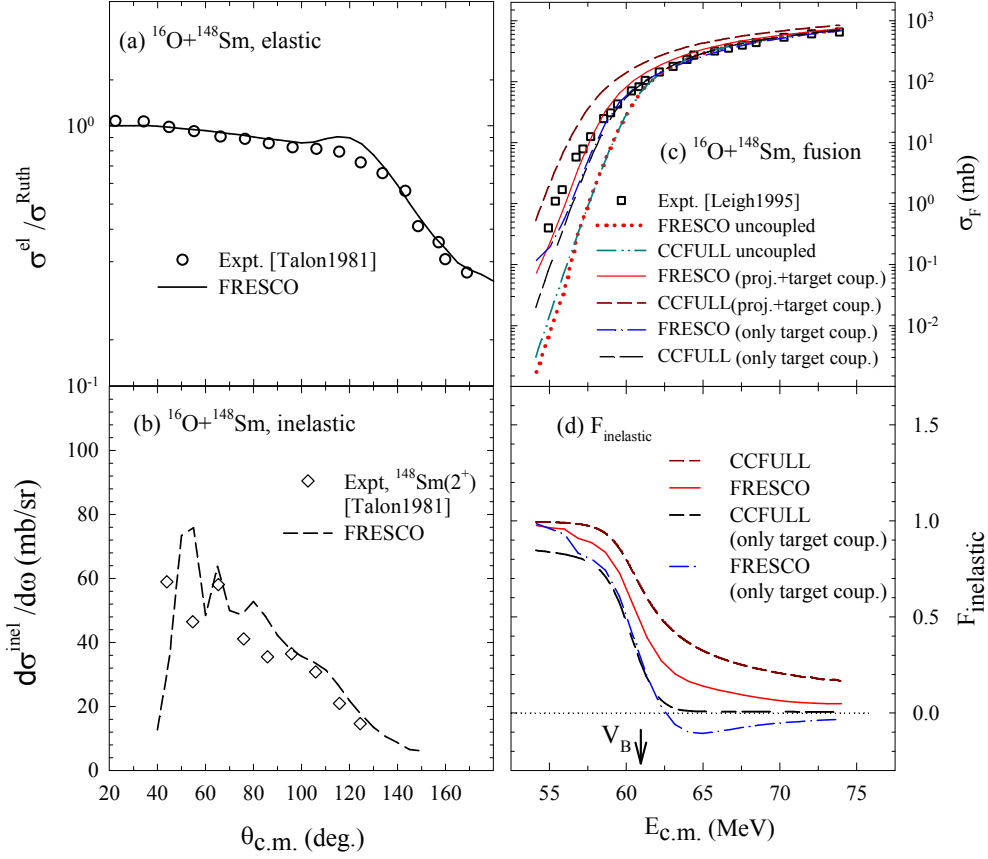


Figure 6.11: (a,b) Experimental cross section for elastic (circles) and inelastic scattering corresponding to 2^+ (0.55 MeV) state of ^{148}Sm (diamonds) taken from Ref. (Talon1981: [164]) are compared with FRESKO results. (c) Experimental fusion cross sections from Ref. (Leigh1995: [165]) are represented by squares along with the theoretical results for fusion obtained from both FRESKO and CCFULL are represented by lines. (d) The quantity $F_{\text{inelastic}}$ obtained from the results of CCFULL and FRESKO with (without) projectile excitation are represented by dashed (long-short) and solid (dash-dot) lines respectively.

Fig. 6.11(c) along with the experimental data [165]. The results of the coupled-channels calculations using FRESKO reasonably reproduces elastic, fusion and one of the inelastic channels simultaneously. A small deviation in the calculations from the experimental data is expected due to (i) exclusion of some of the inelastic and transfer channels in the coupling and (ii) absence of long range imaginary potential to simulate these excluded direct reaction channels. On the other hand, CCFULL does not calculate elastic or any direct reaction cross section. So, only the fusion cross sections have been calculated using the same parameters as used in FRESKO, and the results are shown as dashed line in Fig. 6.11(c). Once again, a difference in

fusion cross sections calculated with full couplings from two codes is observed. This difference has been amplified in the calculation of $F_{\text{inelastic}}$ as shown in Fig. 6.11(d). The above calculations have been repeated using both the codes without including the projectile excitation and the corresponding values for fusion and $F_{\text{inelastic}}$ have also been plotted in Fig. 6.11(c) and 6.11(d) respectively. The difference in this case is mainly prevalent at above-barrier energies. The comparative study in the above example suggests that one should couple several directly populated excited states of projectile and target and use realistic parameters for potential and couplings to explain simultaneously the elastic and all non-elastic channels. And this is possible when a more generalized code like FRESKO is used and the experimental data for both fusion and elastic along with as many direct reaction channels are available for the particular reaction system.

6.3 Summary & Conclusions

The influence of internal degrees of freedom is of fundamental importance in describing the different phenomena which may occur during a collision - nucleon-transfers, fusion, etc. The coupling of the low-lying excitations of colliding nuclei to their relative motion has significant influence on cross sections of elastic scattering, complete fusion, as well as all intermediate peripheral channels. To this effect, a simultaneous description of elastic scattering, inelastic excitations and one-nucleon transfer channels has been attempted using the optical potential and structural deformation parameters determined in the previous chapters. New spectroscopic factors have been exclusively assigned for some states in residual nuclei populated by the nucleon-transfer reactions. A direct effect of inelastic couplings in calculating the fusion cross section through a multidimensional barrier is seen to be model dependent. Such a comparison between experimental and theoretical values of reaction observables can be useful as a test for nuclear reaction models.

Chapter 7

Future outlook

In this thesis work, crucial aspects of nuclear collectivity, on an absolute scale, have been systematically addressed along an isotopic chain of stable nuclei, by heavy-ion inelastic scattering with ${}^7\text{Li}$ and ${}^{12}\text{C}$ probes. The elaborate set of experimental data and theoretical calculations presented here for the low-lying transitions in different Sn isotopes is expected to provide an insight into the probe-dependence of the basic excitation mechanisms in nuclei, for deducing the intrinsic deformation characteristics. The present considerations also illustrate the path and problems that would arise when one discusses the deformation properties, and the exclusive intrinsic contributions of the neutron and proton distributions, for unstable chains of isotopes from upcoming facilities, exploring such probe-dependent characteristics. Besides the collective low-lying excitations, such features of probe-dependent inelastic scattering could also be explored for the known quadrupole and octupole resonances ($E_x > 5$ MeV) in nuclei.

Additionally, the effects of dynamic structural couplings in nuclear collisions that influence the cross sections of other reaction channels, such as transfer processes as well as fusion, have been discussed in this thesis, which also act as a test for available nuclear models. Impending studies of similar reactions with weakly bound unstable nuclei, e.g. ${}^{11}\text{Be}$ or ${}^{11}\text{Li}$ [168–170], where incorporating coupled-channels

effects is an issue, are also of tremendous interest. Such nuclei are known to have larger radii as well as significantly enhanced reaction cross sections compared to their stable counterparts. Measurements with weakly bound stable nuclei such as ${}^7\text{Li}$, with better understood structures, are relatively easier, due to the higher beam intensities. The understanding of the reaction dynamics for such stable projectiles acts as a reference for investigating (i) the dynamic effects of probe-size and nature of probe-target interaction, with unstable projectiles, on target structural parameters, that are expected to be of similar complexity as discussed in this thesis, and (ii) the preferential J and Q selectivity of single nucleon transfer processes in populating different excited states of the residual nuclei, wherefrom, new spectroscopic factors can be extracted. Such detailed studies with unstable projectiles are expected to provide a good foundation towards understanding their reaction mechanisms and the impact on fusion cross sections.

A satisfactory compliance is also reported in the present work between the results of heavy-ion scattering and level-lifetime measurement, with reduced uncertainties, for the ${}^{120}\text{Sn}$ isotope. In the near future, a similar investigation could be attempted to explore the lifetime and branching ratio for the decay of the 3_1^- state in ${}^{120}\text{Sn}$ into its $E1$ (strong) and $E3$ (weak) components, with no exclusive measurements till date, and compare the $B(E3; 0_{g.s.}^+ \rightarrow 3_1^-)$ value with that from nuclear scattering. In addition, fresh measurements, employing either the particle- γ coincidence technique (crucial for selecting weak transitions), or from inclusive γ yields, for the 2_1^+ , 3_1^- and 4_1^+ level-lifetimes in the other stable and unstable Sn isotopes, with suitable target-backing combinations, can also be expected to lead to improved estimates, to address the existing discrepancies between the different measurements of the transition probabilities. This also draws attention to the need for improved theoretical calculations to systematically explain the trend of the collective properties ranging from the neutron-deficient to the neutron-rich isotopes.

Bibliography

- [1] E. Epelbaum, H.-W. Hammer, and Ulf-G. Meißner. *Rev. Mod. Phys.*, 81:1773–1825, 2009.
- [2] Gertrude Scharff-Goldhaber. *Phys. Rev.*, 90:587–602, 1953.
- [3] A. Bohr and B. R. Mottelson. *Nuclear Structure*, volume 2. Benjamin, New York, 1975.
- [4] A. M. Bernstein, V. R. Brown, and V. A. Madsen. *Comments Nucl. Part. Phys.*, 11(5):203–215, 1983.
- [5] V. R. Brown and V. A. Madsen. *Phys. Rev. C*, 11:1298–1311, 1975.
- [6] M. E. Rose. *Elementary Theory of Angular Momentum*. Dover, New York, 1995.
- [7] Samuel S. M. Wong. *Introductory Nuclear Physics*. Wiley-VCH, Weinheim, Germany, 2 edition, 2004.
- [8] J. Suhonen. *From Nucleons to Nucleus*. Springer, Berlin, Germany, 2007.
- [9] V. F. Weisskopf. *Phys. Rev.*, 83:1073, 1951.
- [10] N. A. Jelley. *Fundamentals of Nuclear Physics*. Cambridge University Press.
- [11] A. G. Sitenko and V. K. Tartakovskii. *Lectures on the theory of the nucleus*. Pergamon, United Kingdom, 1975.

-
- [12] George F. Bertsch. *Scientific American*, 248:62–73, 1983.
- [13] Thomas Möller. *Aspects of nuclear collectivity studied in projectile Coulomb excitation experiments*. PhD thesis, Technische Universität, Darmstadt, 2014.
- [14] R. da Silveira. *Rainbow effects in nuclear scattering*. 1989.
- [15] V. I. Chuev, Yu. A. Glukhov, V. I. Manko, et al. *Phys. Lett. B*, 42:63 – 65, 1972.
- [16] W. T. Pinkston and G. R. Satchler. *Nucl. Phys.*, 27:270–283, 1961.
- [17] A. Ansari and P. Ring. *Phys. Rev. C*, 74:054313, 2006.
- [18] S. Terashima, H. Sakaguchi, H. Takeda, et al. *Phys. Rev. C*, 77:024317, 2008.
- [19] N. Baron, R. F. Leonard, John L. Need, et al. *Phys. Rev.*, 146:861, 1966.
- [20] G. Bruge, J.C. Faivre, H. Faraggi, and A. Bussiere. *Nucl. Phys. A*, 146:597–658, 1970.
- [21] P. Barreau and J. B. Bellicard. *Phys. Rev. Lett.*, 19:1444–1446, 1967.
- [22] T. H. Curtis, R. A. Eisenstein, D. W. Madsen, and C. K. Bockelman. *Phys. Rev.*, 184:1162, 1969.
- [23] N. G. Jonsson, A. Backlin, J. Kantele, et al. *Nucl. Phys. A*, 371:333, 1981.
- [24] D. G. Alkhazov, Y. P. Gangrskii, I. K. Lemberg, and Y. I. Udralov. *Bull. Acad. Sci. USSR (Phys. Ser.)*, 28:149, 1965.
- [25] Irving O. Morales, P. Van Isacker, and I. Talmi. *Phys. Lett. B*, 703:606 – 608, 2011.
- [26] A. Banu, J. Gerl, C. Fahlander, et al. *Phys. Rev. C*, 72:061305(R), 2005.

-
- [27] D. C. Radford, C. Baktash, J. R. Beene, et al. *Nucl. Phys. A*, 746:83c – 89c, 2004.
- [28] P. Doornenbal, P. Reiter, H. Grawe, et al. *Phys. Rev. C*, 78:031303, 2008.
- [29] C. Vaman, C. Andreoiu, D. Bazin, et al. *Phys. Rev. Lett.*, 99:162501, 2007.
- [30] T. Otsuka, T. Suzuki, R. Fujimoto, et al. *Phys. Rev. Lett.*, 95:232502, 2005.
- [31] L. Gaudefroy, O. Sorlin, D. Beaumel, et al. *Phys. Rev. Lett.*, 97:092501, 2006.
- [32] J. Cederkäll, A. Ekström, C. Fahlander, et al. *Phys. Rev. Lett.*, 98:172501, 2007.
- [33] A. Ansari. *Phys. Lett. B*, 623:37 – 42, 2005.
- [34] A. Jungclaus, J. Walker, J. Leske, et al. *Phys. Lett. B*, 695:110 – 114, 2011.
- [35] M.C. East, A.E. Stuchbery, A.N. Wilson, et al. *Phys. Lett. B*, 665:147 – 151, 2008.
- [36] R. Kumar, M. Saxena, P. Doornenbal, et al. *Phys. Rev. C*, 96:054318, 2017.
- [37] J. M. Allmond, A. E. Stuchbery, A. Galindo-Uribarri, et al. *Phys. Rev. C*, 92:041303(R), 2015.
- [38] S. Raman, C. W. Nestor, and P. Tikkanen. *At. Data Nucl. Data Tables*, 78:1–128, 2001.
- [39] B. Pritychenko, M. Birch, B. Singh, and M. Horoi. *At. Data Nucl. Data Tables*, 107:1 – 139, 2016.
- [40] H. Jiang, Y. Lei, G. J. Fu, et al. *Phys. Rev. C*, 86:054304, 2012.
- [41] O. Beer, A. El Behay, P. Lopato, et al. *Nucl. Phys. A*, 147:326–368, 1970.

-
- [42] W. Makofske, W. Savin, H. Ogata, and T. H. Kruse. *Phys. Rev.*, 174:1429–1441, 1968.
- [43] R. J. Lombard and X. Campi-Benet. *Nucl. Phys.*, 83:303 – 320, 1966.
- [44] C. J. Veje. *Mat. Fys. Medd . Dan. Vid. Selsk.*, 35:1, 1966.
- [45] V. Gillet, B. Giraud, and M. Rho. *Phys. Rev.*, 178:1695–1697, 1969.
- [46] V. Nanal, R. Pillay, J. N. Karande, et al. *Proceedings of HIAT09, Venice*, TH-07:174, 2009.
- [47] H. Bethe und J. Ashkin. *Experimental Nuclear Physics*. Cambridge University Press, 1953.
- [48] A. Chatterjee, K. Ramachandran, S. Singh, et al. *DAE Symp. Nucl. Phys.*, 45A:145, 2002.
- [49] R. Palit, S. Saha, J. Sethi, et al. *J. Phys.: Conf. Ser.*, 420:012159, 2013.
- [50] H. Tan, W. Hennig, M. Walby, et al. In *2008 IEEE Nucl. Sci. Symp. Conf. Rec.*, pages 3196–3200, 2008.
- [51] R. Palit, S. Saha, J. Sethi, et al. *Nucl. Instrum. Methods Phys. Res. A*, 680:90 – 96, 2012.
- [52] G. R. Satchler. *Direct Nuclear Reactions*. Clarendon Press, Oxford, 1983.
- [53] C. H. Dasso and S. Landowne. *Comput. Phys. Comm.*, 46:187 – 191, 1987.
- [54] J. Fernández-Niello, C. H. Dasso, and S. Landowne. *Comput. Phys. Comm.*, 54:409 – 412, 1989.
- [55] M. Dasgupta, A. Navin, Y. K. Agarwal, et al. *Nucl. Phys. A*, 539:351 – 369, 1992.

- [56] K. Hagino, N. Rowley, and A. T. Kruppa. *Comput. Phys. Commun.*, 123:143–152, 1999.
- [57] I. J Thompson and F. M. Nunes. *Nuclear Reactions for Astrophysics*. Cambridge University Press, New York, 2009.
- [58] G. R. Satchler. *Nucl. Phys.*, 45:197 – 208, 1963.
- [59] G. R. Satchler and W. G. Love. *Physics Reports*, 55:183 – 254, 1979.
- [60] N. Austern, R. M. Drisko, E. C. Halbert, and G. R. Satchler. *Phys. Rev.*, 133:B3–B16, 1964.
- [61] M. Beckerman. *Rep. Prog. Phys.*, 51:1047–1103, 1988.
- [62] C. L. Jiang, H. Esbensen, K. E. Rehm, et al. *Phys. Rev. Lett*, 89:052701, 2002.
- [63] K. Hagino and N. Takigawa. *Prog. Theo. Phys.*, 123:1061–1106, 2012.
- [64] A. Diaz-Torres, I. J. Thompson, and C. Beck. *Phys. Rev. C*, 68:044607, 2003.
- [65] M. Yahiro, K. Ogata, T. Matsumoto, and K. Minomo. *Progress of Theoretical and Experimental Physics*, 2012(1), 2012.
- [66] N. Austern and J. S. Blair. *Ann. Phys.*, 33:15–64, 1965.
- [67] A. M. Bernstein. *Advances in Nuclear Physics*, volume 3. Springer, 1969.
- [68] J. Cook, A. K. Abdallah, M. N. Stephens, and K. W. Kemper. *Phys. Rev. C*, 35:126–136, 1987.
- [69] T. Davinson, V. Rapp, A.C. Shotter, et al. *Phys. Lett. B*, 139:150–153, 1984.
- [70] Dao T. Khoa, W. von Oertzen, and A. A. Ogloblin. *Nucl. Phys. A*, 602:98 – 132, 1996.

- [71] I. Tanihata, T. Kobayashi, O. Yamakawa, et al. *Phys. Lett. B*, 206:592 – 596, 1988.
- [72] A. Krasznahorkay, A. Balanda, J. A. Bordewijk, et al. *Nucl. Phys. A*, 567:521 – 540, 1994.
- [73] C. W. De Jager, H. De Vries, and C. De Vries. *Atomic Data and Nuclear Data Tables*, 14:479, 1974.
- [74] Randolph Pohl, Aldo Antognini, François Nez, et al. *Nature*, 466:213–216, 2010.
- [75] S. Kopecky, J. A. Harvey, N. W. Hill, et al. *Phys. Rev. C*, 56:2229–2237, 1997.
- [76] F. G. Perey and G. R. Satchler. *Nucl. Phys. A*, 97:515 – 528, 1967.
- [77] C. Beck, N. Keeley, and A. Diaz-Torres. *Phys. Rev. C*, 75:054605, 2007.
- [78] B. Buck and A. C. Merchant. *Journal of Physics G: Nuclear Physics*, 14:L211, 1988.
- [79] L. C. Chamon, B. V. Carlson, L. R. Gasques, et al. *Phys. Rev. C*, 66:014610, 2002.
- [80] W.J. Vermeer, M.T. Esat, J.A. Kuehner, et al. *Phys. Lett. B*, 122:23 – 26, 1983.
- [81] M. Kumar Raju, J.N. Orce, P. Navrátil, et al. *Phys. Lett. B*, 777:250 – 254, 2018.
- [82] W.J. Thompson and J.S. Eck. *Physics Letters B*, 67:151 – 154, 1977.
- [83] L. Jarczyk, B. Kamys, A. Magiera, et al. *Nucl. Phys. A*, 518:583 – 592, 1990.
- [84] H. G. Bohlen, M. R. Clover, G. Ingold, et al. *Z. Phys. A*, 308:121–131, 1982.

-
- [85] H. Crannell, T. A. Griffy, L. R. Suelzle, and M. R. Yearian. *Nucl. Phys. A*, 90:152, 1967.
- [86] H. Rebel. *Elastic and Inelastic Scattering of Alpha Particles and the Folding Model*. 1974.
- [87] D. T. Khoa, E. Khan, G. Colò, and N. Van Giai. *Nucl. Phys. A*, 706:61, 2002.
- [88] D. T. Khoa. *Phys. Rev. C*, 68:011601, 2003.
- [89] A. Kundu, S. Santra, A. Pal, et al. *Phys. Rev. C*, 99:034609, 2019.
- [90] A. Kundu, S. Santra, A. Pal, et al. *Phys. Rev. C*, 100:024614, 2019.
- [91] D. L. Hendrie. *Phys. Rev. Lett.*, 31:478–481, 1973.
- [92] R. K. Jolly. *Phys. Rev.*, 139:B318–B330, 1965.
- [93] P. P. Singh, Q. Li, P. Schwandt, et al. *Pramana - J. Phys.*, 27:747, 1986.
- [94] X Chen, Y-W Lui, HL Clark, et al. *Physical Review C*, 76:054606, 2007.
- [95] L. R. Gasques, A. S. Freitas, L. C. Chamon, et al. *Phys. Rev. C*, 97:034629, 2018.
- [96] V. Yu. Ponomarev. private communication.
- [97] V. G. Soloviev. *Theory of Atomic Nuclei: Quasiparticles and Phonons*. Institute of Physics Publishing, Bristol, 1992.
- [98] Tomoaki Togashi, Yusuke Tsunoda, Takaharu Otsuka, et al. *Phys. Rev. Lett.*, 121:062501, 2018.
- [99] S. H. Sie, J. S. Geiger, , et al. *AECL-4147*, page 14, 1972.
- [100] B. Hrastnik, V. Knapp, and M. Vlatkovic. *Nucl. Phys.*, 89:412, 1966.

-
- [101] J. Bryssinck, L. Govor, V. Yu. Ponomarev, et al. *Phys. Rev. C*, 61:024309, 2000.
- [102] E. K. Warburton, J. W. Olness, and A. R. Poletti. *Phys. Rev.*, 160:938–963, 1967.
- [103] S. Devons, G. Manning, and D. St. P. Bunbury. *Proc. Phys. Soc. A*, 68:18–31, 1955.
- [104] K. Kitao, Y. Tendow, and A. Hashizume. *Nuclear Data Sheets*, 96:241 – 390, 2002.
- [105] S. Das, S. Samanta, R. Bhattacharjee, et al. *Nucl. Instrum. Methods Phys. Res. A*, 841:17 – 23, 2017.
- [106] R. Bhattacharjee, S. S. Bhattacharjee, K. Basu, et al. *Phys. Rev. C*, 90:044319, 2014.
- [107] R. Nordhagen, B. Elbek, and B. Herskind. *Nucl. Phys. A*, 104:353 – 385, 1967.
- [108] R. G. Stokstad, I. A. Fraser, J. S. Greenberg, et al. *Nucl. Phys. A*, 156:145 – 169, 1970.
- [109] A. Gavron. *Phys. Rev. C*, 21:230–236, 1980.
- [110] C. M. Jachcinski, D. G. Kovar, R. R. Betts, et al. *Phys. Rev. C*, 24:2070–2075, 1981.
- [111] Jun Chen. *Nucl. Data Sheets*, 149:1 – 251, 2018.
- [112] G. C. Ball, J. S. Forster, F. Ingelbretsen, and C. F. Monahan. *Nucl. Phys. A*, 180:517 – 528, 1972.
- [113] J. C. Wells and N. R. Johnson. *LINESHAPE: A Computer Program for Doppler Broadened Lineshape Analysis*, page 44. 1991.

- [114] K. Nakai, J. L. Québert, F. S. Stephens, and R. M. Diamond. *Phys. Rev. Lett.*, 24:903–906, 1970.
- [115] P. J. Nolan and J. F. Sharpey-Schafer. *Rep. Prog. Phys.*, 42:1–86, 1979.
- [116] A. E. Blaugrund. *Nucl. Phys.*, 88:501 – 512, 1966.
- [117] J. Lindhard, M. Scharff, and H. E. Schiott. *Mat. Fys. Medd. Dan. Vid. Selsk.*, 33, 1963.
- [118] L. C. Northcliffe and R. F. Schilling. *At. Data Nucl. Data Tables*, 7:233 – 463, 1970.
- [119] J. F. Ziegler. *The Stopping and Ranges of Ions in Matter*, volume 3. Pergamon Press, 1980.
- [120] H. Paul and A. Schinner. *Nuclear Instruments and Methods in Physics Research Section B: Beam Interactions with Materials and Atoms*, 209:252–258, 2003.
- [121] W. M. Currie. *Nucl. Instr. Methods*, 73:173 – 185, 1969.
- [122] URL <www.srim.org>.
- [123] P. H. Stelson, F. K. McGowan, R. L. Robinson, and W. T. Milner. *Phys. Rev. C*, 2:2015–2022, 1970.
- [124] A. Kundu, S. Santra, A. Pal, et al. *Phys. Rev. C*, 100:034327, 2019.
- [125] Aage Bohr and Ben R. Mottelson. *Phys. Rev.*, 89:316–317, 1953.
- [126] G. Watanuki, Y. Miyanishi, and M. Yasuno. *Progress of Theoretical Physics*, 59:790–803, 1978.
- [127] G. Scharff-Goldhaber, C. B. Dover, and A. L. Goodman. *Ann. Rev. Nucl. Sci.*, 26:239–317, 1976.

-
- [128] R. Graetzer, S. M. Cohick, and J. X. Saladin. *Phys. Rev. C*, 12:1462–1468, 1975.
- [129] E. Teller and J. A. Wheeler. *Phys. Rev.*, 53:778–789, 1938.
- [130] A. Bohr and B. R. Mottelson. *Kgl. Dan. Vidensk. Selsk. Mat. Fys. Medd.*, 27(16):1 – 174, 1953.
- [131] A. W. Sunyar. *Phys. Rev.*, 98:653–657, 1955.
- [132] M. A. J. Mariscotti, G. Scharff-Goldhaber, and B. Buck. *Phys. Rev.*, 178:1864–1886, 1969.
- [133] Y. P. Varshni and S. Bose. *Phys. Rev. C*, 3:958–960, 1971.
- [134] P. H. Stelson and L. Grodzins. *Nucl. Data Sheets A*, 1:21 – 102, 1965.
- [135] A. Kundu, S. Santra, A. Pal, et al. *Phys. Rev. C*, 95:034615, 2017.
- [136] F. Pougheon and P. Roussel. *Phys. Rev. Lett.*, 30:1223, 1973.
- [137] D. M. Brink. *Phys. Lett. B*, 40:37, 1972.
- [138] G. Morrison. *Journal de Physique Colloques*, 33:C5 111–C5 126, 1972.
- [139] R. F. Casten, E. R. Flynn, Ole Hansen, and T. J. Mulligan. *Nucl. Phys. A*, 180:49–68, 1972.
- [140] M. J. Bechara and O. Dietzsch. *Phys. Rev. C*, 12:90, 1975.
- [141] E. J. Schneid, A. Prakash, and B. L. Cohen. *Phys. Rev.*, 156:1316, 1967.
- [142] M. Conjeaud, S. Harar, and Y. Cassagnou. *Nucl. Phys. A*, 117:449–471, 1968.
- [143] T. Ishimatsu, K. Yagi, H. Ohmura, et al. *Nucl. Phys. A*, 104:481–496, 1967.

-
- [144] J. P. Schiffer, S. J. Freeman, J. A. Caggiano, et al. *Phys. Rev. Lett.*, 92:162501, 2004.
- [145] J. P. Schiezer, G. C. Morrison, R. H. Siemssen, and B. Zeidman. *Phys. Rev.*, 164:1274, 1967.
- [146] S. Cohen and D. Kurath. *Nucl. Phys. A*, 101:1, 1967.
- [147] G. Tungate, D. Kramer, R. Butsch, et al. *J. Phys. G: Nucl. Phys.*, 12:1001, 1986.
- [148] K. Becker, K. Blatt, H. J. Jansch, et al. *Nucl. Phys. A*, 535:189, 1991.
- [149] Md. Moin. Shaikh, S. Roy, S. Rajbanshi, et al. *Phys. Rev. C*, 90:024615, 2014.
- [150] P. K. Rath, S. Santra, N. L. Singh, et al. *Phys. Rev. C*, 79:015601(R), 2009.
- [151] P. K. Rath, S. Santra, N. L. Singh, et al. *Nucl. Phys. A*, 874:14–31, 2012.
- [152] M. Dasgupta, P. R. S. Gomes, D. J. Hinde, et al. *Phys. Rev. C*, 70:024606, 2004.
- [153] M. Dasgupta, D. J. Hinde, K. Hagino, et al. *Phys. Rev. C*, 66:041602(R), 2002.
- [154] A. Kumari and R. Kharab. *Nucl. Phys. A*, 941:38 – 47, 2015.
- [155] P. K. Rath, S. Santra, N. L. Singh, et al. *Phys. Rev. C*, 88:044617, 2013.
- [156] A. Kundu, S. Santra, A. Pal, et al. *Phys. Rev. C*, 94:014603, 2016.
- [157] H. Kumawat, V. Jha, V. V. Parkar, et al. *Phys. Rev. C*, 86:024607, 2012.
- [158] M. K. Pradhan, A. Mukherjee, P. Basu, et al. *Phys. Rev. C*, 83:064606, 2011.
- [159] C. S. Palshetkar, Shital Thakur, V. Nanal, et al. *Phys. Rev. C*, 89:024607, 2014.

-
- [160] Md. M. Shaikh, S. Roy, S. Rajbanshi, et al. *Phys. Rev. C*, 93:044616, 2016.
- [161] A. Mukherjee, Subinit Roy, M. K. Pradhan, et al. *Phys. Lett.B*, 636:91–95, 2006.
- [162] L. F. Canto, P. R. S. Gomes, J. Lubian, et al. *J. Phys. G: Nucl. Part. Phys.*, 364:015109, 2009.
- [163] C. Y. Wong. *Phys. Rev. Lett.*, 31:766, 1973.
- [164] P. Talon, N. Alamanos, M. Laméhi-Rachti, et al. *Nucl. Phys. A*, 359:493 – 508, 1981.
- [165] J. R. Leigh, M. Dasgupta, D. J. Hinde, et al. *Phys. Rev. C*, 52:3151–3166, 1995.
- [166] R. G. Stokstad, Y. Eisen, S. Kaplanis, et al. *Phys. Rev. Lett.*, 41:465–469, 1978.
- [167] A. B. Kurepin and R. M. Lombard. *Phys. Lett. B*, 37:55 – 57, 1971.
- [168] J. P. Fernandez-Garcia, M. Cubero, L. Acosta, et al. *Phys. Rev. C*, 92:044608, 2015.
- [169] M. Cubero, J. P. Fernandez-Garcia, M. Rodriguez-Gallardo, et al. *Phys. Rev. Lett.*, 109:262701, 2012.
- [170] A. Sanetullaev, R. Kanungo, J. Tanaka, et al. *Phys. Lett. B*, 755:481, 2016.